Semitransparent perovskite solar cells for perovskite-based tandem photovoltaics

Zur Erlangung des akademischen Grades eines

Doktor-Ingenieurs

von der KIT-Fakultät für
Elektrotechnik und Informationstechnik
des Karlsruher Instituts für Technologie (KIT)

angenommene

Dissertation

von

Ihteaz Muhaimeen Hossain (M.Sc.)
geb. in Dhaka

Tag der mündlichen Prüfung:	23. Oct 2020
Hauptreferent:	Dr. Ulrich W. Paetzold
Korreferenten:	Prof. Dr. Bryce S. Richards
	Prof. Dr. Heinz Kalt

Kurzfassung

Erneuerbare Energietechnologien auf der Grundlage der Photovoltaik werden in Zukunft eine bedeutende Rolle bei der Deckung des weltweiten Energiebedarfs spielen. Dazu muss der Wirkungsgrad der etablierten und marktbeherrschenden Photovoltaik-Technologie - kristallinem Silizium (c-Si) - erhöht werden. Der Wirkungsgrad von c-Si-Solarzellen ist jedoch bereits nahe an seiner fundamentalen Grenze von ≈29%, und daher stellen weitere Verbesserungen aus wissenschaftlicher Sicht eine Herausforderung dar. Eine Strategie zur weiteren Verbesserung des Wirkungsgrades ist die Kombination eines Halbleiters mit hoher Bandlücke (≈1.7 eV) mit einer c-Si-Einfachsolarzelle (1.1 eV) in einer Tandemkonfiguration mit vier Anschlüssen (4T). Vielversprechende Kandidaten sind Organometall-Halogenid-Perowskit-Materialien, die in letzter Zeit aufgrund ihrer potenziell niedrigen Herstellungskosten und hervorragenden optoelektronischen Eigenschaften große Aufmerksamkeit hervorgerufen haben. Perowskit/c-Si-Tandemsolarzellen haben bereits fast die fundamentale Wirkungsgrad-Grenze von c-Si-Single-Junction-Solarzellen überschritten, wobei weitere Verbesserungen absehbar sind. Um den Wirkungsgrad von Perowskit/c-Si-Tandemsolarzellen weiter zu verbessern, müssen einige zentrale Herausforderungen bewältigt werden. Diese Herausforderungen können in optische und elektrische Verluste kategorisiert werden. Zu den optischen Verlusten gehören parasitäre Absorptions- (vorwiegend durch die Elektroden aus transparentem leitfähigem Oxid (TCO)) und Reflexionsverluste innerhalb des Schichtstapels sowie die Verwendung einer nicht idealen Bandlücke des Perowskit-Absorbers. Elektrische Verluste entstehen durch nichtstrahlende Rekombinationsprozesse innerhalb des Bulk-Materials oder an den Grenzflächen innerhalb des Perowskit-Schichtstapels sowie durch nicht optimale Extraktion der erzeugten Ladungsträger.

Der Schwerpunkt dieser Arbeit liegt auf der Minimierung der optischen Verluste, indem ihr Ursprung untersucht und neue Strategien zu ihrer Überwindung entwickelt werden. Als Ausgangspunkt wird eine neuartige hauseigene und vielseitige, bei niedrigen Temperaturen prozessierbare, auf Nanopartikeln basierende Elektronentransportschicht entwickelt, um Perowskit-Einfachsolarzellen auf TCOs mit geringer parasitärer Absorption herzustellen. Perowskit-Solarzellen mit dieser Elektronentransportschicht weisen Wirkungsgrade von über 18% auf. Weiterhin werden in dieser Arbeit zur weiteren Verbesserung des Lichteinfangs in Tandem-Solarzellen neuartige nanophotonische Frontelektroden und alternative TCOs entwickelt. Zunächst wird gezeigt, dass die nanophotonischen Frontelektroden nicht nur die Kurzschlussstromdichte in der Perowskit-Top-Solarzelle verbessern, sondern auch die Transmission im nahen Infrarot-Bereich erhöhen und damit den Wirkungsgrad der c-Si-Bottom-Solarzelle stark verbessern. Zweitens werden qualitativ hochwertige alternative TCOs mit einer hauseigenen Sputter-Technik erforscht, die in Bezug auf Reflexions- und parasitäre Absorptionsverluste kommerziell erhältliche TCOs übertreffen. Diese Konzepte werden angewendet um hocheffiziente 4T-Perowskit/c-Si-Tandemsolarzellen mit Wirkungsgraden von bis zu 27.3% herzustellen, was nicht nur den derzeitigen Rekord-Wirkungsgrad von c-Si-

Einfachsolarzellen übertrifft, sondern auch einer der bisher höchsten Werte für 4T-Perowskit/c-Si-Tandemarchitekturen ist. Darüber hinaus wird zum ersten Mal eine detaillierte experimentelle Untersuchung der optimalen Bandlücke des Perowskit-Absorbers in realistischen 'state-of-the-art‘ 4T-Perowskit/c-Si und Perowskit/CIGS-Tandemsolarzellen durchgeführt. Es wird gezeigt, dass ein breiter Bereich von Bandlücken zwischen 1.65-1.74 eV zu ähnlichen Wirkungsgraden führt, was die Anforderungen an die exakte Bandlücke des Perowskit-Absorbers in hocheffizienten Tandemsolarzellen lockert.

Abstract

Renewable energy technologies based on photovoltaics will play a significant role to meet the global electricity demand in the future. In order to meet this, the power conversion efficiency (PCE) of the established and market dominating photovoltaic technology – crystalline silicon (c-Si) – needs to be increased. However, the PCE of c-Si solar cells is already close to its fundamental limit of ≈29% and, therefore, further improvements are challenging from a scientific point of view. One strategy to further improve the PCE is to combine a wide-bandgap semiconductor (≈1.7 eV) with a c-Si solar cell (1.1 eV) in a four-terminal (4T) tandem configuration. Promising candidates for the wide-bandgap semiconductor are organometal halide perovskite materials that gained significant attention recently due to their potentially low fabrication costs and outstanding optoelectronic properties. To date, perovskite/c-Si tandem solar cells have almost surpassed the fundamental PCE limit of single-junction c-Si solar cells with further improvements being foreseeable. In order to improve the PCE of perovskite/c-Si tandem solar cells, some key challenges need to be overcome. These challenges can be categorized into optical and electrical losses. Optical losses involve parasitic absorption (predominately by the transparent conductive oxide (TCO) electrodes) and reflection losses within the layer stack as well as the use of non-ideal bandgap of the perovskite absorber. Electrical losses arise from non-radiative recombination processes inside the bulk or at the interfaces of the perovskite layer stack or poor extraction of the generated charge carriers.

In this thesis, a focus is set on tackling the optical losses by investigating their origin and developing novel strategies to overcome them. As a starting point, a novel in-house and versatile low temperature processable nanoparticle-based electron transport layer is developed in order to fabricate single-junction perovskite solar cells on TCOs that exhibit low parasitic absorption losses. Perovskite solar cells with this electron transport layer demonstrates PCEs above 18%. Next, to further improve light harvesting in tandem solar cells, novel nanophotonic front electrodes and alternative TCOs are developed. First, it is shown that the nanophotonic front electrodes not only improve the short-circuit current density in the perovskite top solar cell but also increase the near infrared transmission and, consequently, strongly improve the PCE of the c-Si bottom solar cell. Second, high-quality alternative TCOs are explored using an in-house sputtering technique that outperform commercially available TCOs in terms of reflection and parasitic absorption losses. Employing these concepts, highly efficient 4T perovskite/c-Si tandem solar cells with PCEs up to 27.3% are fabricated, which not only exceeds the current record PCE of single-junction c-Si solar cells, but also is one of the highest reported for 4T perovskite/c-Si tandem architectures to date. Furthermore, for the first time, a detailed experimental investigation about the optimum bandgap of the perovskite absorber in realistic 4T state-of-the-art perovskite/c-Si and perovskite/CIGS tandem solar cells is performed. It is shown that a wide range of bandgaps between 1.65-1.74 eV yields similar PCEs, which releases constraints on the exact bandgap of the perovskite absorber in highly efficient tandem solar cells.

Table of Contents

1. Introduction

Since pre-industrial times, earth's surface temperature has increased by 1.0 °C.[1] This is primarily due to the burning of fossil fuels such as coal, natural gas and oil for electricity and heat.[2] Burning these natural resources releases carbon dioxide, methane and other greenhouse gasses into the atmosphere that trap sun's irradiation and increase overall earth's surface temperature.[3] This rise in the temperature is already showing significant effects such as the melting of the Arctic and Antarctic ice caps,[1,4] which if not stopped, could reshape out planet. Further consequences include an increase in the sea level, which can have devastating effects on low-lying coastal wild-lives and habitats, impact on biodiversity and ecosystem, ocean acidity, etc.[1,5] Therefore, initiatives must be taken to reduce our carbon footprint.[6]

Even with our climate under threat from greenhouse gasses, global electricity needs are expected to increase.[7] Projections estimate that by 2040, countries like China, India and other developing nations will be the major consumer of electricity, while demand from more developed nations remains fairly unchanged.[7] Therefore, renewable sources such as wind and solar must play a crucial role to provide the required electricity demand and sustain the future of our earth. Today, solar energy contributes to only a small but respectable fraction of the total electricity generation (3%), but the future electricity demand requires it to become a major contributor of electricity.[7] It is expected that by 2040, solar energy will surpass the global power generation capacity of both coal and gas.[7]

Meeting the energy demand in future will be challenging if sufficient development in the solar energy technologies is not achieved with a focus on the economics of power generation. Therefore, a reduction in the levelized cost of electricity (LCOE) is required, which is defined as the average cost of electricity by a technology over its lifetime. Although a strong economic viability of solar photovoltaic (PV) was shown in a report in 2018 for Germany,[8] the LCOE can further be reduced by increasing the power conversion efficiency (PCE) of solar cells. In this regard, a reduction in the LCOE could be limited for the currently established silicon PV as its PCE is already very close to its fundamental limit. One approach to surpass this is to combine highly efficient wide-bandgap semitransparent perovskite solar cell (s-PSC) as a top cell in conjunction with a crystalline-silicon (c-Si) solar cell as a bottom cell to form a tandem solar cell as shown in **Fig. 1.1**.

Perovskite PV is a thin-film based technology with perovskite crystals as the absorber material. This PV technology has shown enormous progress[9,10] and to date demonstrates PCE > 25% in solution-processed opaque devices (**Fig. 1.2**).[10] Additional advantages for perovskite absorbers include feasibility of upscaling from laboratory small scale to large areas via roll-to-roll processing,[9,11] which can reduce the manufacturing cost. Furthermore, owing to its wide bandgap feature, s-PSCs can be combined with a bottom solar cell in a tandem architecture.[12] In combination with c-Si solar cells, PCEs of perovskite-based tandem devices have already surpassed the record PCE of a single-junction crystalline-

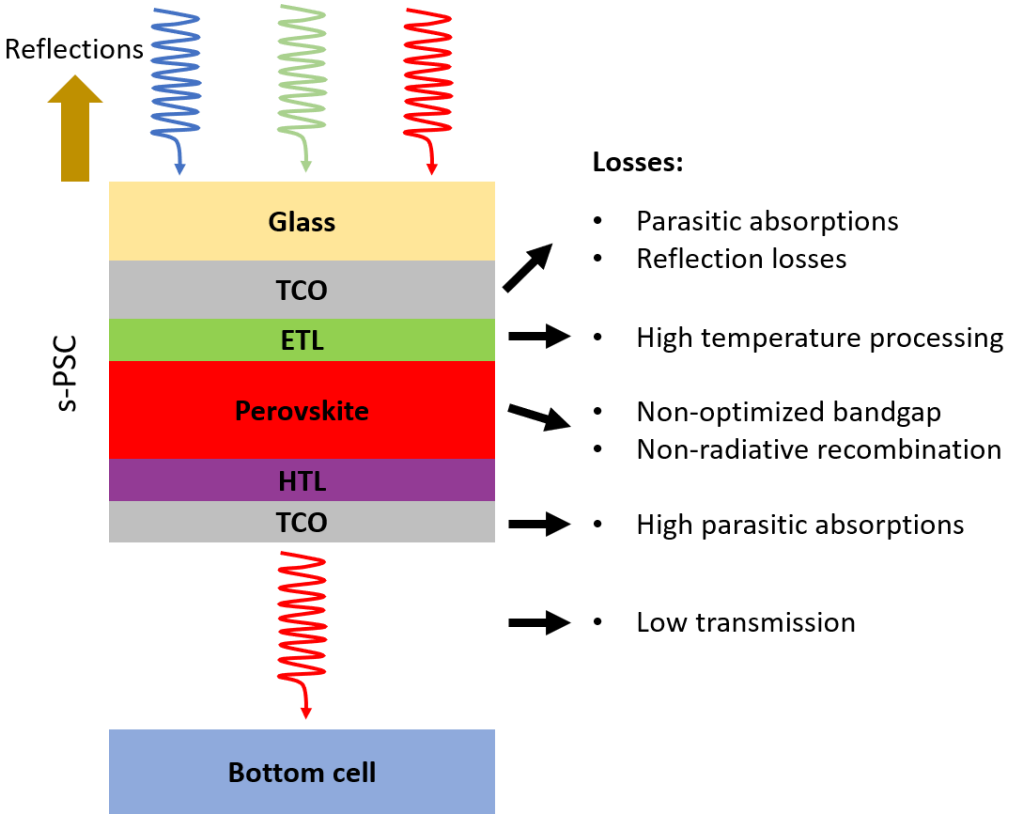

Fig. 1.1. Schematic representation of four-terminal tandem solar cell with semitransparent perovskite solar cell (s-PSC) as the top cell. High parasitic absorption and reflection losses lead to low transmission in a top s-PSC. Additional challenges include high temperature processed electron transport layer, non-optimum bandgap and high non-radiative recombination losses in the perovskite absorber.

silicon solar cell to date.[10,13,14] Not only this has been shown for perovskite/c-Si solar cells but also for perovskite/CIGS solar cells as well.[10] However, there is still room for further developments. The primary losses that currently limit the PCE are: (i) optical losses due to reflections from various interfaces,[15] parasitic absorptions within the layer stack,[16] and non-ideal bandgaps,[14,17,18] (ii) non-radiative recombination losses occurring inside the bulk or at the interfaces of the perovskite absorber layer,[19–27] and poor extraction and transport of charges by charge transport layers.[28–30] Fig. 1.1 illustrates the various layers that are responsible for some of these losses in a perovskite-based tandem device.

In regard to the extraction of electrons, PSCs conventionally use electron transport layers (ETLs) comprising of mesoporous TiO_2,[28–35] which resulted in some of the highest PCEs for opaque perovskite solar cells (o-PSCs).[31–34] From an optical point of view for obtaining high PCE in tandem architectures, mesoporous TiO_2 is undesirable. Since it can only be processed on fluorine-doped tin oxide (FTO) electrode, which is highly absorbing both in the visible and in the near infrared wavelengths, it will result in reduced transmission in s-PSCs and hence, loss in the PCE of tandem devices. The underlying reason of utilizing FTO electrode is the requirement of a high annealing temperature (> 450 °C) that ensures satisfactory layer quality of mesoporous TiO_2 ETL.[31–34] Because of this, transparent conductive oxides (TCOs) that exhibit reduced parasitic absorption losses[36,37] as well as

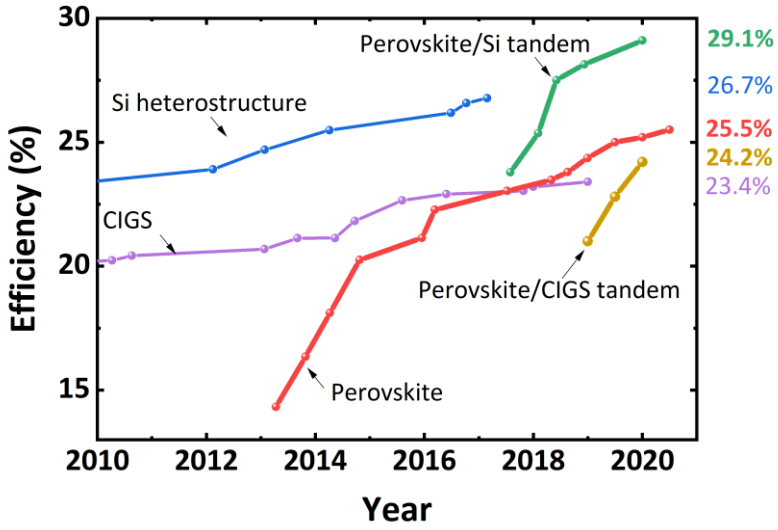

Fig. 1.2. Efficiency chart of various solar energy technologies. Figure adapted from NREL efficiency chart.[10]

low-cost flexible plastic substrates required for future roll-to-roll processing, are not compatible. Therefore, alternative ETLs must be investigated to overcome the limitations of high temperature processing in this layer. Thus, in this thesis, the following research question (RQ) is investigated:

RQ 1 – Can pre-synthesized nanoparticle-based TiO_2 and SnO_2 be used as an alternative electron transport layer to fabricate efficient perovskite solar cells?

In order to improve the PCE in perovskite-based tandem devices, reflection and parasitic absorption losses must be minimized. The prominent parasitic absorption loss in a top s-PSC stems from the TCO electrodes (both front and rear).[15,16,36–38] Reflection losses originate from various interfaces that forms the tandem stack, however, a considerable share is associated to the TCOs.[39,40] Both absorption and reflection losses decrease the transmission of the top s-PSCs, leading to a reduction in the PCE of the bottom solar cells in tandem architectures and hence, an overall reduction in device PCE. Thus, further investigations are required in the field of TCO electrodes to reduce these optical losses for tandem PV. In this regard, light management with nanostructures – textures significantly smaller than the wavelength of visible light – can be employed to reduce reflections and improve transmission.[41–43] Besides this, alternative materials can be explored that exhibit reduced optical losses. Several materials show such properties, which would be beneficial for perovskite-based tandem applications, if employed.[36,37] Therefore, in order to reduce these losses, this thesis investigates the following research question:

RQ 2 – What is the role of nanophotonic light management concepts or alternative transparent conductive oxide electrodes in improving the PCE of perovskite-based tandem devices?

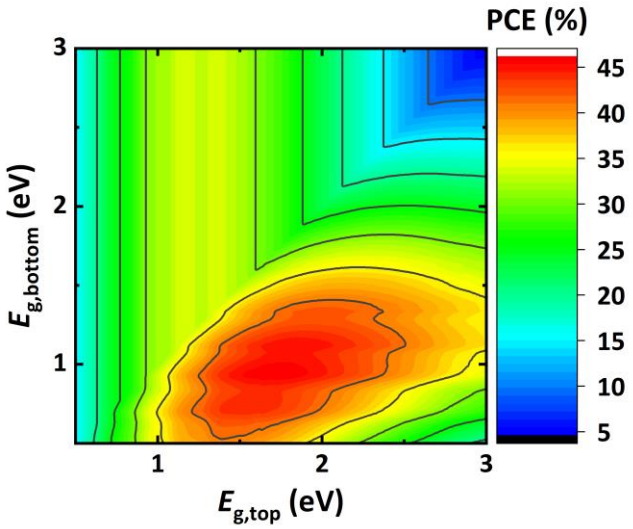

Fig. 1.3. Theoretical power conversion efficiency (PCE) as a function of top and bottom sub-cell bandgap in four-terminal (4T) architecture without parasitic absorption or transmission losses.

Another aspect which is highly important to consider both from optical and electrical point of view for maximizing the PCE in a tandem device architecture is the optimum bandgap of the perovskite absorber. In optical terms, detailed-balance calculations[17,18] and energy yield modelling[44] suggest a wide-range of bandgaps are suitable for the top perovskite absorber for maximizing the PCE in a perovskite-based four-terminal tandem device architecture. A four-terminal tandem device implies that the top solar cell and the bottom solar cell are optically connected as one device but can work independently (see discussions in chapter 2, section 2.3 and 2.4 for more details). A bandgap between 1.60-1.85 eV is assumed to be the optimum for the top absorber in such a tandem device (see **Fig. 1.3**). Only one experimental study regarding the optimum bandgap was carried out for perovskite/CIGS tandem solar cells, the resultant net efficiencies of which, were not reflected in their reported champion efficiency.[45] From an electrical standpoint, one needs to consider that widening the bandgap (> 1.73 eV) of the top perovskite absorber is detrimental to device performance due to extensive non-radiative recombination processes in such architectures,[19–27] which are neglected in simulations. Therefore, a detailed experimental investigation is necessary with real prototypes to examine the effect of various bandgaps in the optimum range of the top perovskite absorber to maximize the PCE in perovskite-based tandem solar cells. Thus, in this thesis, the following research question is investigated:

RQ 3: What is the optimal bandgap of the perovskite absorber in the top s-PSC in real prototype devices for maximizing the PCE of perovskite-based tandems?

Outline of the thesis

This introductory chapter is followed by chapter 2, which provides the reader with a review of the fundamentals required to follow the content of this thesis. The chapter discusses

the working principles governing single-junction and tandem solar cells. Furthermore, the chapter outlines the material properties of perovskite absorbers and light management within a solar cell.

In chapter 3, the various fabrication methods and the characterization tools used in this thesis are introduced.

Chapter 4 deals with *RQ 1* and presents a study for perovskite solar cells with two different types of ETLs based on nanoparticles: TiO_2 and SnO_2. These nanoparticle-based ETLs are deposited at a low temperature (up to 150 °C), enabling deposition on TCO electrodes with low parasitic absorption losses. A comparative study between the two ETLs is also presented in this chapter.

Chapter 5 deals with *RQ 2*. A nanophotonic light management concept is applied by nano structuring TCOs to reduce reflection losses and to improve the PCE in perovskite/c-Si tandem devices.

Chapter 6 presents further research in improving the performance of perovskite-based tandem PV. In the first part of this chapter, a detailed experimental investigation is carried out with real prototype devices to investigate *RQ 3*. In the second part, alternative TCO electrodes are explored for investigating *RQ 2* and improving the PCE in perovskite/c-Si tandem devices.

In chapter 7, the key results of this thesis are summarized, and an outlook is presented.

2. Fundamentals

This chapter discusses the fundamental working principle of solar cells. Furthermore, it includes a brief introduction to perovskite solar cells, tandem architectures and light management.

2.1 Working principle of solar cells

Semiconductor physics of a solar cell

While the photovoltaic market is dominated by crystalline silicon solar cells that employ a p-n architecture, a wide range of solar cells with other architectures or layer sequences exist in the literature.[46–48] For instance, organic solar cells with bulk heterojunctions and amorphous silicon solar cells employ a p-i-n layer sequence. The focus of this thesis which is the perovskite solar cells (PSCs), also use the p-i-n layer sequence. In a p-i-n layer sequence, an absorber layer (denoted by i) is sandwiched between a hole transport layer (denoted by p) and an electron transport layer (denoted by n). Two electrodes, one of which is at least optically transparent, are used to extract the photo-generated charge carriers of the solar cell to an external load. The basic working principle involves three steps as illustrated in **Fig. 2.1**a: (i) absorption of incident photons by an absorber material, (ii) generation of free charge carriers, and (iii) extraction of the charge carriers through selective contacts.

Depending on the energy of the incoming photon and the bandgap of the absorber material, either of the following processes occur (see Fig. 2.1b): (i) absorption of photons with energy of the photon equal to or higher than the bandgap of the absorber and thereby, exciting an electron from the valence band to the conduction band and hence, leaving a hole (which behaves like a positively charged particle) in the valence band, or (ii)

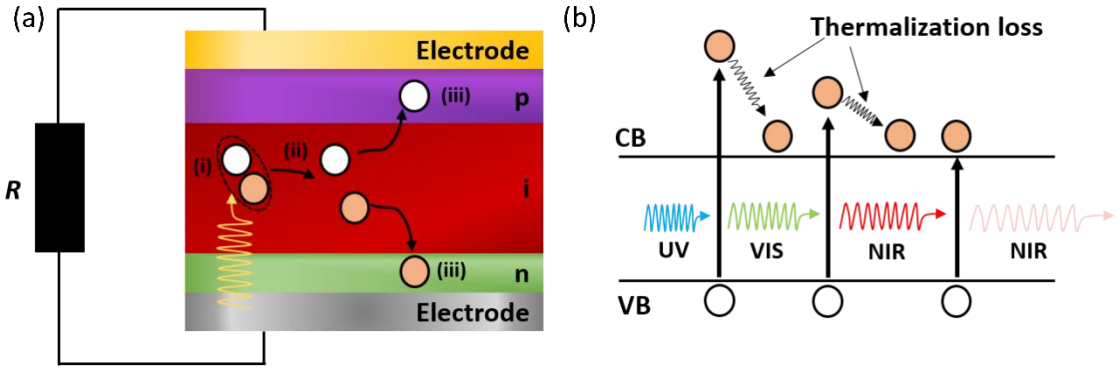

Fig. 2.1: (a) Schematic illustration of the basic working principle in a p-i-n heterostructure layer sequence solar cell. The physical process (i) denotes absorption of photons, (ii) generation of free charge carriers and (iii) selective extraction of charges. (b) Visualization of the absorption process in an absorber for photons with various energies. If the energy of the photon is above the bandgap, the excited electron loses the excess energy by thermalization. If the energy of the photon is lower than the bandgap, it is transmitted. CB and VB stands for conduction band and valence band, respectively.

transmission of photons when their energy is lower than the bandgap. If the photon energy exceeds than the bandgap, the excited electron in the conduction band undergoes a subsequent relaxation to the edge of the conduction band through lattice vibrations (phonons). This process is known as thermalization (see Fig. 2.1b for a comparison between ultra-violet (UV), visible (VIS) and near infrared (NIR) radiations). This limits the maximum energy harvested by each photon to the bandgap of the absorber material.

The absorption process also depends on the energy of the incoming photons. Higher energy photons are absorbed within a short distance inside the absorber, while lower energy photons are absorbed deeper inside the material (see absorption coefficient of a typical perovskite film in Fig. 2.2). This implies that the thickness of the absorber should be sufficiently large (especially for low energy photons) to maximize the absorption process. To quantify the amount of light absorbed by an absorber for a given thickness, the Beer-Lambert law is used:[49]

$$I(E,z) = I_0 e^{-\alpha(E)z} \tag{2.1}$$

where, $I(E, z)$ is the intensity of light for a photon with certain energy (E) after propagating a distance (z) inside the semiconductor and I_0 is the incident intensity.

Subsequent to absorption, both electrons and holes can recombine, if not extracted. The fundamental bulk recombination processes that exist in a typical solar cell are bimolecular (radiative), Auger (non-radiative) and Shockley-Read-Hall recombination (non-radiative). Both bimolecular radiative and Auger recombination are inevitable processes. Bimolecular radiative recombination occurs when an electron recombines with a hole and emits a photon. It is pronounced in direct bandgap semiconductors and light emitting diodes (LEDs) rely on this mechanism. The Auger recombination requires high charge carrier concentrations, which often exists due to heavy doping or high level injection under

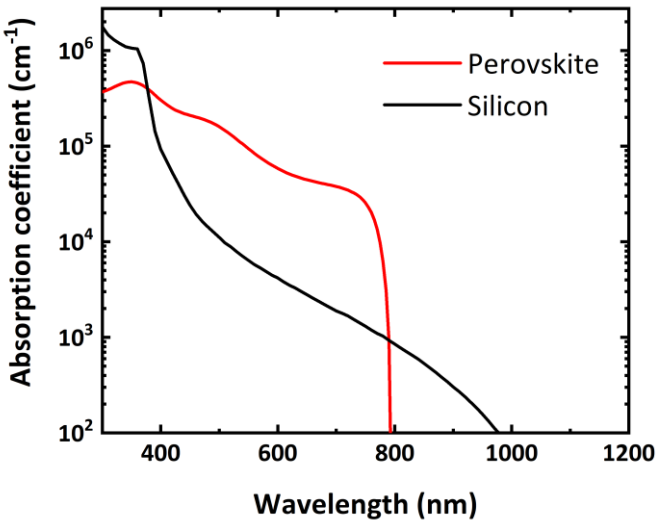

Fig. 2.2: Absorption coefficients of a perovskite film and silicon absorber. The data are obtained from references [211,212].

concentrated sunlight. While in silicon solar cells operated under 1 sun conditions, Auger recombination process is of relevance and sets the fundamental power conversion efficiency limit, for perovskite solar cells, under such operating conditions, it is irrelevant due to the presence of low charge carrier concentration. The Shockley-Read-Hall recombination is a non-radiative trap-assisted recombination process and is governed by defects present inside the bulk of the absorber layer. Thus, one of the main challenges for fabricating highly efficient solar cells is to reduce defect densities and suppress the Shockley-Read-Hall recombination. A key characteristic for the quality of an absorber is the charge carrier diffusion length (l_{diff}), which denotes the average distance electrons and holes diffuses in the semiconductor in between photo-generation of charge carriers and recombination. Therefore, it is very essential to consider a smaller thickness of the absorber to reduce the recombination processes for an efficient solar cell operation. Therefore, given the conditions for maximizing the absorption as well as reducing the recombination process, the thickness (t) of the absorber should be:

$$1/\alpha < t < l_{\text{diff}} \tag{2.2}$$

Typical charge carrier diffusion lengths for organometal halide perovskites are in the order of several microns, whereas typical thicknesses of the absorber in perovskite solar cells is only several hundred of nanometers.[50] Thus, from this perspective, perovskite absorbers are an excellent material for solar cell application.

Band diagram

Perovskite solar cells have a p-i-n heterostructure layer sequence but care must be taken in order to understand its working principle. While conventional p-i-n (e.g. amorphous silicon solar cells) solar cells exhibit both diffusion (due to the chemical potential) and drift currents (due to the presence of a built-in voltage), the latter is less relevant for PSCs.

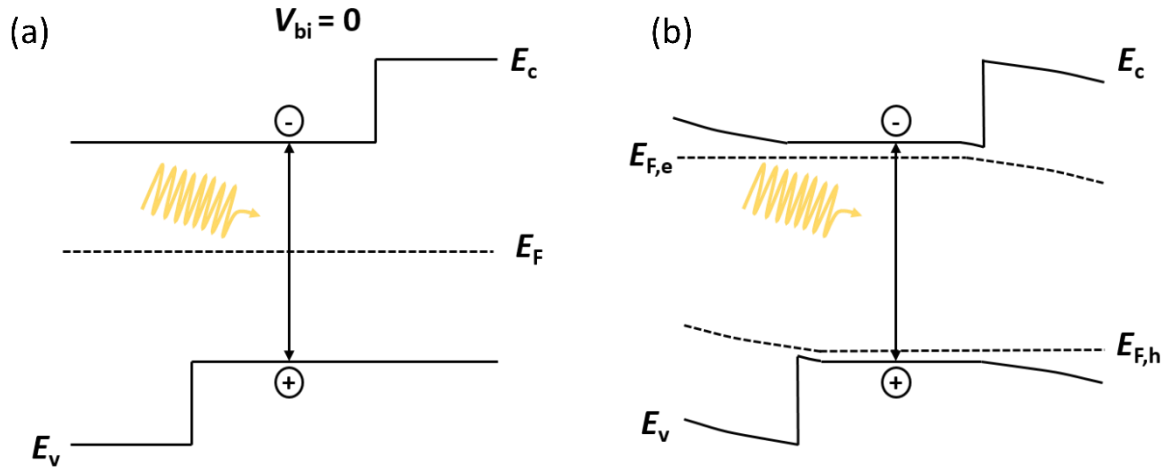

Fig. 2.3: Schematic illustrations of the band diagram in a p-i-n heterostructure illuminated under (a) short-circuit and (b) at an operating condition. Schematics adapted from [213]. V_{bi} stands for built-in voltage.

Several studies have shown that a flat band scenario describes best the working principle in PSCs,[51,52] implying that the charge separation occurs mostly due to the presence of the chemical potential, i.e., diffusion of charges. Furthermore, as discussed by Würfel *et al*. in great detail, that it is the selectivity of the charge transport layers that plays the most crucial role for an efficient charge separation, instead of the built-in voltage.[53] The selectivity is achieved by a large electron (hole) conductivity in the n-type (p-type) layer, allowing electrons (holes) to flow easily while efficiently blocking holes (electrons). By numerical simulations, Würfel *et al*. even demonstrated that a p-i-n (or n-i-p) solar cell could be very efficient if there is no built-in voltage at all or if a small built-in voltage is even opposing the diffusion of charge carries. Simplified schematics of the band diagram for a flat band solar cell under illumination at short-circuit conditions and at operating condition are illustrated in **Fig. 2.3**. Under continuous illumination and at short-circuit conditions, the fermi energy (E_F) stays constant throughout the device and the additional photo-generated electrons and holes are efficiently extracted by the contact layers (Fig. 2.3a), simply by introducing sufficiently high band offsets. At this condition, a net current (I_{ph}) flows through the device. Under continuous illumination and at an operating condition, the Fermi energy splits into quasi-Fermi levels for electrons residing at energy $E_{F,e}$ and holes at energy $E_{F,h}$ with $E_{F,e}$ and $E_{F,h}$ aligning with the Fermi levels of the n-type and p-type layers, respectively (Fig. 2.3b). At this condition, both voltage and current are generated simultaneously by the solar cell and a power is delivered.

Characteristics of a solar cell

The operating principle of a solar cell can be represented by a simple one-diode or two-diode model (**Fig. 2.4**a,b). The photocurrent is represented by a current source in parallel to one or two diodes with a series resistance (R_s) and a shunt resistance (R_{sh}). The presence of R_s is due to the fact that the photogenerated charges experience some resistances as they are injected in their selective contacts, and transported through the transport layers and the electrodes. The R_{sh} arises when the photogenerated charges flow within the device through grain boundaries, defects or direct contact between the two electrodes. Such losses are represented by a current (I_{sh}) flowing through a parallel or shunt resistance. The simple one-diode model can already effectively describe behavior of good solar cells. However, the two-diode model can result in a further description of experimental data as it includes the recombination mechanisms of the charge carriers as well. The relation between the net current I and the voltage V is given by the Shockley equation:[49]

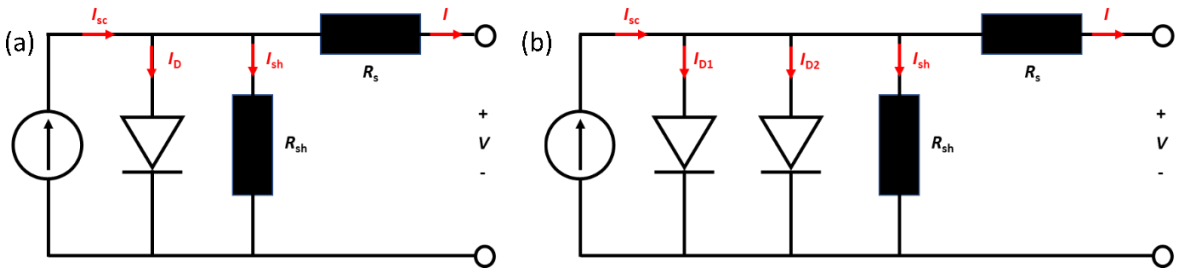

Fig. 2.4: Schematic illustration of (a) one-diode and (b) two-diode model of a solar cell.

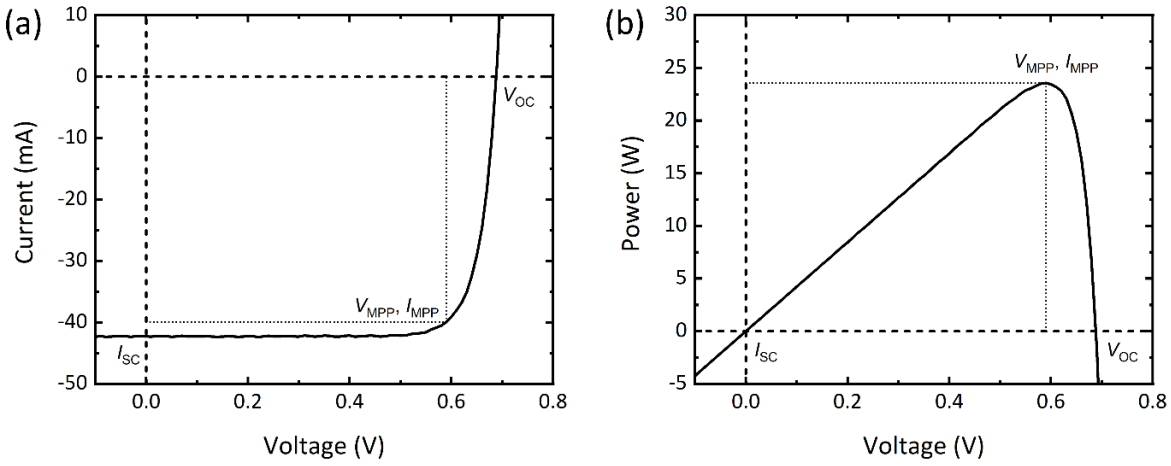

Fig. 2.5: (a) Current-voltage (*I-V*) characteristic curve and (b) power dependency of a typical silicon solar cell. At voltage $V = 0$, the current flowing through the solar cell is short-circuit current, I_{SC}. At current $I = 0$, the voltage across the solar cell is the open-circuit voltage, V_{OC}. Both at $I = I_{SC}$ and $V = V_{OC}$, the output power $P = 0$. The output power maximizes at the maximum power point where $I = I_{MPP}$ and $V = V_{MPP}$.

$$I(V) = I_0 e^{\frac{qV}{k_B T}-1} - I_{ph} \tag{2.3}$$

where, I_0 is the dark saturation current, q is the charge of an electron, k_B is the Boltzmann constant, V is the voltage, I_{ph} is the photocurrent and T is the temperature of the solar cell.

The performance of a solar cell is determined from its *I-V* characteristics. **Fig. 2.5** shows a typical *I-V* curve and the output power (*P*) of a solar cell. The *I-V* characteristic curve follows the same pattern similar to a diode with an offset of I_{SC}. As the voltage increases from short-circuit condition ($V = 0$ V), power ($P = IV$) delivered by the solar cell increases until it maximizes. This is defined as the maximum power point (MPP) of the solar cell. At this point, the current flowing through the device is $I = I_{MPP}$ at a voltage $V = V_{MPP}$, resulting a power $P_{MPP} = I_{MPP} \times V_{MPP}$. Further increase in the voltage reduces the output I_{ph} as the current through the diode, I_d, increases. As a result, *P* decreases. At open-circuit condition, $I_{ph} = I_d$ and the *P* is zero. In order to maximize the power conversion efficiency (PCE) in real solar cells or solar modules, a PID controller is equipped in a feedback loop such that the device always operates close to the MPP. The area under the *I-V* characteristics or the ratio between P_{MPP} to the I_{SC} and V_{OC} is defined as the fill factor (*FF*) of a solar cell and is given by:[49]

$$FF = \frac{P_{MPP}}{I_{SC}.V_{OC}} \tag{2.4}$$

Both R_s and R_{sh} influence the *FF* of a solar cell. Ideally, in order to maximize *FF*, the R_s and R_{sh} should be low and high, respectively. The PCE of a solar cell can then be represented as:[49]

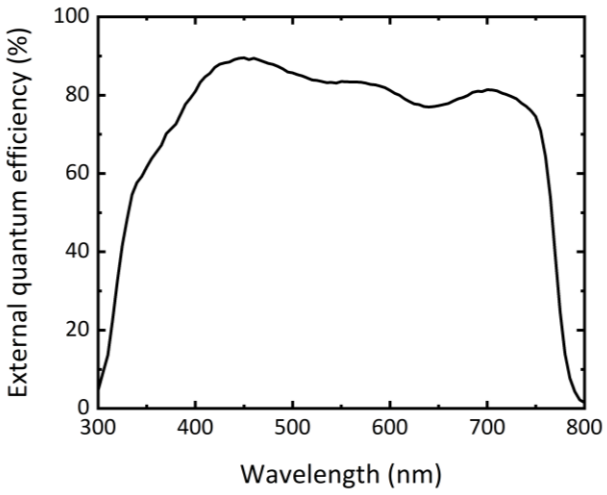

Fig. 2.6: External quantum efficiency of a typical perovskite solar cell.

$$\mathrm{PCE} = \frac{I_{SC}.V_{OC}.FF}{P_{input}} \tag{2.4}$$

where, P_{input} is the incident power of light. Under standardized test condition, an irradiation of 1000 $\mathrm{Wm^{-2}}$ with an AM 1.5G (air mass global, optical path length = 1.5 times earth's atmosphere, obtained using a solar simulator) spectrum at 25 °C is considered as the incident power.[54] The AM 1.5G irradiation spectrum includes optical absorptions due to atmospheric gases such as ozone, carbon dioxide and water vapor and represents the optical path length that the sun's irradiation has crossed the atmosphere considering an incident angle of 48.2° to the northern hemisphere.[54]

While solar simulator presents the overall performance of a solar cell under simulated AM 1.5G irradiation spectrum, external quantum efficiency (EQE) measurements show the spectrally resolved response of the solar cell (**Fig. 2.6**). It is defined as the ratio between number of extracted electron-hole pairs ($N_{\mathrm{e,h}}$) to the number of incident photons ($N_{\mathrm{p}}(\lambda)$):

$$\mathrm{EQE}(\lambda) = \frac{\mathrm{d}N_{\mathrm{e,h}}(\lambda)}{\mathrm{d}N_{\mathrm{p}}(\lambda)} = \frac{1}{\mathrm{e}}\frac{\mathrm{d}J_{\mathrm{sc}}(\lambda)}{\mathrm{d}\phi_{\gamma}(\lambda)} \tag{2.5}$$

where, $\phi_{\gamma}(\lambda)$ is the photon flux per unit area at wavelength (λ) and $J_{\mathrm{SC}}(\lambda)$ is the short-circuit current density. Integrating equation **2.5** weighted by the photon flux yields the short-circuit current density of a solar cell and is given by:[55]

$$J_{\mathrm{sc}} = \mathrm{e}\int_{0}^{\infty} \mathrm{EQE}(\lambda)\phi(\lambda)\mathrm{d}\lambda \tag{2.6}$$

Analysis of EQE spectra provide more information than just the J_{SC}. For example, surface recombination and amount of parasitic absorption losses in a solar cell can also be estimated. A weak EQE in the short wavelengths indicates front surface recombination,[56] while a weak EQE in the long wavelengths indicates incomplete absorption or too short

diffusion lengths of the charge carriers.[57] Furthermore, analyzing and comparing absorptance and EQE spectra reveal parts of the spectrum that do not yield any photocurrent, which can be attributed to parasitic absorption or reflection losses within the layer stack.[58]

2.2 Light management

As shown earlier, the absorption coefficient is a material-specific property and varies for different absorber materials. Therefore, a semiconductor absorber with a high absorption coefficient is a preferred choice for the application in solar cells. However, not all materials possess this property. Therefore, light management concepts are often employed to enhance absorption.[41,58–65] The concepts rely on increasing the optical path length of light inside the absorber. One way to maximize absorption of the incident photons is to employ opaque back electrodes with a high reflectivity that allow the light to pass through the absorber material a second time, and thus increase the optical path length by two times and enhances the probability of absorption. Another way to increase the optical path length is to introduce textures such as microstructures (textures with dimensions on the order of multiple wavelengths).[58–63] Yablonovitch *et al*. showed in his work the maximum achievable path length (l_{eff}) for a weakly absorbing material. He demonstrated that for an isotopically scattering (Lambertian) textured surface in an ergodic system (under steady state condition, a temporally averaged light-intensity distribution is identical to a statistical phase-space intensity distribution), the l_{eff} can be expressed as:[66,67]

$$l_{\mathrm{eff}} = 4n^2 d \tag{2.7}$$

where, n is the refractive index of the medium and d is the thickness of the absorber layer. Here, a factor of n^2 is present due to an enhancement of the density of states inside the absorber material compared to the surrounding air. A factor 2 arises from the increase in the average path of the scattered rays by the Lambertian surface and an additional 2 comes from the presence of a white reflector that doubles the optical path length. Further increase in the absorption is possible at the expense of angular selectivity and can be expressed as $4n^2d/\sin^2(\theta)$, where θ is the acceptance angle.

In addition to micro-textures, nanostructures (textures with dimensions in the order of the wavelength of incoming light) can be employed to enhance absorption. The improvement is due to the coupling of incident light in highly discretized modes that are supported by the nanostructures.[68,69] Although Yu *et al*. demonstrated an enhancement in the optical path length by $12x4n^2$ for nanostructures for a strong subwavelength-scale electric-field confinement, the fundamental limit is reduced to **Equation 2.7** when the complete phase-space is considered.

A real working solar cell device comprises of multiple layers such as transparent conductive oxides (TCOs), charge transport layers and various buffer layers in addition to the absorber material. Due to the presence of these additional layers, solar cells experience parasitic absorption losses and reflection losses. The parasitic absorption loss is the incident light

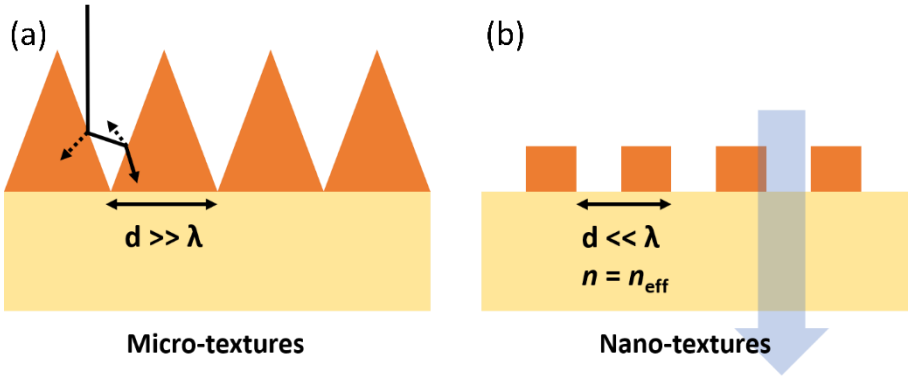

Fig. 2.7: Schematics of (a) micro-textures and (b) nano-textures for reducing reflection losses. The micro-textures enable light in-coupling by multiple reflections at its surface while nano-textures forms a so called effective refractive index medium.

that is absorbed by other layers inside a solar cell stack and results in a loss of the photocurrent. Therefore, TCOs[15,36,37] with low near infrared absorptions and various charge transport layers[28–30,70] with wide bandgaps are preferred in solar cells in order to reduce such parasitic absorption losses. The reflection losses originate from the difference in the refractive indices of two adjacent layers in the solar cell stack. The reflectance (*R*) between two adjacent layers is given by:

$$R = \left(\frac{n_1 - n_2}{n_1 + n_2}\right)^2 \tag{2.8}$$

where, n_1 and n_2 are the refractive indices of the two layers, respectively. Thus, a high contrast between two adjacent layers leads to an increased reflection loss. In order to reduce reflection losses, anti-reflection coatings (ARCs) are used in solar cells. These layers could be a single-layer coating or multilayer.[58,66] While single-layer ARCs are limited to a small range of wavelengths and strongly sensitive to incident angles, multilayer coatings can extend this range.[59] The principle of an ARC relies on the destructive interference of the reflected light. The thickness, *d* is given by:

$$d = m\left(\frac{\lambda}{4n}\right) \tag{2.9}$$

where, *n* is the refractive index of the anti-reflection layer and λ is the wavelength. Other strategies to reduce reflection losses involve micro- and nano-texturing. Micro-textures scatter light by multiple reflections at its surface, and thereby, increases the probability of light in-coupling and hence, reduces reflection losses (see **Fig. 2.7**a).[38,59,61] The nanotextures, in which the dimension of the structures are smaller than the wavelength of the incident light, behaves like a gradient index film, and forms a so called effective refractive index medium.[41,71,72] Thereby, a gradual change in refractive index is achieved, which reduces reflections and therefore, improves light in-coupling (see Fig. 2.7b). Further details regarding parasitic losses and reflection losses due to the TCOs in perovskite solar cells are discussed in section 2.5.

2.3 Detailed balance limit of solar cells

The maximum theoretical efficiency of a solar cell with an absorber bandgap, E_g, is determined by the detailed balance limit. It was first proposed by Shockley and Queisser in 1961 and therefore, the maximum PCE for a certain bandgap material is typically called the Shockley-Queisser limit of a solar cell.[73] The model assumes a blackbody irradiation and calculates the PCE of a solar cell assuming:

(i) absorptance = 100%, for photons with hν > E_g;
(ii) absorptance = 0, for photons with hν < E_g;
(iii) one photon generates one electron-hole pair generation;
(iv) perfect collection, i.e., external quantum efficiency of 100%,

where, hν is the energy of the photon. The maximum PCE in a single-junction solar cell is 30% and is attained for a bandgap of ≈1.1 eV. However, considering an AM 1.5G irradiance spectrum, the maximum PCE that can be attained by a single-junction solar cell is ≈33% for a bandgap of 1.34 eV.[74] In a follow-up study, De Vos calculated the fundamental efficiency limit of a tandem solar cell in 1979.[75] A tandem solar cell is a multi-junction solar cell with two or more sub cells with various bandgaps. This study showed that an optimum bandgap exists for each sub cell in a two-cell tandem device. Considering the same assumptions as Shockley and Queisser, a maximum PCE of 42.3% is obtained with a top cell bandgap of 1.9 eV and a bottom cell bandgap of 1.0 eV. Simulating a two-cell tandem device for AM 1.5G irradiation spectrum, even a higher PCE > 45% can be obtained for a wide range bandgap as shown in chapter 1, **Fig. 1.2**. Further details regarding the working principle of a tandem solar cell are discussed in the follow up section 2.4.

2.4 Tandem solar cells

Operating principle of a tandem solar cell

The foremost reason for the efficiency limit (≈33%) of a single-junction solar cell is the bandgap of the absorber that limits the V_{OC}, as higher energy photons always undergo significant thermalization losses (Fig. 2.1b). One way to overcome this is to use a tandem architecture as shown in **Fig. 2.8**a. The exemplary illustration shows a top cell with a wider bandgap (E_{g1} = 1.55 eV) absorber stacked on top of a bottom cell with a smaller bandgap (E_{g2} = 1.1 eV) material. Thus, photons with higher energies (hν > E_{g1}) are absorbed and with smaller energies (hν < E_{g2}) are transmitted by the top cell. The transmitted photons are absorbed by a bottom cell. As a result, the thermalization losses are reduced compared to a single-junction and the PCE of the tandem device is increased and as already discussed in section 2.3, the maximum theoretical PCE surpasses 45% for a tandem architecture.

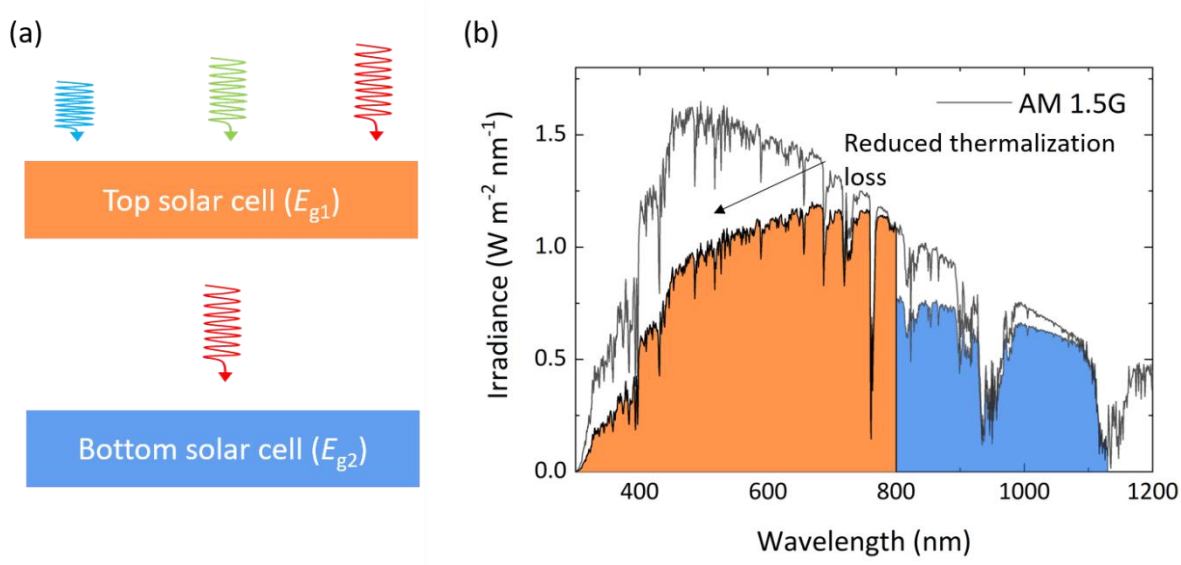

Fig. 2.8: (a) Schematic illustration of a tandem solar cell with two sub cells: top solar cell of E_{g1} and bottom solar cell of E_{g2} and (b) corresponding absorption of the irradiance spectrum AM 1.5G. The top solar cell absorbs photons up to 800 nm. The bottom solar cell absorbs the transmitted photons beyond 800 nm up to its bandgap.

A critical requirement in a tandem solar cell architecture is to find the optimum bandgaps of the top and the bottom solar cells. Arbitrary bandgaps will not maximize the PCE, rather optimum bandgaps (E_{g1} ≈1.80 eV, E_{g2} ≈1.0 eV)[17,18] for the two sub cells are required as shown before in chapter 1, Fig. 1.2. Similar trends are also demonstrated in energy yield studies, which estimate the power generated by a solar cell over a period of one year depending on the weather and location[44,76,77] As a bottom cell, Si is an excellent choice, as the bandgap of Si is very close to the optimum bandgap of the bottom cell.[13,34,63,78,79] However, other technologies exist today such as CIGS[34,36,80] and low bandgap perovskites (in lab scale).[81,82] For the top cell, perovskite semiconductors are an excellent choice (see section 3.6) as it can be deposited as a wide-bandgap semiconductor (already demonstrated PCEs > 25%[10] in opaque devices) and offers bandgap tunability.[83,84] Further details regarding the influence of the bandgap in a top perovskite solar cell for a tandem architecture is discussed in Chapter 6.

Tandem solar cell architecture

The most common tandem configurations are a two-terminal (2T),[63,78–80] or a four-terminal (4T) architecture.[13,14,34,81,82] In the 2T architecture, both sub cells cells are monolithically connected, while in the 4T architecture, the two sub cells are mechanically stacked (**Fig. 2.9**). Each architecture offers its own advantages and disadvantages. The 2T architecture requires only one TCO layer, which reduces parasitic absorption losses. However, it also implies a series connection of both sub cells, which requires current matching of both sub cells to maximize the PCE and, in turn, imposes shortcomings to the bandgap combinations.[18,78,85] Only a narrow range of bandgaps can maximize the PCE. The 4T architecture allows each sub cell to operate independently at their MPPs and the constraints in the fabrication of the sub cell are less as each sub cells can be fabricated

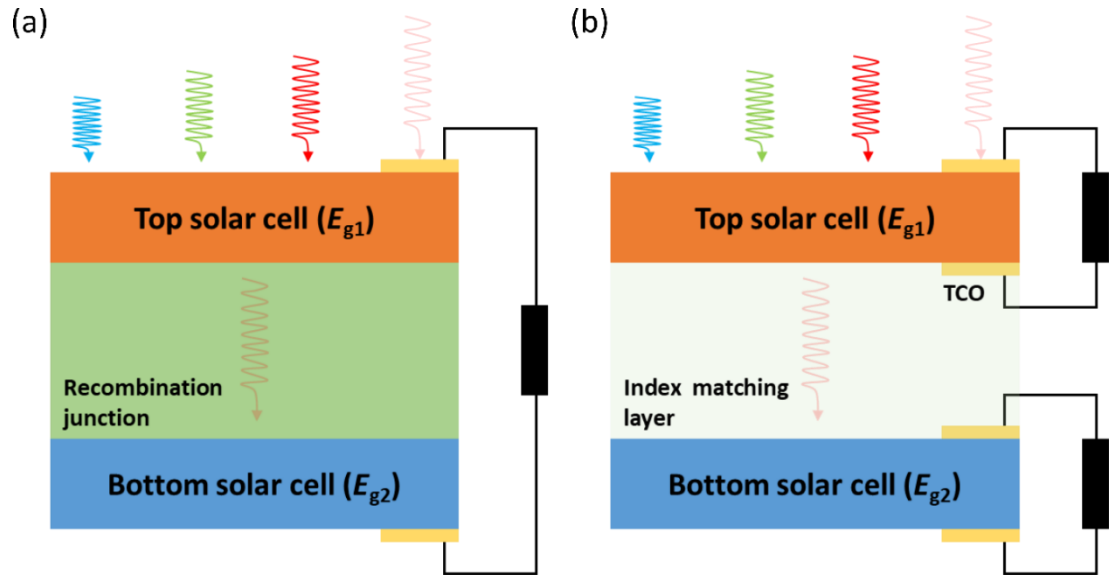

Fig. 2.9: Schematic illustrations of a (a) two-terminal (2T) tandem architecture and (b) four-terminal (4T) tandem architecture. In 2T architecture, both sub cells are monolithically interconnected. In 4T architecture, both sub cells are optically interconnected and can work independently.

independently. Furthermore, since current matching is not crucial, the limitation on the top solar cell absorber's bandgap is reduced.[18,44] As a result, a wide range of bandgaps (1.60-1.85 eV) are suitable for this configuration. Nevertheless, this configuration requires additional electrical equipment such as two inverters instead of one, which can effectively increase the LCOE. Furthermore, since the two sub cells are optically connected, intermediate index matching layers are required to reduce the optical losses.[38] Moreover, it is difficult to minimize parasitic absorption in this architecture as additional TCO electrodes, charge transport layers and optical spacer are used.

2.5 Perovskite solar cells

Crystallography of perovskite

Perovskites are materials with a general chemical formula of ABX_3. The basic crystal structure consists of a unit cell with A, B and X atoms residing at the corners, at the center and at the facets of the cube, respectively (**Fig. 2.10**).[86] Besides the cubic phase, there are other phases such as tetragonal or orthorhombic, the formation of which depends highly on the temperature[86,87] and stoichiometry.[86] In an organometal halide perovskite crystal, A is a monovalent cation (such as methyl ammonium: CH_3NH_3; formamidinium: CH_3NH_2; cesium: Cs^+; etc.), B is a divalent metal cation (such as lead: Pb^{2+}; tin: Sn^{2+}), and X is a halogen (such as chloride: Cl^-; bromide: Br^-; iodide: I^-). To determine if a certain composition exhibits a stable crystal structure, the Goldsmith's tolerance factor (t)[88] serves as an estimation and can be calculated using the following relation:

$$t = \frac{r_A + r_B}{\sqrt{2}(r_B + r_X)} \tag{2.7}$$

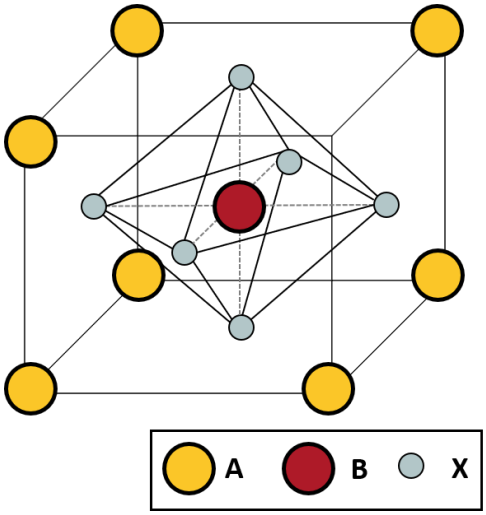

Fig. 2.10: Schematic illustration of the cubic phase crystal structure of a perovskite absorber.

where, r_A, r_B, and r_X are the ionic radii of the respective atoms. A stable cubic crystal structure is typically formed when t is within the range $0.9<t<1.0$.[86] The most widely investigated perovskite material for solar cells is methyl ammonium lead iodide (MAPI), with the chemical formula $CH_3NH_3PbI_3$ and has a tolerance factor of 0.91.[89] Recent studies show that replacing CH_3NH_3 with CH_3NH_2 and a certain amount of Cs^+ can greatly improve the tolerance factor (close to 1) and enhance the stability of the material.[86] If the size of the A atoms is beyond the limit of the tolerance factor such that a cation cannot fit inside the cubic lattice, a 2D or quasi-2D perovskite is formed instead of a bulk 3D structure. This structure can either be a Ruddelsen-Popper[90,91] or Dion-Jacobson[92] phase of the perovskite absorber. Examples of such molecules for PSC applications are butyl ammonium,[91] phenylethylammonium,[93] iso-butylammonium,[13,94] 1,3-propanediamine (PDA),[92] etc. These molecules improve the stability of the absorber due to the presence of long hydrophobic chains,[95] or strong hydrogen bonding.[92]

Properties of metal-halide perovskite absorbers

Perovskite absorbers exhibit material properties that are highly suitable for solar cell application. This includes a high absorption coefficient,[96] high charge carrier mobilities,[97] a low bimolecular recombination rate,[97] long diffusion lengths[50] and tunable bandgaps.[83,84] A sharp absorption onset is present in perovskite absorbers due to the direct nature of the bandgap.[96] Therefore, for fabricating PSCs, thicknesses of ≈300-400 nm are sufficient for absorbing most of the incident light. Along with sharp optical absorption edge, these perovskite absorbers also present high charge carrier mobilities of ≈10 $cm^2\ V^{-1}\ s^{-1}$ and a low bimolecular recombination.[97] Therefore, long diffusion length of the charge carriers, exceeding 1 µm, have been observed in perovskites.[50] Furthermore, the bandgap of the absorber can be varied by tuning the composition of the material.[83,84,98] By replacing iodide with bromide in lead based perovskite absorbers, the bandgap can be tuned between 1.5-2.3 eV. This is due to the fact that when smaller bromide ions replace iodide ions, the

lattice constant of the crystal structure is decreased and thereby, resulting an increase in the bandgap. On the other hand, replacing the divalent cation lead with tin, lower bandgaps (1.1 eV to 1.4 eV) are achieved.[82] This makes perovskite absorber an interesting material for various applications such as in tandem photovoltaics,[99] lasers[84] and LEDs.[100]

Perovskite solar cell architecture

A PSC is fabicated in either a p-i-n or n-i-p architecture.[101] The absorber material is sandwiched between two charge transport layers. Typically, TiO_2[31–35,102] or SnO_2[70,103,104] are used as the n-type selective contact or electron transport layer (ETL) and spiro-OMeTAD[105,106] as the p-type selective contact or hole transport layer (HTL) in the n-i-p configuration. For the p-i-n configuration, the ETL and the HTL are replaced by C_{60}[28,101] and PEDOT:PSS[107] or NiO_x[108] layers, respectively. Nevertheless, many other transport materials exist as shown in **Fig. 2.11**[28,101,103,105] and novel charge transport materials are investigated nowadays. For the extraction of charges, typically, a TCO such as tin-doped indium oxide (ITO) or fluorine-doped tin oxide (FTO) is used in order to in-couple from one side,[36] while a rear opaque electrode (gold, silver, or copper) is used on the other side to reflect the incident light and thus to increase the optical path length of light within the perovskite absorber.[109] In the case of s-PSCs, the rear opaque electrode is replaced with TCOs such as ITO or zinc-doped indium oxide (IZO).

Losses in perovskite solar cells

Since perovskite absorbers typically consist of poly-crystalline thin films and several layers are required to fabricate an efficient PSC, there are several non-radiative recombination losses that can reduce the V_{OC}. This includes defect-assisted recombination, interface-

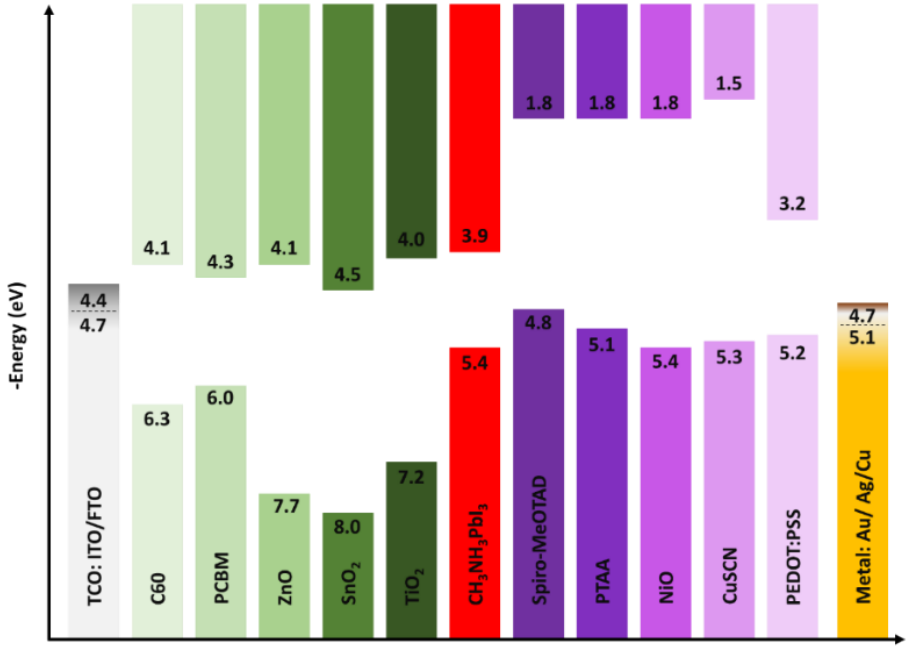

Fig. 2.11: Overview of different transport layers suitable as load carrier selective transport layers materials (energy values according to references [28,103,105,214]).

induced recombination and band-tail recombination.[110–117] The defect-assisted recombination originates mainly from point defects such as interstitials, vacancies, and antisites.[110–112] These defects are nearly either positively or negatively charged, as they have either holes or electrons localized in their vicinity. The interface-induced recombination arises from the mismatch of energy levels, surface defects, and charge-carrier back transfer.[113–117] Such defects can block transfer of charges or cause band bending near the contacts, resulting in increased non-radiative recombination. Overall, these recombination losses reduce the V_{OC} in a PSC. Another commonly known experienced phenomenon that exists in a PSC is hysteresis.[118,119] This arises due to the ion migration and in the presence of electronic charge traps. The probable reason in the origin of ion migration is the iodide ions in the perovskite absorbers, that exhibit low activation energies. Furthermore, these mobile ions can accumulate at the interface and since they act as traps, can further increase non-radiative recombination.[120] The effect of these can be observed in the *J-V* characteristics as a difference in the forward and reverse scan. The hysteresis index (*HI*) is calculated using the following relation:

$$HI = \frac{Area\ under\ FW\ scan}{Area\ under\ BW\ scan} \tag{2.8}$$

where, FW and BW are the forward and backward scans, respectively. An *HI* of 1 implies no hysteresis. Hysteresis in the *J-V* characteristics may lead to an over- or under-estimation of the solar cell PCE. Therefore, a commonly established protocol followed by the research community is to report device performance under a voltage at or close to the MPP.[121]

Stability of perovskite solar cells

PSCs are yet to overcome one of its prime challenges for future commercialization, i.e., the poor stability, which can be ascribed to intrinsic material instability in the presence of moisture, ultra-violet radiation and thermal stress.[89,122–125] The moisture related instability is mainly due to the hygroscopic nature of the amine group, that leads to an irreparable damage of the perovskite, forming lead iodide and methylamine.[123] The ultra-violet degradation is mostly prominent in TiO_2 based PSCs[89] and arises from the light-induced desorption of surface-adsorbed oxygen.[124] Next to the ultra-violet instability, perovskite absorbers are sensitive to thermal stress. With increasing temperature, MAPI shows a degradation by releasing methyl ammonium iodide in the gas phase and leaving behind PbI_2.[125] In recent years, several strategies have been undertaken to improve the stability of the perovskite absorber showing promising stability of up to 1000 hours under continuous operation. This includes optimization of the stoichiometry by including Cs forming double or triple cation perovskite absorber,[32] as well as the use of 2D perovskites,[126,127] and novel charge transport layers.[128]

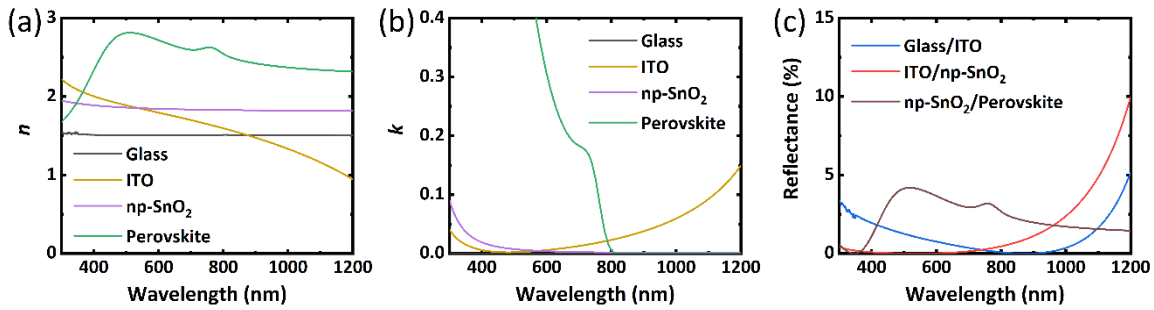

Fig. 2.12: (a) Refractive index (*n*) and (b) extinction coefficient (*k*) of glass, ITO, np-SnO_2 and perovskite. (c) Reflectance of glass/ITO, ITO/np-SnO_2 and np-SnO_2/perovskite interfaces.

Properties of tin-doped indium oxide and its effect on PSCs

The layer stack of a complete PSC typically consists of either one or two sputtered TCO electrodes, depending whether the solar cell is opaque or semitransparent. Along with FTO, ITO is often used as the TCO for PSCs due to its high conductivity[36] (sheet resistance = 8-15 Ω/sq) and optical transparency[36] (exceeding > 85%) in the visible spectrum. Both features are excellent for opaque PSCs as perovskite absorbers based on Pb are wide bandgap semiconductors (>1.5 eV). The low sheet resistance of the ITO is associated to the high charge carrier concentrations (≈10^{21}/cm^3), originating from the partial substitutions of the indium atoms by the tin atoms and the formation of oxygen vacancies in ITO.[129,130] Due to this high carrier concentration, the plasma frequency of the ITO exists in the near infrared wavelength ranges.[39,40] As a result, a strong dispersion in the refractive index of the ITO, leading to very small values of refractive index above 800 nm as shown in **Fig. 2.12**a. Due to this, when subsequent layers deposited on ITO, strong Fresnel reflection losses can be observed as shown in Fig. 2.12c. Furthermore, due to this high carrier concentration, ITO exhibits high extinction coefficient (Fig. 2.12b) as these free carriers absorb in the near infrared wavelengths,[36,40] which can result in strong parasitic absorption losses and poor performance of perovskite-based tandem devices. Therefore, it is evident that one cannot simply implement the same ITO used in opaque PSCs for tandem application. In order to reduce these losses, several strategies are discussed in chapter 5 and chapter 6.

3. Methods and Characterizations

This chapter discusses all the applied methods for the fabrication of a typical perovskite solar cell (PSC) used in this thesis, deposition of planar and nanostructured transparent conductive oxide (TCO) electrodes and synthesis of nanoparticles of titanium dioxide (np-TiO_2) electron transport layer (ETL). The chapter also outlines the techniques used to characterize the fabricated devices and materials.

Acknowledgments and contributions

The major part of the experiments carried out for thesis is conducted by Ihteaz M. Hossain. Ihteaz M. Hossain also acknowledges the support of Moritz Schultes for providing IO:H substrates, Fabian Schackmar and Florian Mathies for inkjet printing of np-TiO_2, Saba Gharibzadeh for preparation of double cation perovskite absorber layers, Katharina Goth for fabricating periodic nanostructured ITO samples, Yidenekachew J. Donie and Mohamed S. Adbelkhalik for disordered nanostructured ITO, Isabel Allegro for AFM measurements, David Ritzer for patterning TCOs and Michael Bruns XPS measurements.

3.1 Fabrication and synthesis

In this section, the methods used to fabricate perovskite solar cells (PSCs), nanostructured ITO (NS ITO), sputter various transparent conductive oxides (TCOs) and synthesize nanoparticles of TiO_2 (np-TiO_2) are discussed in detail.

3.1.1 Synthesis of TiO_2 nanoparticles

This section describes the synthesis of the np-TiO_2. A schematic of the synthesis process is illustrated in **Fig. 3.1**. The synthesis process comprises of three critical steps: (i) a non-hydrolytic sol-gel synthesis of np-TiO_2, (ii) extraction and purification of the np-TiO_2, and (iii) dispersing in a suitable solvent.

The following precursor materials are required for the syntheses of np-TiO_2:

(i) Titanium (IV) chloride, $TiCl_4$ (Acros Organics)
(ii) Niobium (V) chloride, $NbCl_5$ (Alfa Aesar)
(iii) Anhydrous ethanol, EtOH (Acros Organics)
(iv) Benzyl alcohol, BnOH (Acros Organics)
(v) Diethyl ether, Et_2O (Honey well)
(vi) Diethylene glycol monoethyl ether, DEGEE (Sigma Aldrich)
(vii) 1-butanol (Sigma Aldrich)
(viii) Titanium diisopropoxide bis acetonyl acetate, $Ti(O\text{-}iPr)_2(acac)_2$ (Sigma Aldrich)

In the first step of the synthesis of undoped np-TiO_2, 4.5 mmol of $TiCl_4$ is added dropwise to 2 ml of EtOH in a glass vial. In order to synthesize the np-TiO_2 doped with Nb^{5+} for improved conductivity, $TiCl_4$ is added to a 0.17 M solution of $NbCl_5$ dissolved in EtOH. This

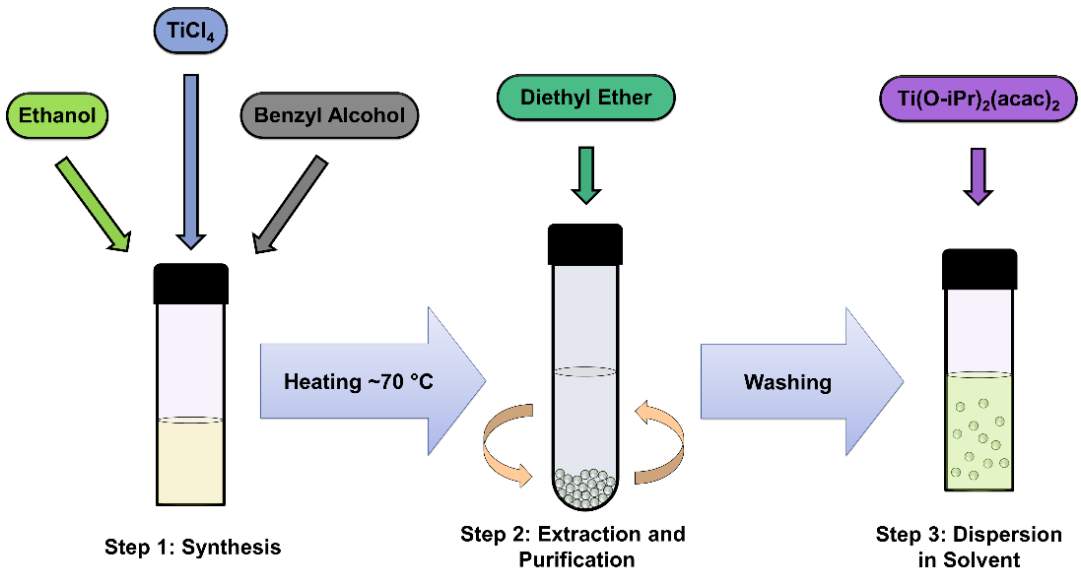

Fig. 3.1: Schematic illustration of the nanoparticles of TiO_2 synthesis. The three main steps of the synthesis process are: (i) non-hydrolytic sol-gel synthesis of np-TiO_2, (ii) extraction and purification of the np-TiO_2, and (iii) dispersing in a suitable solvent. Reproduced with permission from ACS Applied Energy Materials,[139] © American Chemical Society.

accounts to 7 at.% niobium ions (Nb^{5+}) in the mixture. A continuous stirring is necessary at this step to mix the solutions well. This step is processed inside a glovebox to avoid any contact of moisture with $TiCl_4$, that can form toxic gaseous hydrochloric acid (HCl). To the resulting mixture, 10 ml of BnOH is added. A greenish solution is obtained. Next, the obtained solution is heated to ≈70 °C in an oil bath that speeds up the rate of reaction. The final solution is obtained after 16 h of continuous heating. At this moment, the solution appears hazy. To vary the size of the np-TiO_2, similar synthesis is carried out but for 9 h, 22 h, and 29 h of heating.

In the second step, the as-prepared np-TiO_2 is precipitated and washed. 4 ml of this solution is transferred to a 50 mL centrifuge tube in which 10 ml of Et_2O is added to precipitate the np-TiO_2. The centrifugation is carried out at a speed of 8000 rpm for 3 min to obtain white np-TiO_2 separated from the solvent. The supernatant is removed and 10 ml EtOH is added to begin the washing step. At this moment, the centrifuge tube is vigorously stirred to disperse the np-TiO_2 in EtOH. When the particles are dispersed in EtOH, 10 ml of Et_2O is added. This solution is again centrifuged at the same speed for the same time and the purification cycle (EtOH washing, Et_2O precipitation, centrifuging) is repeated at least 2 times to obtain the np-TiO_2 ready to be dispersed in a suitable solvent.

In the last step, a dispersion of the np-TiO_2 is formed by adding EtOH, DEGEE or 1-butanol to the nanoparticles. For this, 12 ml of the solvent is added. The final solution is obtained after the addition of 180 µl of $Ti(O\text{-}iPr)_2(acac)_2$ that prevents agglomeration of the nanoparticles. After stirring at room temperature for at least 1 h, a clear greenish solution is obtained, ready to be deposited as an ETL.

3.1.2 Sputtering technique

Sputtering is a physical vapor deposition technique to deposit thin films on wafers or substrates.[131,132] Although there are other physical vapor deposition techniques, one key advantage of sputtering is the ability to deposit the desired material keeping it at room temperature. Using this technique, metals and dielectrics can be uniformly deposited with a low level of impurity.

Sputtering process

The sputtering process relies on a plasma between two electrodes as shown in **Fig. 3.2**. At the cathode, a target material is placed which is to be sputtered. The anode is the wafer or substrate where the material is desired. Inside the sputtering chamber, argon (Ar) gas is injected and kept at a certain pressure, usually between 1-10 mtorr.[133,134] When an electrical potential is applied between the anode and the cathode, stray electrons inside the chamber initiate the formation of the plasma. These stray electrons are called the secondary electrons which are needed to sustain the plasma and become primary electrons inside the plasma. When they collide with Ar atoms, electrons are removed from Ar atoms, thus forming positively charged Ar^+ ions. Due to the presence of an electric field, the Ar^+ ions are accelerated towards the target, and upon hitting the target material,

momentum and energy transfer occurs between the Ar^+ ions and the surface atoms. If the energy is greater than the lattice bonding or vibrational energies, surface atoms from the target material are dislodged and ejected. A flux of these ejected atoms then travel to the anode where they are deposited uniformly on the substrate.

Types of sputtering techniques

There are various types of sputtering techniques. The simplest forms include planar diode sputtering, magnetron sputtering, and reactive sputtering. Depending on the power supply, sputtering can also be classified as DC sputtering,[133] radio-frequency (RF) sputtering[135] or pulsed-DC sputtering.[136] The sputtering process described above is the operating principle of a planar diode sputtering. One of the main problems of the planar diode sputtering is the slow rate and the requirement of a high voltage to have sufficient secondary electrons in the chamber. The efficiency of this secondary electrons can be increased by trapping these electrons near the target material using magnetic fields. This is called magnetron sputtering,[133] which results in an increased deposition rate, reduced voltage, and at the same time, a reduction of the substrate temperature which arises from the bombardment of high energy electrons. In reactive sputtering,[135] instead of using Ar as the only gas inside the chamber, some other gases such as oxygen (O_2), nitrogen (N_2) or hydrogen (H_2) are also injected. In doing this, the target material can react with the gas

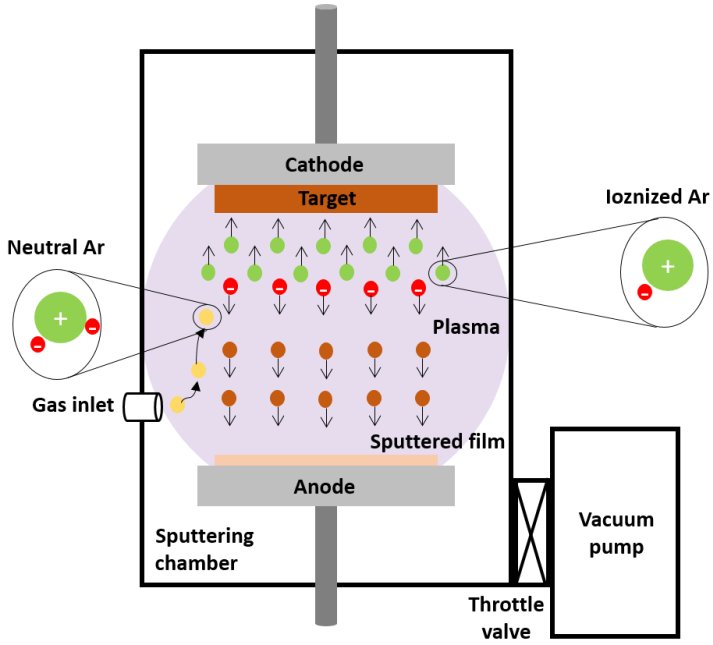

Fig. 3.2: Schematic illustration of a sputtering process. The target material is the cathode and the substrate on which the material is deposited is the anode. Inside the sputtering chamber, argon (Ar) gas forms the plasma due to an applied voltage between the anode and the cathode. When stray electrons collide with the Ar atoms, they are ionized. These Ar^+ ions are accelerated towards the target, which up on hitting the target material, releases atoms. These ejected atoms travel to the anode where they are deposited uniformly on the substrate.

molecules to form a compound. For instance, in the case of reactive sputtering of silicon in the presence of O_2, SiO_2 can be deposited on a substrate.

While a DC power supply is shown in Fig. 3.2 for sputtering, an alternating power supply may be used instead. This is crucial for sputtering of insulating materials as charges can build up if a constant DC supply is applied over time in a DC sputtering. This may lead to arcing that can damage the target and a poor quality in the deposited film. Therefore, an RF is commonly employed to deposit non-conducting materials. However, this comes at the cost of reduced deposition rate and a high voltage compared to DC sputtering. Another method to deposit insulating materials at a high rate is to use pulsed-DC sputtering. In this method, the arcing is avoided for insulating materials without affecting the deposition rate. Here, a reverse bias is applied for a very short period of time (typically in the order of hundreds of μs) to discharge the accumulated charges.

3.1.3 Fabrication of a typical perovskite solar cell

In this thesis, the PSCs are fabricated in n-i-p architecture. **Fig. 3.3** shows a schematic of the fabrication of standard n-i-p architecture prepared in this group. The fabrication of PSCs in this architecture comprises of the deposition of the electron transport layer (ETL) on a transparent conductive oxide electrode followed by the deposition of the perovskite active layer, hole transport layer (HTL) and the rear electrode. Various deposition techniques are employed to realize each layer. The transparent conductive oxide electrodes are obtained by sputtering the target material. The ETLs are deposited with various deposition methods: spin coating, blade coating, inkjet printing and slot-die coating. The perovskite absorber layers and the HTLs are obtained by spin coating method, although inkjet printing and evaporation of the both the layers are feasible in this research group.[108,137] The buffer layers, anti-reflection coatings and the opaque electrodes are obtained using thermal evaporation. In the case of semitransparent perovskite solar cells (s-PSCs), gold fingers are deposited to increase the conductivity of the rear TCO. The discussions below describe the fabrication of each of these layers in detail.

Sputtering of front transparent conductive oxide electrode

Typically, tin-doped indium oxide (ITO) is used as the TCO electrode, either purchased commercially (Luminescence Technology) or sputtered in-house. Two types of ITO electrodes are sputtered in-house: ITO_v and ITO_n. ITO_v is used as the TCO for the devices in chapter 6, section 6.1, while ITO_n is used as the TCO in chapter 6, section 6.2. Zinc-doped indium oxide (IZO) is also sputtered in-house as the front TCO electrode in the PSC. Hydrogen-dope indium oxide (IO:H) is obtained from the collaboration partner, ZSW. The deposition parameters are given is **Table 3.1**.

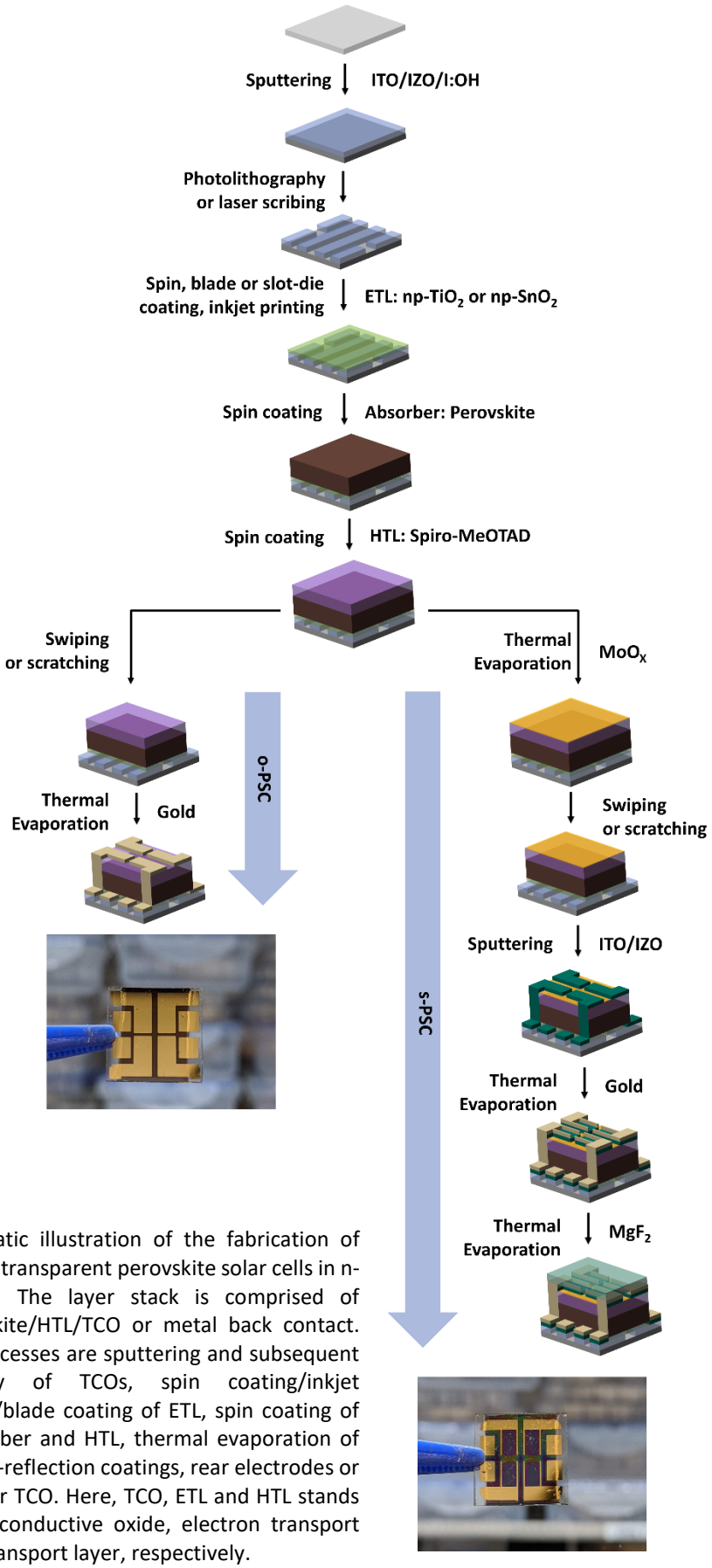

Fig. 3.3: Schematic illustration of the fabrication of opaque and semitransparent perovskite solar cells in n-i-p architecture. The layer stack is comprised of TCO/ETL/Perovskite/HTL/TCO or metal back contact. The involved processes are sputtering and subsequent photolithography of TCOs, spin coating/inkjet printing/slot-die/blade coating of ETL, spin coating of perovskite absorber and HTL, thermal evaporation of buffer layer, anti-reflection coatings, rear electrodes or sputtering of rear TCO. Here, TCO, ETL and HTL stands for transparent conductive oxide, electron transport layer and hole transport layer, respectively.

Table 3.1: Sputtering parameters of the TCO electrodes.

Sputtering parameters/TCO	ITO (commercial)	ITO_v	ITO_n	IZO	IO:H
Sputtering type	-	DC	DC	RF	DC
Power (W)	-	50	250	240	600
Pressure (mTorr)	-	0.8	1.1	1.5	7.5
Temperature (°C)	-	300	300	25	25
Sputtering gas (type)	-	Ar	Ar	Ar	Ar
Reactive gas (type/%)	-	O_2/3.5	O_2/12.5	O_2/1	O_2/1.7%, H_2/3.4
Deposition time (s)	-	2000	570	1015	210
Layer thickness (nm)	140	135	170	165	230
Post conditioning	-	-	-	-	Vacuum annealing 200 °C, 75 min

Deposition of the electron transport layer

Two types of ETLs are investigated in this work: (i) np-TiO_2 and (ii) nanoparticles of SnO_2 (np-SnO_2). The np-TiO_2 electrode is deposited on ITO using spin coating, blade coating, inkjet printing and slot-die coating (**Fig. 3.4**) methods.

For spin coating, the np-TiO_2 dispersed in EtOH is used. In the spin coating approach, the np-TiO_2 dispersion is casted at the center of the ITO substrate and spun at 7000 rpm for 60 s (Fig. 3.4a). This high rotational speed generates a centrifugal force and the np-TiO_2 is consequently deposited uniformly over the substrates. During the rotation, the film also dries. A follow-up annealing of 100 °C for 30 min over a hot plate is necessary to obtain a compact layer with a thickness of ≈30-35 nm.

In inkjet printing, the ink consists of np-TiO_2 dispersion in DEGEE along with 5 vol. % triethylene glycol monoethyl ether (Fig. 3.4b). The printing is performed using a Fujifilm Dimatix DMP 2831 inkjet printing system with a DMC11610 cartridge. The printer uses a piezoelectric material in an ink-filled chamber to create droplets of inks. For this, an 18 V pulse of 15 µs width with a jetting frequency of 5kHz is applied to the piezoelectric

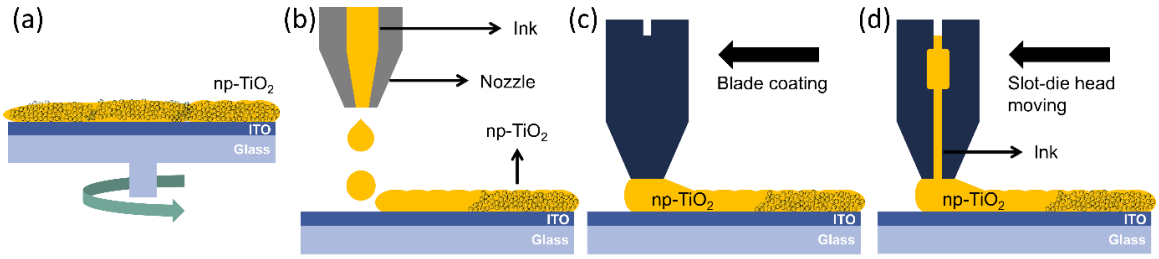

Fig. 3.4: Schematic illustration of the deposition of np-TiO_2 using various deposition technique: spin coating, inkjet printing, blade and slot-die coating. Reproduced with permission from ACS Applied Energy Materials, [139] © American Chemical Society.

material. This changes the shape of the piezoelectric material and creates a pressure in the fluid and consequently, a droplet of ink is ejected from the nozzle. During printing, 10 pL of the ink is used and both the ink and the substrate plate are held at controlled temperatures of 35 °C and 22 °C. A drop spacing of 35 µm and subsequent drying in vacuum for 2 min, before annealing at 100 °C leads to a compact film of ≈35 nm.

The np-TiO_2 is also deposited with blade coating technique (Fig. 3.4c) using the dispersion in EtOH. For this, a Zehntner ZAA 2300 system blade coater is used. The system uses a running blade with a variable speed setting. A diluted np-TiO_2 dispersion in EtOH (1:2.5) is dropped on the samples and the blade is moved over the substrate at a speed of 6 mm/s. After an annealing step at 100 °C for 30 min, a 30-35 nm thick layer is obtained.

For slot-die coating of np-TiO_2, the dispersion in 1-butanol is used (Fig. 3.4d). After diluting to 50 vol %, slot-die coating is performed with an nTact Coating System nRad in a controlled cleanroom condition, at a temperature of 23 °C with a relative humidity of 50%. In slot-die coating, the layer is obtained by the flow of the ink through a slot-die head on a moving substrate. A 6-8 µm thick wet layer is obtained to ensure a final dry layer of ≈35 nm. The drying is performed by keeping the samples for 2 min at the room temperature, followed by 1 min at 55 °C, and finally annealing at a temperature of 100 °C.

For the np-SnO_2 ETL, a colloidal dispersion of np-SnO_2 (Alfa Aesar) of ≈15 wt% is used. The dispersion is diluted to 2.04 wt% in de-ionized water and spin-coated at a speed of 4000 rpm for 30 s. A follow-up annealing step of either 150 °C or 250 °C for 30 min is used to obtain the ETL with a thickness of ≈10 nm.

Deposition of the perovskite absorber

Three different perovskite absorbers are used for the fabrication of PSCs in this thesis: (i) MAPI ($CH_3NH_3PbI_3$), (ii) triple cation ($Cs_{0.1}(MA_{0.17}FA_{0.83})_{0.9}Pb(I_{0.83}Br_{0.17})_3$), and (iii) double cation ($FA_{0.83}Cs_{0.17}Pb(I_{1-y}Br_y)_3$), where $0.24 \leq y \leq 0.56$. The following precursors are used:

(i) Methylammonium iodide, MAI (Greatcell solar)
(ii) Formamidinium iodide, FAI (Greatcell solar)
(iii) Methylammonium bromide, MABr (Greatcell solar)
(iv) *n*-butyl ammonium bromide, *n*-BABr, (Greatcell solar)

(v) Cesium iodide, CsI (Alfa Aesar)
(vi) Lead iodide, PbI_2 (TCI or Alfa Aesar)
(vii) Lead bromide, $PbBr_2$ (TCI or Alfa Aesar)
(viii) Lead chloride, $PbCl_2$ (Merck)
(ix) Lead acetate trihydrate, $Pb(CH_3CO_2)_2{\cdot}3H_2O$ (Merck)
(x) N,N-dimethylformamide, DMF (Merck)
(xi) Dimethyl sulfoxide, DMSO (Merck)
(xii) γ-butyrolactone, GBL (Merck)
(xiii) Isopropanol, IPA (Merck)
(xiv) Chlorobenzene, CB (Merck)

MAPI is deposited in two different methods. The first method consists of solution of $CH_3NH_3PbI_3$ prepared from the precursors of MAI, $PbCl_2$, $Pb(CH_3CO_2)_2{\cdot}3H_2O$. For this, two separate solutions are prepared: (i) $Pb(CH_3CO_2)_2{\cdot}3H_2O$ and MAI are dissolved in DMF in a ratio of 1:3, and (ii) $PbCl_2$ and MAI dissolved in DMF in a ratio of 1:3. Solution 2 is then mixed with solution 1 to obtain ≈20% $PbCl_2$ in the final solution. Spin coating is performed at 3000 rpm for 30 s and annealing at 115 °C for 10 min inside a glovebox environment (0.1 ppm O_2 and 0.1 ppm H_2O) forms the ≈300−350 nm thick $CH_3NH_3PbI_3$ layer. The second method consists of an anti-solvent approach and is only used to deposit the perovskite absorber on slot-die coated np-TiO_2. The $CH_3NH_3PbI_3$ solution is prepared from a mixture of PbI_2 and MAI (ratio 1:1) dissolved in GBL, DMSO, and DMF in a ratio of 1:1:1. The spin coating is performed in two separate steps inside the glovebox (0.1 ppm O_2 and 0.1 ppm H_2O): (i) 1000 rpm for 15 s, and (ii) 4000 rpm for 45 s. Toluene is released 25 s before the end of the second step. The samples are annealed at 100 °C for 10 min to obtain a final layer of thickness ≈335−340 nm.

Triple cation perovskite is prepared from the precursors of MABr, FAI, PbI_2 $PbBr_2$ and CsI. For this, two separate solutions are prepared: (i) a precursor solution of FAI (1 M), PbI_2 (1.1 M), MABr (0.2 M), and $PbBr_2$ (0.2 M) in DMF:DMSO in a ratio of 4:1, and (ii) a stock solution of CsI in DMSO (1.5 M). An 88.9 µL aliquot of solution 2 is transferred into solution 1 to prepare the final mixture. Two spin-coating steps are used to obtain the desired layer: (i) 1000 rpm for 10 s and (ii) 6000 rpm for 20 s. 100 µL CB is released 5-7 s before the end of the second step and the samples are annealed at 100 °C for 1 h.

Double cation perovskite is prepared for both 3D and 2D/3D perovskite heterojunction layers. For preparing the 3D perovskite absorber layers of five different bandgaps, the amount of bromide content in the precursor solution is varied between $0.24 \leq y \leq 0.56$ in steps of $\Delta y = 0.08$. The perovskite precursor solution is prepared by dissolving 0.83 mmol FAI, 0.17 mmol, $((2 - 3 \times y))/2)$ mmol PbI_2, and $(3/2 \times y)$ mmol $PbBr_2$ in a 1 mL solvent mixture of DMF and DMSO (4:1). Two spin-coating steps are used to obtain the desired layer inside the glovebox (0.1 ppm O_2 and 0.1 ppm H_2O): (i) 1000 rpm for 10 s and (ii) 5000 rpm for 30 s. 100 µL CB is released 5−7 s before the end of the second step and the samples are annealed at 100 °C for 1 h.

To obtain the 2D/3D perovskite heterostructure, 2 mg/mL of *n*-BABr in isopropanol is prepared. 100 µL of *n*-BABr solution is spin-coated dynamically on 3D perovskite at 5000 rpm for 30 s with a subsequent annealing at 100 °C for 5 min inside the glovebox (0.1 ppm O_2 and 0.1 ppm H_2O).

Spin coating of the hole transport layer

N,N'-di-p-methoxy phenylamine)-9,9'-spirobifluorene, spiro-OMeTAD (Luminescence Technology) is deposited by spin-coating at 4000 rpm for 30 s. The precursor solution is prepared from 80 mg of spiro-OMeTAD dissolved in 1 mL CB with the additives of 17.5 µL lithium salt solution and 28.5 µL 4-tert butylpyridine (Sigma Aldrich). The lithium salt solution is prepared by dissolving 520 mg lithium bis(trifluoromethanesulfonyl) imide (Sigma Aldrich or Merck) in 1 mL of acetonitrile (Sigma Aldrich or Merck). After the deposition, the samples are left for oxygen doping in ≈25% relative humidity condition for ≈12 h.

Thermal evaporation of the buffer layer, opaque electrode and the anti-reflection coating

The 10 nm thick buffer layer of MoO_X (Sigma Aldrich or Merck) deposited on the HTL and the 165 nm anti-reflection coating of MgF_2 (Sigma Aldrich or Merck) on the rear ITO are thermally evaporated using Lesker Spectros PVD system or Angstrom Engineering at a rate of ≈0.8 Å/s and 3-4 Å/s, respectively under a pressure of 6 x 10^{-6} mbar. The buffer layer and the anti-reflection coating are deposited only for fabricating s-PSCs. For opaque perovskite solar cells (o-PSCs) as shown in Fig. 3.2, a rear Au contact (60 nm or 75 nm) is evaporated directly on the HTL using a Vactec Coat 320 evaporator system. The resultant active area of the o-PSCs is 10.5 mm^2.

Sputtering of rear transparent conductive oxide electrode

The s-PSCs are fabricated employing TCO electrodes on the rear side. For this, either an ITO or an IZO layer is sputtered on the buffer MoO_X layer (Fig. 3.2). In contrast to front TCO electrodes, the rear TCO electrodes are sputtered at room temperature (25 °C). Along with low temperature deposition, the power is lowered so that the heat developed due to the bombardment on the substrate during sputtering is reduced. Since sputtering is not directional, sharp edges are not obtained and the active layer is not clearly defined. Therefore, shadow masks with defined area are used for characterizing these s-PSCs (see section 3.2.1 for more details). After the deposition of the rear TCO electrodes, gold fingers are deposited to increase the conductivity further. The sputtering parameters used to deposit these rear TCOs can be found in **Table 3.2**.

Table 3.2: Sputtering parameters of the rear TCO electrodes.

Sputtering parameters/TCO	ITO	IZO
Sputtering type	DC	RF
Power (W)	50	100
Pressure (mTorr)	0.8	1.5
Temperature (°C)	25	25
Sputtering gas (type)	Ar	Ar
Reactive gas (type/%)	O_2/2.5	O_2/1
Deposition time (s)	2310	2550
Post conditioning	-	-
Layer thickness (nm)	165	165

3.1.4 Fabrication of nanostructured ITO

NS ITO is fabricated to reduce reflection losses and improve light in-coupling. Two configurations of NS ITO are fabricated: (i) periodic, and (ii) disordered. In the following sections, the fabrication process of periodic and disordered NS ITO is discussed in detail.

Periodic nanostructured ITO

The periodic NS ITO is fabricated by employing soft-imprinting molds of nanostructures and subsequent sputtering of ITO. **Fig. 3.5**a shows the schematic to obtain the periodic NS ITO. To fabricate periodic NS ITOs, first a master structure is fabricated on silicon wafer using electron beam lithography for periods p = 200 nm, 300 nm, 400 nm and 500 nm. The geometrical filling fraction of the master structure, which is defined by the ratio of the nanostructured area to the total area:

$$Filling\ Fraction = \frac{\pi d^2}{4p^2} \tag{3.1}$$

is set to 0.35 with a depth of 100 nm. These parameters are close to the optimum and is obtained from simulation study carried out by Goth.[138] The master structure is then replicated on a bilayer mold of hard polydimethylsiloxane (hPDMS) and PDMS. A mixture of hPDMS with a cross-linker in a ratio of 1:1 (outgassed for 30 min in a desiccator) is spin coated on the master structure at a speed of 5000 rpm for 30 s, followed by an annealing

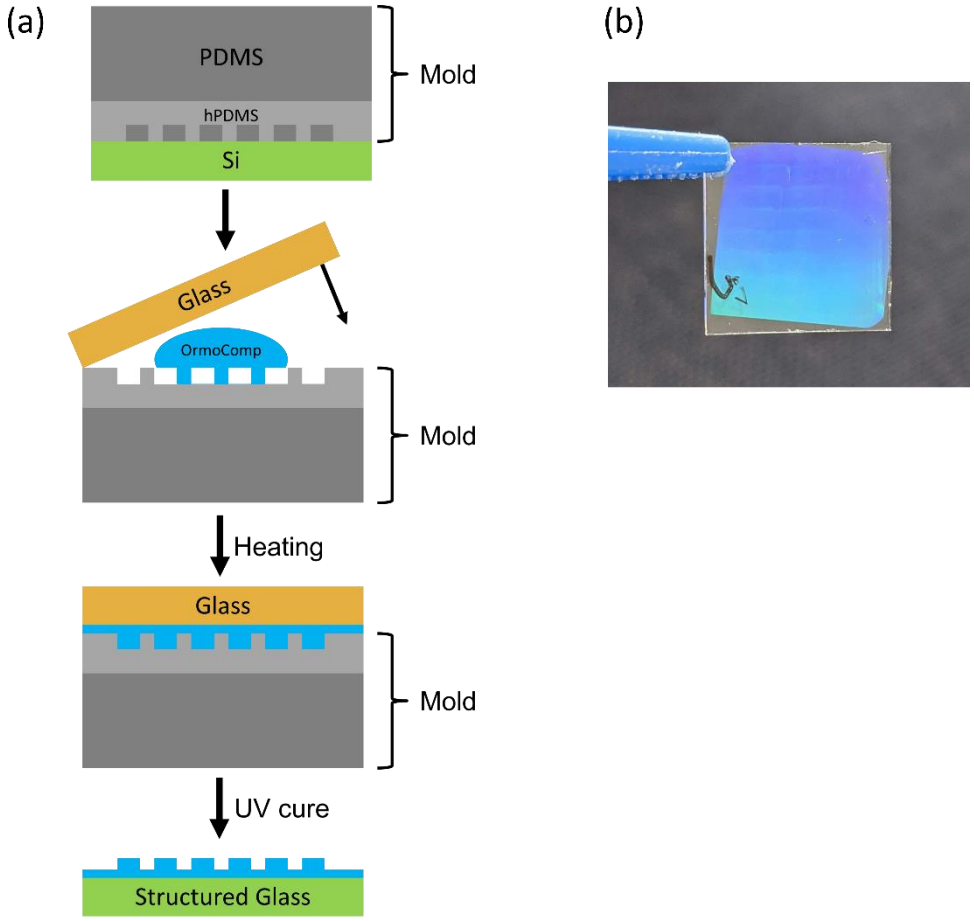

Fig. 3.5: (a) Schematic illustration of the fabrication of periodic nanopillars. First a mold of hPDMS and PDMS with predefined nanostructured dimensions is prepared. Next critical step involves application of OrmoComp on this mold and pressing with a glass substrate, followed by heating and annealing steps. Finally, sputtering of ITO leads to the formation of NS ITO. (b) Picture of a period nanostructured ITO demonstrating diffraction of light. Adapted from reference [138].

of 10 min at 60 °C. Next, the PDMS is mixed with a curing agent (in ratio 10:1 and outgassed for 30 min in a desiccator) is drop-casted on the sample and heated at 60 °C for 1 h, followed by 100 °C for another 1 h. The mold is then carefully removed from the silicon wafer.

To obtain the nanopillars, a commercial polymer named OrmoComp is drop-casted on the nanostructure mold and pressed with a glass substrate under a small weight (300 mg). This stack is left on the hotplate for 5 min at 60 °C. The stack is then UV exposed for 5 min to cure the resist and followed by carefully removing the nanostructured glass superstrate from the stamp. The obtained samples are then heated at 130 °C for another 30 min.

Finally, ITO is sputtered on the nanostructures to obtain the NS ITO. The sputtering conditions are as follows: power = 50 W, pressure = 0.8 mTorr, temperature = 25 °C, sputtering gas = Ar with 2.5% O_2 as the reactive gas, deposition time = 2000 s. A subsequent post annealing at 200 °C for 15 min improves both the transmission and conductivity of the final NS ITO. The planar ITO, which is the reference TCO, is fabricated by sputtering ITO directly on glass in the same sputtering run.

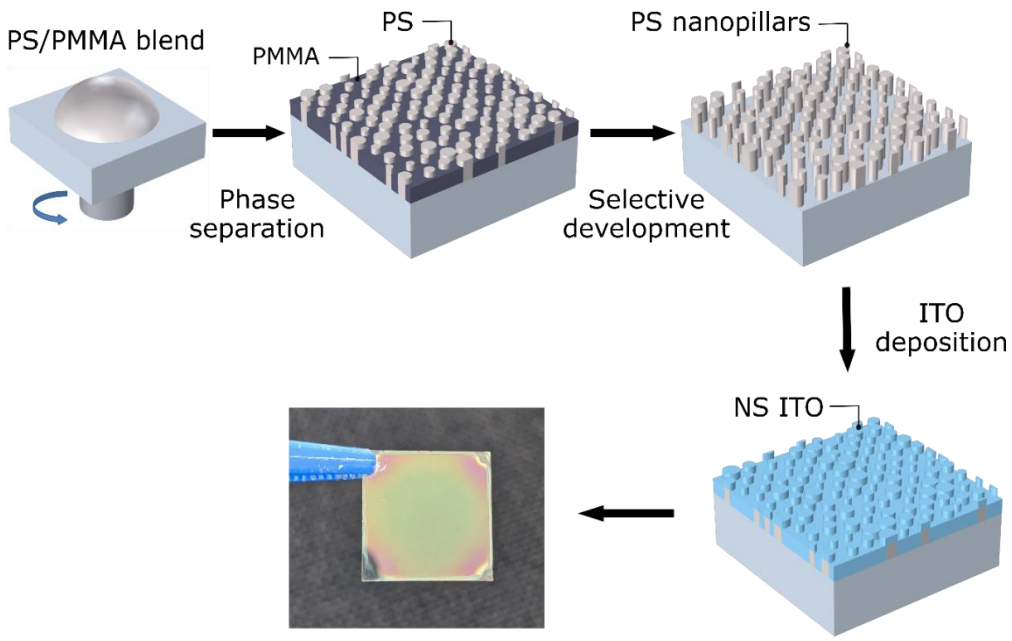

Fig. 3.6: Schematic illustration of the fabrication of disordered nanostructured ITO (NS ITO). PS and PMMA stands for polystyrene and poly(methyl methacrylate), respectively. A blend of PS and PMMA is first spin coated on a glass substrate. After selective development of PMMA, PS nanopillars are obtained. Finally, sputtering of ITO leads to the formation of NS ITO. Adapted with permission from reference [71], © 2020 Optical Society of America.

Disordered nanostructured ITO

Polymer blend lithography is employed to fabricate disordered NS ITO. **Fig. 3.6** shows the schematics to obtain disordered NS ITO. A blend of polystyrene, PS (molecular weight: 3.25k, Sigma Aldrich) and poly(methyl methacrylate), PMMA (molecular weight: 5.50k, Sigma Aldrich) dissolved in methyl ethyl ketone, MEK (Sigma Aldrich) in a mass ratio of 4/6, 15 mg/ml is used. The solution is placed on a hot plate at 100 °C for an hour to dissolve the solution. A 40 µl aliquot of the solution is spin coated onto the glass substrate at a speed of 3000 rpm for 30 s at a humidity ≈45%). The samples are then exposed to O_2 plasma for 30 s at a power of 50 W. Finally, the PS nanopillars are obtained by developing the samples in acetic acid (concentration of 99%, Alfa Aesar) that removed the PMMA. The ITO is sputtered on the nanopillars of PS in the same manner as described previously for periodic NS ITO.

3.2 Characterization Techniques

To evaluate the performance of the fabricated PSCs, the devices and layers are characterized electrically and optically with various tools. Details regarding each tool are described in the following section.

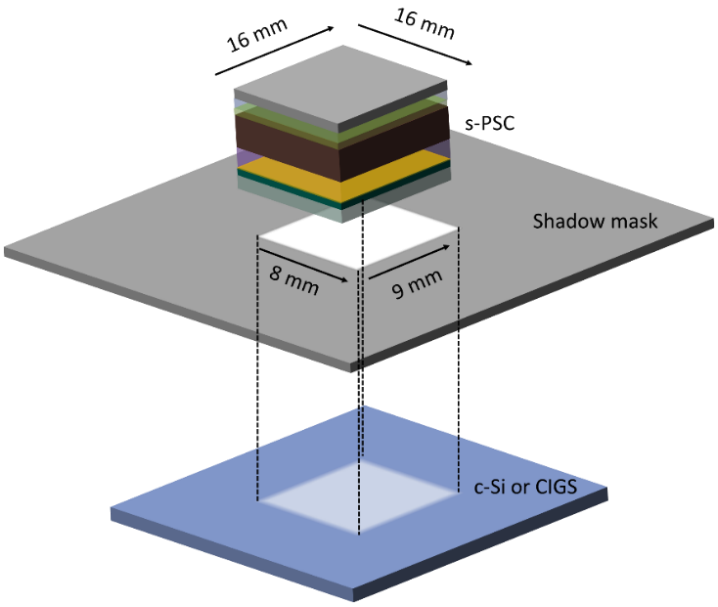

Fig. 3.7: Schematic illustration of a tandem solar cell measurement setup. The bottom crystalline-silicon (c-Si) or CIGS solar cells are measured through a filter of a top perovskite solar cell. A filter consists of the same layer stack as the s-PSCs and have optical properties as that of the s-PSCs but with a larger area. An aperture area is defined with the shadow masks to measure the bottom solar cells. Adapted with permission from reference [99], © John Wiley & Sons.

3.2.1 Electrical characterization

Current density-voltage (*J-V*) characteristics

The performance of the fabricated PSCs is determined by a solar simulator. Typical current density-voltage (*J-V*) characteristic of a solar cell is shown in **Fig. 2.4**. The *J-V* characteristics of the investigated PSCs are measured using a class AAA Newport solar simulator (xenon lamp). The measurements are performed under standard test conditions. This means that the PSCs are illuminated at 1000 W/m^2 with a continuous illumination of AM 1.5G, keeping the devices at 25 °C. The voltage is swept from open-circuit voltage (V_{OC}) condition to short-circuit current density (J_{SC}) and vice-versa using a Keithley 2400 source meter. This allows the determination of hysteresis in PSCs. A constant sweeping rate of 600 mV/s is used. The temperature of the samples is actively controlled using a self-made Peltier element control circuit. For the o-PSCs, the devices are measured without any shadow masks as the active area is clearly defined by the overlap between the ITO and gold layouts. For s-PSCs, shadow mask of 5.6 mm^2 is employed to define an aperture area for the devices.

The c-Si solar cell or CIGS solar cell is measured either stand-alone or under the filters of s-PSCs prepared during the fabrication of the solar cells. A filter consists of the same layer stack as the s-PSCs and have optical properties as that of the s-PSCs but with a larger area (16 mm x 16 mm). The schematic of a tandem measurement setup is illustrated in **Fig. 3.7**. An air gap exists between the sub-cells as no additional material is used as a spacer

between the top s-PSC filters and the bottom solar cells. A shadow mask with an aperture area of 72 mm^2 or 165 mm^2 is used to define the active area. The final power conversion efficiency (PCE) of the 4T tandem configuration is obtained by the sum of the top s-PSC PCE and the bottom c-Si or CIGS solar cell PCE.

External quantum efficiency

As discussed in section 2.1 Chapter 2, external quantum efficiency (EQE), measurements are performed to determine the spectral response of the PSCs. The measurements are carried out using a Bentham PVE300 system. In contrast to the solar simulator, light is incident on the sample with a much lower intensity that results in a reduction of signal-to-noise ratio. Therefore, the EQE system uses a lock-in amplifier technique with a reference signal having a chopping frequency of ≈930 Hz, which reliably improves the signal-to-noise ratio. Integration times of 500 ms are used to obtain the signal.

Four-point probe technique

Four-point probe measurements are performed to measure the sheet resistance of the TCOs. The schematic of a typical four-point probe setup is illustrated in **Fig. 3.8**. The outer pins 1 and 4 are used to drive a current through the film. This generates a voltage across the resistance of the film. The inner pins 2 and 3 measure the generated voltage. Since, there is no current flowing though pins 2 and 3, the voltage drop across these contacts is neglected. Here, a custom made four-point setup is used to measure sheet resistances of various TCOs. The setup includes an S-302 four-point probe mounting stand and a Picotest M3500A multi-meter. The sheet resistance can be calculated by:

$$R_{sh} = \frac{\pi}{\ln(2)} \frac{\Delta V}{I} \tag{3.2}$$

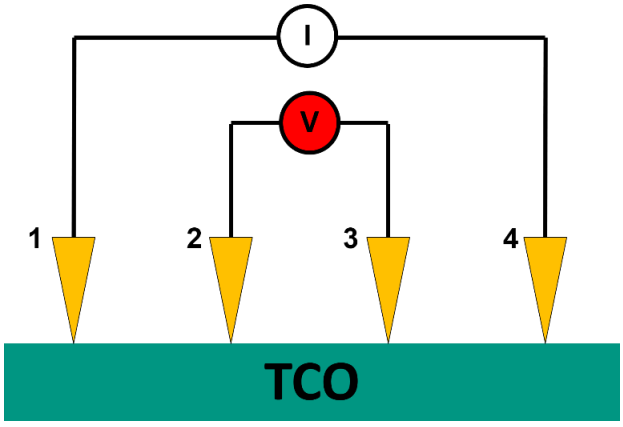

Fig. 3.8: Schematic illustration of a four-point probe setup for measuring sheet resistance of transparent conductive oxide (TCO) electrodes.

3.2.2 Optical characterization

Spectrophotometry

Spectrophotometry measurements spectrally resolves the amount of light that is absorbed, reflected and transmitted by a layer stack or a certain material. A typical spectrophotometer consists of a white light source coupled to a monochromator and a detector placed inside an integrating sphere (**Fig. 3.9**a). The monochromator selects the desired wavelength of light. For transmittance (*T*) measurements, a test sample is placed in front of the integrating sphere (position 1). The measurement is performed by collecting the transmitted light through the sample using the detector. A reflectance (*R*) measurement is performed by placing the test sample at the end of the integrating sphere (position 2). The reflected light from the sample is collected by the detector. The absorptance (*A*) is calculated from the following equation:

$$A = 1 - T - R \tag{3.3}$$

In order to measure the *T* and *R* of various layers investigated in this thesis, a PerkinElmer Lambda 1050 spectrophotometer is used. Typical transmittance and reflectance spectra measured for IZO on glass are shown in Fig. 3.9b,c. Furthermore, by knowing the thickness (t) of the layer, the absorption coefficient (α), which is a measure of the penetration depth of light for a material, can then be calculated. The absorption coefficient is given by:

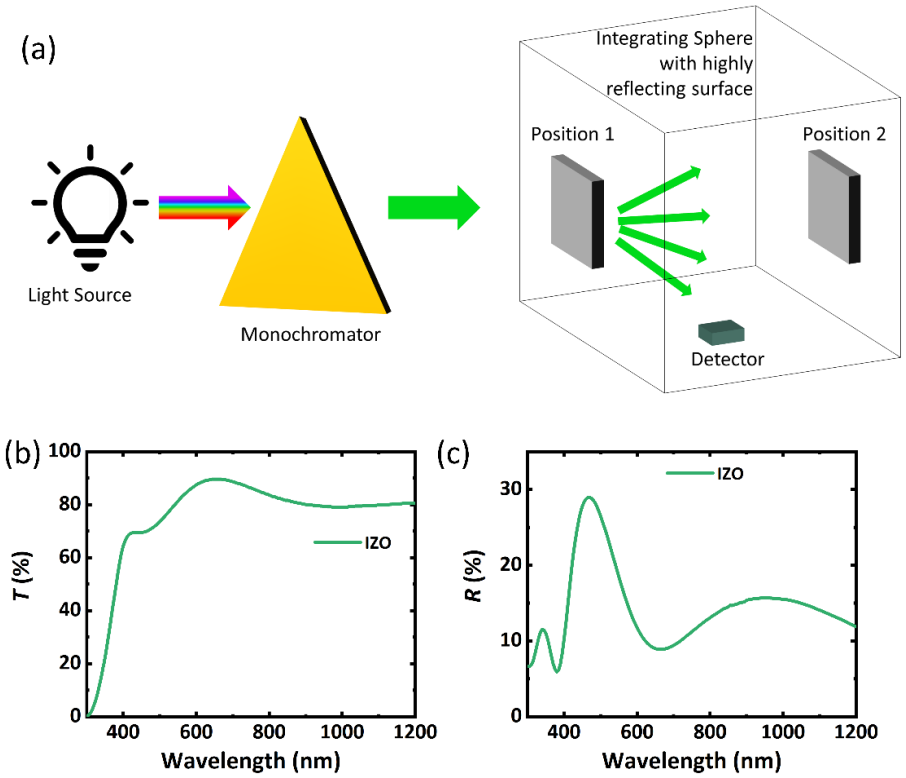

Fig. 3.9: (a) Schematic illustration of a spectrophotometry setup. Spectrally resolved light is incident on the sample and then measured by a detector. Typical (b) transmittance (*T*) and (c) reflectance (*R*) spectra of IZO on glass.

$$\alpha = \frac{1}{t}\ln\frac{(1-R)^2}{T} \tag{3.4}$$

Ellipsometry

Ellipsometry is a non-invasive technique for measuring the dielectric properties of thin films. It measures the change in polarization when an incident light of known polarization is reflected from the thin film surface (**Fig. 3.10**a). The change in the polarization is related to the Fresnel reflection coefficients, r_s and r_p and is represented by:

$$\rho = \frac{r_s}{r_p} = \tan\psi \,.\, e^{i\Delta} \tag{3.5}$$

where, ρ is the complex reflectance ratio, tan ψ is the amplitude ratio upon reflection, and Δ is the phase shift. By using an accurate model derived from electromagnetic theory, such as Lorentz model and Drude model, the complex refractive index of the materials can be evaluated. In this thesis, the refractive indices and extinction coefficients of TCOs and charge transport layers are determined using a Woolam Variable Angle Spectroscopic Elliosometry (WVASE). Refractive index and extinction coefficient of commercial ITO can

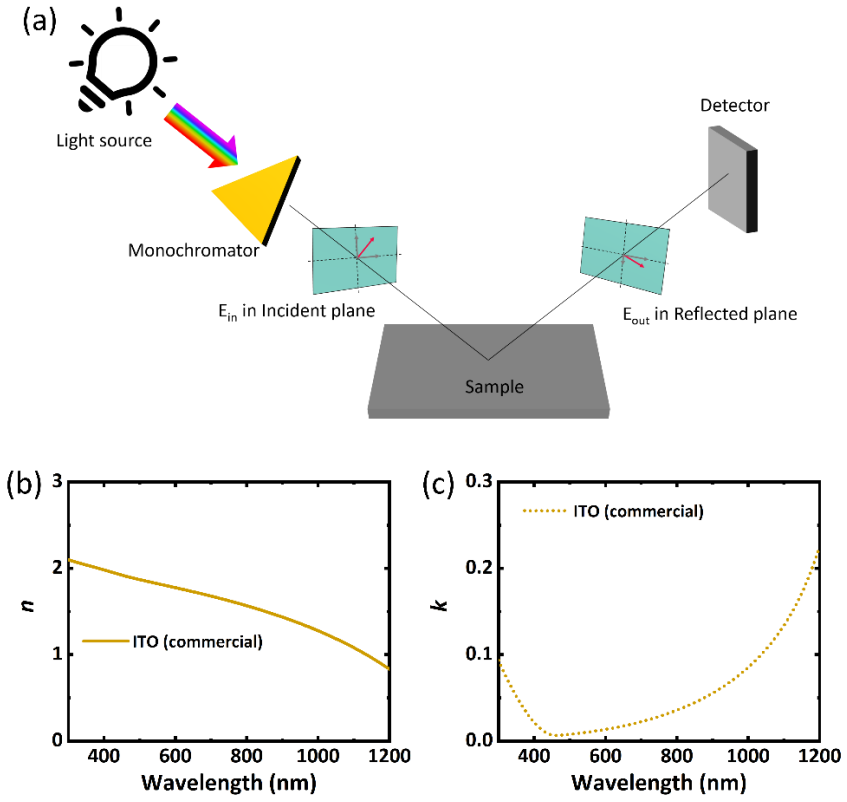

Fig. 3.10: (a) Schematic illustration of an ellipsometry setup. The change in the polarization of light is used to determine the film or sample properties. (b) Refractive index (*n*) and (c) extinction coefficient (*k*) of tin-dope indium oxide (ITO) electrode derived from ellipsometry.

be found in Fig. 3.10b,c. The analysis is performed with the software provided by the manufacturer.

Photoluminescence spectroscopy

Photoluminescence spectroscopy is used to obtain insights about the electronic structure and properties of a material. In this process, an incident light of energy above the bandgap of the material is directed towards a sample, causing an electron to be excited in the conduction band. After thermal relaxation, the exited electron recombines with a hole by emitting photons (**Fig. 3.11**a,b). The emitted light is then spectrally resolved by a monochromator and finally detected by a camera. Two types of photoluminescence measurements are performed in this thesis: (i) steady-state photoluminescence spectroscopy (SSPL), and (ii) time-resolved photoluminescence spectroscopy (TRPL). SSPL spectroscopy investigates the long-term (several micro seconds to milli seconds) average

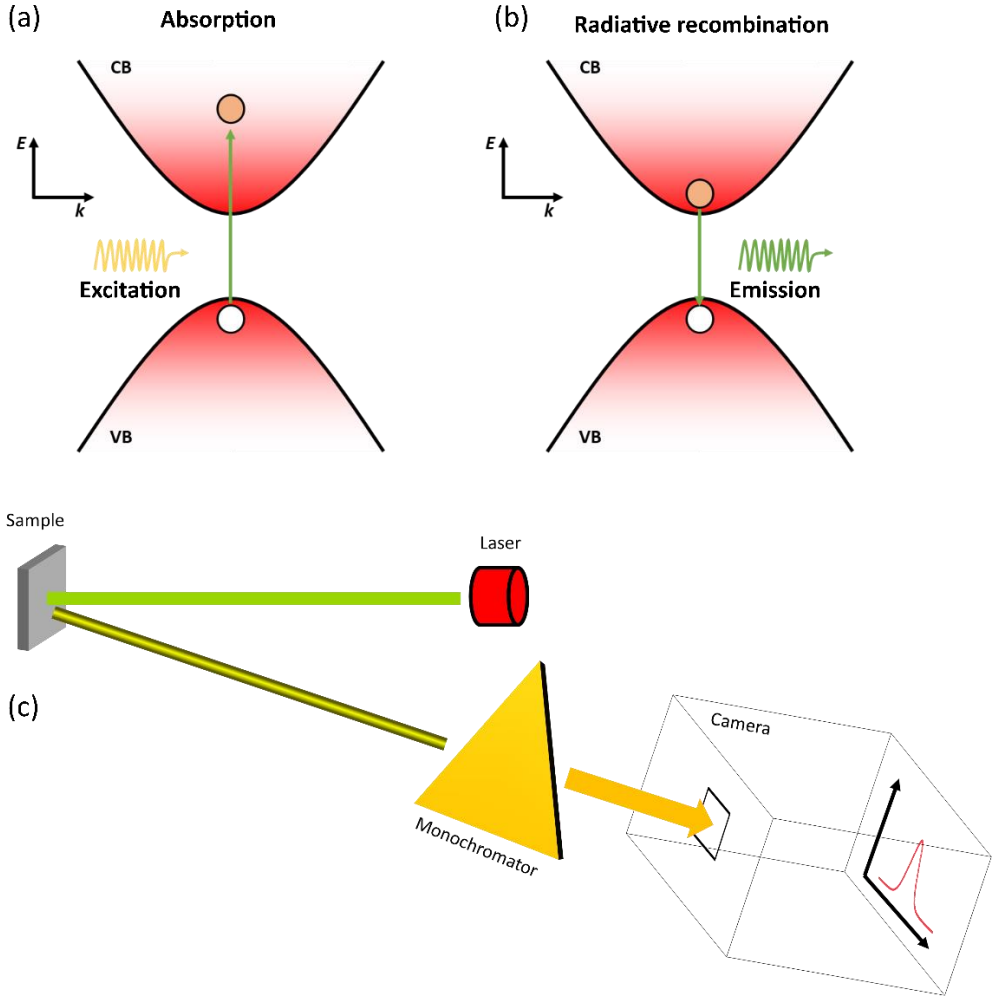

Fig. 3.11: (a) Absorption and (b) radiative recombination processes occurring during a photoluminescence spectroscopy measurement. Photons of energy higher than the bandgap of the material excites an electron from the valence band (VB) to the conduction band (CB). An excited electron in the CB can find a hole in the valance band and relax by emitting a photon. (c) Schematic illustration of a photoluminescence spectroscopy setup. A sample is excited by laser pulses. The excited electrons emit photons which are spectrally resolved by a monochromator and detected by a sensitive camera.

emission from a sample when exited by light. Various properties can be evaluated from such a measurement, for instance, the determination of the bandgap, carrier distribution, phonon scattering or structural homogeneity of the investigated material. TRPL spectroscopy investigates the temporal evolution of the emission from a sample. In such a measurement, the detection window is reduced to several pico seconds in contrast to SSPL. This method can be used to determine the lifetime of charge carriers. In principle, a longer lifetime of the charge carriers is preferred for the absorber materials as it indicates reduced non-radiative recombination losses. Here, SSPL and TRPL measurements are performed for perovskite absorbers or semitransparent PSCs with a custom-made setup. A schematic of the typical photoluminescence spectroscopy setup is illustrated in Fig. 3.11c. A pulsed laser of 532 nm with a repetition rate of 1 kHz or 5 kHz is used to excite the samples. The emission is detected using a CCD camera, PIMAX512 fed by an ACTON spectrometer. For TRPL, a gated mode with a gate opening time of 3 ns is used. The measurements are performed in air.

3.2.3 Material characterization

X-ray diffractometry

To investigate the crystallinity of a material, X-ray diffractometry (XRD) is performed. Every crystalline material has a clear signature due to its unique crystal structure as the atoms are arranged in a regular order. When these atoms are excited with electromagnetic wave of wavelengths in the same order as the lattice dimension, they scatter light (**Fig. 3.12**). The scattered or also referred as reflected wave can interfere constructively if the following condition is satisfied:

$$2d\sin\theta = n\lambda;\ n = 1, 2, 3.... \tag{3.6}$$

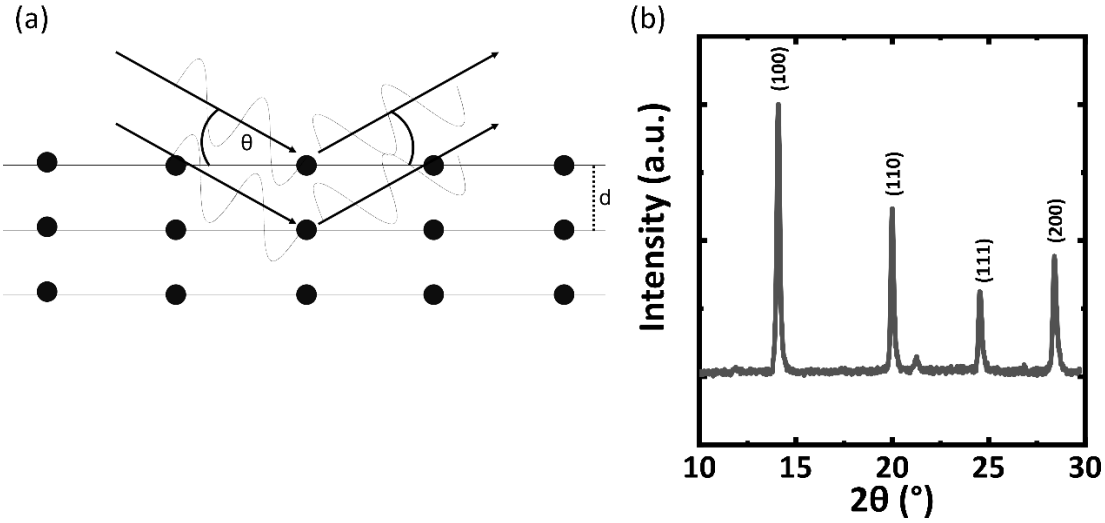

Fig. 3.12: (a) X-ray diffraction (XRD): Bragg's law. (b) Typical XRD pattern of a perovskite crystal structure.

where, d is the distance between the planes, θ is the incident angle of the electromagnetic wave, λ is the excitation wavelength and n is a constant. This is known as Bragg's law of diffraction. Each reflection from the planes inside the crystal lattice can be represented by Miller indices. A typical XRD diffraction pattern for a perovskite film is shown in Fig. 3.12b. In addition to the crystallinity, the crystallite size as well as strains induced in the crystal structure can be determined via XRD measurements. In this thesis, XRD measurements are performed to determine the crystal structure of np-TiO_2, perovskite absorbers and TCOs. The measurements are carried out using a Bruker D2 phaser XRD system with a Cu Kα radiation source. Typical excitation powers are 30 keV.

X-ray photoelectron spectroscopy

To obtain an insight about the chemical composition of a certain material, x-ray photoelectron spectroscopy (XPS) is performed. In this technique, x-rays are irradiated on a material in ultra-high vacuum due to which electrons are emitted from the atomic orbitals for the first few nanometers of the material's surface. An electron detector and electron energy analyzer provide the number of electrons that are emitted and their respective kinetic energy (E_k), which are then used to deduce the binding energy (E_B) of respective electrons (**Equation 3.7**). The obtained binding energy is associated to the respective orbital from which the electron is emitted and depends both on the element and its chemical environment. The work function (ϕ) is the minimum energy required to eject an electron from the material outside its surface.

$$h\nu = E_k + E_B + \phi \tag{3.7}$$

Here, XPS measurements are performed on np-TiO_2 using a K_α^+ XPS spectrometer from Thermo Fisher Scientific. The samples are analyzed using a micro-focused, monochromated Al K_α X-ray source with a spot size of 400 µm. The spectra are fitted with one or more Voigt profiles, and referenced to C 1s peak of hydrocarbon at 285.0 eV binding energy.

Scanning electron microscopy

Since the dimension of the investigated layers are in the order of few tens to hundreds of nanometers, ordinary optical microscope cannot resolve these layers. Thus, a scanning electron microscope (SEM) is used to visualize them. In a SEM setup, beams of electrons produced with an electron gun that are accelerated by a large potential (tens of kilo volts) inside a vacuum chamber. The path of the beam is controlled with some deflection coils before focusing them on the sample using condensing lenses. Up on interaction with a sample, the electrons are either backscattered or secondary electrons are created. In some cases, x-rays are also emitted. All these signals are detected using very sophisticated detectors to produce a final image of the sample. Here, the SEM images are obtained for investigating perovskite absorber layers, charge transport layers and TCOs. The measurement is performed using a Leo 1530 (Zeiss) SEM with both in-lens and secondary

detectors. Typical accelerating voltages of 5−10 keV with aperture of 30 µm are used to obtain the images.

Atomic force microscopy

The surface roughness of a layer is determined using atomic force microscopy (AFM). This measurement provides information about the topography of the sample surface with a high resolution in orders of a few nanometers. The AFM system comprises of a cantilever, an X-Y stage, a Z-scanner and a position scanner (**Fig. 3.13**a**)**. A laser beam, which is directed towards the cantilever, is reflected onto the position scanner. The X-Y stage is used to move around the sample surface and if there is a change in the surface topography, the position of the Z-scanner is altered. Thus, an image of the surface morphology is obtained. A non-contact or tapping method is used to obtain the surface morphology of the investigated samples, which helps in retaining the tip sharpness and leaves the surface unharmed. In this thesis, AFM is performed to determine the morphology of NS ITO and surface roughness of various TCOs. An AFM image of a periodic NS ITO is shown in Fig. 3.13b. The samples are investigated in ambient conditions with an AFM system from dimension icon, Veeco with a NanoScope V controller. Typical scan sizes are 5 µm x 5 µm or 10 µm x 10 µm with resolutions of up to 512 x 512 pixels.

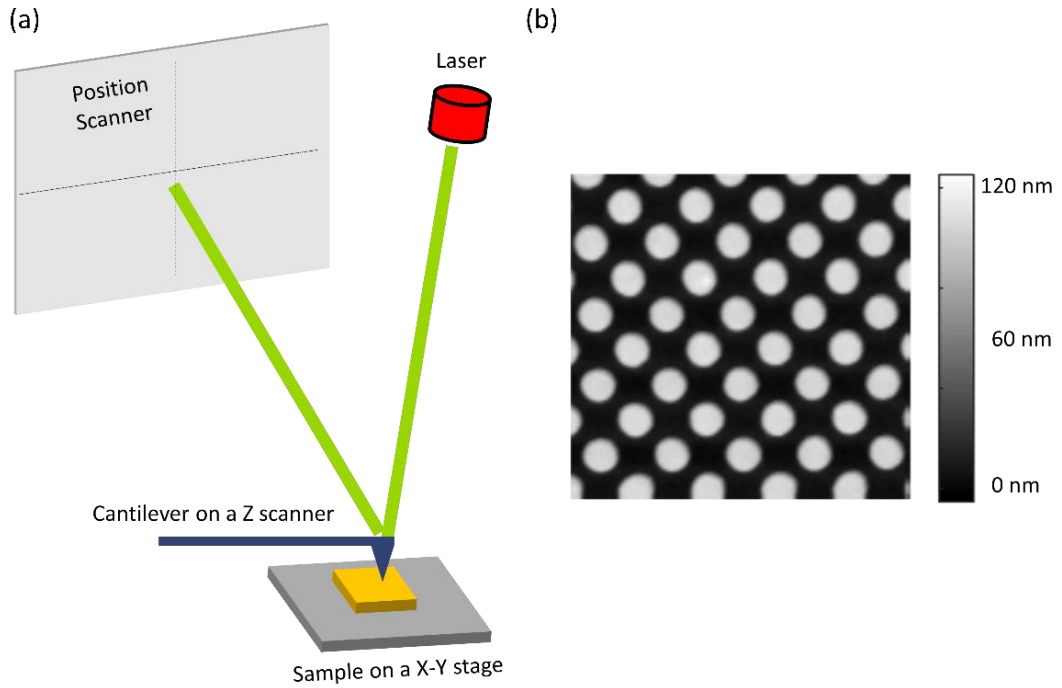

Fig. 3.13: (a) Schematic illustration of an atomic force microscopy setup. (b) Atomic force microscopy (AFM) image of periodic nanostructured ITO.

4. Nanoparticle-based electron transport layers for semitransparent perovskite solar cells

This chapter deals with research question 1 and discusses nanoparticle-based electron transport layers (ETLs) for perovskite solar cells (PSCs). It includes a detailed study of the various material properties of said nanoparticles. Two types of nanoparticle-based ETLs are investigated: (i) nanoparticles of titanium dioxide (np-TiO_2), and (ii) nanoparticles of tin oxide (np-SnO_2). An in-house synthesis is employed to prepare the np-TiO_2. Furthermore, in-depth studies regarding various synthesis parameters and some compelling features of the np-TiO_2 are described. The np-SnO_2, extensively used as an alternative ETL in this thesis, is purchased from a commercial manufacturer. The chapter concludes with a comparative study of the optical properties and the photovoltaic characteristics of the PSCs fabricated with these ETLs.

Acknowledgments and contributions

The major part of this chapter on the nanoparticle-based electron transport layer for perovskite solar cells was already published in reference [139]. *The publication of the research article was a collaboration between KIT, IMEC and Solliance. In this collaboration, Ihteaz M. Hossain conducted and analyzed most of the synthesis of np-TiO_2, material characterization (optical), and fabrication of perovskite solar cells. Ihteaz M. Hossain acknowledges the support of Adrian Mertens in the analysis of the optical constants and the support of Jonas Alexander Schwenzer, who performed the initial studies of the development of np-SnO_2 ETL in this research group.*

The significant advancement in the field of perovskite photovoltaics is a result of a better comprehension of the crystallization dynamics of the absorber layer,[140] the compositions of the absorber material,[32,34] the passivation of defects,[91] a superior electron- and hole-transport layers (ETLs and HTLs) with improved charge selectivity,[70,80] and well-aligned energy levels with the absorber.[141] In terms of ETL, a lot of materials were previously investigated to fulfill the following criteria: (1) wide-bandgap of the ETL to avoid any parasitic losses, (2) well-aligned energy level to the highest occupied molecular orbital of the perovskite absorber layer to ensure a barrier-free transfer of electrons to the respective ETL and reduce energy losses, and (3) a fast extraction of electrons to the respective contact. Therefore, several ETLs including TiO_2,[48] SnO_2,[142] ZnO,[142] WO_3,[142] and organic fullerenes[143] were studied in literature regarding the above criteria.

The most widely used ETL is TiO_2 with which some of the highest power conversion efficiencies (PCEs) of the perovskite solar cells (PSCs) are reported.[31–34] TiO_2 possesses fast charge extraction of charges with mobilities of 0.1-10 $cm^2/V\,s$.[144] To achieve high PCEs, the TiO_2 ETL is deposited in a sequence of a compact layer followed by a mesoporous structure. The compact TiO_2 acts as a blocking layer,[145] thus preventing holes from reaching the transparent conductive oxide (TCO) in a n-i-p architecture. The mesoporous layer acts as scaffold for the perovskite absorber.[146] One important aspect to consider here is the deposition of the TiO_2 transport layer. The deposition of high-quality TiO_2 ETL for efficient PSCs involves solution processing of the precursor material and a post-annealing of > 450 °C to ensure the crystalline anatase phase of TiO_2.[35,147] This crystalline phase ensures high mobility in TiO_2 ETL. The annealing step is very high in energy demand and incompatible with conventional TCO electrodes such as indium-doped tin oxide (ITO) or low-cost flexible plastic substrates. As a consequence, this process is not adequate for upscaling techniques that involve roll-to-roll fabrication of PSCs. Moreover, fluorine-doped tin oxide (FTO) substrates must be employed to fabricate PSCs. FTO electrodes are compatible with high-temperature annealing processes, but are not suitable for efficient perovskite/c-Si or perovskite/CIGS tandem solar cells due to their high near-infrared (NIR) parasitic absorption (also see **Appendix, Fig. A. 4.1**).[36] Both of these factors motivate the research to alternative approaches to process the TiO_2 or investigation of different materials as ETLs.

In order to overcome the limitation of high temperature processing of TiO_2, an alternative approach is described in this study as the first strategy with the promise of up-scalable and highly transparent semitransparent perovskite solar cells (s-PSCs) for tandem architecture. This includes pre-synthesis of in-house nanoparticles of titanium-dioxide (np-TiO_2) in its crystalline anatase phase and the subsequent deposition of the np-TiO_2 on a substrate as the ETL at a lower temperature, which is compatible with ITO or flexible substrates. The material properties as well as the photovoltaic performance of the fabricated PSCs on the various synthesis parameters are investigated in detail including the effect of doping, synthesis time and solvent systems.

As a second strategy, commercially available nanoparticle of tin-oxide (np-SnO_2) is also investigated for PSCs. In recent studies, focus is placed on SnO_2 ETL due to following

reasons: (i) bulk mobility of SnO_2 is significantly higher than TiO_2 (100 times),[148] (ii) SnO_2 is a wide-bandgap material,[70] resulting in less parasitic absorption, and (iii) SnO_2 has a deep conduction band,[148] indicating a better electron extraction from the absorber and ensuring improved hole blocking. Moreover, it is reported that SnO_2 exhibits excellent chemical stability in comparison to TiO_2[89] and can be deposited at low temperatures, ensuring the feasibility of roll-to-roll processing and compatibility with highly transparent ITO electrodes.[142] In order to compare and find the optimum ETL for the application in perovskite-based tandems, a comparative study based on the photovoltaic performance and stability of the PSCs with these two ETLs are discussed at the end of this chapter.

4.1 np-TiO_2 ETL for perovskite solar cells

The overall performance of the fabricated PSCs depends highly on the material properties of the ETL. Therefore, in this section, the crystallinity and the bandgap of the synthesized np-TiO_2 are investigated. Moreover, since the np-TiO_2 are prepared in-house, several processing parameters (size, solvent system and doping) are investigated, which allows additional degrees of freedom to obtain np-TiO_2 with compelling features.

4.1.1 Material properties of np-TiO_2

The synthesis process described in the chapter 3, section 3.1 results in the formation of crystalline np-TiO_2. In order to investigate the crystal structure and the type of polymorph, X-ray powder diffraction (XRD) measurements are carried out with a K_α excitation obtained from a Cu source. The nanoparticles are drop-casted from the dispersion on a silicon substrate and allowed to dry before being investigated. A strong reflection peak at $2\theta \approx 25.3°$ indicates the presence of the <101> plane of the crystal lattice (**Fig. 4.1**). Furthermore, weak reflection peaks at $2\theta \approx 37.7°$, 47.7°, and 54.0° represent the existence of <004>, <200> and <105> planes, respectively. These results prove the crystalline nature of the synthesized nanoparticles. In order to determine the phase of the np-TiO_2, the obtained XRD peaks are compared to the literature reflection peaks of the anatase and the

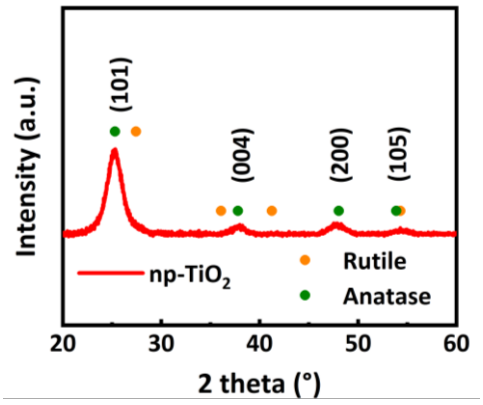

Fig. 4.1: X-ray diffraction (XRD) pattern of np-TiO_2 (red) presented with the typical positions of anatase TiO_2 (green) and rutile TiO_2 (orange) phase. The presence of the typical reflection peaks from plane <004>, <200> and <105> and the absence of the typical reflection peak at $2\theta \approx 27.4°$ of the rutile polymorph indicates that the np-TiO_2 crystallize in its anatase phase. Reproduced with permission from ACS Applied Energy Materials, [139] © American Chemical Society.

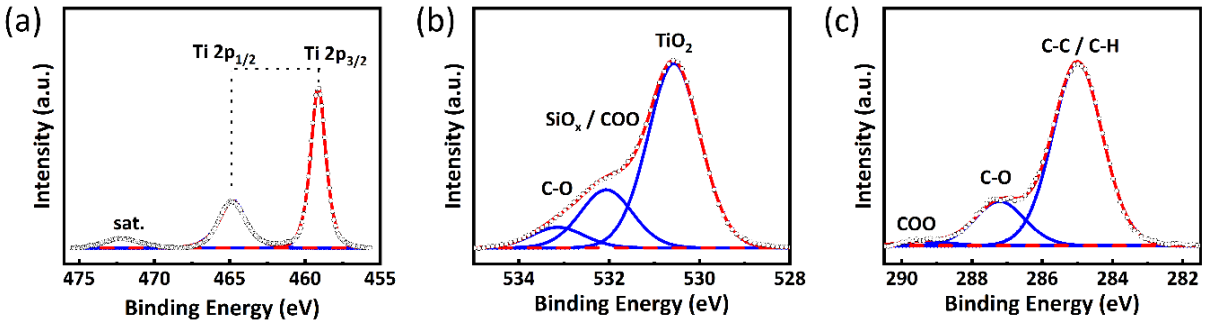

Fig. 4.2: (a) Ti 2p, (b) O 1s and (c) C 1s x-ray photoelectron spectra of np-TiO_2 drop-casted on Si substrates. Reproduced with permission from ACS Applied Energy Materials, [139] © American Chemical Society.

rutile phase of the np-TiO_2 (green and orange dots, respectively in **Fig. 4.1**).[139] The presence of the typical reflection peaks from plane <004>, <200> and <105> and the absence of the typical reflection peak at 2θ ≈27.4° of the rutile polymorph clearly indicates that the np-TiO_2 crystallize in its anatase phase.

X-ray photoelectron spectroscopy (XPS) measurements are performed to confirm the presence of stoichiometric np-TiO_2 (**Fig. 4.2**). For this, np-TiO_2 are also drop-casted on silicon substrates so that a continuous film of np-TiO_2 is formed on the surface. The sample is excited using a micro-focused, monochromated Al K_α X-ray source with a spot size of 400 µm, significantly smaller than the area of the sample. Voigt profiles are used to fit the obtained results with C 1s peak of hydrocarbon at 285.0 eV binding energy as reference (Fig. 4.2c). The main Ti $2p_{3/2}$ peak of the Ti 2p spin-orbit doublet at 459.1 eV and O 1s peak at 530.6 eV proves the formation of TiO_2 (Fig. 4.2a-b).[149,150] The O 1s peak at 532.1 eV depicts the native oxide of non-covered Si substrate.[151] The other C-O groups (C 1s = 287.2 eV, O 1s = 533.1 eV) and O=C-O groups (C 1s = 289.3 eV, partly O 1s = 532.1 eV) seen in the spectra can arise from solvent residues.[152]

Spectrophotometric measurements are conducted to determine the bandgap of np-TiO_2. 20 µL of the np-TiO_2 dispersion is diluted in ethanol (x100 times) and placed in a cuvette. The absorbance spectrum shows increased absorption below 375 nm (**Fig. 4.3**a). Using the absorbance spectrum and the well-known Tauc plot method, the bandgap of the np-TiO_2 is determined. The following relation is used:

$$(\alpha h\nu)^{1/n} = \beta(h\nu - E_g) \tag{4.1}$$

where, α is the absorption coefficient, h is the plank's constant, ν is the frequency, β is a constant, E_g is the optical bandgap, and n denotes the nature of the transition. Since the crystalline structure of the np-TiO_2 obtained is anatase in nature, the type of optical transition is indirect.[153] Therefore, using n = 2, $(\alpha h\nu)^{1/2}$ is plotted versus hν (Fig. 4.3b). The x-intercept of the slope reveals the bandgap of the np-TiO_2. The obtained bandgap for the synthesized np-TiO_2 is 3.19 eV, and in line with the values of the indirect bandgap of anatase TiO_2 (3.20 eV) reported in the literature.[154]

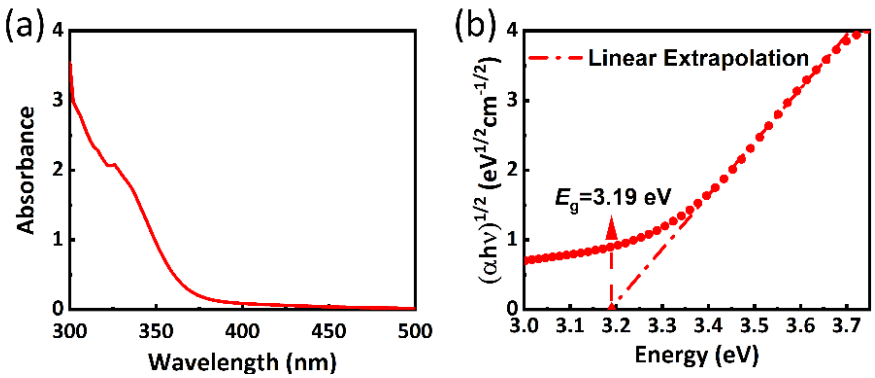

Fig. 4.3: (a) Absorbance spectrum of np-TiO_2 dispersed in ethanol. (b) Tauc plot indicating the indirect bandgap of np-TiO_2 (E_g = 3.19 eV). Reproduced with permission from ACS Applied Energy Materials, [139] © American Chemical Society.

4.1.2 Additional features of np-TiO_2

The synthesis procedure described chapter 3, section 3.1 forms stoichiometric np-TiO_2 in its crystalline anatase phase as concluded in the previous section. The in-house preparation of the np-TiO_2 also allows further possibility to tune the properties of nanoparticles. In this regard, the influence of doping and variations of the synthesis parameters such as time and solvent systems are investigated, which demonstrate some more appealing features of the np-TiO_2.

First, the doping of the np-TiO_2 is investigated. Although previously it was reported that np-TiO2 can be doped with yttrium,[155] here, the np-TiO_2 is doped with Nb^{5+} to improve the conductivity of the ETL. During the first step of the synthesis as discussed on chapter 3, section 3.1, $NbCl_5$ (7 at. %) is included as additional material in the precursor solution. To investigate the presence of Nb^{5+} ions, XPS measurements are performed, similar to the procedure described earlier. The peak at 207.4 eV shown in **Fig. 4.4**a corresponding to the

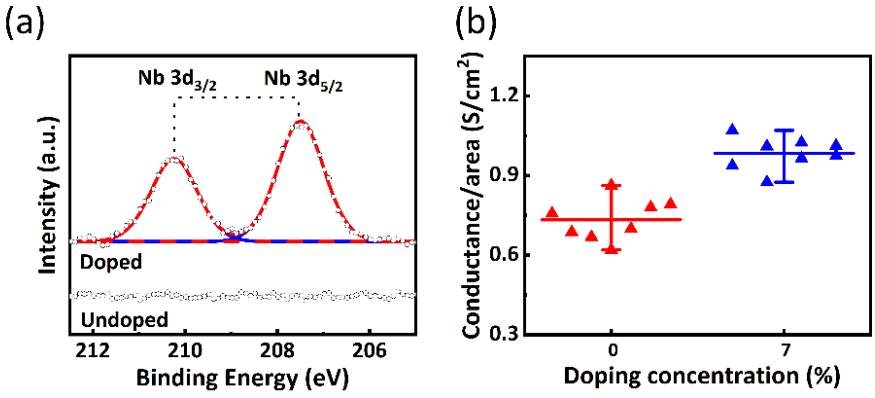

Fig. 4.4: (a) X-ray photoelectron spectroscopy in the energy range of the Nb 3d spin-orbit doublet of undoped (bottom) and Nb-doped np-TiO_2 (top). The Nb $3d_{5/2}$ peak at 207.4 eV proves the presence of Nb^{5+} (b) Conductance of np-TiO_2 electron transport layer for undoped (0%) and doped (7%) layers. Improved conductivity is achieved for np-TiO_2 doped with Nb^{5+}. Reproduced with permission from ACS Applied Energy Materials, [139] © American Chemical Society.

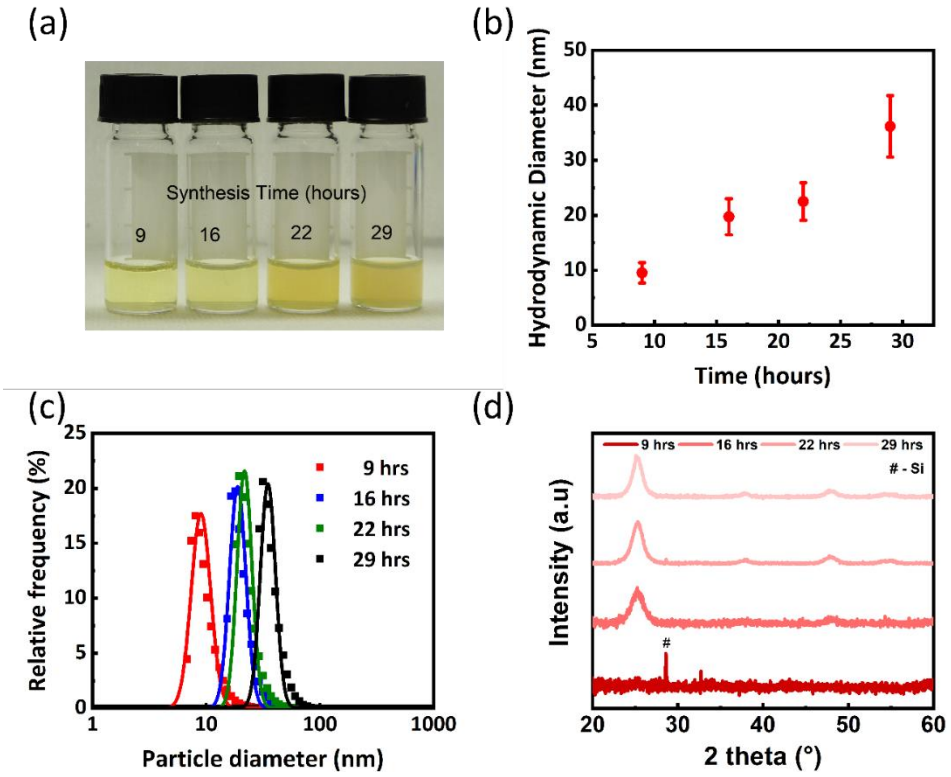

Fig. 4.5: (a) Picture of synthesized np-TiO_2, (b) hydrodynamic diameter or size, (c) relative frequency extracted from the dynamic light scattering (DLS) measurements, and (d) the evolution of the X-ray diffraction (XRD) analysis for 9 h, 16 h, 22 h, and 29 h of synthesis. Reproduced with permission from ACS Applied Energy Materials, [139] © American Chemical Societv.

Nb $2d_{5/2}$ orbital, which indicates the presence of Nb^{5+} ions in the np-TiO_2. In contrast, no additional feature is detected around this binding energy for the undoped np-TiO_2. In order to examine the effect of Nb^{5+} on the conductivity of the np-TiO_2 ETL, np-TiO_2 layers with and without Nb^{5+} are compared. Both layers are deposited on ITO substrates, followed by gold back contacts, forming the following architecture: ITO/np-TiO_2/Au. The measured conductance for both the layers is plotted in Fig. 4.4b and reveals that the conductance of the np-TiO_2 is increased in the presence of Nb^{5+}.These results indicate that the np-TiO_2 can be doped with Nb^{5+} using this synthesis technique and a further enhancement in the conductivity is possible.

Second, the synthesis time is varied to control the size of the particles. An increase in the synthesis time results in a cloudy solution as shown in **Fig. 4.5**a, which indicates the presence of the larger particles in the dispersion. The size of the particles is determined using dynamic light scattering (DLS) technique. This technique is based on the statistical analysis of the scattered light from particles suspended in a dispersion and assumes a spherical shape of the particles. Therefore, this measurement presents only an approximation of the size of the nanoparticles, with a certain size distribution. The measurement depicts an asymmetry and a positive skewness in the size distribution of the nanoparticles (Fig. 4.5c).

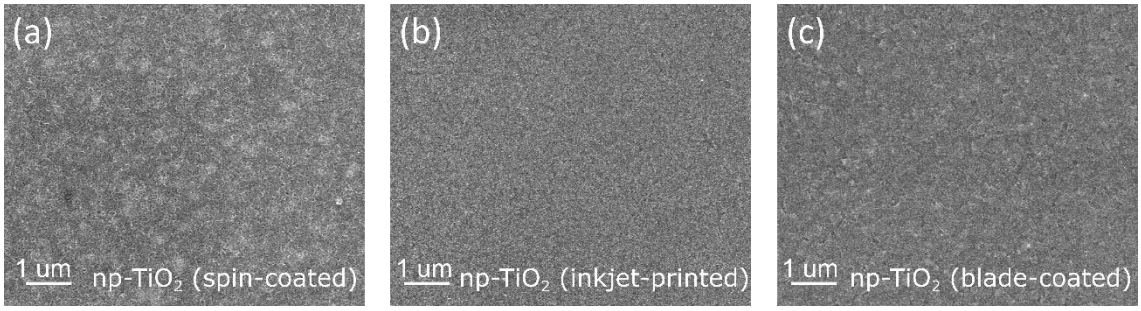

Fig. 4.6: Top-view scanning electron microscopy (SEM) images of (a) spin-coated, (b) inkjet-printed, and (c) blade-coated np-TiO_2 ETL. Reproduced with permission from ACS Applied Energy Materials, [139] © American Chemical Society.

This positive skewness could arise from the presence of either larger/agglomerated nanoparticles or non-spherically shaped nanoparticles. The obtained data fitted with a log normal distribution reveal that the average hydrodynamic diameter of the np-TiO_2 varies between ≈9 nm to ≈36 nm depending on the synthesis time (9-29 h). In order to evaluate the minimum time required to obtain the np-TiO_2 in its crystalline form, the crystallinity of the np-TiO_2 for these different hours of synthesis is also investigated. The evolution of the XRD pattern depicted in Fig. 4.5d shows that the np-TiO_2 crystallizes in its anatase phase only for synthesis time > 16, whereas the for the 9 h synthesis, the particles are still amorphous. However, it should be noted that a cut-off time certainly exists between 9 h and 16 h, between which the phase transition takes place. Overall, these results show that this synthesis technique allows a facile way to obtain np-TiO_2 of various sizes merely by varying the synthesis time.

Third, the solvent system of the np-TiO_2 is investigated. The choice of solvent is very crucial as the boiling point plays a vital role to obtain a smooth and pinhole-free film on a substrate. It is especially important for upscaling techniques like inkjet printing, slot-die coating and blade coating as these deposition techniques demand high boiling point of the solvent. For inkjet printing and slot-die coating, a high boiling point solvent keeps the nozzle wet and allows free-flowing of the ink before (**Fig. 3.4**). In this study, the np-TiO_2 are dispersed in three different solvent systems: (i) ethanol (boiling point: 78.4 °C), (ii) diethylene glycol monoethyl ether (boiling point: 202 °C), and (iii) 1-butanol (boiling point: 153 °C), for various deposition techniques. For spin and blade coating, np-TiO_2 dispersed in ethanol is used. The dispersion in diethylene glycol monoethyl ether is used for inkjet printing, while the dispersion in 1-butanol is used for slot-die coating. To check the uniformity and homogeneity of the np-TiO_2 ETL, the dispersions in these solvents are deposited on glass/ITO substrates. Scanning electron microscopy (SEM) images of the

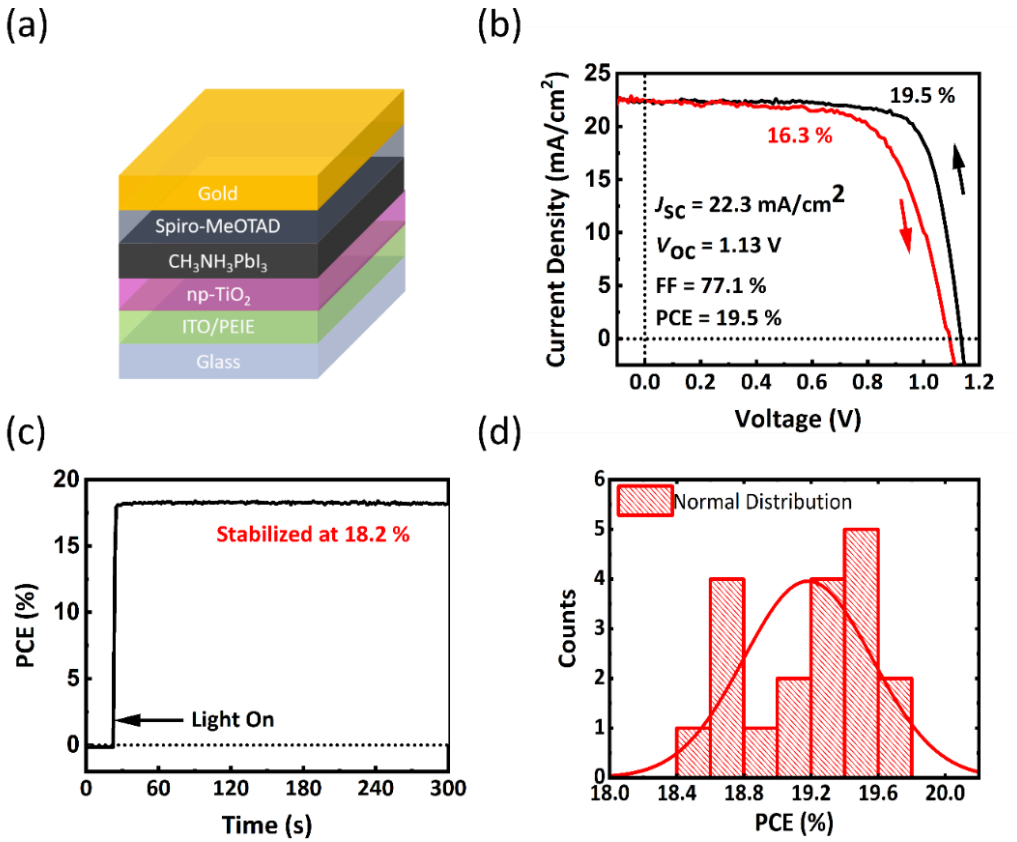

Fig. 4.7: (a) Schematic of a perovskite solar cell (PSC) fabricated with np-TiO_2 ETL. (b) Current density versus voltage (*J-V*) characteristic in backward and forward scans represented in black and red, respectively. (c) Power conversion efficiency (PCE) at constant voltage near the maximum power point measured under continuous AM 1.5G illumination for 5 min. (d) Statistical distribution of the PCE of the 19 devices fabricated with np-TiO_2 ETL. Reproduced with permission from ACS Applied Energy Materials, [139] © American Chemical Society.

np-TiO_2 ETLs in Fig 4.6a-c reveal similar layers with even coverage all over the ITO substrate, indicating a homogeneous ETL for all deposition techniques.

4.1.3 Photovoltaic characteristics with np-TiO_2

Highly efficient perovskite solar cells with np-TiO_2

In this section, photovoltaic characteristics of PSCs with np-TiO_2 are demonstrated. For the fabrication of PSCs, np-TiO_2 ETL is spin-coated from the dispersion in ethanol on the substrate and subsequently annealed at 100 °C for 30 min. Tin-doped indium oxide (ITO) electrodes/substrates are used to fabricate these PSCs as these np-TiO_2 can be processes at such low temperatures. The annealing step ensures that the solvents are evaporated and a mortar is formed between the nanoparticles by the titanium diisopropoxide bis acetonyl acetate precursor.[156] A follow-up $MAPbI_3$ as the absorber layer, spiro-OMeTAD as

hole transport layer and a rear Au electrode completes the opaque device as illustrated in **Fig. 4.7**a.

The current-density versus voltage (*J*–*V*) measurements under air-mass 1.5 global (AM 1.5G) illumination of the champion solar cell exhibit a J_{SC} of 22.3 mA/cm^2, a V_{OC} of 1.13 V and a fill factor (FF) of 77.1%, leading to a PCE of 19.5% when measured from V_{OC} to J_{SC}, i.e., backward scan (Fig. 4.7). The performance of the devices is reproducible, and an average of 19 devices resulted in a PCE of approximately 19.2% as shown in Fig. 4.7d. The apparent hysteresis leads to a reduced PCE of 16.3% when measured in the forward direction, i.e., J_{SC} to V_{OC}. The hysteresis is often observed in n-i-p architecture of PSCs employing compact ETLs and the origin of it is usually associated to trapping of charges and ion migrations as discussed in chapter 2, section 2.5.[119,157,158] In order to obtain the real output power of the PSC, stabilized power output at constant illumination, close to the maximum power point (MPP), is measured. The immediate rise of the PCE to 18.2% (average of 19 devices, ≈17.4%) as shown in Fig. 4.7c and negligible drop in the efficiency over 5 mins demonstrate that the np-TiO_2 ETLs are an excellent material for PSCs. Overall, these results show that nanoparticle based TiO_2 ETLs deposited at low temperatures can

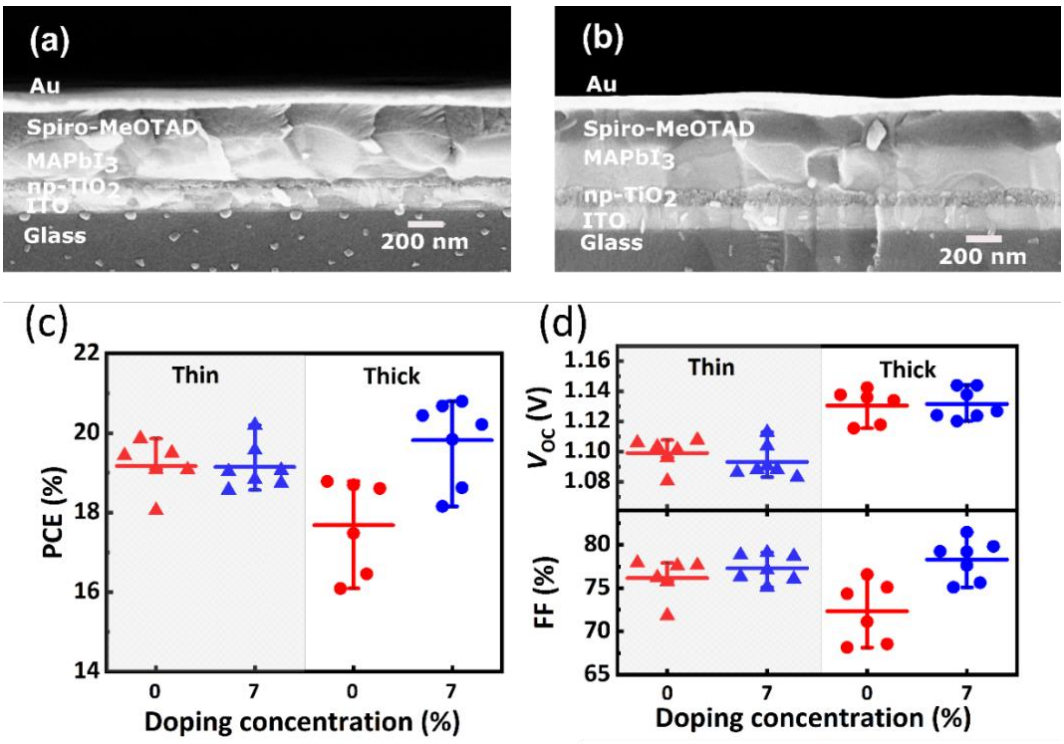

Fig. 4.8: Cross-section scanning electron microscopy image of perovskite solar cells with (a) thin (≈30-35 nm) and (b) thick (≈70-75 nm) np-TiO_2 electron transport layers. Statistical distribution of (c) power conversion efficiency (PCE), (d) open-circuit voltage (V_{OC}), and fill factor (FF) of perovskite solar cells with undoped (0%) and doped (7%) np-TiO_2 as a thin (triangle, ≈30–35 nm) and thick (round, ≈70–75 nm) electron transport layers. Reproduced with permission from ACS Applied Energy Materials, [139] © American Chemical Society.

yield highly efficient PSCs and potentially be used on flexible substrates for roll-to roll processing.

Doping of np-TiO_2 enables thick electron transport layers

A remarkable feature of the in-house synthesis is the feasibility of doping the np-TiO_2 with Nb^{5+} as discussed previously, which leads to an enhancement in the conductivity of the np-TiO_2 ETLs. Increased conductivity is crucial for rough substrates, which requires thick ETLs to ensure a closed and compact film and avoids formation of shunts within the device. Furthermore, for large-scale fabrications, thicker layers are beneficial as they are more lenient to variations and inaccuracies of the deposition process. To demonstrate the importance of doping, np-TiO_2 electron transport thin (≈30–35 nm) and thick (≈70–75 nm) layers are deposited to fabricate PSCs (**Fig. 4.8**a-b). Ideally, a thick np-TiO_2 layer would impede the transport of the charges compared to a thin np-TiO_2 ETL and affect the FF of the device. This is seen here as a reduction in both the FF and PCE (by ≈1.5%), for the undoped np-TiO_2 (compare red triangles and red circles in Fig. 4.8a-b). For the np-TiO_2 doped with Nb^{5+}, instead of a reduction in the FF for the thicker layer, a slightly improved FF is noted (compare blue triangles and blue circles in Fig. 4.8a-b). The improved FF here for the thicker layers is a direct consequence of the increased conductance of the ETL due to the doping of np-TiO_2 as discussed in the section 4.1.2. Furthermore, the V_{OC} is also improved, which might be associated to the increased thickness of the ETL. Overall, these findings show that doping of the np-TiO_2 is crucial for PSCs where thick ETLs are applicable.

Robustness of np-TiO_2 electron transport layer

Another advantage of the in-house synthesis of np-TiO_2 is the feasibility to control the size of the np-TiO_2 as described earlier. The size will in turn influence the surface topography and the thickness of the ETL. PSCs fabricated with different sizes of np-TiO_2 show the

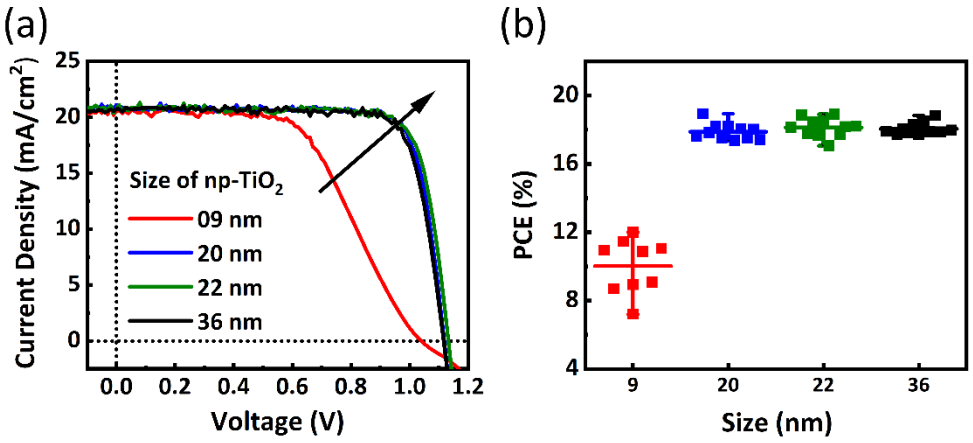

Fig. 4.9: (a) Current density-voltage (*J*–*V*) characteristics and statistical distribution of the power conversion efficiency (PCE) for PSCs with np-TiO_2 ETL hydrodynamic diameter/size of 9 nm, 20 nm, 22 nm, and 36 nm. A critical threshold size of the nanoparticles exits for efficient PSCs. Reproduced with permission from ACS Applied Energy Materials, [139] © American Chemical Society.

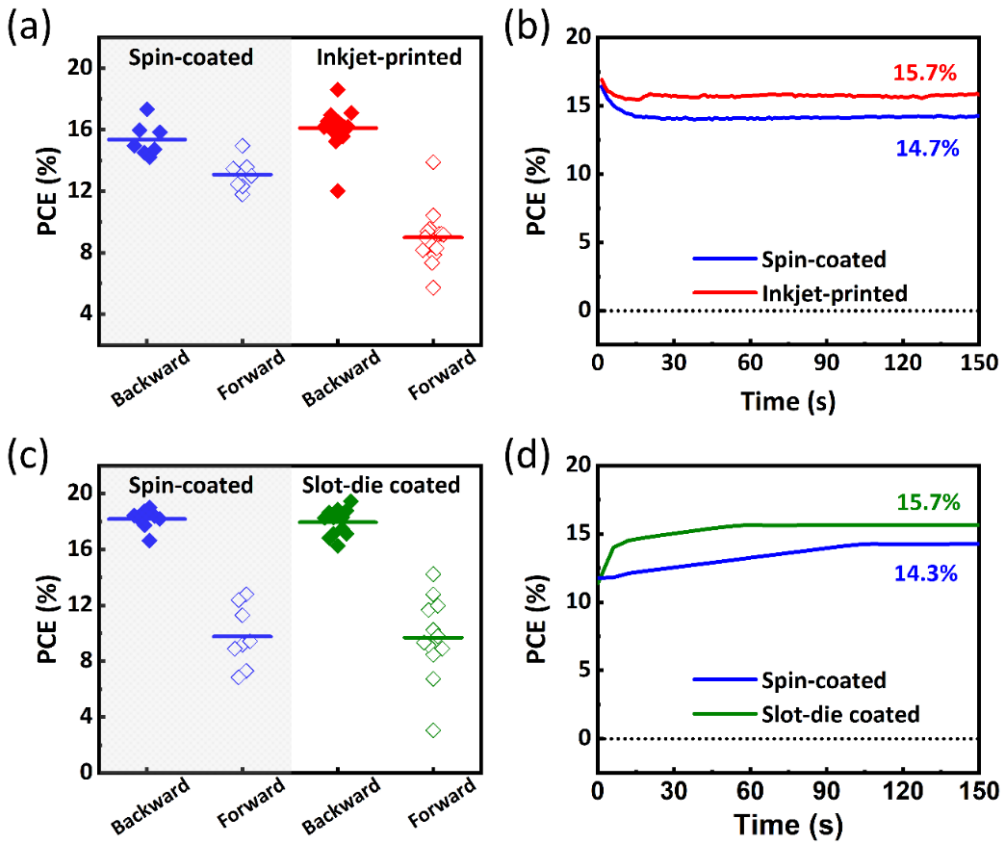

Fig. 4.10: Statistical distribution of the power conversion efficiency (PCE) in (a) and (c) for PSCs with np-TiO_2 ETL deposited with spin coating, inkjet printing and slot-die coating. PCE at constant voltage near the maximum power point measured under continuous AM 1.5G illumination for 5 min is also represented in (b) and (d). Reproduced with permission from ACS Applied Energy Materials, [139] © American Chemical Society.

existence of a critical threshold size of the nanoparticles for efficient PSCs (**Fig. 4.9**). For np-TiO_2 with a size > 20 nm, comparable performance (PCE ≈18%) is achieved. This indicates that np-TiO_2 with a wide size range can be used to fabricate PSCs with similar PCEs, indicating the robustness of this ETL for PSCs. Nevertheless, for np-TiO_2 with a size < 20 nm, the PSCs exhibit low PCE ≈9%, mainly due to the poorer FF, lower V_{OC} and a "S"-shape in the *J–V* characteristic curve. One of the reasons for the poor performance of the PSCs with smaller np-TiO_2 ETL could be the lower electron mobility of the amorphous phase of the np-TiO_2 compared to its anatase phase.[147]

Compatibility of np-TiO_2 electron transport layer with up scalable deposition techniques

In the previous section, homogeneous ETL with uniform coverage of np-TiO_2 ETL is deposited for various deposition techniques. Furthermore, perovskite absorbers deposited on these layers demonstrate comparable surface morphologies and grain sizes (see **Appendix**, **Fig. A. 4.2**). In order to compare the influence of these ETLs on the performance of PSCs, devices are fabricated based on np-TiO_2 ETL deposited using scalable inkjet printing and slot-die coating techniques. The devices are fabricated in two different

batches and compared to their reference spin-coated np-TiO_2 ETLs. As shown in **Fig. 4.10**, the PSCs with both inkjet-printed and slot-die coated np-TiO_2 ETL exhibit high PCEs (> 15.5%). Similar PCEs in the backward scan compared to the respective spin-coated np-TiO_2 are demonstrated for both the inkjet-printed and slot-die coated np-TiO_2 ETL. Interestingly, the PCE at a constant voltage near the MPP for the champion devices with both inkjet-printed and slot-die-coated np-TiO_2 exceeds the PCE of the spin-coated reference. For both scalable techniques, a stabilized PCE of up to 15.7% is achieved. These findings indicate that np-TiO_2 ETL can be deposited using both inkjet printing and slot-die coating to realize PSCs with high PCEs, and paves a way for cost-effective, high-throughput and large-area PSCs.

4.2 np-SnO_2 ETL for perovskite solar cells

Although TiO_2 is the most widely employed ETL for PSCs, SnO_2 has been studied significantly in recent years as an alternative transport layer.[159–163] SnO_2 is a very promising candidate for applications in PSCs due to its better optical and electrical properties as well as chemical stability and low processing temperatures, compared to TiO_2. SnO_2 is investigated in PSCs both in compact and mesoporous architecture[159,160,162] and is demonstrated to be deposited via various techniques. For instance, sol-gel method,[70] atomic layer deposition,[141] and chemical bath deposition[164] are among the promising techniques. First study with np-SnO_2 as ETL for PSCs reported a PCE up to ≈16%.[129] Later, Jiang *et al*. demonstrated commercially available np-SnO_2 synthesized by sol-gel technique for PSCs with significantly improved PCE (19.9%) and photo-stability.[70] Afterwards, Yang. *et al*. modified the np-SnO_2 ETL by ethylene diamine tetra acetic acid (EDTA) complex to further improve the PCE of the PSCs up to 21.5%.[129] To date, this study is one of the highest reported efficiencies with np-SnO_2 as the ETL in n-i-p architecture of PSCs. In their work, the np-SnO_2 ETL is deposited both on glass/ITO and flexible substrate at a significantly low processing temperature of ≈60 °C, and thus, demonstrating the compatibility of np-SnO_2 ETL with roll-to-roll processing and alternative TCO electrodes compared to FTO substrates. Because of the high performance and better stability of PSCs with SnO_2 ETL, PSCs are also investigated with np-SnO_2 ETL in this thesis. In the following chapters,

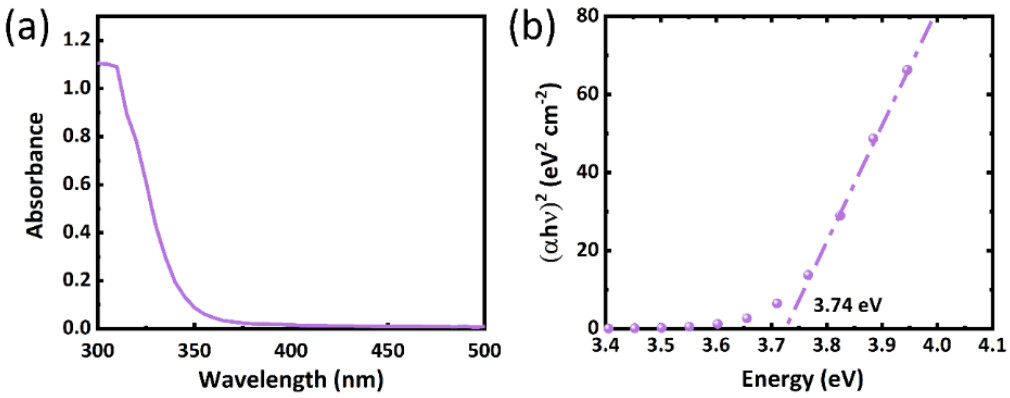

Fig. 4.11: (a) Absorbance spectrum of np-SnO_2 dispersed in de-ionized water. (b) Tauc plot indicating the direct bandgap of np-SnO_2 (E_g = 3.74 eV).

np-SnO_2 (bought commercially) is used as the ETL in its n-i-p architecture for PSCs. To obtain further insights, the np-SnO_2 are characterized and their properties are discussed in light of this study and literature.

4.2.1 Material properties of np-SnO_2

The np-SnO_2 are commercially available from the chemical company Alfa Aesar. The colloidal dispersion of the np-SnO_2 is dispersed in water and has a concentration of ≈15%. Spectrophotometric measurements are conducted to determine the bandgap of np-SnO_2. For this, a similar procedure is applied as for the np-TiO_2. The absorbance spectra of the np-SnO_2 dispersion is shown in **Fig. 4.11**a. Using equation **4.1**, the direct bandgap of the np-SnO_2 is determined to be 3.74 eV from the Tauc plot (Fig. 4.11b), which is in good agreement with the literature.[70] The np-SnO_2 used in this study is characterized more in detail in the work of Jiang *et al*.[70] The np-SnO_2 are stoichiometric and crystalline in nature with a tetragonal SnO_2 lattice structure.[70] The size of the nanoparticles, determined with transmission electron microscopy (TEM) in that study, is ≈3-4 nm.[70] In the following section, a comparison between the optical properties and the photovoltaic characteristics of the PSCs fabricated with np-TiO_2 and np-SnO_2 ETLs is discussed.

4.3 Comparison between np-TiO_2 and np-SnO_2 ETL

Both np-TiO_2 and np-SnO_2 exhibit promising material properties. In the following sections, the ETLs deposited with np-TiO_2 and np-SnO_2 are characterized in more detail. Initial studies include optical properties, photo physics and morphology of these layers. Finally, both opaque perovskite solar cells (o-PSCs) and s-PSCs fabricated with these ETLs are analyzed.

4.3.1 Optical properties, photo-physics and morphology

Ellipsometry measurements are performed on ETLs of np-TiO_2 and np-SnO_2 deposited on glass to evaluate the optical constants (refractive index, *n* and extinction coefficient, *k*). **Fig. 4.12** shows the refractive index and the extinction coefficient of np-TiO_2 and np-SnO_2

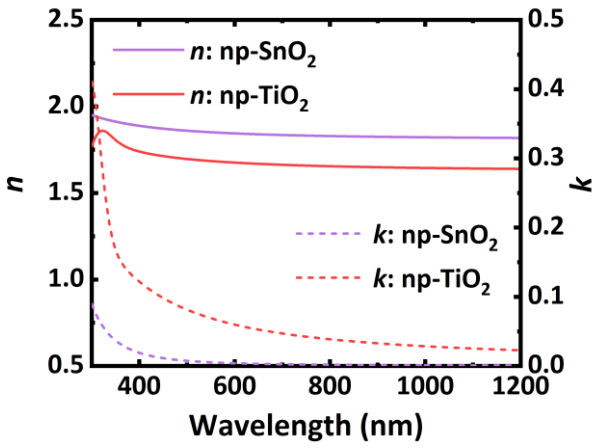

Fig. 4.12: Optical constants (*n*, *k*) of np-TiO_2 and np-SnO_2.

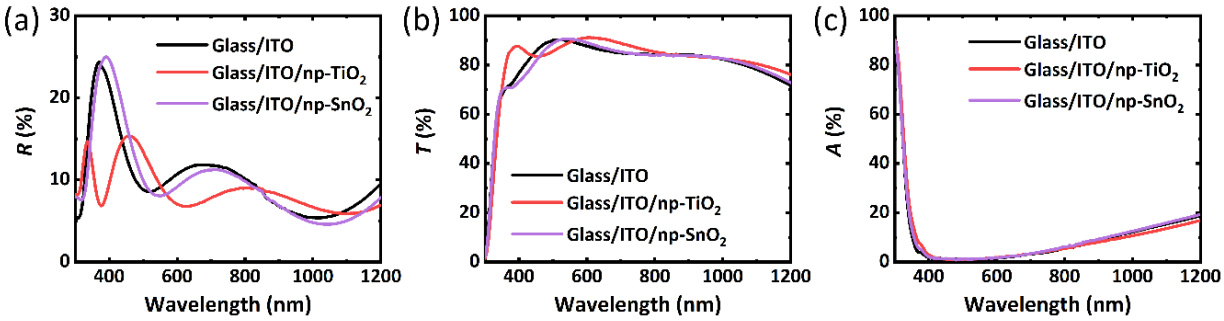

Fig. 4.13: (a) Reflectance (*R*), (b) Transmittance (*T*) and (c) Absorptance (*A*) of the layer stacks: glass/ITO, glass/ITO/np-TiO_2 and glass/ITO/np-SnO_2.

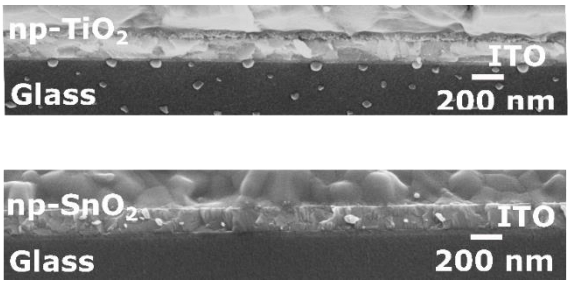

Fig. 4.14: Cross-section scanning microscopy images of np-TiO_2 and np-SnO_2 on glass/ITO substrates.

layers. Both layers exhibit high refractive index (> 1.63) and is almost non-dispersive in the wavelength range 400-1200 nm. Compared to np-TiO_2 ETL, a higher refractive index is noted for np-SnO_2 ETL. The high extinction coefficient of the np-TiO_2 ETL below 400 nm is due to the smaller bandgap of the np-TiO_2. Nevertheless, np-TiO_2 exhibits significantly higher extinction coefficient in the wavelength range 400-1200 nm, indicating that np-TiO_2 ETL is susceptible to increased parasitic absorption losses in the PSCs, if thick layers are used.

For the spectrophotometric measurements, the ETLs are deposited on glass/ITO substrates, which is the TCO electrode for the PSCs. This measurement is carried out to obtain the transmittance (*T*), and the reflectance (*R*) of the layers on glass/ITO/ETL with glass/ITO as the reference stack (**Fig. 4.13**). *T*, *R* and *A* (calculated from **Equation 3.3**) of the ITO layer are slightly modified when np-SnO_2 are deposited atop (Fig. 4.13a-c). For np-TiO_2, the reflectance is reduced significantly, and a strong modification of the interference peaks are observed. The reduction of the reflectance is due to a smaller refractive index of the np-TiO_2, resulting in a lower Fresnel reflection at the ETL/air interface (Fig. 4.13a). Hence, the maximum of the transmittance is slightly increased (Fig. 4.13b). The variation of the interference peak position indicates that the thickness of the np-TiO_2 ETL differs from the np-SnO_2. Cross-sectional scanning electron microscopy (SEM) conducted on both ETLs on ITO reveals that the np-TiO_2 forming a compact layer on top of the ITO with a thickness of ≈30-50 nm, while thickness of the np-SnO_2 ETL stands below 10 nm (**Fig. 4.14**).

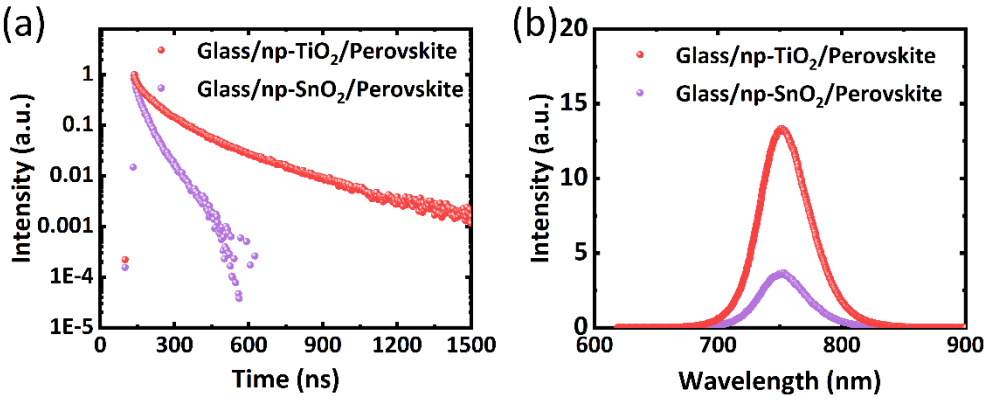

Fig. 4.15: (a) Time-resolved and (b) steady-state photoluminescence spectra of layer stack: glass/np-TiO_2/perovskite and glass/np-SnO_2/perovskite.

The efficient extraction and transport of the electrons from the absorber layer to the respective contact are the two important criteria of a good ETL. To investigate this, steady-state photoluminescence (SSPL) and time-resolved photoluminescence (TRPL) spectroscopy measurements are carried out on glass/np-TiO_2/perovskite and glass/np-SnO_2/perovskite layers (**Fig. 4.15**). The samples are excited with a pulsed laser with a wavelength of 532 nm (with energy above the bandgap of the perovskite absorber). The TRPL shows an extremely fast decay of the photoluminescence with np-SnO_2 as the ETL, while a slow decay is detected for np-TiO_2 (Fig. 4.15a). The corresponding lifetimes of the charge carriers extracted by fitting to a stretched exponential function are of 38 ns and 133 ns for np-SnO_2 and np-TiO_2, respectively. The fast decay with the np-SnO_2 ETL implies that the electrons which are created upon excitation are immediately extracted by the ETL, indicating a fast separation of electrons from the holes before they recombine radiatively in the absorber layer or non-radiatively at defect/interfacial sites. The comparatively longer lifetime and slow extraction with the np-TiO_2 indicates the existence of an electron barrier between the absorber and the ETL. This slow extraction of charges could be due to the shallower conduction band or the lower electron mobility of TiO_2 compared to np-SnO_2 ETL.[129,143,165] Nevertheless, the improved lifetime could also indicate a possible reduced number of defects or traps within the perovskite absorber due to a better film morphology.[166] All these results are also in line with the SSPL measurements. Compared to the np-TiO_2 ETL, the photoluminescence intensity is reduced significantly with np-SnO_2 ETL, further indicating the superior mobility of the np-SnO_2 ETL.

4.3.2 Photovoltaic characteristics of PSCs with nanoparticle-based ETL

In this section, the photovoltaic parameters of o-PSCs and s-PSCs fabricated in a same batch with np-TiO_2 and np-SnO_2 are discussed. The device stack is as follows: glass/ITO/(**np-TiO_2** or **np-SnO_2**)/$MAPbI_3$/Spiro-OMeTAD/(**Au** or **MoO_X/ITO**). The ETLs, np-TiO_2 and np-SnO_2 are deposited at low annealing temperatures of 100 °C and 150 °C, respectively. For the fabrication of s-PSCs, a thin 10 nm MoO_X buffer layer is used to prevent damage to the underlying Spiro-OMeTAD or the perovskite absorber upon sputtering. It should be noted that the overall performance of this specific batch of samples is comparatively low, mainly due to the use of old precursor materials and solvents. The

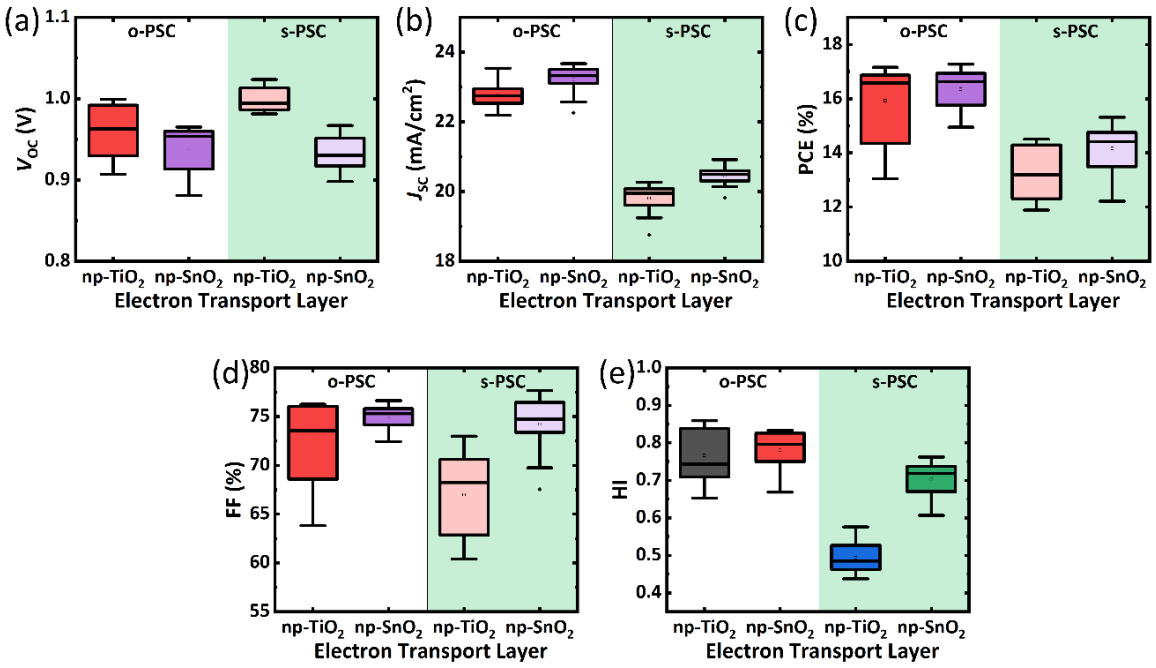

Fig. 4.16: (a) Open-circuit voltage (V_{OC}), short-circuit current density (J_{SC}), power conversion efficiency (PCE), fill factor (FF) and hysteresis index (HI) of opaque perovskite solar cell (o-PSC) and semitransparent perovskite solar cell (s-PSC).

statistical analysis of the V_{OC}, J_{SC}, FF and PCE for at least 10 samples are presented in **Fig. 4.16**a-e. It is observed that the V_{OC} is ≈30 mV higher for o-PSCs with np-TiO_2 ETL in comparison to np-SnO_2 ETL. The difference is further increased to ≈70 mV in s-PSCs. The improved V_{OC} with np-TiO_2 could be associated with the longer lifetime of the charge carriers as already discussed is section 4.3.1. In contrast to the V_{OC}, the mean of the J_{SC} for both o-PSCs and s-PSCs are increased with np-SnO_2 ETL. The average PCE of the PSCs with np-TiO_2 and np-SnO_2 are similar for opaque devices, although the spread in the distribution is smaller for np-SnO_2 ETL. The smaller spread indicates more reproducible devices are fabricated with np-SnO_2 ETL. For s-PSCs, the FF and consequently the PCE are significantly better with np-SnO_2 ETL. PSCs with both ETLs present hysteresis in their *J-V* characteristics. The hysteresis index (*HI*) calculated shows that np-TiO_2 ETL devices are more affected compared to the np-SnO_2 ETL (Fig. 4.16e). This could be ascribed to enhanced charge accumulations due to slow extraction of charges at the perovskite/ETL interface.[70] This is in line with the time-resolved photoluminescence results which also revealed the poor extraction of charges by the np-TiO_2 ETL. One way to resolve this is to employ thin layers of fullerenes, such as C_{60}, which have demonstrated to modify the surface of the TiO_2, reducing ion migration by passivating defects and extract the electrons more efficiently.[70,120,143]

In order to obtain insights about the optical properties of the two layer stacks, the optical properties of the s-PSCs are compared (**Fig. 4.17**). A higher reflectance between 300-650 nm is observed for np-SnO_2 stack. This high reflection could be associated to the presence of a very thin layer np-SnO_2 ETL that only slightly modifies the ITO substrate. The

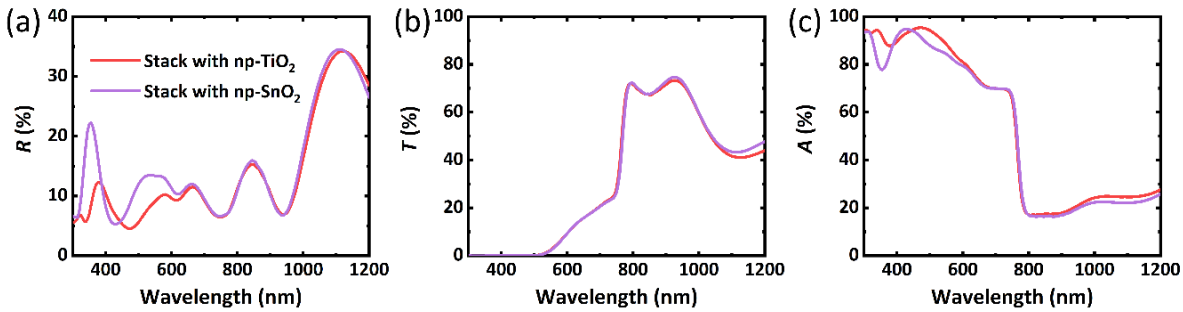

Fig. 4.17: (a) Reflectance (*R*), (b) transmittance (*T*) and (c) absorptance (*A*) of the semitransparent perovskite solar cell (s-PSC) layer stack with np-TiO_2 and np-SnO_2 electron transport layers.

transmittance spectra with both ETLs are comparable, with strong interferences and a maximum transmittance of ~75% is achieved. The low transmission above 1000 nm is due to the high reflection (Fig. 4.17a) and strong parasitic absorptions (Fig. 4.18c) for both the stacks. The absorptance of 20-30% in the near infrared wavelengths below the bandgap of the perovskite absorber is due to the parasitic losses associated with the front ITO and rear ITO. Detailed discussion and several strategies to overcome this are discussed in Chapter 5 and Chapter 6. The comparatively improved transmittance in the near infrared wavelengths with the np-SnO_2 ETL stack is due to the reduced absorptance, which is in line with the measured extinction coefficients of the two ETLs.

To determine the real power of the PSCs fabricated with both np-TiO_2 and np-SnO_2, the fabricated devices are characterized by MPP tracking (**Fig. 4.18**a). PSCs with both ETLs remain stable during the course of these measurements. Moreover, a small increase in the PCE is observed for the np-SnO_2, which is due to the light soaking effect.[167] Long-term stability and shelf lifetime are also investigated for PSCs fabricated with np-TiO_2 and np-SnO_2 ETLs. Here, instead of $MAPbI_3$ as the absorber layer, triple cation (TC) perovskite absorber based on FA, MA and Cs is used, which is reported to be intrinsically more stable than $MAPbI_3$.[32] For this, o-PSCs are fabricated for both the architectures and the MPP at constant voltage near the maximum power is measured over several days. It is shown that devices with np-TiO_2 show a decay in the power output and remain unstable on day 1 (Fig. 4.18b-c). However, they tend to stabilize and improve in PCE with time. In contrast, np-SnO_2 based devices are stable from day 1. The observed improvement in the PCE is independent of the ETL and is related to the reduction in trap-assisted non-radiative recombination and strain relaxation in the triple cation perovskite absorber.[168]

4.4 Discussions and conclusion

In this chapter, alternative ETLs (np-TiO_2 and np-SnO_2) are investigated for fabricating PSCs with the aim to reduce the depositing temperature of the ETL. Compared to the most widely used ETL (mesoporous TiO_2), which requires high annealing temperatures (> 450 °C),[31–34] these ETLs require processing temperatures of below 150 °C. The reason behind this low processing temperature is the pre-synthesis of TiO_2 and SnO_2 into their crystalline form. Furthermore, due to low processing temperatures of these ETLs, the

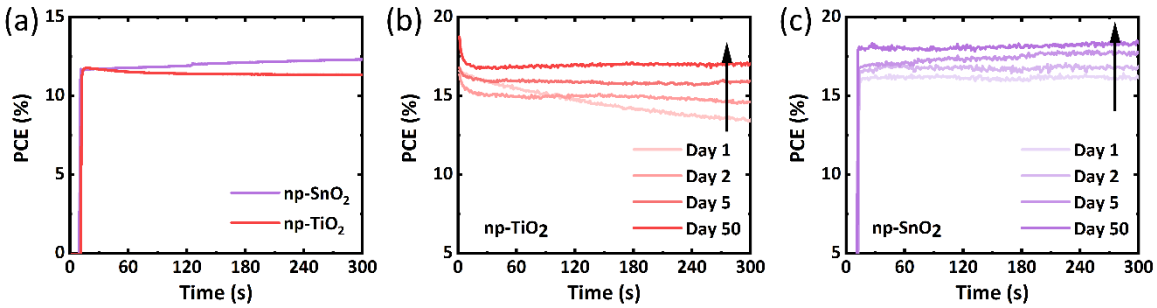

Fig. 4.18: (a) Power conversion efficiency (PCE) of the s-PSCs at a constant voltage near the maximum power point for PSCs fabricated np-TiO_2 and np-SnO_2 electron transport layers. Evolution of the PCE of PSCs fabricated with triple cation perovskite absorber with (b) np-TiO_2 and (c) np-SnO_2 electron transport layers.

fabrication of PSCs is not restricted to FTO substrates (which can withstand high processing temperature) but rather can be fabricated on ITO substrates, which exhibit lower parasitic absorption losses. In this thesis, in-house synthesis is performed for np-TiO_2 while np-SnO_2 is commercially purchased.

Experimental investigations and analyses from XRD and XPS show that the in-house synthesis of np-TiO_2 led to the formation of stoichiometric, crystalline TiO_2 in its anatase phase. Furthermore, the synthesis route permits tuning of additional properties of the np-TiO_2 through doping, synthesis time and solvent system. Similar to a previous study where np-TiO_2 was doped with yttrium to improve the conductivity,[155] the addition of Nb^{5+} as a dopant here, increases the conductivity of the np-TiO_2. Here, it is demonstrated that doping is beneficial, especially where thick layers of ETLs are required. Moreover, comparable performance in PSCs for a large variety of sizes of np-TiO_2 makes these np-TiO_2 a robust charge transport layer. Furthermore, not only high PCEs (>18%) are demonstrated for PSCs with spin-coated np-TiO_2, but also high-performance PSCs are achieved with these np-TiO_2 deposited using industrial large-scale deposition techniques such as blade coating, inkjet printing or slot-die coating, all due to the feasibility of obtaining dispersions of np-TiO_2 in various solvent systems. This paves a way for large area PSCs or modules.

The commercial np-SnO_2 promises to be an alternative ETL for PSCs as well. The np-SnO_2 are crystalline in nature and have a wider bandgap than the np-TiO_2. Optically, both np-SnO_2 and np-TiO_2 present high refractive index and low extinction coefficient, which is crucial for PSCs. With both ETLs, similar transmittance in near infrared wavelength range is achieved. In terms of photovoltaic performance, PSCs fabricated with np-SnO_2 ETL show comparable PCE but an improved charge extraction as is demonstrated by time-resolved photoluminescence spectroscopy. These results are also consistent with literature where both np-TiO_2 and np-SnO_2 ETLs were compared.[70] The devices with np-SnO_2 ETL also present reduced hysteresis and higher stability than the np-TiO_2 ETL.

Overall, both np-SnO_2 and np-TiO_2 are excellent choices as ETLs for fabricating efficient PSCs and potential four-terminal perovskite-based tandem devices. However, considering the improved stability and reduced hysteresis of the PSCs, np-SnO_2 ETL is employed in the following chapters for further developments of s-PSCs and tandem photovoltaics.

5. Nanophotonic electrodes for perovskite-based tandem photovoltaics

This chapter deals with research question 2 and discusses the development of nanostructured transparent conductive oxide electrodes for reducing optical losses in semitransparent perovskite solar cells and perovskite/crystalline-silicon (c-Si) tandem solar cells. The developed nanostructured transparent conductive oxide electrodes enhance optical transmittance by reducing reflection losses at transparent conductive oxide interfaces. Here, two types of structural configurations for the nanostructures are explored: periodic and disordered. A comprehensive study on the optical and electrical properties of the fabricated nanostructured transparent conductive oxide electrodes is discussed. In the end, optimized nanostructured transparent conductive oxide electrodes are implemented into s-PSCs and perovskite/c-Si tandem solar cell configuration that exhibit enhanced current generation and improved power conversion efficiency compared to planar device architectures.

Acknowledgements and contributions

The major part of the research study discussed in this chapter was published in reference [71]. The work was a collaboration between KIT and ISFH. In this study, Ihteaz M. Hossain contributed the fabrication and characterizations of perovskite solar cells and the tandem architecture. Disordered nanostructures were fabricated by Yidenekachew J. Donie and Mohamed S. Adbelkhalik. The periodic nanostructures were fabricated by Katharina Goth and Raphael Schmager. The energy yield simulations were performed by Raphael Schmager. Ihteaz M. Hossain acknowledges the support of Adrian Mertens, Saba Gharibzadeh and Diana Rueda-Delgado for fruitful discussions.

Recently, perovskite-based tandem photovoltaics received a lot of attention in the scientific community. This is due to the wide bandgap of the lead-based organic-inorganic perovskite as the top cell's absorber. Tremendous progress has been made in the last decade and as a result, the power conversion efficiency (PCE) of the current state-of-the-art perovskite/crystalline-silicon (c-Si) tandem solar cell already reached 29.1% in two-terminal tandem architecture.[10] Although the PCE of perovskite/c-Si tandem solar cell obtained is remarkable various optical losses including reflection losses at interfaces, reduced transmission of the top cell due to parasitic absorption within the layers are some of the bottlenecks that needs to be overcome.[25,38,169,170]

Light management concepts are typically employed to overcome the optical losses.[15] Both micron- and nano-scale textures have been demonstrated for perovskite solar cells (PSCs) for reducing the optical losses. The micron-scale textures, which is commonly employed at the front air/glass interface allow the light to undergo multiple interactions with the textured surface and increase the probability for light in-coupling.[58–63] The potential of micro-textures with different geometries such as regular pyramids,[60] inverted pyramids,[134] cones,[62,171] and random textures[58,63] were investigated as light in-coupling element into PSCs, which lead to a 4% reduction in reflection losses in most cases. In contrast to micron-scale textures, nano-scale textures can be easily integrated into the thin film layers of PSCs.[41,42,64,65,69,172–177] Investigated textures include nanophotonic front and rear electrodes,[41,64,65] patterned charge transport,[173,174] corrugated substrates,[172,177] and active perovskite layers.[69,175,176] The nanophotonic front electrodes, the charge transport layers and the corrugated substrates reduce reflection losses by introducing a gradual matching of the refractive index forming a so-called effective refractive index medium, thus suppressing the Fresnel reflection losses.[41,173,174] The textured rear electrode also improves light absorption through scattering and surface plasmonic resonance excited by the corrugation.[65] Patterned active layers demonstrate improved light absorption by enhancing the light-coupling to the quasi-guided modes of the perovskite absorber.[69,175,176] Previous studies have also demonstrated that nanophotonic front electrodes enhance optical transmittance and reduce reflectance both in the visible and near-infrared wavelength ranges.[72] They demonstrated an improvement of 8% absolute.[72] Therefore, nanotexturing a TCO would not only be beneficial for both opaque single junction PSC, but also be compelling for perovskite-based tandem architectures. However, these nanostructures are yet to be explored for semitransparent perovskite solar cells (s-PSCs) and tandem architectures in real prototype devices.

In this chapter, nanostructured tin-doped indium oxide (NS ITO) electrode is employed in s-PSCs and in 4T tandem perovskite/c-Si tandem architecture. These nanostructured ITO reduce the prominent reflection losses at the ITO interfaces as discussed earlier in chapter 2, section 2.5 and improve the transmission. Two configurations of NS ITO are investigated: periodic and disordered. In the follow-up sections, detailed optical and electrical properties of the NS ITO and PSCs fabricated with NS ITO are discussed.

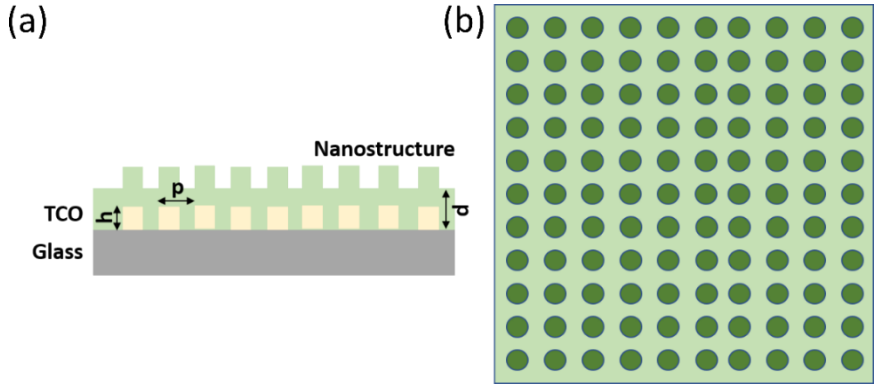

Fig. 5.1: Schematic illustration of periodic nanostructured TCO: (a) side-view and (b) top-view. The periodic nanostructures have a height *h* and are separated with a periodicity of *p*. Up on deposition of a transparent conductive oxide (TCO) electrode conformally, periodic nanostructured TCO electrodes are obtained.

5.1 Periodic nanophotonic electrodes

This section discusses morphological, optical and electrical properties of periodic NS ITO for improved light in-coupling. The morphological properties are obtained with atomic force microscopy (AFM). Spectrophotometric measurements are performed to determine the optical responses of these NS ITO. The fabricated NS ITO electrodes are also characterized by four-point probe technique to determine their electrical properties.

Morphology and opto-electronic properties of periodic NS ITO

The periodic nanostructured ITO comprises of nanopillars made of a polymer material called OrmoComp deposited in an ordered fashion with a constant periodicity by soft-imprinting of polymers using molds of nanostructures (**Fig. 5.1**). A follow-up

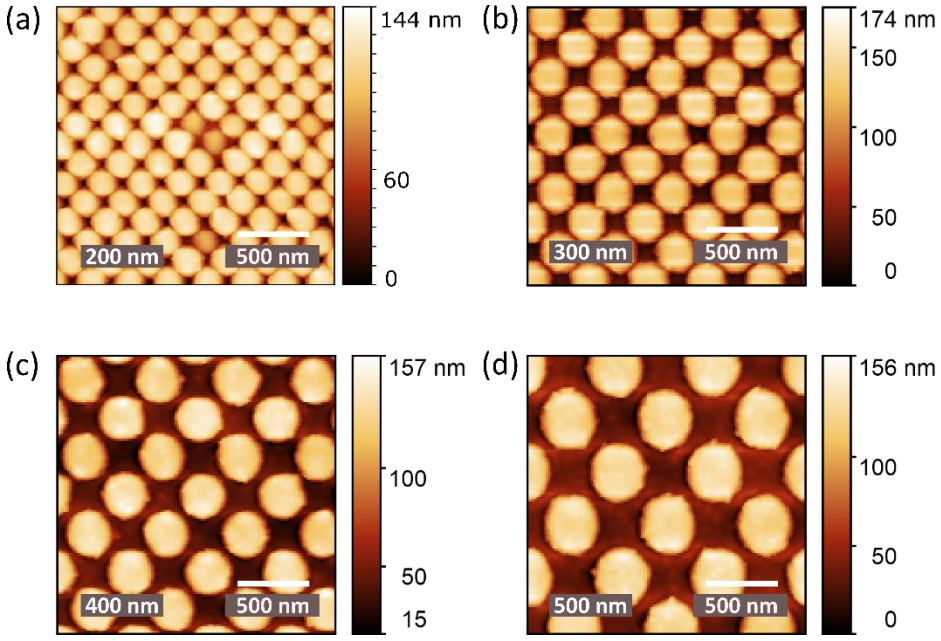

Fig. 5.2: Atomic force microscopy images of nanostructured ITO electrode fabricated with soft-imprinting for periods, p = 200 nm, 300 nm, 400 nm and 500 nm.

deposition of ITO results in a corrugated NS ITO. Details regarding the fabrication of periodic NS ITO can be found in chapter 3, section 3.1.4.

Previous study from Khan *et al*. showed that the smaller periods maximize the transmission for a broad range of wavelengths (300-900 nm).[72] Here, the period (*p*) of the nanostructures is varied between 200-500 nm to determine the optimum period that leads to higher optical transmittance. Thus, the period of the NS ITO is tuned by varying periods of polymer nanostructures. The atomic force microscopy (AFM) images of the fabricated NS ITO are shown in **Fig. 5.2** for all the given periods. The period of the nanostructures is consistent with the period of the master structure, deviating only by ±12 nm. The height (*h*) of the NS ITO is also consistent in line with the height of the master structure (100 nm) as shown in **Fig. 5.3**. An increase in the diameter of the nanostructures is noted, especially for the smaller periods. This increase is associated to an increased filling fraction of the NS ITO, which is also noticeable in the AFM images. Overall, AFM analysis show that soft-imprinting process yields highly periodic NS ITO with excellent quality. Further information regarding the height, the period and the diameter extracted from the AFM images can be found in **Table 5.1**.

Spectroscopic measurements conducted on the fabricated NS ITO samples reveal that all NS ITOs demonstrate an improvement in transmittance and a reduction in reflectance for 800-1200 nm (**Fig. 5.4**). The smallest period (*p* = 200 nm) shows the strongest improvement in transmission for the entire wavelength range between 300-1200 nm, with a relative enhancement of ≈5% compared to planar ITO. The improvement here is attributed to the gradual matching of the refractive index of the NS ITO and air, resulting in an effective refractive index. This effective refractive index is achieved for the incident light as the dimensions of the nanostructures are smaller than the incident wavelength. For the p ≥ 300 nm, strong dips are noted, which are also seen in the reflectance spectra. These dips are attributed to the excitation of the waveguide-modes by the incident light in the ITO layer.[72,178] Furthermore, as the period is increased, a shift of the dips towards the

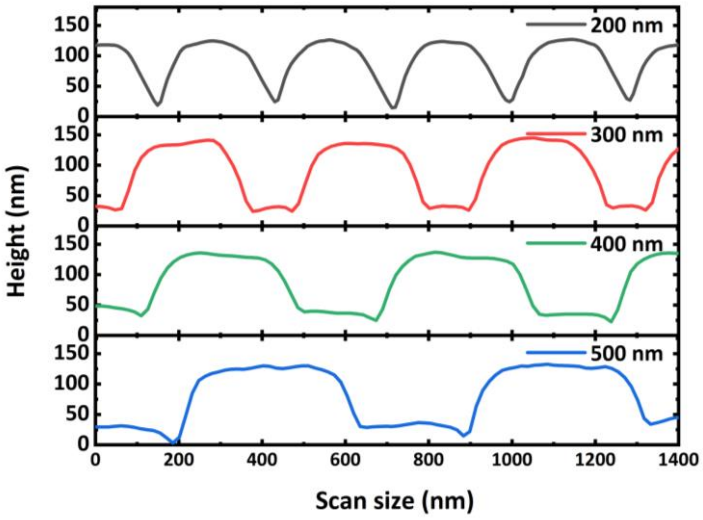

Fig. 5.3: The height profile of nanostructured ITO for periods, *p* = 200 nm, 300 nm, 400 nm and 500 nm.

higher wavelengths is also noted. Thus, by tuning the periodicity, a desired transmittance for a particular range of wavelengths can also be obtained. For the application in tandem photovoltaics, the smallest periodicity should be preferred as the improvement is for a wide range of wavelengths. Overall, the findings show that with NS ITO, reflection losses are effectively reduced, and the transmittance is improved significantly.

The improved light in-coupling for NS ITO results in a tradeoff in increased sheet resistance. Higher sheet resistance (approximately 4 times) is noted for NS ITO with the smallest period that demonstrated the maximum transmittance in comparison to the planar ITO. The increased sheet resistance could be associated to possible cracks, increased surface area or number of grain boundaries in the ITO.[179] The measurement also shows that the periodicity of the NS ITO influences the sheet resistance. As the period is increased, the

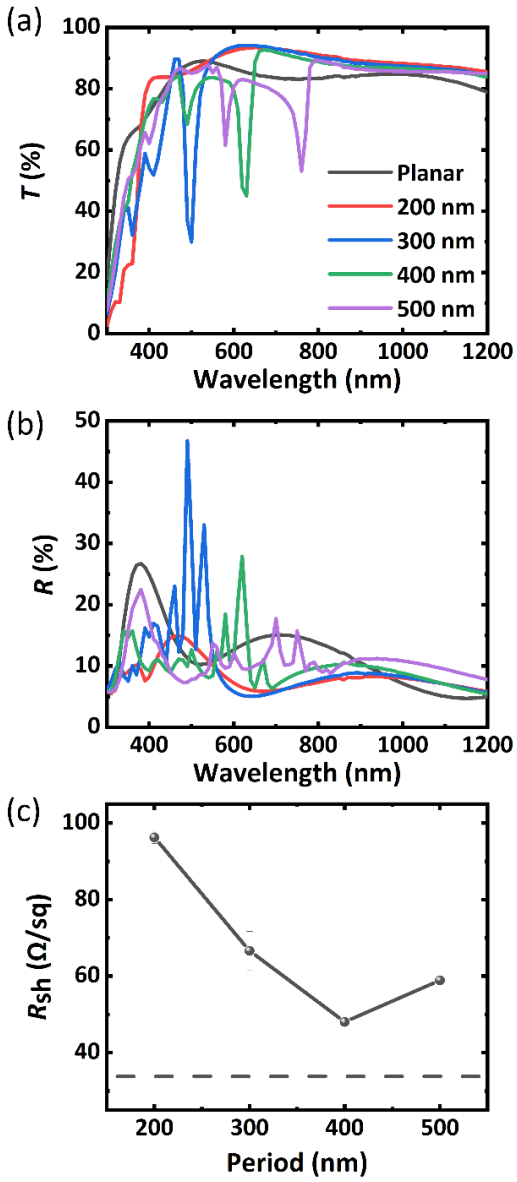

Fig. 5.4: (a) Transmittance (*T*), (b) reflectance (*R*) and (c) sheet resistance (R_{sh}) of the nanostructured ITO electrode ITO for periods, *p* = 200 nm, 300 nm, 400 nm and 500 nm.

sheet resistance drops from 96 Ω/sq to 50 Ω/sq for periods up to 400 nm. For 500 nm, the sheet resistance increases which could be related to the inhomogeneous sputtering of the ITO.[132] Overall, these results show that both transmission and sheet resistance of the fabricated NS ITO are intertwined and suggest that a balance must be obtained between the optical and the electrical peroperties of the NS ITO so that an overall improvement is achieved in the performance of perovskite-based tandem devices.

Table 5.1: The period (*p*), height (*h*), measured diameter and theoretical diameter of the nanostructured ITO electrode ITO for periods, p = 200 nm, 300 nm, 400 nm and 500 nm.

Master Structure (nm)	*p* (nm)	*h* (nm)	*Measured diameter (*nm)	*Theoretical diameter (nm)*
200	191	90	230	134
300	296	100	267	200
400	388	95	300	268
500	506	100	386	335

5.2 Disordered nanophotonic electrodes

This section discusses morphological, optical and electrical and properties disordered NS ITO for improved transmittance. The morphological properties are investigated with AFM and scanning electron microcopy (SEM). Spectrophotometric measurements are performed to determine the optical responses of the disordered NS ITO. The fabricated NS ITOs are characterized by four-point probe technique to determine their sheet resistances.

Morphology and opto-electronic properties of disordered NS ITO

A schematic of the side-view and the top-view of the disordered nanostructured TCO electrode is depicted in **Fig. 5.5**. In contrast to the periodic NS ITO, the nanostructures in the disordered NS ITO are oriented randomly and with a certain average inter-distance

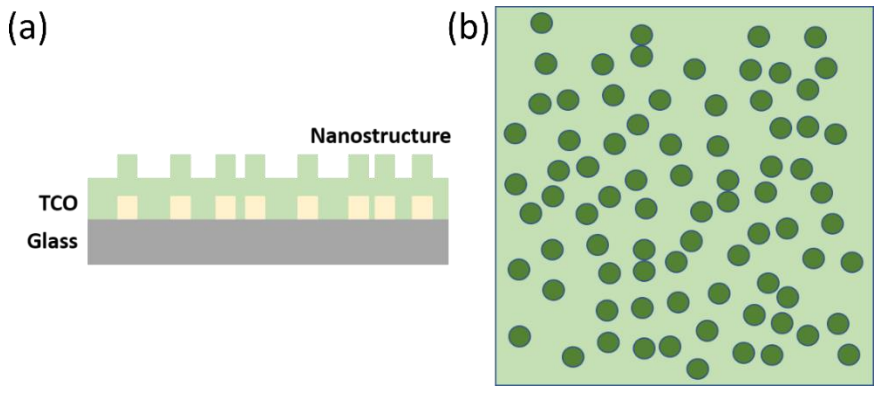

Fig. 5.5: Schematic of disordered nanostructured TCO: (a) side-view and (b) top-view.

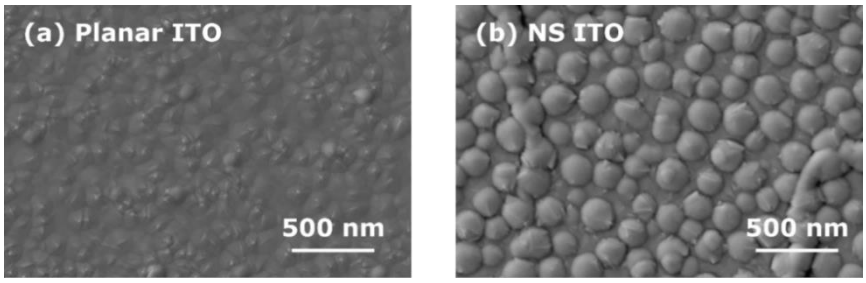

Fig. 5.6: Top-view scanning electron microscopy images of planar and nanostructured ITO (NS ITO) electrode. Reproduced with permission from reference [71], © 2020 Optical Society of America.

between the nanostructures. Polymer blend lithography is employed to fabricate the disordered NS ITO. A blend mixture of poly(methyl methacrylate) (PMMA) and polystyrene (PS) is deposited on a glass substrate using spin-coating and by selective development of the PMMA, self-assembled nanopillars made of polystyrene (PS) are obtained. Subsequent sputtering of the ITO on the nanopillars of PS forms the predominantly conformal NS ITO electrode (**Fig. 5.6**). Further details regarding the fabrication of disordered NS ITO can be found in chapter 3, section 3.1.4.

Similar to the periodic nanostructures, an optimization of the nanostructures is performed by varying the inter-distance between the nanostructures. In order to tune the inter-distance between the nanostructures, the mass ratio of PS in the blend mixture, spin-coating speed of the blend and molecular weight of the polymers are varied. Three different NS ITO electrode with inter-distances varying from 210-550 nm are fabricated (**Fig. 5.7**), at the same time, ensuring a similar height of 110-135 nm (also see **Fig. 5.9**b). A blend ratio of 4/6 between PS/PMMA results in NS ITO with an inter-distance of 210 nm. By increasing the mass ratio of the PS in the blend mixture, an inter-distance of ≈310 nm is achieved. Further increase in the interdistance to 550 nm is obtained by increasing the molecular weight of the PS.

Analogous to the peridic nanostructures, the highest transmission (7% relative) and lowest reflection is attained for the smallest spacing of 210 nm inter-distance (**Fig. 5.8**a) and up on increassing the spacing, the transmission is reduced and the reflection loss is increased

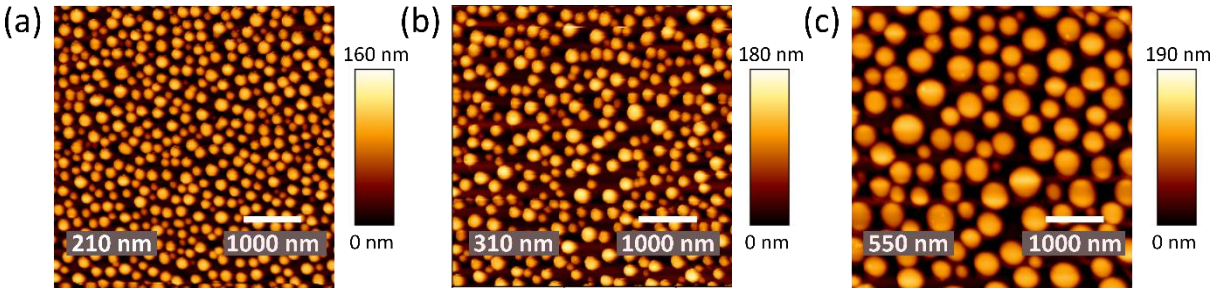

Fig. 5.7: Atomic force microscopy images of nanostructured ITO for average inter-distance of (a) 210 nm, (b) 310 nm and (c) 550 nm. Reproduced with permission from reference [71], © 2020 Optical Society of America.

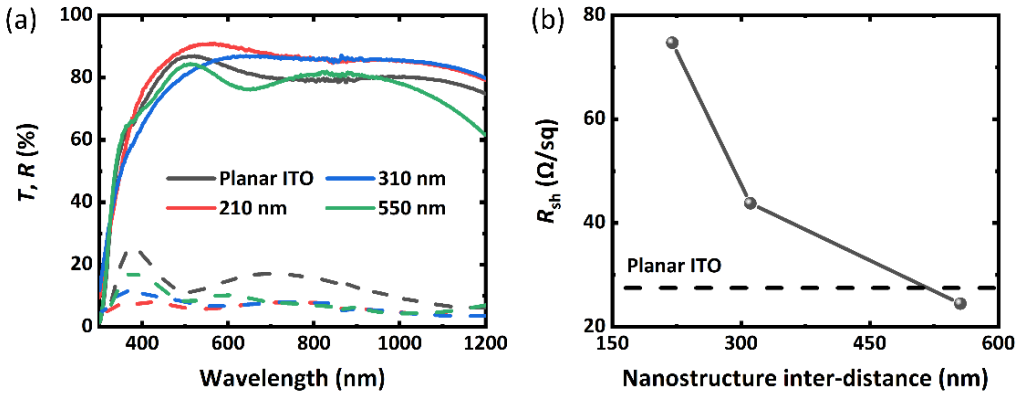

Fig. 5.8: (a) Transmittance (*T*) and reflectance (*R*) represented by solid and dashed lines, respectively, of various nanostructured ITO and (b) their corresponding sheet resistances (R_{sh}). Reproduced with permission from reference [71], © 2020 Optical Society of America.

(300-700 nm). The relative enhancement with the lowest inter-distance is slightly higher for disordered NS ITO than the periodic NS ITO. This higher enhancement might be due to the difference in the refrative index of PS and OrmoComp, which act as the nanopillars for disordered and planar NS ITO, respectively. However, further investigations are necessary by fabricating and comparaing both types of TCOs in a same batch. Another apparent difference to the peridic NS ITO is the absence of dips in the transmittace or the reflectance spectra. Rather, a broadband drop is observed, which is due to the wide distribution of size of the nanopillars in disorderd NS ITO (see **Fig. 5.9**a and also Fig. 5.4 and Fig. 5.8 transmittance spectra). This absence is attributed to the excitation of the leaky modes for a wide range of wavelengths (below the periodicty) instead of specific *k*-vectors, which is present for periodic NS ITO.[180]

Electrically, the sheet resistance (R_{sh}) is also influenced by the spacing of the nanostructures similar to the periodic nanostructures. Thus, the smallest spacing - 210 nm shows the highest sheet resistance. Overall, these results indicate that employing nanostructures enable a path to improve the optical properties for the application of solar

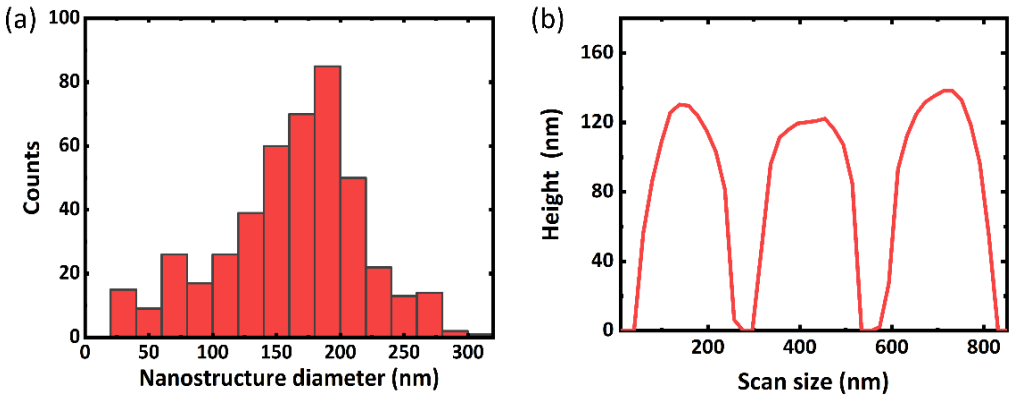

Fig. 5.9: (a) Statistical analysis of the (a) diameter of the nanostructures and (b) the height profile of nanostructured ITO electrode for 210 nm spacing derived from AFM measurement. Reproduced with permission from reference [71], © 2020 Optical Society of America.

cells, however, with a trade-off in the electrical properties. In the following section, s-PSCs are fabricated and the performance of perovskite-based tandem devices with nanostructures are explored.

5.3 Photovoltaic characteristics of perovskite solar cells with nanostructured ITO

In this section, the photovoltaic performances of the fabricated s-PSCs and the 4T perovskite/c-Si tandem solar cell are demonstrated with NS ITO. Based on the previous observations, both periodic and disordered NS ITO having the smallest period or inter-distance of ≈200 nm demonstrated the highest transmittance. However, with disordered NS ITO, the relative enhancement is slightly higher than the periodic one. In addition to this, the fabrication of the disordered NS ITO involves fewer steps in comparison to the periodic NS ITO. Moreover, in a recent submitted study by Donie *et al*., it is shown that the disordered nanopillars of PS can be deposited by inkjet printing, which is beneficial for upscaling, cost-effectiveness and flexibility in design.[181] Therefore, in this study, s-PSCs are fabricated with disordered NS ITO with the smallest spacing that depicted the highest transmittance.

5.3.1 Semitransparent perovskite and perovskite/c-Si tandem solar cells

In order to evaluate the performance of perovskite/c-Si tandem solar with NS ITO, s-PSCs are fabricated with the following layer stack: glass/**planar ITO** or **NS ITO**/np-SnO_2/ perovskite/spiro-MeOTAD/MoO_X/ITO (**Fig. 5.10**a,b). A triple cation perovskite layer is deposited as the absorber layer. Cross-section SEM image shows a homogenous perovskite absorber layer is formed on the nanostructured electrode, which is also structured. However, a planarization is achieved for subsequent layer stack. The semitransparent devices are completed by the hole transport layer spiro-MeOTAD, a MoO_X buffter layer and a rear ITO.

The current density-voltage (*J-V*) characteristics of the champion device is depicted in **Fig. 5.11**a. The s-PSC demonstrate an improved short-circuit current density (J_{SC}) of ≈2% compared to the planar reference. The improved J_{SC} is attributed to the reduction of the reflection losses and increased absorption above the bandgap (300-760 nm) of the perovskite absorber (Fig. 5.11c). The improved J_{SC} is also reflected in the external quantum efficiency (EQE) measurement (Fig. 5.11b). In accordance to the improved absorptance (Fig. 5.11c), an enhanced EQE over a broad spectral range is observed. The improvement

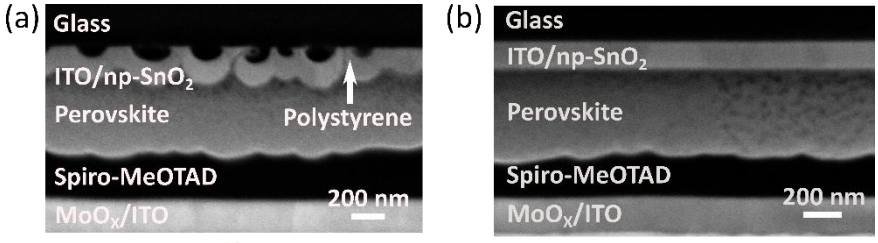

Fig. 5.10: Cross-section scanning electron microscopy (SEM) image of (a) nanostructured and (b) planar s-PSCs. Adapted with permission from reference [71], © 2020 Optical Society of America.

in the J_{SC} is also consistent for more than one investigated sample and different bandgaps of the perovskite absorber layer. Six samples fabricated in two separate batches for two different bandgaps show an improvement of approximately 3% (average) in the J_{SC} (**Fig. 5.12** and **Appendix**, **Fig. A. 5.1**). Overall, these results show that reducing the reflection losses by nano structuring the ITO leads to an improvement in the J_{SC} of the fabricated PSCs.

Although the J_{SC} obtained with NS ITO electrodes surpasses the J_{SC} of the planar ITO electrodes, both the open-circuit voltage (V_{OC}) and the FF are affected (see **Appendix**,

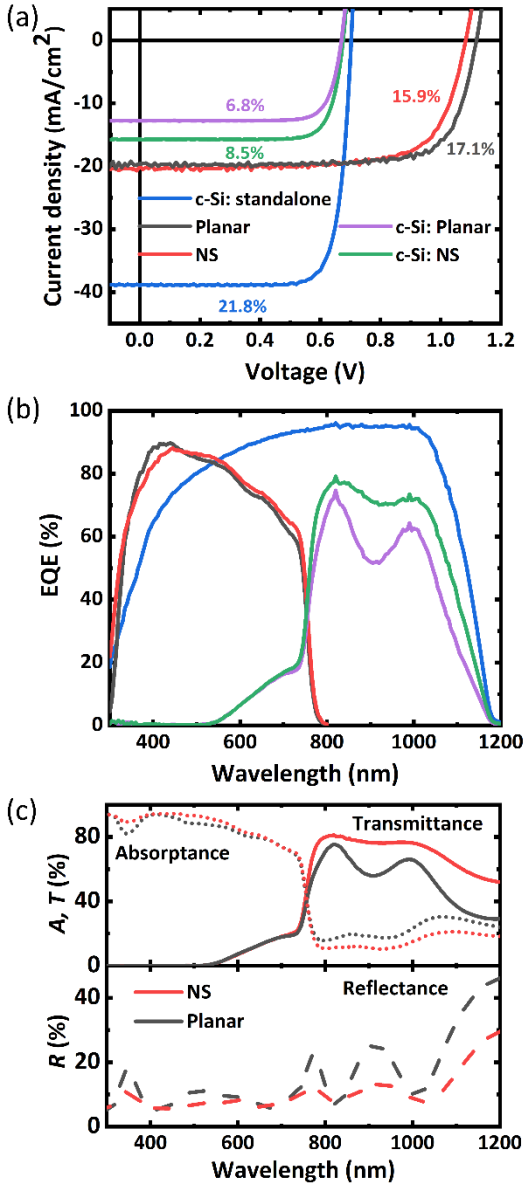

Fig. 5.11: (a) Current density-voltage characteristics and (b) external quantum efficiency (EQE) of semitransparent perovskite solar cells (s-PSCs) fabricated with nanostructured (NS) and planar ITO electrode, crystalline-silicon (c-Si) solar cell measured stand-alone configuration and under filters of s-PSCs with NS and planar ITO electrode. (c) Reflectance (*R*), Transmittance (*T*) and absorptance (*A*) of filters of s-PSCs with NS and planar ITO electrode. Adapted with permission from reference [71], © 2020 Optical Society of America.

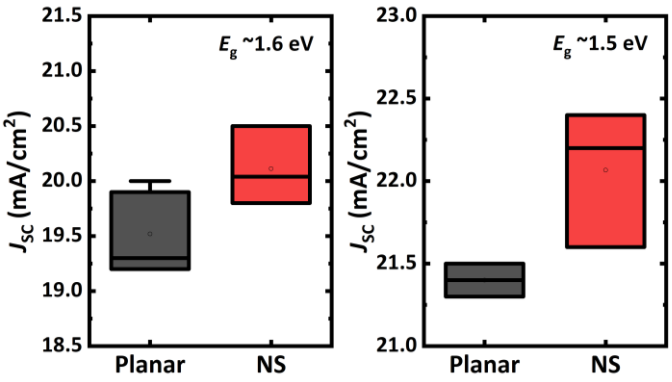

Fig. 5.12: Statistical analysis of short-circuit current densities (J_{SC}) of s-PSCs fabricated with planar and nanostructured (NS) ITO electrode. Adapted with permission from reference [71], © 2020 Optical Society of America.

Fig. A. 5.2 for further details). The V_{OC} is reduced by ~40 mV and the FF drops by 5% (Fig. 5.11a). Time-resolved photoluminescence measurement in **Fig. 5.13** shows a fast decay in the photoluminescence, indicating a reduced lifetime of the charge carriers in the NS ITO electrode-based device. This suggests a higher non-radiative recombination processes at the interface of NS ITO/np-SnO_2 or np-SnO_2/perovskite. The drop in the FF is associated to a slight observable shunt and an increase in the series resistance in the *J-V* characteristic of the PSC (series resistance with planar ITO: 70.2 Ω and series resistance NS ITO-PSC: 81.4 Ω). The increased series resistance can be attributed to the increased R_{sh} discussed earlier, which can mainly originate from the cracks that appear in the NS ITO (see Fig. 5.10a). Although the impact of the increased R_{sh} is not so severe in these fabricated s-PSCs (due to the small active area of 10.5 mm^2), the effect will not be insignificant for large area devices or modules. Therefore, further investigations are needed to reduce this loss. Overall, due to the reduction of both V_{OC} and the FF, the PCE of the s-PSC with NS ITO electrode is decreased compared to the planar reference, leading to 15.9% in the backward scan. Both nanostructured and planar devices exhibit hysteresis in their *J-V* characteristics, although the impact is slightly higher in NS ITO based s-PSCs. In order to obtain the real PCE, the s-PSCs are measured under constant illumination and at constant voltage near the maximum power point. No decay is observed for either of the two stacks and the champion s-PSC with NS ITO electrode shows a similar stable performance as the planar one, reaching a PCE of 15.0%. A summary of the results can be found in **Table 5.2**.

One of the advantages of the 4T tandem architecture is the mechanical-stacking of the s-PSC atop of c-Si solar cell to form perovskite/c-Si tandem solar cells. Therefore, now the prospect of 4T tandem device with NS ITO is discussed. Details regarding the measurement protocol is described in the chapter 3, section 3.2.1. Filters of s-PSCs (fabricated with NS ITO electrode and planar ITO electrode) with identical layer stack as the s-PSCs described earlier are fabricated and stacked on top of the bottom c-Si solar cell and the *J-V* parameters as well as the EQE are measured. The bottom cell is an interdigitated back contact (IBC) c-Si solar cell with a stand-alone PCE 21.8% (Fig. 5.11a and **Appendix**,

Fig. A. 5.3) measured under standard test conditions (AM 1.5G, temperature 25 °C). The comparatively lower PCE of the bottom c-Si solar cell with respect to the efficient devices already published in the literature is due to the weak EQE response in the short wavelengths (300-800 nm). This is weak response is present because of the fact that the employed c-Si solar cell has an optimized anti-reflection coating for the 4T tandem application. An analysis regarding other types of bottom solar cell is further discussed in the next section **5.3.2**. In the 4T tandem architecture, the bottom c-Si solar cell under the filter of NS ITO configuration outperforms the planar ITO configuration. A remarkable improvement in the PCE is achieved for the filtered c-Si solar cell with NS ITO leading to a PCE of 8.5% compared to the 6.8% with planar ITO s-PSC stack. This significant improvement is due to the increased transmittance of the s-PSC with NS ITO electrode, enhancing the bottom solar cell's J_{SC} by 2.9 mA/cm^2 (≈23% relative) compared to the planar reference case. The enhanced EQE below the bandgap of the s-PSC also confirms this improvement. The increment in the J_{SC} leads to an overall enhancement in the PCE of the 4T tandem architecture, leading to a stabilized PCE of 23.5%, which is 0.7% higher than the planar ITO configuration. It should be noted that the overall stabilized PCE of the 4T tandem architecture with NS ITO electrode is still low and is due to the poor FF and reduced PCE of the top s-PSCs. However, the novel NS ITO electrode for s-PSC has great potential, which is discussed in the next section. Further results can be found in **Table 5.2**.

Table 5.2: Photovoltaic parameters of top s-PSCs, bottom c-Si solar cells and tandem architectures.

Parameters/Device Architecture	s-PSC		c-Si			4T perovskite/c-Si	
	Planar	NS	Stand-alone	Filtered Planar s-PSC	Filtered NS s-PSC	Planar	NS
V_{OC} (V)	1.12	1.08	0.70	0.67	0.67	-	-
J_{SC} (mA/cm^2)	19.6	20.0	38.9	12.8	15.7	-	-
FF (%)	78	73	80	80	80	-	-
PCE (%)	17.1	15.9	21.8	6.8	8.5	23.9	24.4
SPCE (%)	16.0	15.0	-	-	-	22.8	23.5

5.3.2 Nanostructured ITO and its potentials

NS ITO electrode promises to reduce the reflection losses and enhance transmission below the bandgap of s-PSCs. As a result, a bottom cell in a 4T tandem configuration can benefit the from the improved transmission of light. However, due to the electrical losses (V_{OC} and FF), the overall gain in the 4T tandem architecture is small. In order to evaluate the potential of the NS ITO electrode in a 4T tandem architecture, a brief analysis is performed considering a similar V_{OC} and FF for both NS ITO and planar ITO s-PSC without any

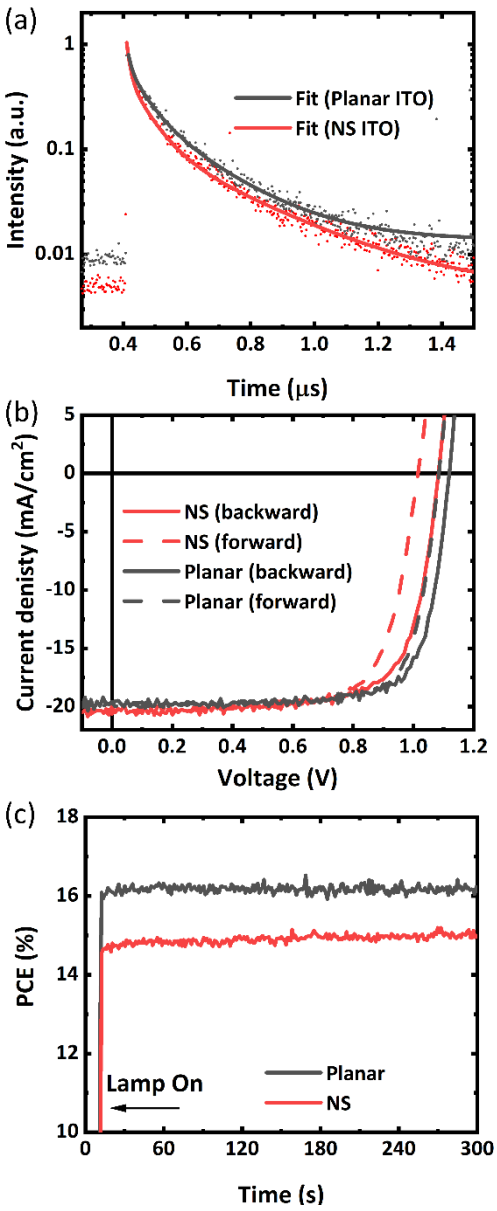

Fig. 5.13: (a) Time-resolved photoluminescence of perovskite absorber on planar and nanostructured (NS) ITO electrodes. (b) Current density-voltage characteristics in backward and forward scan directions and (c) stabilized power conversion efficiency (PCE) of semitransparent perovskite solar cells (s-PSCs) fabricated with nanostructured (NS) and planar ITO electrode. Adapted with permission from reference [71], © 2020 Optical Society of America.

hysteresis and assuming state-of-the-art c-Si solar cell with an enhanced EQE (labelled as Cell A)[182] and a CIGS solar cell (labelled as Cell B)[183] as the bottom cells. Therefore, the PCEs of the top s-PSCs with NS ITO electrode and planar ITO electrode are considered as 17.4% and 17.1%, respectively. In the case of the state-of-the-art bottom cells, the bottom solar cell's EQE is derived by weighting the transmittance of the respective top cell with the EQE of the stand-alone bottom solar cell. Cell A has a reported PCE of 26.1% and depicts an enhanced EQE (compare Fig. 5.11b and **Fig. 5.14a**) for the entire wavelength range 300-1200 nm. Due to the enhancement of the EQE response, especially below the bandgap of the top s-PSC, an improved PCE of 9.5% is obtained. The potential PCE of the 4T tandem

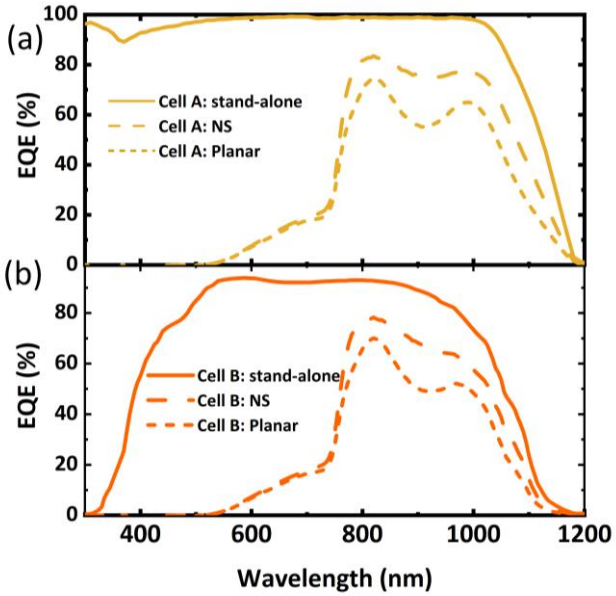

Fig. 5.14: External quantum efficiency (EQE) of c-Si solar cell adapted from **[**[182]**]**, referred as Cell A and CIGS solar cell adapted from **[**[183]**]**, referred as Cell B. The EQE of the devices are also presented in stand-alone or four-terminal tandem configuration under filters of semitransparent perovskite solar cells fabricated with planar or nanostructured ITO. Adapted with permission from reference [71], © 2020 Optical Society of America.

architecture is 27.0%, which is 1.1% higher than the c-Si solar cell used in this study. In the case of the planar ITO electrode stack, the potential PCE calculated is only 24.9% and is significantly smaller even than the stand-alone PCE of Cell A. In the case of Cell B in the 4T tandem configuration, which represents an all thin film tandem architecture, the potential PCE is reduced to 25.2% and is mostly due to the high bandgap and the weak EQE response of the CIGS.

Table 5.3: Photovoltaic parameters: J_{SC} and PCE of top s-PSCs, bottom c-Si solar cells and tandem architectures.

Stack	J_{SC} (mA/cm^2)			Potential PCE (%)				
	Stand-alone	Filtered Planar s-PSC	Filtered NS s-PSC	Stand-alone	Filtered Planar s-PSC	Filtered NS s-PSC	4T Planar	4T NS
Top planar	19.6	-	-	17.1[a]	-	-	-	-
Top NS	20.0	-	-	17.4[a]	12.8	-	-	-
Bottom c-Si (this work)	38.9	12.8	15.7	21.8	6.8	8.5	23.9[d]	25.9[e]
Bottom Cell A (c-Si [182])	42.6	13.2[f]	16.4	26.1	7.8[b]	9.6[b]	24.9[d]	27.0[e]
Bottom Cell B (CIGS [183])	35.9	11.2[f]	13.7	21.7	6.4[c]	7.8[c]	23.5[d]	25.2[e]

[a]The PCE of the top s-PSCs are estimated considering same V_{OC}, FF and no hysteresis for both planar and NS ITO based devices. The following parameters are considered to calculate the PCE: [b]Cell A: FF – 0.843; V_{OC} – 0.697 V, [c]Cell B: FF – 0.793; V_{OC} – 0.716 V. [d]Sum of PCEs of top planar device and bottom cell. [e]Sum of PCEs of top NS device and bottom cell. [f]By weighting the EQE of the stand-alone cell with the transmission of the respective filter, the J_{SC} is obtained.

Thus, two critical requirements of a 4T tandem architecture can be derived from this analysis: (i) in order to maximize the overall PCE, a bottom solar cell with enhanced EQE response below the bandgap of the top PSC should be considered, and (ii) a high transmission of the top cell is required (obtained with NS ITO electrode here) so that the PCE of the tandem architecture is higher than the stand-alone PCE of the sub-cells. In summary, the NS ITO based tandem solar cells shows the potential to improve the PCE significantly compared to it planar counterparts. Further information can be found in **Table 5.3**.

5.3.3 Energy yield analysis for perovskite solar cells with NS ITO

Nanostructured ITO are more robust in terms of angular selectivity, therefore, the dependence on the angles of incidence (AOI)[180] of the light is reduced. Therefore, this feature of reduced angular selectivity with nanostructures is very interesting for solar energy harvesting applications as the power generated by solar cells is highly dependent on the AOI of light, which changes throughout the day. To investigate this for the 4T perovskite/c-Si tandem architecture, the specular transmittance of the s-PSCs with NS ITO electrode and planar ITO electrode are compared for various AOI. For oblique angles, the specular transmittance with the NS ITO electrode drops only slightly, while a significant reduction in the transmittance is observed for the planar ITO case (**Fig. 5.15**).

To obtain more insights EQE measurements are performed on each the sub-cells and the J_{SC} is determined (**Fig. 5.16**). **Table 5.4** summarizes the obtained J_{SC}. It is evident that up to

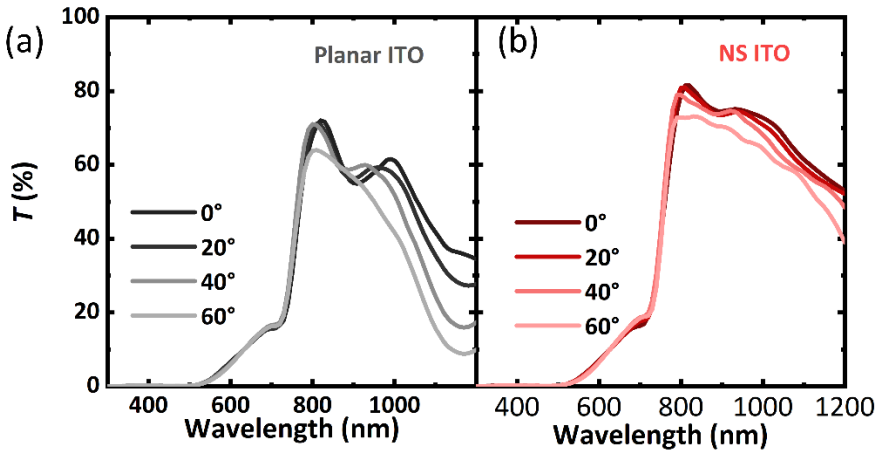

Fig. 5.15: Specular transmittance (*T*) of semitransparent perovskite solar cells with (a) planar ITO and (b) NS ITO for various angles of incidence. For oblique angles, the specular transmittance with the NS ITO electrode drops only slightly, while a significant reduction in the transmittance is observed for the planar ITO stack. Adapted with permission from reference [71], © 2020 Optical Society of America.

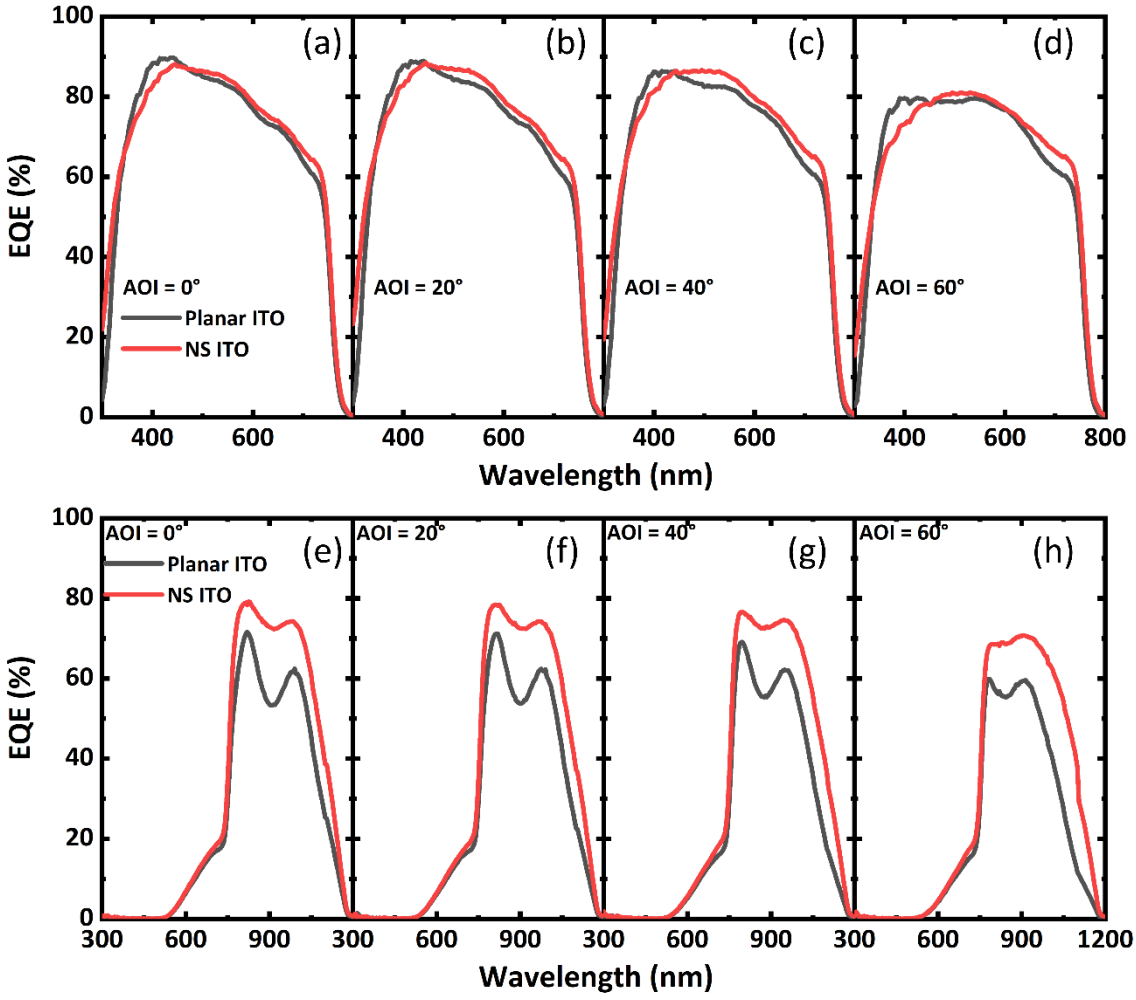

Fig. 5.16: External quantum efficiency (EQE) of (a-d) top semitransparent perovskite solar cells (s-PSCs) with planar and nanostructured (NS) ITO electrode and bottom crystalline silicon solar cell measured under filters of s-PSCs for angles of incidence (AOI) = 0°, 20°, 40° and 60. Adapted with permission from reference [71], © 2020 Optical Society of America.

AOI = 40°, the EQE of the top s-PSCs are comparable, with a slightly better current with the NS ITO electrodes as shown in the normalized data (**Fig. 5.17**). For AOI = 60°, the EQE is reduced significantly for both planar and NS ITO-based devices. This is due to the fact that at large AOI, the reflectance losses are increased and results in poor light in-coupling. In terms of bottom c-Si solar cell, the drop in the EQE with NS ITO stack is not as severe as the planar ITO stack. The EQE is significantly higher compared the planar ITO stack for all investigated AOI. At AOI = 60°, an absolute increase in J_{SC} of 3.5 mA/cm^2 is achieved with the NS ITO stack. Furthermore, at AOI = 60°, the obtained J_{SC} 0.6 mA/cm^2 higher than at normal incidence. These measurements at oblique angles of incidence are also in line with the transmittance measurements discussed earlier. Overall, the angle dependent study reveals that implementing nanostructures is not only beneficial for improving the J_{SC} at normal incidence but also at oblique angles, which is crucial for the energy yield of the solar cell.

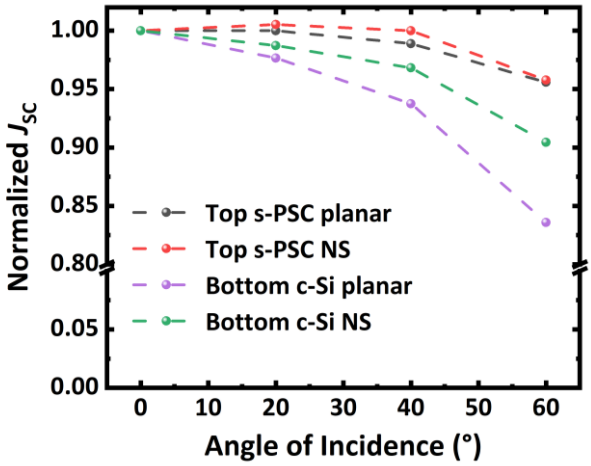

Fig. 5.17: Normalized short-circuit current density (J_{SC}) of the sub cells measured at angles of incidence (AOI) = 0°, 20°, 40° and 60. Reproduced with permission from reference [71], © 2020 Optical Society of America.

Table 5.4: Short-circuit current density (J_{SC}) of top and bottom solar cells in the 4T tandem configuration for various angles of incidence.

Angles of incidence (AOI)	J_{SC} (mA/cm²)			
	Top s-PSC		Bottom c-Si	
	Planar	NS	Planar	NS
0°	18.1	18.9	12.8	15.7
20°	18.1	19.0	12.5	15.5
40°	17.9	18.9	12.0	15.2
60°	17.3	18.1	10.7	14.2

It should be noted that in real world scenarios, along with the changes in the AOI of light, the solar cells also experience very different conditions depending on the location. This includes the daily and seasonal variations of the solar spectrum, irradiation conditions, amount of direct and diffuse light. However, these effects are not included in the key figure-of-merit for photovoltaic research, which is the PCE measured in the laboratory under standard test conditions. The standard test conditions are defined by investigating the test solar cell at a constant temperature of 25 °C under AM 1.5G spectrum. Therefore, to determine the power output of the under realistic irradiation conditions, energy yield analysis must be performed.[44,76,77] Here, the energy yield of the NS ITO electrode-based tandem device is deduced and compared with the planar reference stack. The energy yield framework used is this study relies on the irradiance data based on various locations in the United States of America and normalized EQE of the inspected device architecture. It should be pointed out that to investigate the overall potential of the NS ITO electrode on the energy yield based on the EQE only, the electrical properties (V_{OC}, J_{SC} and FF) of the top sub-cells are assumed to be the same. Using the information provided above, the energy

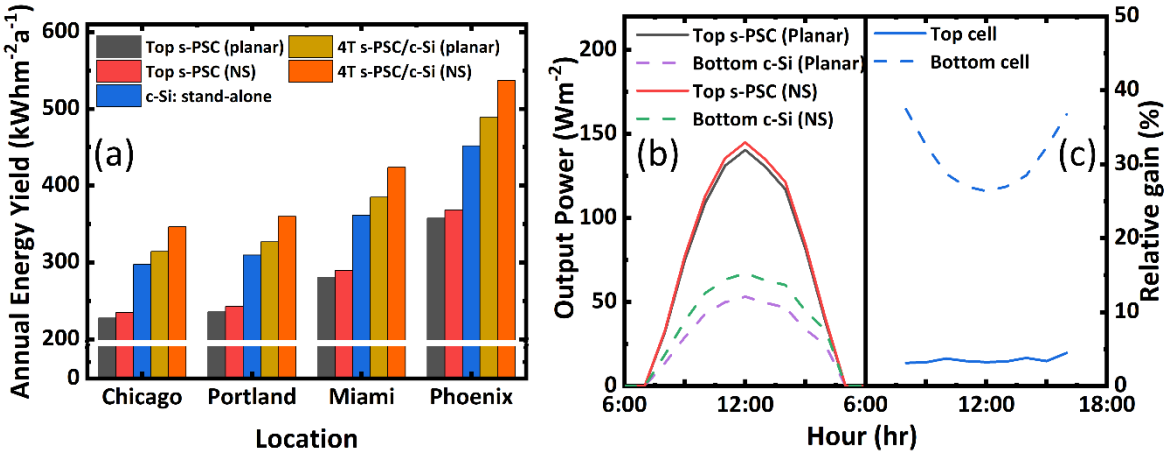

Fig. 5.18: (a) Annual energy yield for various (representative) locations in the United States of America. (b) Output power and (c) relative gains of the top and bottom cell calculated for planar and NS ITO stack on a particular day January 3rd. Reproduced with permission from reference [71], © 2020 Optical Society of America.

yield is calculated (**Fig. 5.18**a), which shows that the energy yield of the tandem architecture based on NS ITO electrode is higher than planar case as well as individual single-junction solar cells, irrespective of the location. A relative improvement of ≈10% is achieved for 4T tandem architecture with NS ITO stack in comparison to the planar reference. This is mainly due to the excellent angular selective response as discussed earlier. On a particular day (January 3rd), both sub-cells in the NS ITO based tandem configuration generate higher power (Fig. 5.18b). The relative gain in the power output of the top solar cell is merely constant throughout the day. A significantly higher (>35%) power output is noted for the bottom solar cell both during the sunrise and the sunset with NS ITO stack. Overall, these results show that due to the robustness in the angular response and improved transmittance of the NS ITO electrode, higher power output can be generated with NS ITO-based 4T tandem solar cells.

5.4 Discussions and conclusion

In this study, nanophotonic electrodes are developed to improve the performance of 4T perovskite/c-Si tandem solar cells. Compared to conventional light management concepts, which commonly uses microtextured foils[58,63] or anti-reflection coatings[184] at the front side of the tandem solar cell, here an alternative method is demonstrated that textures the front TCO interface to enhance the performance of 4T perovskite/c-Si tandem solar cells. This study is the first protype demonstration of implementing these nanostructures in a perovskite/c-Si 4T tandem configuration.

Two different approaches are demonstrated to obtain these nanostructures: (i) soft-imprinting and (ii) polymer blend lithography. Both approaches yield improved transmission for the TCOs. It is demonstrated that when the period or the inter-distances between the nanostructures are relatively small (around 200 nm), an improved transmission is realized for a broad range of wavelengths (300-1200 nm). An enhancement

of ≈5% and ≈7% is observed for periodic ITO and disordered nanostructured ITO, respectively. The broad range of improvement is particularly interesting for tandem solar cells as this leads to enhanced short-circuit current densities for both the sub cells in the tandem configuration. These results are also consistent with existing simulation and experimental results that were already demonstrated in the literature.[72] The improved transmission is attributed to a gradual matching of the refractive index that reduces the overall reflection losses. One particular challenge that still needs to be overcome is the formation of cracks between the nanostructures in the NS ITO. These cracks impede the charge carriers transfer and as a result, an increase in the sheet resistance is observed these TCOs. However, further optimization of the sputtering condition can be employed in future studies to avoid the formation of these cracks.

The reduced reflections with the NS ITO lead to an improved J_{SC} in both top s-PSCs and bottom c-Si solar cells. While for the top s-PSCs, the increase is around ≈3% relative, a significant improvement in the short-circuit current density for the bottom solar cell (≈23% relative) is observed. This improvement in the top s-PSC is comparable to a recently published work, where similar NS TCOs fabricated from nanopillars were employed, but for opaque PSC.[185] The sum of short-circuit current densities by both the sub cells is ≈10% relative higher with the nanostructured ITO stack compared to the planar. This exceeds the enhancement observed previously by Jaysankar *et al*. (3.2% relative) in 4T perovskite/c-Si tandem modules, which incorporated an inverted pyramidal micro-texture at the air/glass interface.[38] This shows that reducing the optical losses at the front TCO interface is also important in improving the J_{SC} in tandem solar cells. Although there is an improvement in the short-circuit current densities, top s-PSCs suffer from enhanced recombination losses. As a result, s-PSCs yielded reduced V_{OC} and PCE. In a recent study, Tochhorn *et al*. already demonstrated that this voltage loss can be overcome by utilizing self-assembled monolayers that conformally covers the nanostructured TCOs.[185] Overall, for the tandem architecture with NS ITO, an improved PCE of 0.7% is achieved. Further analysis reveals a potential increase in the PCE by 2.1% for the NS ITO stack if similar performance of the top s-PSCs is achieved by both planar and NS ITO electrode. Moreover, angle dependent transmittance and EQE measurements show that devices based on NS ITO electrode are more robust and have better angular stability compared to planar stacks. To verify this, angular dependent analysis is extended to energy yield calculations. The results reveal that NS ITO based devices improve the annual output power by a relative ≈10% independent of locations compared to the planar ITO electrode. Thus, it is highly important to overcome the remaining challenges associated with the NS ITO and fully exploit the potentials in perovskite-based tandem architectures.

6. Semitransparent perovskite solar cells for four-terminal tandem architectures

This chapter discusses semitransparent perovskite solar cells for four-terminal perovskite/c-Si and perovskite/CIGS tandem architectures. The first part of this chapter deals with research question 3 and discusses engineering of the bandgap of the perovskite absorber layer to determine the optimum for maximizing power conversion efficiency in a four-terminal tandem architecture. A detailed study of the various properties of the absorber layer is also presented. The second part of this chapter deals with research question 2 and investigates both transparent conductive oxide electrodes present in semitransparent perovskite solar cells to determine the optical loss channels that reduce the power conversion efficiency in the four-terminal tandem architecture. Furthermore, alternative materials are proposed that demonstrate improved overall power conversion efficiency for the perovskite-based four-terminal tandem architecture.

Acknowledgements and contributions

The first part of this chapter on semitransparent perovskite solar cells for four-terminal tandem architectures with engineered bandgap is already published in reference [99]. This publication is a collaboration between KIT, ISFH and ZSW. The research article is an equally-shared work between Ihteaz M. Hossain and Saba Gharibzadeh. In this collaboration, Ihteaz M. Hossain contributed the fabrication of the semitransparent perovskite solar cells and characterizations related to the four-terminal architecture. The second part of this chapter discusses the transparent conductive oxide electrodes for semitransparent perovskite solar cells. Part of the second chapter is already submitted in reference [186] for publication. Ihteaz M. Hossain acknowledges the support of Saba Gharibzadeh, Isabel Allegro, David Ritzer, Adrian Mertens and Michael Hetterich in various experimental procedures. Ihteaz M. Hossain also acknowledges the support of Mortiz Schultes and Erik Ahlswede of Zentrum für Sonnenenergie und Wasserstoff-Forschung Baden-Württemberg (ZSW) for providing samples and discussions. Finally, Ihteaz M. Hossain acknowledges

various fruitful discussion with Somayeh Moghadamzadeh, Paul Fassl, Yidenekachew Donie and Raphael Schmager during the course of this study.

A critical requirement in a tandem solar cell architecture is to find the optimum bandgaps and the materials for the top and bottom solar cells as discussed in chapter 2, section 2.4. To date, the choice of the bottom solar cell has been straight forward since the bandgap of the established technologies in photovoltaic industry is ≈1.0 eV: crystalline-silicon (c-Si) has a bandgap of ≈1.1 eV and copper indium gallium selenide's (CIGS) bandgap can be varied between 1.0-1.2 eV. Next to the already established technologies, low-bandgap perovskite solar cells (PSCs) are another viable option as the bandgap can be tuned from 1.1-1.3 eV by the partial substitution of Pb^{2+} with Sn^{2+} and furthermore, it would allow for all solution-processed, low-cost tandem photovoltaics.[82] In terms of the top solar cell, wide-bandgap PSCs are interesting candidates as the bandgap of the absorber can be tuned between 1.5-2.3 eV by varying the stoichiometry of the material.[84,98]

Due to ease in the current matching condition in the four-terminal (4T) tandem architecture, a wide range of bandgaps (1.60-1.85 eV) for the top perovskite absorber can demonstrate very high PCE with the optimum at 1.81 eV as shown in simulations.[17,18] The current record 4T perovskite/c-Si tandem device (28.2%) uses a bandgap of 1.63 eV (extracted from external quantum efficiency measurement),[14] whereas a bandgap of 1.68 eV was demonstrated to be the optimum for 4T perovskite/CIGS tandem solar cells (25.9%).[45] Both of these studies use significantly smaller bandgaps than the optimum for the top perovskite absorber in tandem configurations as demonstrated in simulations, which raises the question of the optimum bandgap of the top absorber in perovskite-based tandem PV for real prototype devices.

One of the reasons for this difference is the non-radiative recombination losses and imperfect contact properties of the wide bandgap PSCs that affect the device performance, and result in a large open-circuit voltage (V_{OC}) deficit (defined by E_g/q-V_{OC}).[25,38,169,170] Wide bandgap perovskite absorber conventionally uses a bromine-rich stoichiometry to increase the bandgap.[25,34,58,63,80,98,187] In such compositions, recombination loss mechanism are dominated by photo-induced phase segregation and subsequent funneling of charge carriers into iodide-rich lower bandgap regions.[19] Furthermore, these wide bandgap materials present a higher number of deep defect states[20,21,188] and a stronger interfacial recombination in full devices,[22–24] all of which result in a strong V_{OC} deficit.[25–27,189] It was recently demonstrated by our research group that a 2D Ruddlesden–Popper (2D-RP) structure can passivate the bulk perovskite absorber and reduce the V_{OC} deficit.[13,91] The 2D passivation is obtained by depositing a thin layer of *n*-butylammonium bromide (*n*-BABr) on the perovskite absorber, forming a 2D/3D heterostructure that passivates the surface defects and demonstrates an improvement in the lifetime of the charge carriers. Thus, the 2D/3D heterostructure mitigates non-radiative recombination losses and PSCs fabricated with these heterostructures demonstrated an enhanced V_{OC} (≈80 mV) compared to the reference bulk 3D absorber.[91]

Next to the recombination losses that affect the electrical properties, optical losses such as reflections at interfaces and parasitic absorption within the layer stack reduce the transmission of the top solar cell and decreases the overall PCE in the tandem architecture.[15,16,71,190] One of the main sources of these optical losses are the transparent

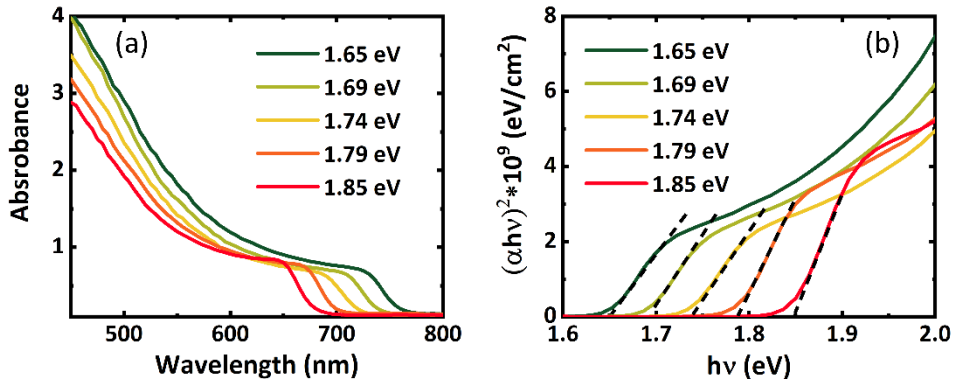

Fig. 6.1: (a) Absorbance spectra and (b) Tauc plots of the spin-coated layers with bandgaps 1.65 eV, 1.69 eV, 1.74 eV, 1,79 eV and 1.85 eV for the 2D/3D perovskite heterostructure. Adapted with permission from reference [99], © John Wiley & Sons.

conductive oxide (TCO) electrodes as discussed in chapter 2, section 2.5 and thoroughly in chapter 5. Fluorine-doped tin oxide (FTO) is a commonly employed front TCO for opaque PSCs, however it shows strong parasitic absorption losses both in the visible and near infrared wavelengths (see also **Appendix Fig. A. 4.1**),[36,191] and is thus not feasible for perovskite-based tandem applications. Another widely used front TCO is tin-doped indium oxide (ITO), which shows significantly reduced absorption losses compared to FTO, however, the absorption and reflection losses in the near infrared wavelengths due to the free charge carriers[39,192] may still limit the overall PCE for tandem devices. Therefore, further work must be carried out to improve the optical properties of ITO to make it more suitable for tandems applications or alternate materials must be investigated to replace it. In the literature, several material with improved electrical properties and low optical losses already exist that promise to replace ITO, for example zinc-doped indium oxide (IZO), hydrogenated indium oxide (IO:H) and others.[36,58,80]

In the first part of this chapter, the aspect of the optimum bandgap of the perovskite absorber in a 4T tandem architecture is experimentally investigated. For this, PSCs with engineered bandgaps are fabricated and a 2D/3D heterostructure is incorporated to reduce the V_{OC} deficit. Semitransparent perovskite solar cells (s-PSCs) are mechanically-stacked with c-Si and CIGS bottom solar cells to determine the optimum bandgap for the 4T perovskite/c-Si and perovskite/CIGS multi-junction solar cells. In the second part of the chapter, a detailed investigation on the optical properties of different TCOs is carried out to identify the optical loss mechanisms in a 4T perovskite/c-Si tandem architecture. Finally, s-PSCs with TCO electrodes with improved optical properties are fabricated to enhance the PCE in perovskite/c-Si tandem solar cells.

6.1 Bandgap tuning of perovskite absorbers

In this section, the influence of the bandgap of the top wide-bandgap perovskite absorber on the performance of 4T-tandem perovskite-based tandems is investigated in detail. Initially, the material properties of perovskite films with various bandgaps are studied, followed by the fabrication of opaque perovskite solar cells (o-PSCs) and s-PSCs. Finally,

s-PSCs are mechanically-stacked on top of bottom c-Si and CIGS solar cells to study the device performance of the 4T tandem architecture.

6.1.1 Material properties

Five different bandgaps of double cation perovskite absorbers ($FA_{0.83}Cs_{0.17}Pb(I_{1-y}Br_y)_3$) based on formamidinium (FA) and cesium (Cs) are investigated to determine the optimum bandgap of the top PSC in a 4T tandem architecture. In order to vary the bandgap, the content of bromine ($0.24 \leq y \leq 0.56$) in the precursor solution is varied in steps of $\Delta y = 0.08$. Furthermore, a 2D/3D perovskite heterostructure is obtained for each of these bandgaps by spin coating *n*-butylammonium bromide (*n*-BABr) dissolved in isopropanol on top of the 3D perovskite absorber. The absorptance spectra obtained from spectrophotometric measurements show a shift towards lower wavelengths for increased bromine content (**Fig. 6.1**a), demonstrating the widening of the bandgap. The bandgaps of the perovskite absorbers are determined using **Equation 4.1** and considering a direct optical transition (Fig. 6.1b). A wide range of bandgaps of the perovskite absorber are formed (1.65-1.85 eV), which, according to the simulations[17,75] are in the optimum range to obtain an efficient 4T tandem device. It should be noted that the determination of the bandgaps here might also be affected by the excitonic absorption, which is more pronounced for higher bromide concentrations as observed from the appearance in the excitonic nature of the absorbance spectra. This is why Tauc plot is not the ideal method for the determination of the bandgap. A more accurate estimation of the bandgap would be to use an Elliot fit and obtaining the bandgap from the fitted excitonic continuum.[193] However, for this study, the relative differences in the bandgaps are more important. As a result, the simpler Tauc plot method is employed that is most commonly followed in the literature for perovskite absorbers even though there are various other ways to determine the bandgap.[194]

In order to determine the presence of the 2D structure, x-ray diffraction (XRD) measurements are carried out on these different bandgaps. The results reveal weak but

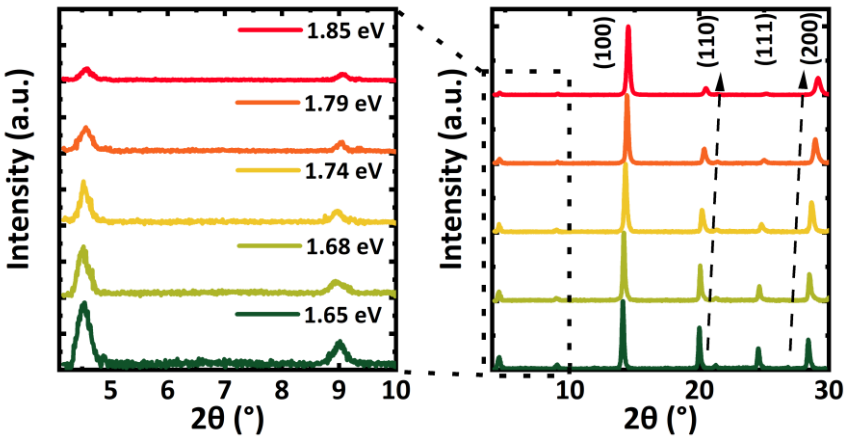

Fig. 6.2: X-ray diffraction (XRD) pattern of the spin-coated layers with bandgaps 1.65 eV, 1.69 eV, 1.74 eV, 1,79 eV and 1.85 eV for the 2D/3D perovskite heterostructure. Adapted with permission from reference [99], © John Wiley & Sons.

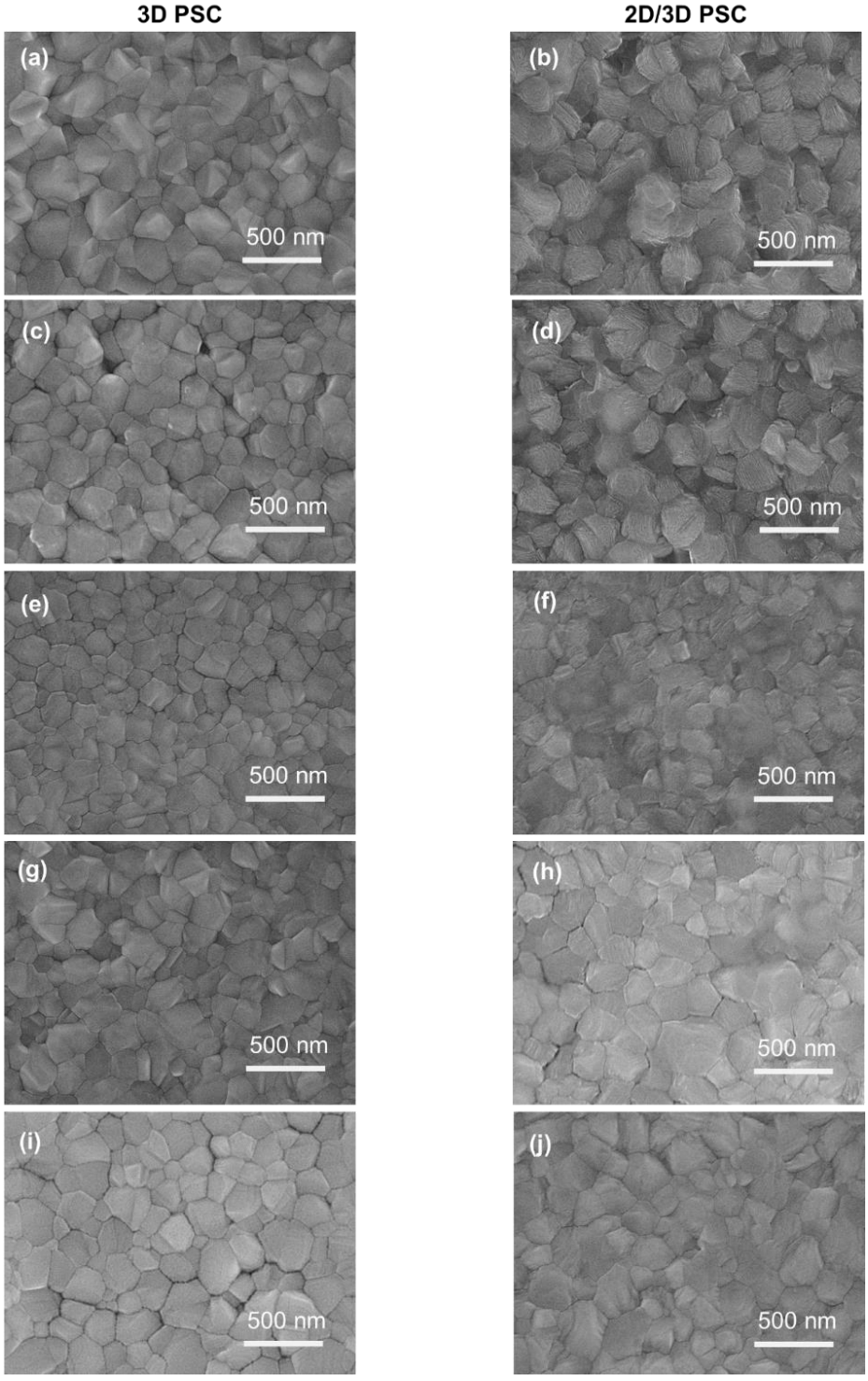

Fig. 6.3: Top-view scanning electron microscopy images of (a, c, e, g, i) 3D perovskite and (b, d, f, h, j) 2D/3D perovskite heterostructure for bandgaps: 1.65 eV, 1.69 eV, 1.74 eV, 1,79 eV and 1.85 eV. Reproduced with permission from reference [99], © John Wiley & Sons.

yet visible peaks at 2θ ≈ 4.5° and 9.0°. These reflection peaks correspond to the 2D material, forming a 2D superlattice with a much larger unit cell compared to the 3D bulk perovskite. Previous study by Gharibzadeh *et al*. showed with the same structure on a 1.73 eV bandgap that the spacing between these superlattices was ≈2 nm and corresponded to a 2D-RP phase of n = 2.[91] Next to the reflection peaks of the 2D phase,

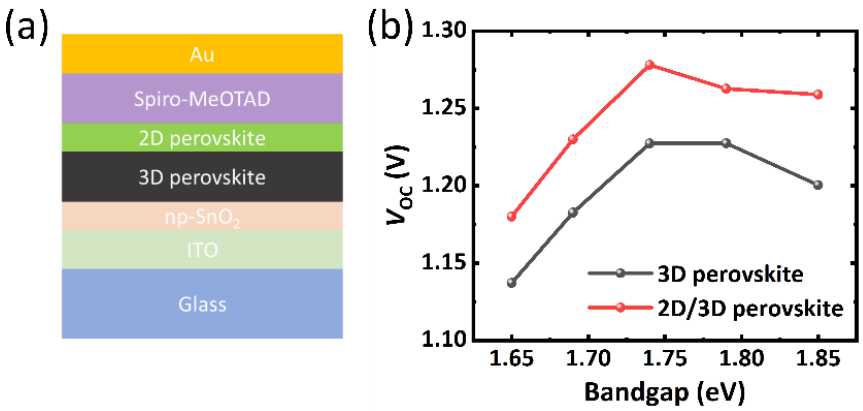

Fig. 6.4: (a) Schematic of the perovskite solar cell (PSC) with 2D/3D perovskite heterostructure. (b) Open-circuit voltage (V_{OC}) as a function of the bandgap of the perovskite absorbers for opaque PSCs. Adapted with permission from reference [99], © John Wiley & Sons.

the XRD measurements show the typical bulk 3D perovskite reflection peaks from the planes (100), (110), (111) and (200). With the increase in bromine concentration, a consistent shift of the reflection peaks towards higher angles are observed. This can be attributed to the increased lattice contraction due to the decrease in the perovskite crystal structure as smaller bromide ions now replace the larger iodide ions.[195] To observe any morphological changes due to the presence of the 2D phase on the bulk 3D perovskite, scanning electron microscopy (SEM) is performed on these samples. The images reveal a minor modification of the surface texture of the films with 2D/3D heterostructure for all bandgaps compared to the bulk 3D reference (**Fig. 6.3**). Thus, it indicates that the 2D layer forms a very thin layer on the surface of the 3D bulk, which is in consistent with the previous studies of Gharibzadeh *et al*. and Doung *et al*.[13,91] In the next section, the performance of the PSCs with 2D/3D heterostructure for various bandgaps is investigated.

6.1.2 Photovoltaic characteristics of perovskite solar cells for optimum bandgap

o-PSCs are fabricated to investigate the effect of the 2D/3D heterostructure on the photovoltaic parameters. The device layer stack is comprised of glass/ITO/ np-SnO_2/ (**2D/3D perovskite** or **3D perovskite**)/spiro-MeOTAD/Au (**Fig. 6.4**a). An in-house sputtered ITO (ITO_v, see chapter 3, section 3.1.3 for more information about the deposition) is used. The open-circuit voltages of the champion devices are shown in Fig. 6.4b. An enhancement of ≈45 mV in the V_{OC} is observed for all investigated bandgaps using the 2D/3D heterostructure, which can be attributed to the reduction in the non-radiative recombination losses as discussed by Gharibzadeh *et al*. and Doung *et al*.[13,91] They show an increase in the lifetime of the charge carriers for 2D/3D perovskite heterostructure compared to the bulk 3D perovskite. Furthermore, a better energetic alignment with the hole transport layer may also result in the overall improvement of the V_{OC}.[196] Fig. 6.4b also shows that the V_{OC} increases linearly with increasing bandgap from 1.65-1.74 eV, independent of the 2D passivation layer. Up on a further increase of the bandgap to 1.85 eV, the V_{OC} reaches a maximum and subsequently decreases. An enhanced V_{OC} deficit

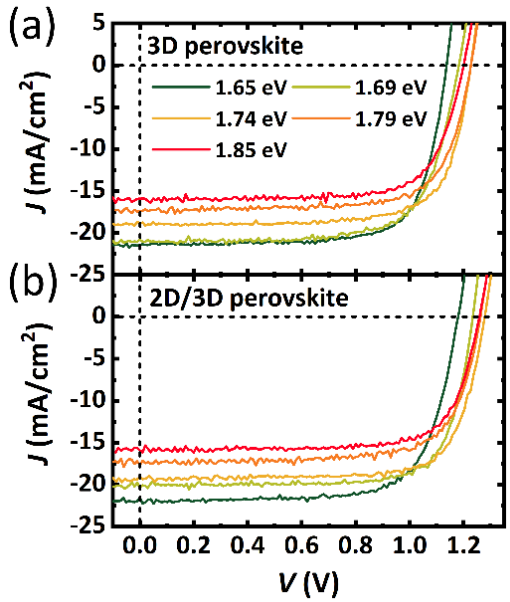

Fig. 6.5: Current density-voltage (*J-V*) characteristics of opaque perovskite solar cells fabricated with (a) 3D perovskite and (b) 2D/3D perovskite heterostructure for bandgaps: 1.65 eV, 1.69 eV, 1.74 eV, 1,79 eV and 1.85 eV.

is a commonly observed phenomenon for PSCs with high bromine content and is attributed to increased recombination losses as discussed earlier.[19–27,188,189] In order to compare the obtained V_{OC} for all the different bandgaps with existing literature, a literature survey of reported champion open-circuit voltages is shown in **Appendix**, **Fig. A.6.1**. The results show that, the 2D passivated PSCs in this study yield high open-circuit voltages over a broad range of bandgaps and are among the highest reported in the literature. Furthermore, to the best of our knowledge, it is the first time an effective 2D passivation approach is reported over such a broad range of bandgaps. More detailed information regarding derivation of the bandgaps from external quantum efficiency (EQE) measurement as well as a table of the V_{OC} and the V_{OC} deficit values can be found in the **Appendix**, **Table A. 6.1**. It should be noted that the V_{OC} of the presented devices here is ≈30 mV lower than in the previous work by Gharibzadeh *et al*. for the same layer stack as

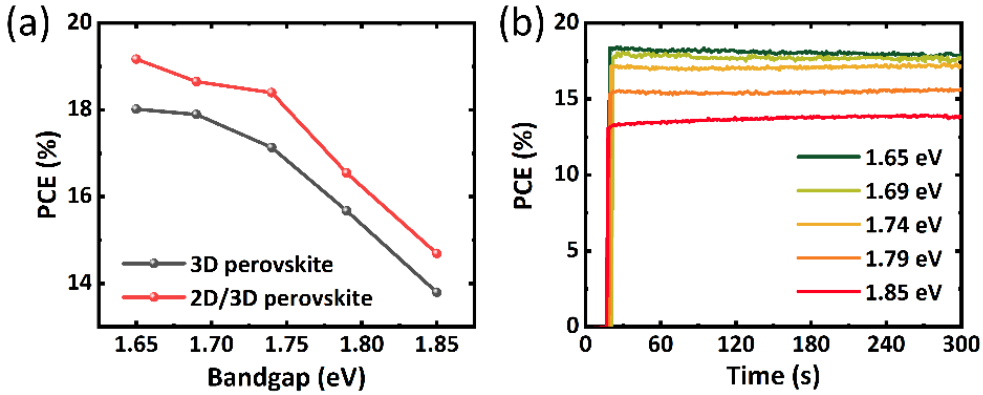

Fig. 6.6: Power conversion efficiency (PCE) derived from (a) current density-voltage characteristics and (b) measuring at a constant voltage near the maximum power point for the various bandgaps of perovskite absorber. Adapted with permission from reference [99], © John Wiley & Sons.

shown in Fig. 6.4c.[91] The probable reason could be the poorer quality of the precursor material PbI_2 from the supplier during the course of this study, which is the key component in fabricating highly efficient PSCs (see Notes at: https://www.tcichemicals.com/eshop/en/us/commodity/L0279/).

Next to the V_{OC}, the fill factor (FF) of the 2D/3D o-PSCs shows an improvement of 1.5-2% absolute compared to the 3D bulk devices (**Table 6.1** and **Fig. 6.5**). The short-circuit current density (J_{SC}) derived from the current density-voltage (*J-V*) characteristic shows a similar reduction with increasing bandgap for both 3D and 2D/3D samples. This is an indication that the thickness of the perovskite absorber is not significantly modified by the addition

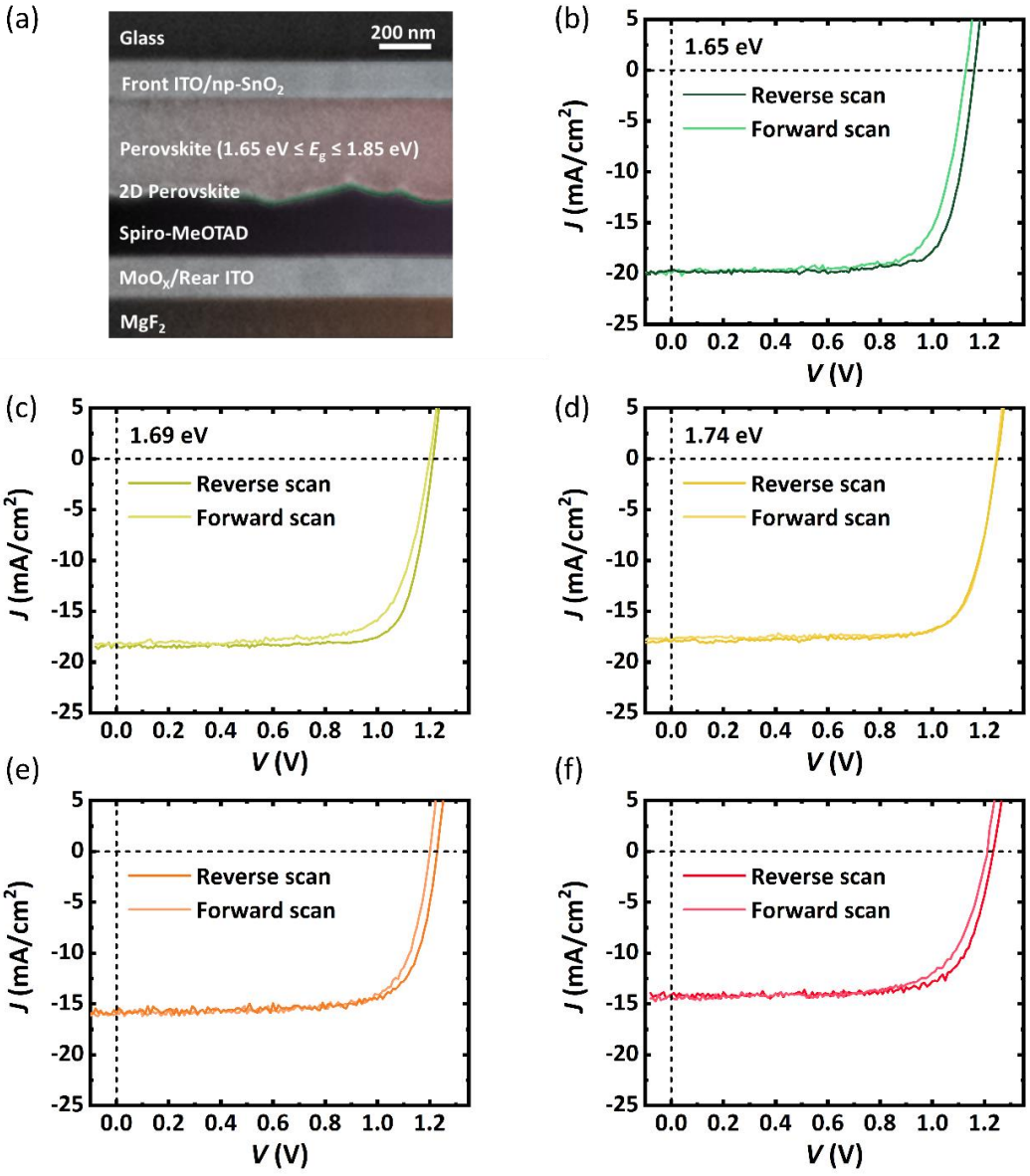

Fig. 6.7: (a) Cross-section scanning electron microscopy image of a semitransparent perovskite solar cell (s-PSC) with 2D/3D perovskite heterostructure. (b-f) Current density-voltage (*J-V*) characteristics of the s-PSCs for bandgaps: 1.65 eV, 1.69 eV, 1.74 eV, 1,79 eV and 1.85 eV. Adapted with permission from reference [99], © John Wiley & Sons.

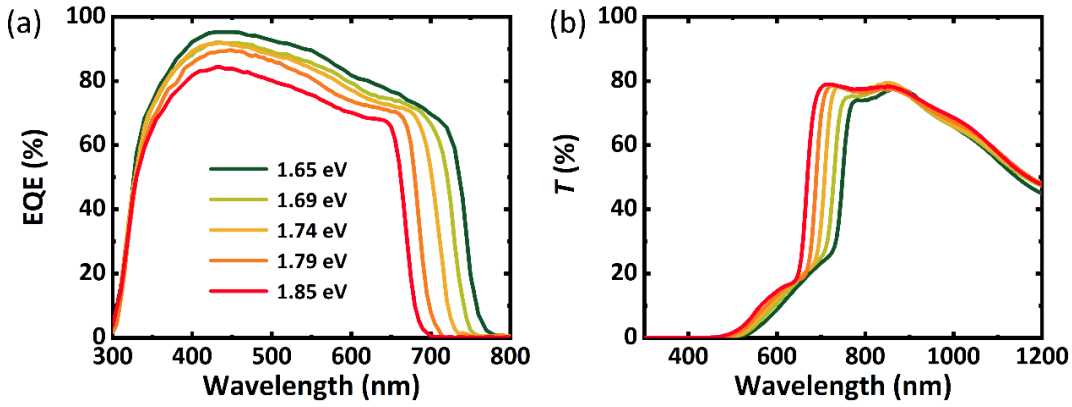

Fig. 6.8: (a) External quantum efficiency (EQE) and (b) transmittance (*T*) of s-PSC stack with perovskite absorber for bandgaps: 1.65 eV, 1.69 eV, 1.74 eV, 1,79 eV and 1.85 eV. Adapted with permission from reference [99], © John Wiley & Sons.

of the 2D layer and charge extraction is efficient. The PCE of o-PSCs with 2D/3D heterostructure derived from *J-V* characteristics shows a significant improvement of 0.8-1.3% absolute compared to the 3D PSCs, mainly due to the improved V_{OC} and FF (**Fig. 6.6**a). The maximum PCE of 19.2% is obtained for the lowest bandgap of 1.65 eV. In addition to the improved PCE, employing 2D/3D perovskite heterostructure does not affect the short-term stability of the devices. Fig. 6.6b shows constant stabilized PCEs of up to 17.9%, 17.6%, 17.2%, 15.6%, and 13.8% with increasing bandgap from 1.65-1.85 eV after 5 min of constant illumination at a voltage near to the maximum power point (MPP).

Table 6.1: Photovoltaic parameters of the perovskite solar cells for different bandgaps.

Bandgap of perovskite absorber (eV)	**J_{SC} (mA/cm²)**		**V_{OC} (V)**		**FF (%)**		**PCE (%)**		**Stabilized PCE (%)**	
	3D	2D/3D	3D	2D/3D	3D	2D/3D	3D	2D/3D	3D	2D/3D
1.65	21.4	21.6	1.13	1.18	73.9	75.3	18.0	19.2	16.8	17.9
1.69	20.8	20.4	1.18	1.23	72.8	74.3	17.9	18.7	16.2	17.6
1.74	18.9	19.1	1.23	1.28	74.0	76.6	17.1	18.4	15.7	17.2
1.79	17.4	17.7	1.23	1.26	73.5	74.2	15.7	16.5	14.7	15.6
1.85	15.9	15.9	1.20	1.26	72.3	73.4	13.8	14.7	12.5	13.8

Having demonstrated the improved device performance with 2D/3D perovskite heterostructure in o-PSCs, next s-PSCs are fabricated by depositing an ITO rear electrode with a buffer layer of MoO_X (**Fig. 6.7**a). In order to enhance the transmission of the s-PSCs, a 150-155 nm layer of MgF_2 anti-reflection coating is also deposited on the rear ITO (see later discussions for more information). The *J-V* characteristics of the fabricated s-PSCs reveal that devices exhibit low hysteresis, and a high FF (Fig. 6.7b-f). A small drop in the V_{OC} of ≈20-30 mV is observed compared to the o-PSCs. This drop is a result of partially shading the active area using a shadow mask (chapter 3, section 3.2.1) to accurately measure the J_{SC} of the s-PSCs (as the area of the s-PSCs is not precisely defined after the

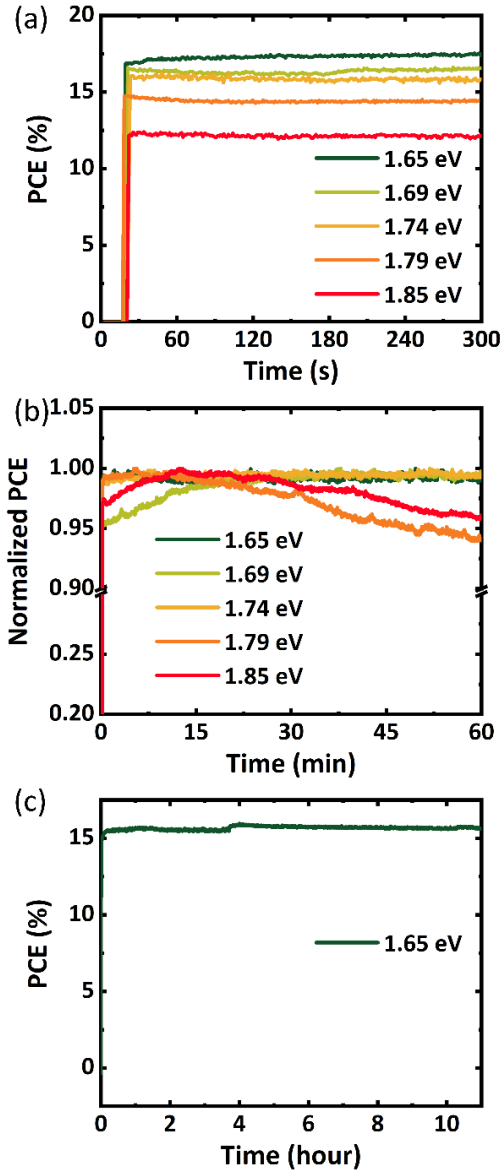

Fig. 6.9: Stability of perovskite solar cells with 2D/3D heterostructure. (a) Power conversion efficiency (PCE) and (b) normalized PCE of semitransparent perovskite solar cells (s-PSCs) with bandgaps: 1.65 eV, 1.69 eV, 1.74 eV, 1,79 eV and 1.85 eV measured at constant voltages near the maximum power point. (c) Long term stability test of s-PSC for bandgap = 1.65 eV. Adapted with permission from reference [99], © John Wiley & Sons.

sputtering of ITO). Therefore, a dark solar cell, which is in forward bias, is formed in parallel with the solar cell under light, leading to a reduction in the V_{OC}. Furthermore, as the fabricated PSCs are semitransparent, the devices show 1-1.5 mA/cm^2 lower J_{SC} than the o-PSCs, which is due to reduced optical path length, and poor reflection by the rear ITO.

EQE measurements conducted on these samples show that the EQE is reduced in the wavelength range between 550-800 nm (**Fig. 6.8**a). In accordance with the absorbance spectra in Fig. 6.1a for increasing bandgap, a consistent shift in the onset of the EQE signal towards shorter wavelengths is also noted. Moreover, a reduced EQE is observed for increasing bandgaps. This might be associated to a poorer charge extraction or an

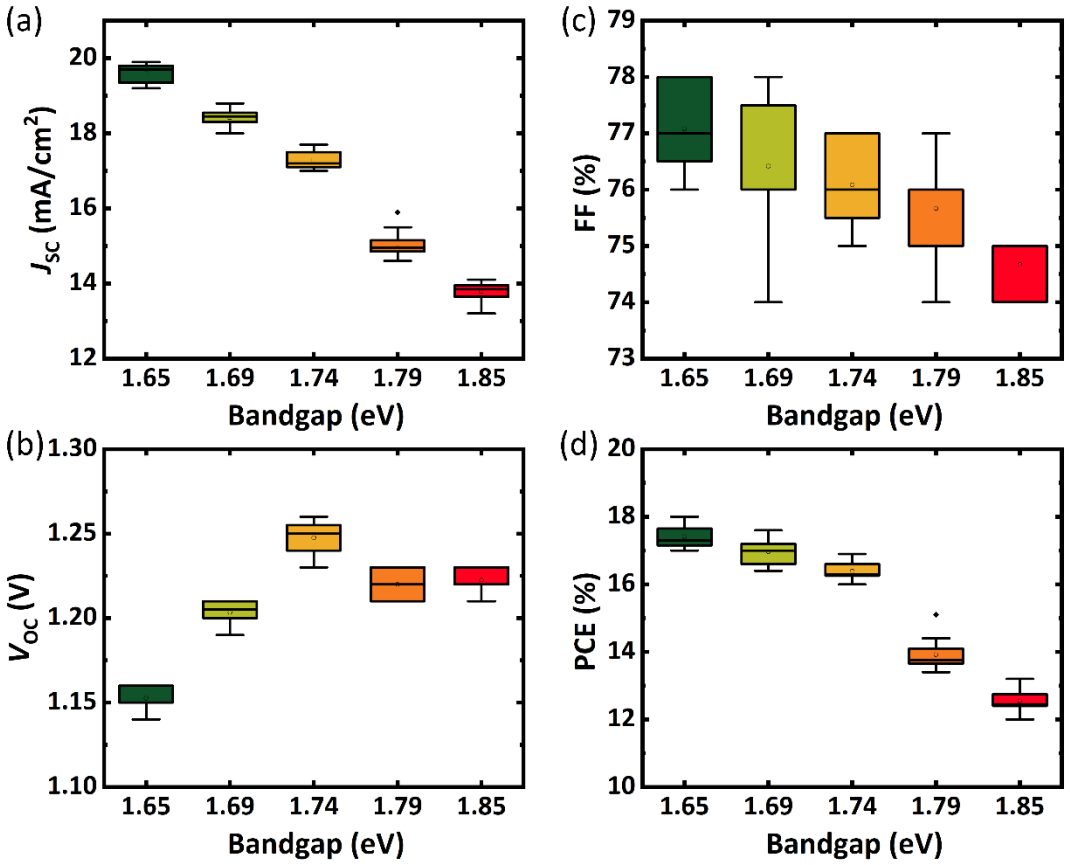

Fig. 6.10: Statistical analysis of the (a) short-circuit current density (J_{SC}), (b) open-circuit voltage (V_{OC}), (c) fill factor (FF) and (d) power conversion efficiency (PCE). Adapted with permission from reference [99], © John Wiley & Sons.

enhanced carrier trapping in the bromine-rich absorber layers.[22,23] Overall, a reduction in the stabilized PCE is observed for the s-PSCs compared to the o-PSCs (**Fig. 6.9**a). The stabilized PCE of the champion devices over a course of 5 minutes are 17.5%, 16.5%, 15.8%, 14.4%, and 12.1% for the bandgaps 1.65 eV, 1.69 eV, 1.74 eV, 1.79 eV and 1.85 eV, respectively. In order to obtain more insights in the stability of the fabricated s-PSCs, the effect of long-term exposures to constant light and bias on the devices is investigated. For a 1-hour exposure of AM 1.5G irradiation at a constant voltage near the MPP, the s-PSCs with bandgap up to 1.74 eV show no reduction in the normalized PCE (Fig. 6.9b). For E_g = 1.79 eV and 1.85 eV, the s-PSCs remain stable for up to 30 mins and then reduces to 96% and 94% of its initial value after 1 hour, respectively. This demonstrates that although the wider bandgap PSCs show short term stability (Fig. 6.10a), they are yet not stable for longer times. Therefore, further investigation is required to improve the stability of PSCs with bandgaps > 1.74 eV. For the E_g = 1.65 eV that depicted the highest PCE, the exposure time is further increased to 11 hours, which shows high stability in the power output (Fig. 6.9c). Further information regarding the statistical analysis of the various parameters

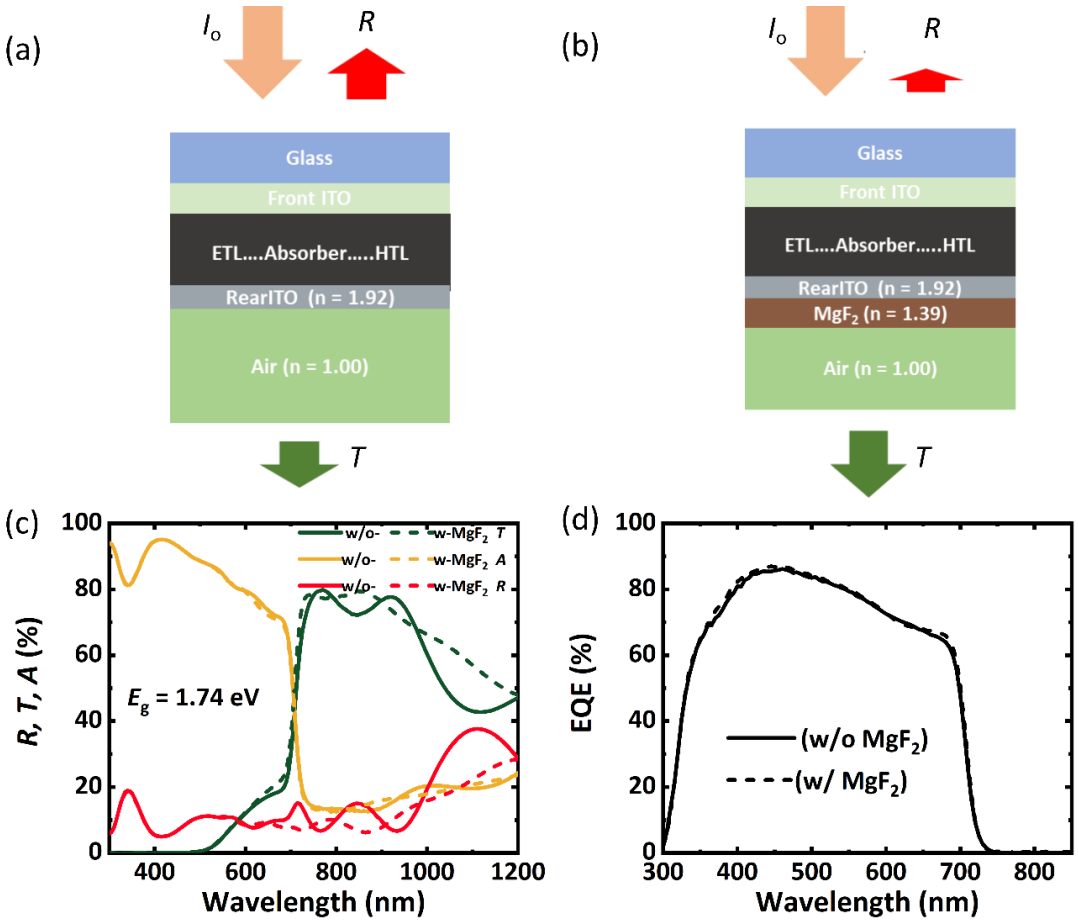

Fig. 6.11: Schematic illustration of the semitransparent perovskite solar cell (s-PSC) stack (a) without MgF_2 and (b) with MgF_2. (c) Reflectance (*R*), transmittance (*T*) and absorptance (*A*) spectra of the s-PSC stack. (d) External quantum efficiency (EQE) spectra of s-PSCs with and without MgF_2. Adapted with permission from reference [99], © John Wiley & Sons.

of the s-PSCs for all the bandgaps shown in **Fig. 6.10** demonstrates a consistent and highly reproducible process.

In order to fabricate 4T perovskite-based tandem devices, s-PSCs filters are fabricated with an area of 256 mm^2 that have exactly the same layer stack as the s-PSCs devices. An average transmittance (*T*) of >70% (up to ≈850 nm) is observed for energies below the respective bandgap of the perovskite absorber (Fig. 6.8b). This high transmittance is a direct consequence of the addition of MgF_2 as an anti-reflection coating in the layer stack (schematic illustration in **Fig. 6.11**a-b), which shows a remarkable enhancement compared to the layer stack without MgF_2 (Fig. 6.11c). The improved transmittance stems solely from a reduced reflectance (*R*) and decreased interference effects in the wavelength range 700-1200 nm. This is attributed to a gradual drop of the refractive index (refractive index of rear ITO/MgF_2/Air stack: 1.92/1.39/1.00) towards the air interface, instead of an abrupt jump as in the case of the ITO/Air interface. Furthermore, the addition of a MgF_2 layer does not affect the absorptance as it is barely affected both above and below the bandgap as shown in Fig. 6.11c. In order to prove whether this has an effect on the J_{SC} of the top s-PSC, EQE measurements are conducted before and after the deposition of MgF_2 (on another

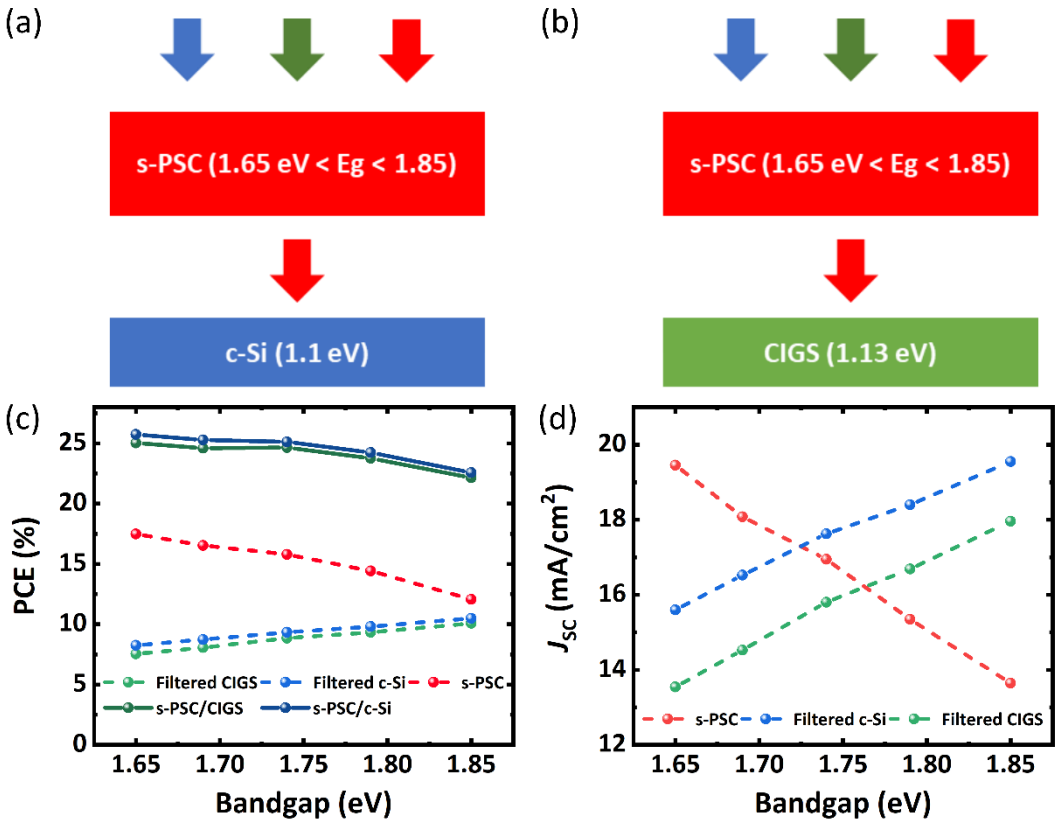

Fig. 6.12: Schematic illustration of four-terminal (a) perovskite/c-Si and (b) perovskite/CIGS tandem architecture with top semitransparent perovskite solar cells with various bandgaps. (c) Power conversion efficiency (PCE) of top s-PSC with 2D/3D heterostructure, filtered c-Si solar cells or CIGS solar cells and respective tandem architectures (calculated). Adapted with permission from reference [99], © John Wiley & Sons.

set of devices). Insignificant differences are observed in the EQE spectra with the integrated J_{SC} differing by only 0.15 mA/cm^2 (Fig. 6.11d).

In order to estimate the achievable 4T tandem solar cell PCE, the s-PSC filters are mechanically-stacked on highly efficient interdigitated back contact (IBC) c-Si (E_g ≈ 1.1 eV, PCE = 23.2%) or CIGS (E_g = 1.13 eV, PCE = 21.2%) solar cells, forming perovskite/c-Si and perovskite/CIGS tandem devices (schematic illustrations in **Fig. 6.12**a-b). For both c-Si solar cell and CIGS solar cells, a quasi-linear increase in the filtered stabilized PCE in observed (Fig. 6.12c). This is due to an increase in the photo-generated current as a higher number of photons is transmitted with increasing bandgap (Fig. 6.8 and Fig. 6.12d). Similar to the PCE, a quasi-linear increase in the J_{SC} from 15.5 mA/cm^2 up to 19.5 mA/cm^2 for the bottom c-Si solar cell is observed. By fitting the J_{SC} with a linear equation, an increase of ≈2 mA/cm^2 per 0.1 eV for both c-Si and CIGS bottom cells is noted. In the case of top s-PSCs, the decrease in the J_{SC} is rather large with a value of −2.86 mA/cm^2 per 0.1 eV. This shows that with increasing bandgap, the J_{SC} lost by the top s-PSC is not fully compensated by the bottom cells. This can to some extent be explained by parasitic absorption losses, arising mainly from the spiro-MeOTAD and the rear ITO, for increasing bandgap. Therefore, the overall PCE of the 4T tandem architecture, especially for wider bandgaps, is now limited

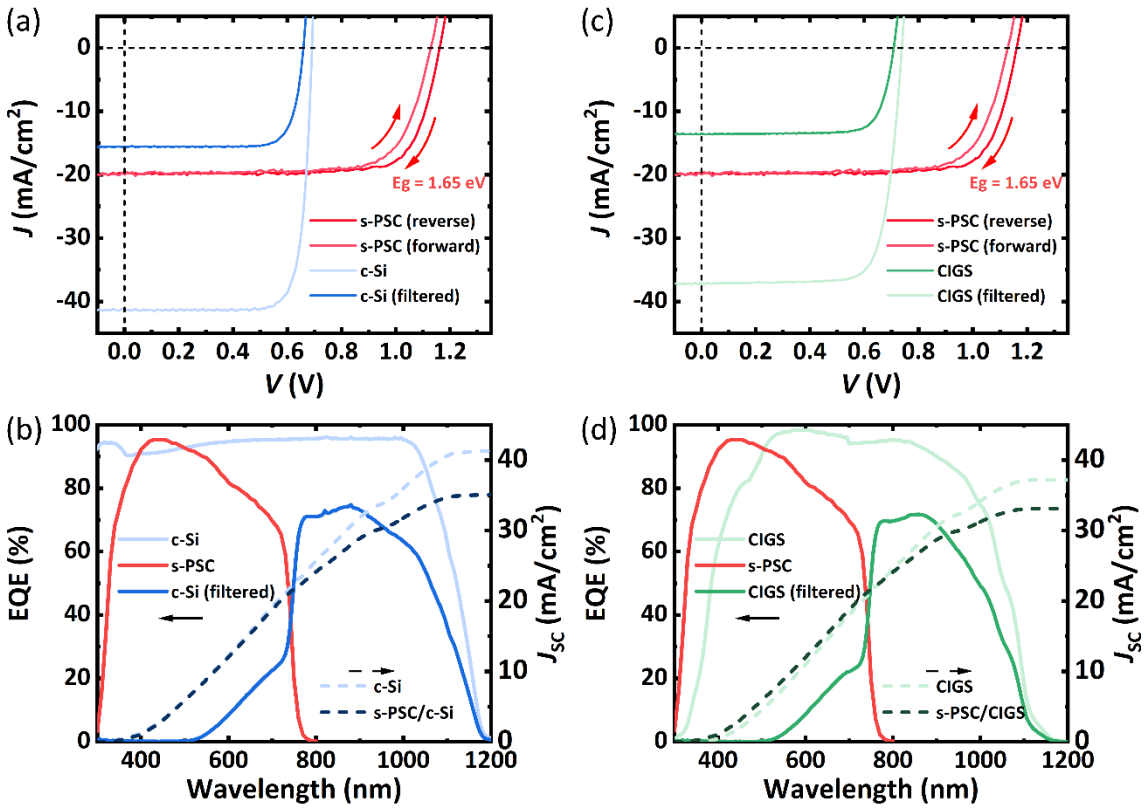

Fig. 6.13: The performance of the champion 4T tandem architectures. (a, b) Current density-voltage (*J–V*) characteristics and (c, d) external quantum efficiency (EQE) of semitransparent perovskite solar cells (s-PSCs) (Bandgap, E_g = 1.65 eV), standalone/filtered c-Si, and standalone/filtered CIGS solar cells. The integrated short-circuit current density (J_{SC}) of the standalone and the 4T tandem solar cells are also provided. Adapted with permission from reference [99], © John Wiley & Sons.

by additional parasitic losses in the top s-PSC along with the enhanced V_{OC} deficit due to an increased bromine-fraction as discussed previously. In contrast to these losses, the relatively small increase in the V_{OC} of ≈3-4 mV per 0.1 eV is observed for the filtered bottom cells, which is a consequence of the increased number of photons and the logarithmic dependency of the V_{OC} on the light intensity.

The maximum PCE obtained in the 4T configuration for perovskite/c-Si and perovskite/CIGS is 25.7% and 25.0% respectively, both with E_g = 1.65 eV for the top s-PSC (Fig. 6.12c). The smaller improvement in the case of CISG is due to its wider bandgap, which reduces the EQE and thus the J_{SC} (by ≈2 mA/cm^2). Up to E_g = 1.74 eV, the PCE of the tandem architectures is very comparable, with no particular trend. The comparable performance up to E_g = 1.74 eV is in line with detailed-balance calculations as well as energy yield modelling for the 4T architecture.[17,44,169,197–199] However, further increase in the bandgap to 1.85 eV results in the decrease of the overall PCE due to the decreased PCE of the top s-PSC in that bandgap region as discussed before. It is important to note here that a shift in the optimum towards lower bandgaps is found in real prototype devices compared to simulations. This means that it is highly important to improve the performance of top

s-PSCs for wider bandgap (1.74-1.85 eV) of the perovskite absorber to improve the overall tandem PCE. Overall, this study is the first detailed experimental examination of such simulations using efficient top s-PSCs with a wide range of bandgaps in combination with bottom c-Si and CIGS solar cells in a 4T tandem configuration.

The *J*–*V* characteristics as well as the EQE responses of the champion perovskite/c-Si and perovskite/CIGS 4T tandem architectures are shown in **Fig. 6.13**. The J_{SC} of the bottom c-Si and CIGS solar cells are reduced to 15.6 mA/cm^2 and 13.6 mA/cm^2, respectively due to the top s-PSC filter. The V_{OC} of the bottom cells is slightly decreased as a result of filtered light intensity. The maximum EQEs of the bottom c-Si and bottom CIGS solar cells are ≈70%, which is in line with the measured transmittance. This shows that if further improvement in the transmission is achieved, the EQE and hence the efficiency of the bottom solar cells in tandem configuration can be enhanced further, leading to an overall increase PCE of the perovskite-based tandem photovoltaics. **Table 6.2** summarizes all the results. In the next section, a strategy to reduce the parasitic absorption loss as well as the reflection loss is discussed.

Table 6.2: Photovoltaic parameters of the champion device configuration.

Solar cell architecture	Measurement protocol	J_{SC} (mA/cm^2)	V_{OC} (V)	FF (%)	PCE (%)	Stabilized PCE (%)
s-PSC (E_g = 1.65 eV)	RS	19.7	1.16	78.7	18.0	**17.5**
	FS	20.0	1.13	74.8	16.9	
c-Si solar cell	Stand-alone	41.4	0.69	81.2	23.2	23.2
	Filtered	15.6	0.66	80.2	8.2	**8.2**
4T perovskite/c-Si	RS	-	-	-	26.2	**25.7**
	FS	-	-	-	25.1	
CIGS	Stand-alone	37.2	0.74	77.0	21.2	21.2
	Filtered	13.6	0.71	78.1	7.5	**7.5**
4T perovskite/CIGS	RS	-	-	-	25.5	**25.0**
	FS	-	-	-	24.4	

6.2 Alternative transport conductive oxide electrodes

Low transmittance of top s-PSCs still limit the overall PCE in a tandem architecture. In Fig. 6.11, it is seen that the s-PSC layer stack transmits only ≈70% of light between 730-850 nm and then decreases to ≈50% at 1200 nm. This decrease in the transmittance is a result of: (i) parasitic absorptions within the layer stack, and (ii) reflections at the various interfaces. The latter are discussed in chapter 2, **Fig. 2.12**. The parasitic absorption losses primarily originate from the front and the rear ITO in this layer stack. In this section, alternative materials are proposed for both front and rear TCO to reduce these optical

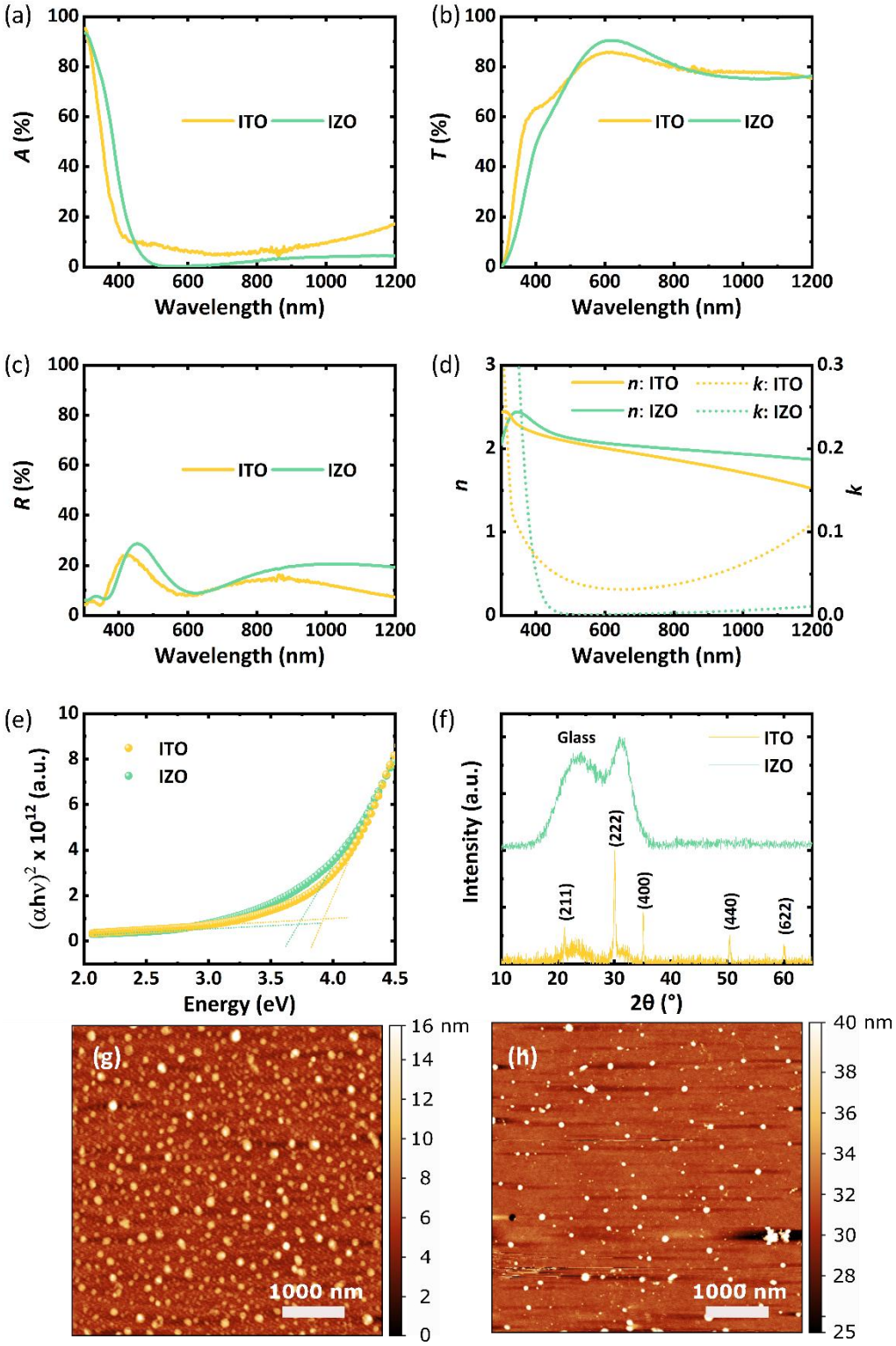

Fig. 6.14: (a) Absorptance (*A*), (b) transmittance (*T*), (c) reflectance (*R*), (d) refractive index (*n*) and extinction coefficient (k), (e) the Tauc plot, and (f) x-ray diffraction of rear ITO and IZO. (g) and (h) shows the atomic force microscopy images of rear ITO and IZO, respectively.

losses and enhance the PCE in tandem architecture. To obtain insights about these TCO electrodes, they are characterized by atomic force microscopy (AFM), XRD, spectrophotometry, four-point probe measurements and hall-effect measurements.

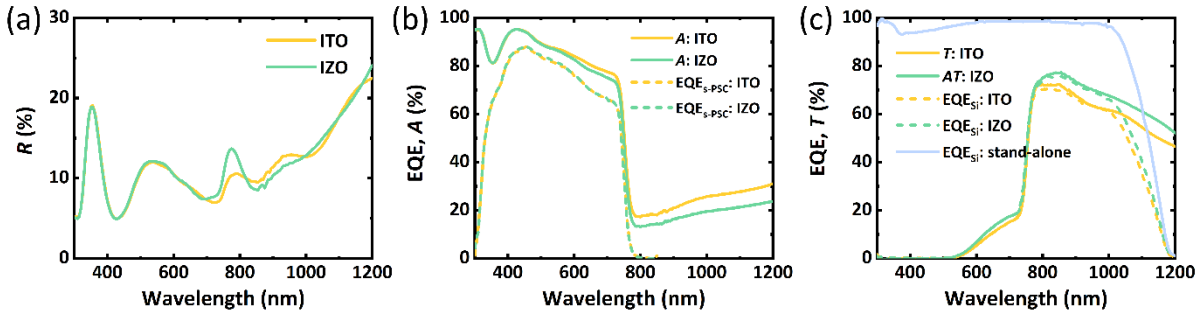

Fig. 6.15: (a) Reflectance (*R*), (b) transmittance (*T*) and (c) absorptance (*A*) of the s-PSC filters fabricated with rear ITO or IZO. The external quantum efficiencies (EQEs) of the top s-PSC and bottom c-Si solar cell are also provided in (b) and (c), respectively.

6.2.1 Rear TCOs for semitransparent perovskite solar cells

In order to reduce the absorption losses, a rear IZO electrode is developed. Details regarding the deposition parameters are discussed in chapter 3. Spectrophotometric measurements conducted on glass/TCO/air show a decrease in the absorptance of rear IZO compared to ITO (5% absolute, see **Fig. 6.14**a, **Table 6.3**). This can be explained by the significantly reduced extinction coefficient of the IZO in comparison to the ITO (Fig. 6.14d). Notably, the absorptance is also decreased between 300-800 nm by 3.8% absolute. Furthermore, a small reduction in the transmittance is also observed for the IZO in the near infrared regime (**Fig. 6.14**b). This is due to the increase in reflectance at the IZO/air interface, originating from the increased refractive index of the IZO (Fig. 6.14d). Since s-PSC stack would either have an anti-reflection layer on the rear TCO or an index-matching layer between the rear TCO of the s-PSC and the bottom cell in a 4T architecture, the increased reflection loss observed here is not a major concern. Electrically, the rear IZO has a higher sheet resistance than the ITO (R_{sh} ≈60 Ω/sq for IZO and R_{sh} ≈50 Ω/sq for ITO). In order to compensate for the higher sheet resistances, gold grids are deposited on the rear TCO to further increase the lateral conductivity (chapter 3, **Fig. 3.3**).[99] Therefore, the increased sheet resistance with the IZO should not affect the device performance considerably. Furthermore, the lower bandgap of the IZO, which is evident from the Tauc plot (Fig. 6.14e), should not affect the performance of the s-PSCs as the photons in the ultra-violet and visible wavelengths are absorbed by the perovskite layer before they reach the rear electrode. XRD measurements are also performed to determine the crystallinity of the TCOs. The results show that the rear IZO is amorphous, whereas the ITO is crystalline in nature (Fig. 6.14f). Details regarding the crystallinity of the ITO are discussed in section 6.2.2. AFM images in Fig. 6.14g-h show that both ITO and IZO have similar surface properties with roughness of ≈2 nm. However, some “particle-like” features are present on the surface of both materials. For ITO, these features are more prominent and approximately 10-12 nm in height, while for the IZO, these are slightly taller and ≈15-20 nm

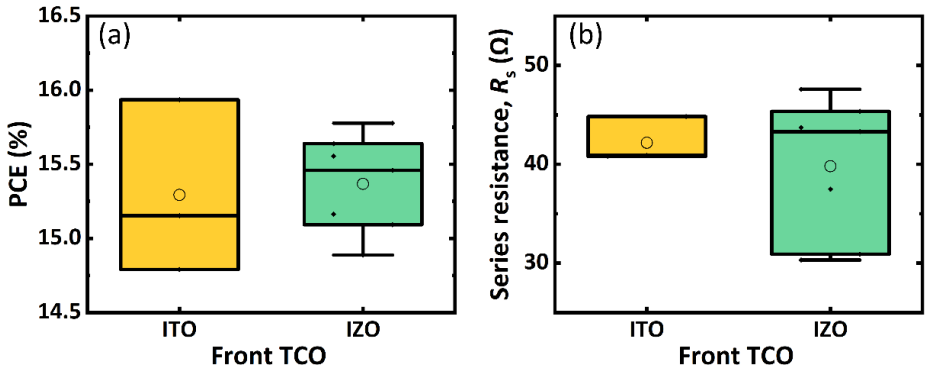

Fig. 6.16: Statistical analysis of (a) power conversion efficiency (PCE) and (b) series resistance R_s derived from the current density-voltage characteristic curve of s-PSCs fabricated with rear ITO and IZO.

in height. The important optical parameters such as bandgap, surface roughness and layer thickness of the ITO and IZO are summarized in Table 6.3.

Table 6.3: Optical bandgap (E_g), layer thickness d, surface roughness (S_{rms}) and optical parameters of the rear ITO and IZO.

TCO	E_g (eV)	d (nm)	S_{rms} (nm)	R (%)		T (%)		A (%)	
				300-800 (nm)	800-1200 (nm)	300-800 (nm)	800-1200 (nm)	300-800 (nm)	800-1200 (nm)
ITO	3.93	160	1.8	12.9	12.4	79.6	77.6	9.6	8.8
IZO	3.72	165	2.0	15.1	19.7	79.2	76.7	5.8	3.8

In order to investigate the optical properties and device performance in a full device-stack, s-PSCs are fabricated with the following layer stack: glass/ITO/np-SnO_2/perovskite/Spiro-OMeTAD/(**ITO or IZO**)/MgF_2. In **Fig. 6.15**a-c the reflectance, transmittance and absorptance spectra of the s-PSC filters is shown. Replacing the ITO with IZO leads to a relative enhancement of 8.9% in the transmittance in the near infrared wavelengths, which is due to the reduction in the parasitic absorption losses. As expected, the reflectance spectra do not show any significant difference for the layer stacks as both are employed with an anti-reflection coating of MgF_2 at the rear side. EQE measurements conducted on both architectures yield similar values with an integrated J_{SC} of ≈18.3 mA/cm^2. However, a small difference exists in the absorptance spectra between 550-780 nm, which could be attributed to the higher parasitic absorption of the rear ITO compared to the rear IZO. Statistical analysis of the PCE shows comparable performance of s-PSCs using both ITO and IZO (**Fig. 6.16**a). The series resistances (R_s) obtained from the *J-V* characteristic are also similar, demonstrating again the comparable electrical properties of both TCOs after the addition of the gold grid (Fig. 6.16b). Next to the performance of the top s-PSC, the 4T tandem architecture is evaluated by mechanically-stacking s-PSC filters on top of a c-Si IBC cell. EQE measurements are conducted in order to extract the photocurrent generated by both configurations. As depicted in Fig. 6.15c, the filtered EQE of the c-Si solar cell is

enhanced in the case of IZO, leading to an increase in the integrated J_{SC} by 1.1 mA/cm^2 (enhancement of 7.7% relative). Overall, these results demonstrate that a rear IZO is a better alternative to a rear ITO for 4T perovskite-based tandem solar cells.

6.2.2 Front TCOs for semitransparent perovskite solar cells

Another important factor to achieve high transmission and reduced reflection losses in a s-PSC layer stack is to utilize a front TCO electrode having high refractive index along with low extinction coefficient in the near infrared wavelengths. In the case of ITO, one strategy would be to employ higher amount of oxygen during the sputtering process.[132,200] This fills

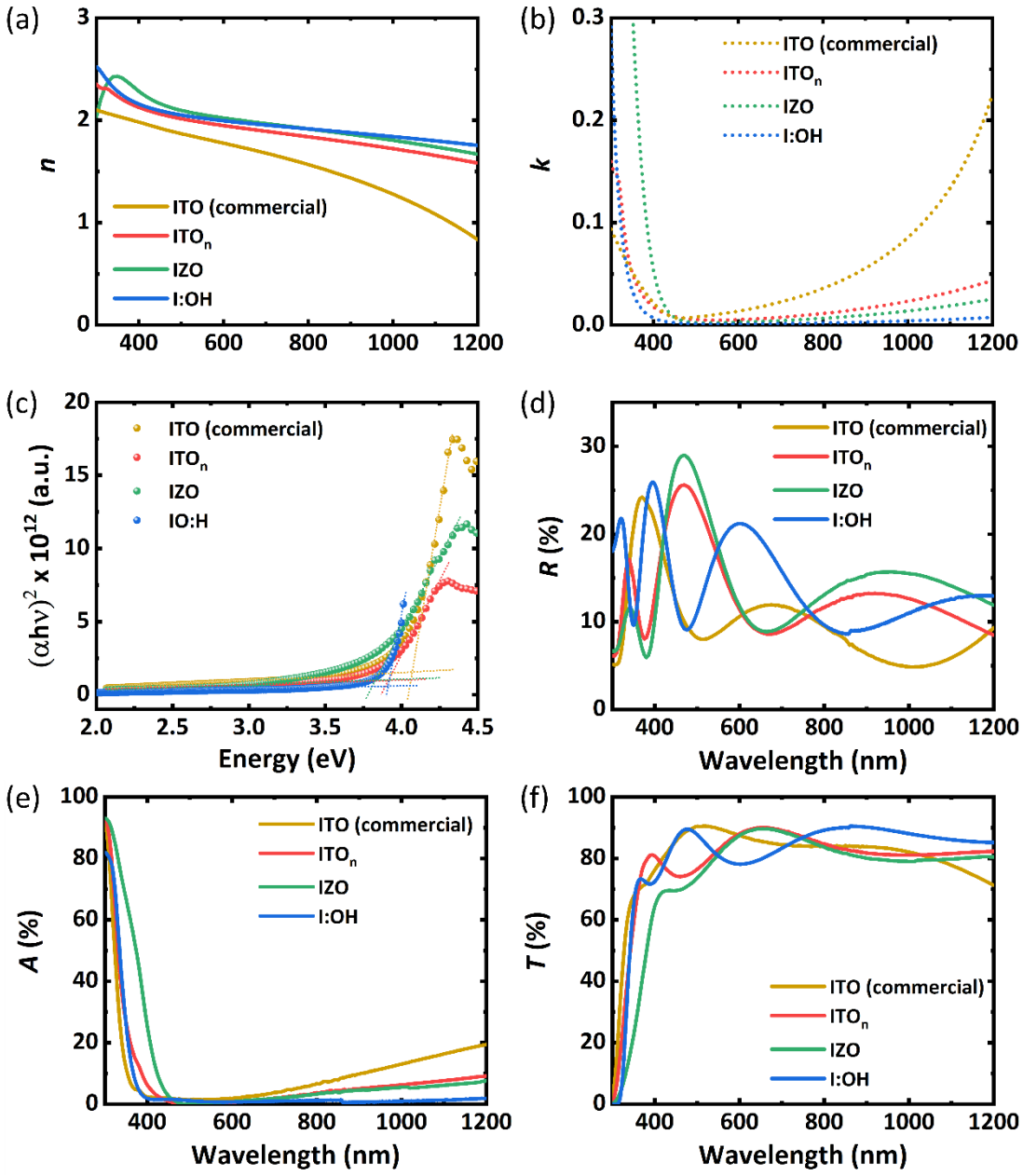

Fig. 6.17: (a) Reflectance (*R*), (b) transmittance (*T*) and (c) absorptance (*A*), (d) refractive index (*n*), (e) extinction coefficient (*k*) and the Tauc plot of the commercial ITO, ITO with 12.5% O_2 (ITO_n) and IZO.

up the oxygen vacancies and decreases the number of free charge carriers in ITO, which leads to a shift in the plasma frequency of the ITO towards longer wavelengths. However, the consequence of this is the increased sheet resistance, which must be compensated by increasing the thickness of the ITO. In this work, 12.5% O_2 content (much higher than the standard process of 3.5% for the conventional front ITO_v in our laboratory) is used to prepare the front ITO and labelled as ITO_n. Along with ITO_n, other materials are investigated that includes IZO or hydrogen-doped indium oxide (IO:H) as front TCO electrodes. Here, an in-house front IZO is developed, while the IO:H is obtained from the collaborator Zentrum für Sonnenenergie und Wasserstoff-Forschung Baden-Württemberg (ZSW). All the above TCO electrodes are compared to a commercial ITO (similar to the front ITO as discussed in section 6.1, also see **Appendix Fig. A. 6.2** and **Fig. A. 6.3** for comparison), conventionally used to fabricate highly efficient o-PSCs. Further information regarding the deposition parameters of ITO_n, IZO and IO:H can be found in the chapter 3.

In the following, the optical and electrical properties of the available front TCO electrodes are analyzed. Ellipsomentric measurements reveal an increase in the refractive indices for ITO_n, IZO and IO:H electrodes compared to commercial ITO (**Fig. 6.17**a), especially in the near infrared wavelengths. At the same time, the extinction coefficients in the near infrared wavelengths for these TCO electrodes are reduced (Fig. 6.17b). The decrease in the extinction coefficient can be attributed to the reduction in the charge carrier concentration (evaluated from Hall-effect measurements) by 1 order of magnitude compared to the commercial ITO as shown in **Table 6.4**. Furthermore, spectrophotometric measurements conducted on these TCOs on glass reveal an increased loss in reflections (Fig. 6.17d), which is apparent due to the higher values in refractive indices. The absorptance of these new TCO electrodes is reduced (Fig. 6.17e), which is also in line with the obtained extinction coefficients. As discussed earlier, an increase in the thickness is required to compensate for the reduced free charge carriers in the new TCO electrodes. Therefore, ITO_n, IZO and IO:H are deposited with thicknesses of 170 nm, 165 nm and 230 nm, respectively. Due to this, a shift in the maximum of the interferences is noted both in transmittance and reflectance spectra for all the TCO electrodes. To investigate the bandgaps of these TCO electrodes, Tauc plots are analyzed. **Fig. 6.17**c shows both ITO_n and IO:H have bandgaps (≥ 3.90 eV), which is highly important to reduce any parasitic absorptions in short wavelength ranges. In contrast, IZO has a smaller bandgap of 3.83 eV, which can potentially reduce photocurrents in top s-PSCs. In terms of electrical properties, all the new TCO electrodes have low sheet resistances of ≈24 Ω/sq, however, they are still slightly higher than the commercial ITO (≈15 Ω/sq). Hall-effect measurements reveal that the mobility of the charge carriers in ITO_n is similar to that of commercial ITO. Therefore, for ITO_n, the reduction in the carrier concentration is compensated mostly by the increased thickness to maintain a low sheet resistance. In the case of IZO and IO:H, a significant increase in the mobility is noted as shown in **Table 6.4**. Therefore, for these two TCOs, both improved mobility and thicker layers played a role in maintaining low sheet resistances.

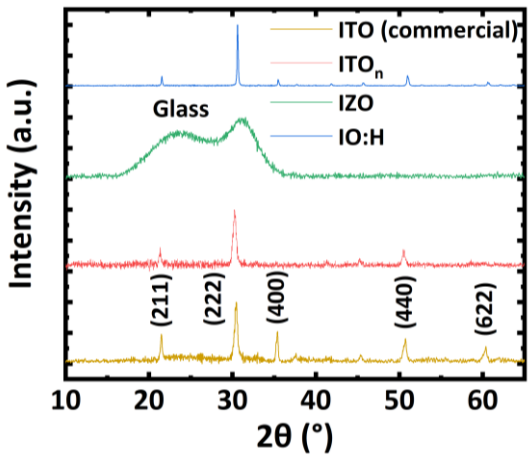

Fig. 6.18: X-ray diffraction (XRD) pattern of the front transparent conductive oxide electrodes: commercial ITO, ITO with 12.5% O_2 (ITO_n) and IZO.

Table 6.4: Layer thickness (d), surface roughness (S_{rms}), bandgap (E_g), sheet resistance (R_{sh}) charge carrier mobility (μ) and charge carrier concentration (n_c) of the front transparent conductive oxide electrodes.

TCO	d (nm)	S_{rms} (nm)	E_g (eV)	R_{sh} (Ω/sq)	μ (cm^2/ V s)	n_c (cm^{-3})
ITO (commercial)	140	4.1	4.05	15	35.1±3.90	$1.05x10^{21}$
ITO_n	170	2.1	3.92	24	36.5±6.30	$0.39x10^{21}$
IZO	165	5.5	3.83	25	47.9±7.60	$0.29x10^{21}$
IO:H	230	1.1	3.91	23	85.8±1.20	$0.17x10^{21}$

In order to investigate the crystallinity of the deposited TCOs, XRD measurements are performed (**Fig. 6.18**). Similar to the rear IZO, the front IZO is also amorphous. The relatively broad peak observed in the XRD pattern originates from the glass substrate. It is also noted that the ITOs (front and rear) and IO:H are crystalline in nature, and the crystal planes are orientated preferentially along the (222) plane. In order to obtain more insights about the crystallite size, the following Debye-Scherrer equation:[201,202]

$$D = \frac{K\lambda}{\beta cos\theta} \tag{6.1}$$

is used, where D is the crystallite size, K is the shape constant (0.9), β and θ are the full width at half maximum and the Bragg's angle (in radians) of the observed peak, respectively. **Table 6.5** summarizes the crystallite sizes for each of the planes. In general, the crystallite sizes along the <222> plane for the front ITOs are smaller than the rear ITO. Compared to the rear ITO that is processed at room temperature, the reduction of the crystallite size for the front ITO_n could be associated to a modification of the nucleation kinetics at higher processing temperature (300 °C).[203] Furthermore, a small shift (0.2°-0.3°)

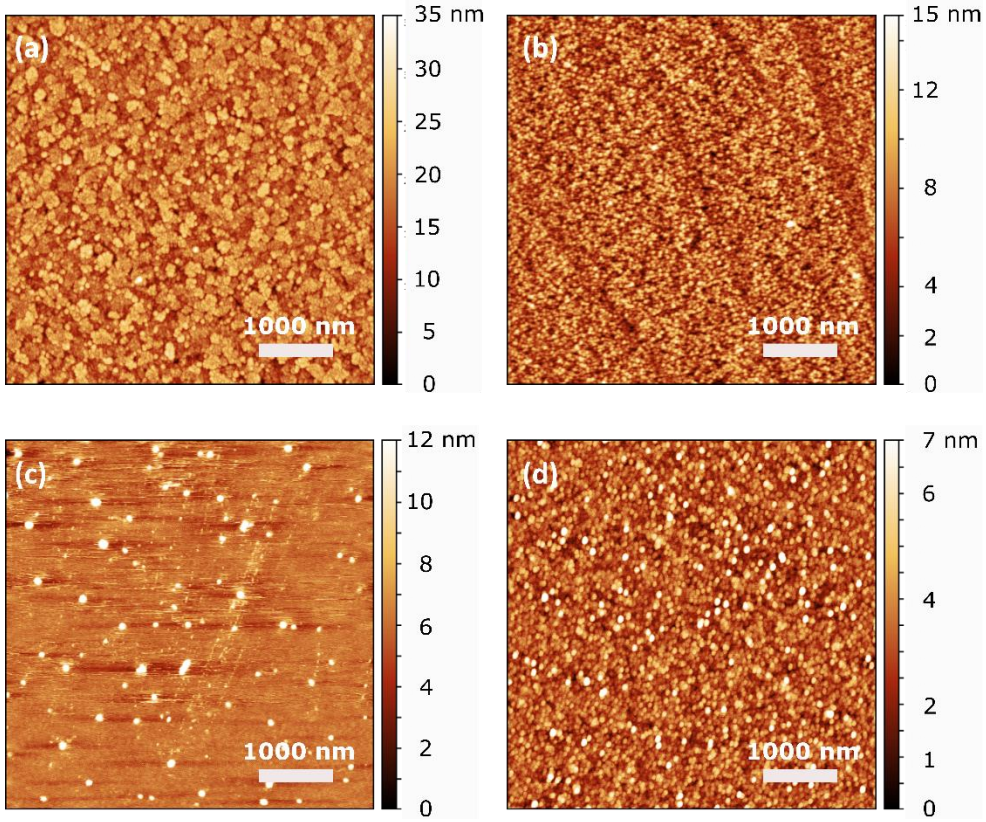

Fig. 6.19: Atomic force microscopy (AFM) images of the commercial (a) ITO, (b) ITO_n (c) IZO and (d) IO:H electrodes.

towards the shorter angles is observed for all XRD peaks for the front ITOs compared to that of the rear ITO. This is an indication that comparatively more Sn^{4+} ions, which are smaller in size (0.71 Å) have replaced the indium (0.80 Å) sites, thus reducing the crystallite size. Interestingly, the orientation of ITO_n along the <400> plane is not observed in the XRD pattern. This indicates that the O_2 vacancies, which usually reside in this plane, are significantly reduced or not present.[204] This is line with the previous observations of slightly higher sheet resistance and increased refractive index of the ITO_n. Comparing commercial ITO and ITO_n with IO:H, considerably sharper reflection peaks with reduced full-width half maxima (FWHM) are noticed. This indicates very high crystallinity of IO:H. This high crystallinity could be associated to the post thermal treatment, which crystallizes the amorphous IO:H deposited at the time of sputtering.[36] Due to this high crystallinity, the crystallite size is also increased. This is an indication that the number of the grain boundaries in IO:H could be reduced compared to the ITOs, resulting in high mobility of the charge carriers.

AFM measurements conducted on the TCOs show that the developed ITO_n is more compact than the commercial front ITO (**Fig. 6.19**). The surface roughness for the all the TCOs is below 6 nm. Interestingly, the IO:H depicts a surface roughness of only ≈1.1 nm. Furthermore, similar to the rear TCOs, the front IZO also shows small features, which are distributed all over the substrates. In order to further investigate the performance of TCOs in tandem architectures, in the next section, an in-depth discussion is presented comparing their photovoltaic performance.

Table 6.5: Analysis of the x-ray diffraction (XRD) spectra of the transparent conductive oxide (TCO) electrodes.

TCO	Plane (*hlk*)	2θ (°)	FWHM (°)	Crystallite size, *D* (nm)
ITO (commercial)	211	21.5	0.257	31.46
	222	30.4	0.439	18.75
	400	35.4	0.264	31.58
	440	50.7	0.473	18.58
	622	60.3	0.484	18.98
ITO_n	211	21.3	0.285	28.36
	222	30.3	0.476	17.29
	400	-	-	-
	440	50.5	0.452	19.4
	622	-	-	-
Rear ITO	211	21.2	0.251	32.20
	222	30.1	0.310	26.53
	400	35.2	0.168	49.60
	440	50.5	0.324	27.11
	622	60.1	0.345	26.60
IO:H	211	21.5	0.158	51.17
	222	30.6	0.172	47.88
	400	35.5	0.175	47.66
	440	51.0	0.273	32.24
	622	60.7	0.290	31.74

6.3 Photovoltaic characteristics of perovskite solar cells with various TCOs

The improved optical properties of the TCOs lead to an enhanced photovoltaic performance of the perovskite/c-Si tandem solar cells. In order to demonstrate this, s-PSCs are fabricated in the following layer stack: glass/(**Commercial ITO** or **ITO_n** or **IZO** or **IO:H**/np-SnO_2/perovskite/Spiro-OMeTAD/MoO_X/IZO/MgF_2. As the absorber, a triple cation ($Cs_{0.1}(MA_{0.17}FA_{0.83})_{0.9}Pb(I_{0.83}Br_{0.17})_3$) perovskite is deposited. A rear IZO is used

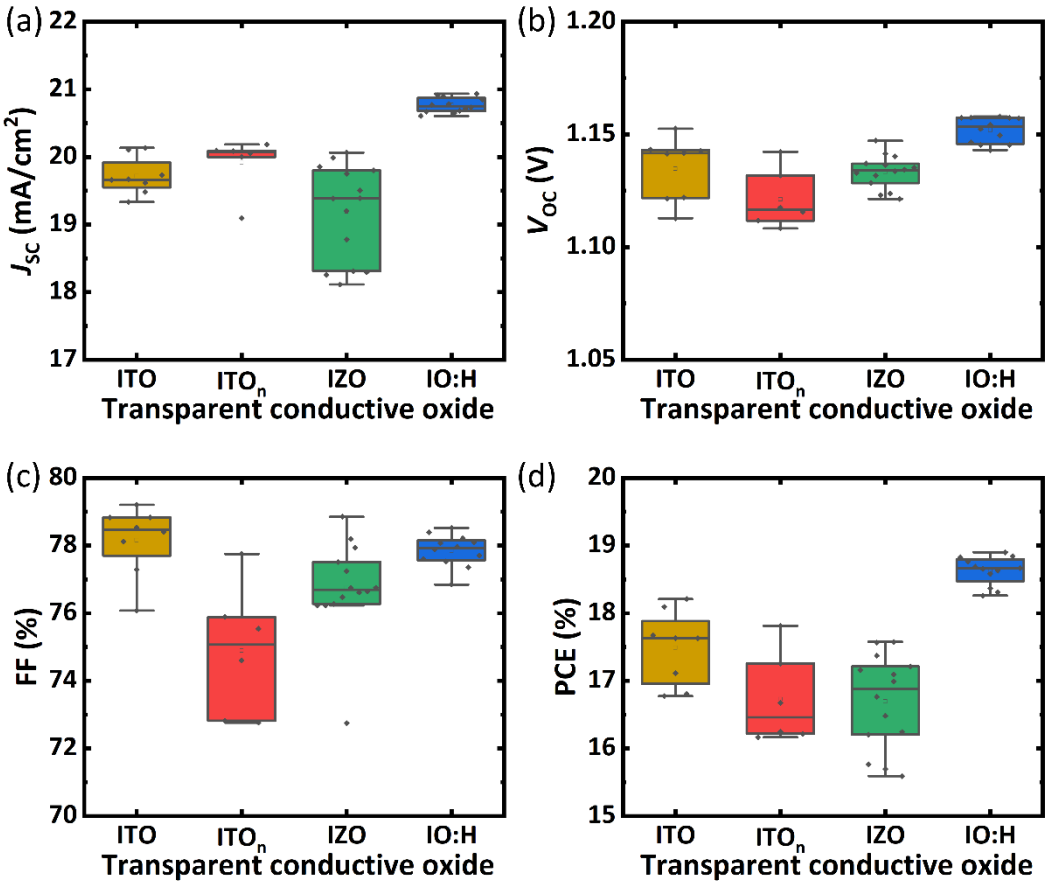

Fig. 6.20: Statistical analysis of the (a) short-circuit current density (J_{SC}), (b) open-circuit voltage (V_{OC}), (c) fill factor (FF) and (d) power conversion efficiency (PCE) of the semitransparent perovskite solar cells (s-PSCs) for different transparent conductive oxide electrodes.

instead of ITO to maximize the transmission of the s-PSCs as discussed before. In **Fig. 6.20**, a statistical analysis of various photovoltaic characteristics is presented. Notably, having IO:H as the front TCO in the s-PSC layer stack shows a significantly higher PCE compared to all other TCO electrodes. The improved average PCE of >18.5% is due to an enhanced J_{SC} and V_{OC}. A discussion on the improvement in the J_{SC} is described later. The enhancement in the V_{OC} could be due to the presence of a smoother surface[2,205] and larger crystallites of the IO:H, leading to a more homogenous np-SnO_2 ETL and thus possibly reducing non-radiative recombination losses. However, further experiments are necessary to explain and understand this effect, which is currently beyond the scope of this thesis. With ITO_n and IZO as the front electrode, slightly lower average PCEs of ≈16.5% and ≈17.0% is noted. The reduced PCE with these TCOs is due to a smaller V_{OC} and lower FF. One of the reasons for the reduced FF with ITO_n and IZO electrodes could be the higher sheet resistance. Surprisingly, ITO_n demonstrates the lowest FF even though the sheet resistance of ITO_n and IZO are similar. One possible cause could be the previously discussed particle-like features

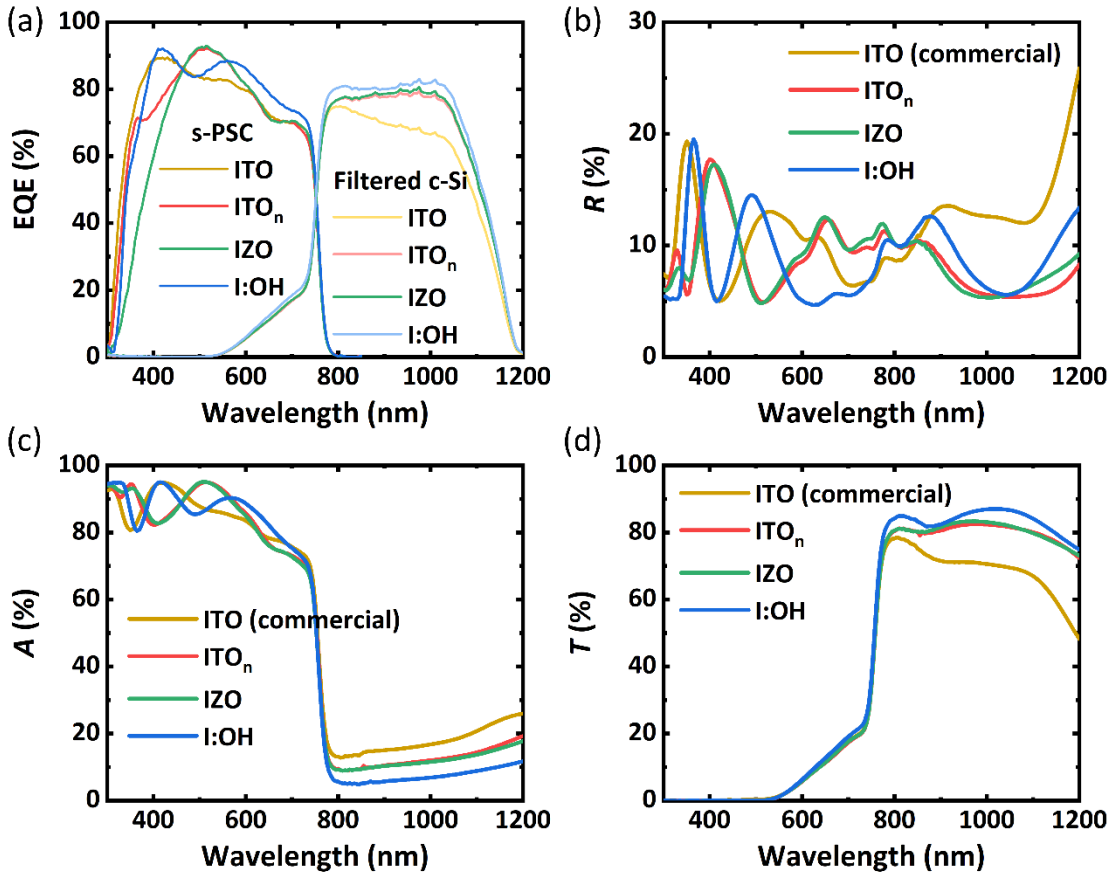

Fig. 6.21: (a) External quantum efficiency (EQE) of the top semitransparent perovskite solar cells (s-PSCs) and filtered bottom crystalline-silicon (c-Si) solar cells for different transparent conductive oxide electrodes. (b) Reflectance (*R*), (c) absorptance (*A*) and (d) transmittance (*T*) spectra of the s-PSC filters for different transparent conductive oxide electrodes.

as shown in the AFM images (Fig. 6.19) that may lead to shunting paths in these devices. However, detailed experimental investigation is necessary in this context.

In terms of J_{SC}, s-PSCs with IO:H demonstrate the highest photocurrents. To comprehend the differences in the J_{SC} between these devices, EQE measurements are conducted (**Fig. 6.21**a). For IO:H, a broadband enhancement is observed from 500 nm up to the bandgap of the perovskite. This improvement can be ascribed to the reduced reflections as shown Fig. 6.21b. Compared to the commercial ITO, a shift in the peak of the EQE spectra is noted for all the TCO electrodes. This is also in line with the absorptance spectra of the s-PSCs (Fig. 6.21c) and it arises due to the difference in the thickness of these TCO electrodes as mentioned before. Interestingly, for ITO_n and IZO, this shift results in a better matching of the EQE maximum to the AM 1.5G irradiation spectra maximum. As a result, a slightly improved J_{SC} is obtained with ITO_n. In case of IZO, the apparent lower average J_{SC} is associated to the smaller bandgap of the IZO, which is noticeable in the EQE spectrum.

The *J-V* characteristics of the champion devices with different TCO electrodes are presented in **Fig. 6.22**. The results show that all devices exhibit hysteresis, however, the

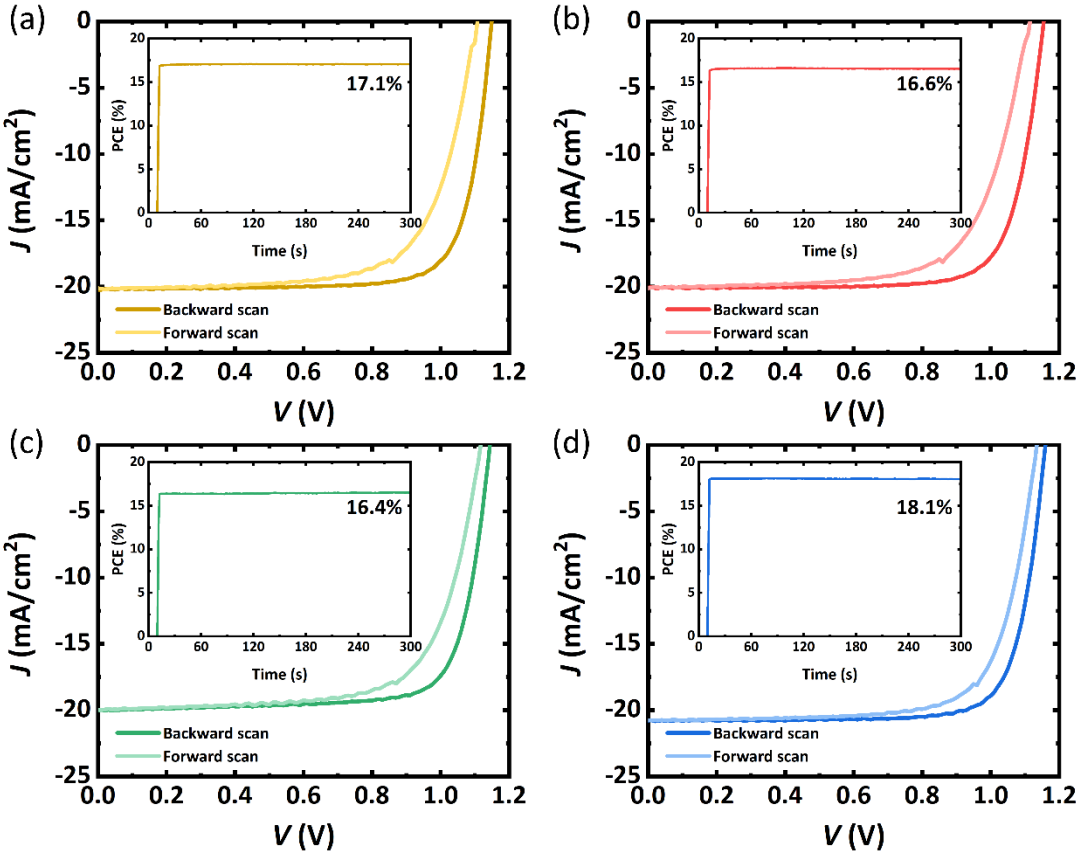

Fig. 6.22: Current density-voltage (*J–V*) characteristics of the champion top semitransparent perovskite solar cells (s-PSCs) fabricated with (a) ITO, (b) ITO_n, (c) IZO and (d) IO:H. The inset corresponds to the stabilized power conversion efficiency (PCE) measured at constant voltages near the maximum power point.

smallest is observed for IO:H. In order to obtain the PCE at MPP, the s-PSCs are measured for 5 minutes under light and at constant voltage near the MPP. Consistent to the *J-V* characteristics discussed earlier, the s-PSCs with IO:H exhibit the highest PCE of 18.1%. s-PSCs fabricated with all the TCOs show no sign of degradation within this short period of time. Further details regarding the photovoltaic parameters for these TCO electrodes can be found in **Table 6.6**.

Before investigating the performance of the 4T perovskite/c-Si tandem solar cell with these TCO electrodes, the transmittance of the s-PSCs is analyzed (Fig. 6.21d). Compared to the commercial ITO, a significantly enhanced transmittance in the near infrared wavelengths is observed for the in-house sputtered TCO electrodes. For IO:H, which already demonstrated to be the better TCO among the four in top s-PSC configuration, the highest transmittance of >85% is also noted for this TCO. The improved transmittance is a result of both reduced reflections and parasitic absorptions as shown in Fig. 6.21b-c. While the reflection losses are reduced as these TCOs have high refractive indices compared to commercial ITO, the parasitic absorptions are reduced due to a reduced number of charge carriers.

The PCE of the champion top and bottom cells in 4T perovskite/c-Si tandem configuration is shown in **Fig. 6.23**. Compared to commercial ITO, an absolute improvement of ≈1% is realized for bottom c-Si solar cell ITO_n and IZO, while a remarkable enhancement of 1.4% is noted for IO:H. This leads to a stabilized PCE of 27.3% for with IO:H as the front TCO electrode, which is 2.4% absolute higher than the commercial ITO. Thus, these results clearly show the importance of utilizing a front TCO that enables reduced optical and electrical losses for enhancing the PCE in tandem devices. Further details regarding the photovoltaic parameters can be found in Table 6.6.

Table 6.6: Photovoltaic parameters of the champion top semitransparent perovskite solar cells, filtered bottom crystalline-silicon solar cell and four-terminal (4T) tandem performance.

TCO	**Measurement protocol**	J_{SC} **(mA/cm²)**	V_{OC} **(V)**	**FF (%)**	**PCE (%)**	**Stabilized PCE (%)**
ITO (commercial)	RS	20.2	1.15	78.2	18.2	**17.1**
	FS	20.1	1.11	70.0	15.6	
	Filtered	15.0	0.66	79.6	7.8	
	4T perovskite/c-Si	-	-	-	-	**24.9**
ITO_n	RS	20.0	1.15	77.5	17.9	**16.6**
	FS	20.1	1.11	69.6	15.6	
	Filtered	16.5	0.66	79.9	8.7	
	4T perovskite/c-Si	-	-	-	-	**25.3**
IZO	RS	19.9	1.14	77.1	17.6	**16.4**
	FS	19.9	1.11	70.2	15.7	
	Filtered	16.7	0.66	80.0	8.8	
	4T perovskite/c-Si	-	-	-	-	**25.2**
IO:H	s-PSC RS	20.6	1.16	78.4	18.8	**18.1**
	s-PSC FS	20.6	1.14	74.8	17.5	
	Filtered	17.4	0.66	78.9	9.2	
	4T perovskite/c-Si	-	-	-	-	**27.3**

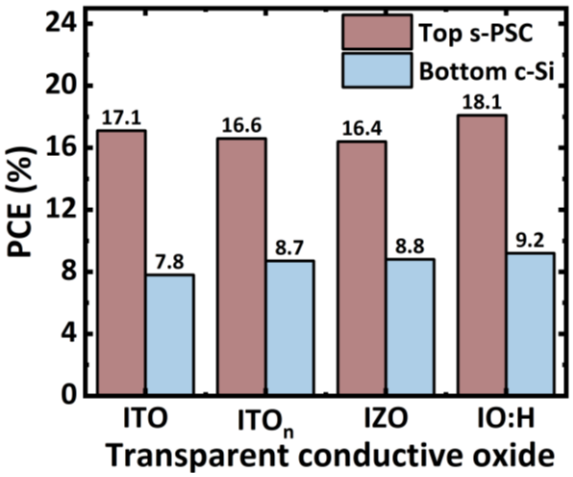

Fig. 6.23: Stabilized power conversion efficiency (PCE) of the top of the top semitransparent perovskite solar cells (s-PSCs) and filtered bottom crystalline-silicon (c-Si) solar cells for different transparent conductive oxide electrodes.

6.4 Discussions and conclusion

In this chapter, s-PSCs for 4T tandem architectures are fabricated and optimized for improved photovoltaic performance. Here, two critical aspects are discussed in detail for improving the overall performance of the tandem devices: (i) what is the optimal bandgap of the top s-PSC absorber for maximizing the PCE, and (ii) what alternative TCOs can be used to suppress parasitic absorptions and reflection losses associated with the TCOs?

In order to maximize the PCE of a tandem solar cell, the optimum bandgap of the top s-PSC must be realized. Detailed balanced calculations show that an optimum bandgap between 1.60-1.85 eV should maximize the PCE in a 4T tandem architecture.[17,18] Although by tuning the composition of the perovskite absorber, the above-mentioned bandgaps can be obtained, however, wider bandgaps with perovskite absorbers above 1.75 eV often leads to increased non-radiative recombination losses.[19,26] These losses are not taken into consideration in detailed-balance calculations and thus, the optimum bandgap in experiments could be different from that of the simulations. Therefore, a detailed experimental investigation for the optimum bandgap of the perovskite absorber in the top s-PSC becomes a prerequisite. So far, there has been only one study where an experimental investigation was carried out, however, detailed analysis was missing. In this study, for the first time, a detailed experimental examination of the influence of the perovskite bandgap on the PCE of 4T tandem solar cells using both c-Si and CIGS solar cells is demonstrated. The results show that the exact bandgap is not very critical for obtaining high efficiencies in this configuration up to bandgaps (1.74 eV). Further increase in the bandgap led to poorer PCEs in the tandem devices, which is ascribed to increased non-radiative recombination losses. As a result, the optimum bandgap of the top perovskite absorber shifts to smaller energies. In this thesis, stabilized PCEs are of 25.7% and 25.0% are achieved for the champion 4T perovskite/c-Si and perovskite/CIGS tandem solar cells for E_g = 1.65 eV. One key aspect that needs to be considered as well is to suppress non-

radiative recombination losses in the bulk or at the interfaces of the perovskite layer. For this, here a 2D/3D perovskite heterostructure is employed by spin-coating *n*-butylammonium bromide on top of the perovskite absorber, which reduces non-radiative recombination losses at the perovskite/HTL interface, and the fabricated devices exhibit an enhanced V_{OC} of around 45 mV.

In the second part of this chapter, the influence of the front and the rear TCO electrodes on the performance of 4T perovskite/c-Si tandem solar cells is investigated. While the rear ITO shows significant parasitic absorption losses, the front commercial ITO, which is widely used to fabricate highly efficient opaque PSCs, incurs significant parasitic and reflection losses in the near infrared wavelengths. These losses affect the PCE in the bottom solar cell of the tandem device. The losses arise due the presence of high carrier concentration in the ITO for maintaining low sheet resistances. By replacing the rear ITO with an IZO electrode, the parasitic absorption losses are significantly reduced, leading to an enhanced transmittance of 8.9% relative in the near infrared wavelengths. Furthermore, it is demonstrated that by replacing the commercial ITO with TCO electrodes having reduced charge carrier concentration (ITO_n/IZO) and improved mobility (IZO and IO:H), these reflection and parasitic absorption losses are suppressed significantly. This leads to an enhanced transmittance (>85% for IO:H) for the s-PSCs fabricated with these TCO electrodes. In other research groups, similar transmittance was realized but they required to have additional micro-textured foils at the front air/glass interface that reduced reflection losses.[13,34] Within the new TCO electrode investigated in this study, the highest PCE is demonstrated with IO:H, demonstrating a stabilized efficiency of 27.3% for the 4T tandem configuration, one of the highest PCE recorded in 4T tandem architecture to date. Thus, these results show that it is highly important to consider alternative TCOs for the application in perovskite-based tandem devices.

7. Conclusion and outlook

To date, the power conversion efficiencies (PCE) of perovskite/crystalline-silicon tandem solar cells have surpassed the PCE of market-dominating single-junction crystalline-silicon (c-Si) solar cells. However, these tandem solar cells still suffer from various optical and electrical losses. While optical losses mainly arise due to reflections and parasitic absorptions due to the transparent conductive oxide (TCO) electrodes, and the non-ideal bandgap of the perovskite absorber, electrical losses appear because of non-radiative recombination or poor extraction of generated charge carriers. This thesis presents multiple strategies for reducing optical losses and improving the PCE of perovskite-based tandem solar cells.

Highly efficient perovskite solar cells conventionally use electron transport layers (ETLs) that require a high-processing temperature (> 450 °C).[31–34] This high-processing temperature limits perovskite solar cells to TCOs that are strongly absorbing and therefore, not ideal for high efficiency perovskite-based tandem solar cells. Hence, as a first strategy to reduce optical losses in perovskites solar cells, alternative electron transport layers (ETLs) are investigated. These ETLs comprise of nanoparticles of TiO_2 (np-TiO_2) and nanoparticles of SnO_2 (np-SnO_2), which can be deposited at a lower temperature (i.e., 100 °C for np-TiO_2 and 150 °C for np-SnO_2). The ability to deposit np-TiO_2 and np-SnO_2 at a significantly reduced temperature made these materials compatible with TCO electrodes that exhibit low near infrared parasitic absorptions, such as ITO, IZO and IO:H.[36,37] Thus, these nanoparticle-based ETLs play a critical role in terms of minimizing the optical losses in perovskite-based tandem solar cells. Furthermore, a detailed comparative study between the two ETLs reveal that np-SnO_2 based PSCs present less hysteresis and improved charge carrier extraction, making it a more promising ETL candidate. However, np-TiO_2 allow more flexibility in terms of tuning various material properties as they are synthesized in-house. This includes enhancing the conductivity of np-TiO_2 by doping it with Nb^{5+}, which is critical where thick ETLs are required. Furthermore, the ability to disperse the np-TiO_2 in various solvent systems makes them compatible with various roll-to-roll processing techniques such as inkjet printing, blade coating, and slot-die coating.

As a second strategy to reduce optical losses, nanophotonic light management concepts or alternative materials for TCOs are explored. The discussions on nanophotonic light management concept can be found in chapter 5, while in chapter 6 alternative materials for TCOs are discussed. Compared to conventional light management concepts, such as microtextured foils[58,63] or anti-reflection coatings[184] at the front side of a tandem solar cell, in this thesis nanophotonic light management is employed by fabricating nanostructured ITO (NS ITO) electrodes. The NS ITO electrodes enable improved light in-coupling by forming an effective refractive index medium. Two approaches are presented to obtain this NS ITO: (i) soft-imprinting to fabricate periodic nanostructures and (ii) polymer blend lithography to fabricate disordered nanostructures. Both demonstrate respective relative enhancements of up to ≈5% and ≈7% relative, over a broad range of wavelengths (300-1200 nm). Due to the reduction of reflection losses, improved short-circuit current

densities of ≈2-3% relative and ≈23% relative for top perovskite and bottom crystalline-silicon (c-Si) solar cells respectively, are achieved. However, a poor open-circuit voltage (V_{OC}) and a reduced fill factor (FF) for semitransparent perovskite solar cells (s-PSCs) with NS ITO leads to only a 0.7% absolute increase in the PCE for 4T perovskite/c-Si tandem solar cells. Further analysis is performed to determine the potential improvement by NS ITO. Considering a similar V_{OC} and FF from both NS ITO and reference planar ITO devices, a potential increase of 2.1% absolute in PCE is expected.

As alternative materials for the reduction of optical losses in TCOs, an in-house sputtering technique is employed to fabricate front TCO electrodes that exhibit reduced carrier concentration in chapter 6. Due to the reduced carrier concentration, an improvement of transmission in the near infrared wavelengths is achieved for the s-PSCs. Transmittance of >85% is demonstrated with IO:H, which enhanced the absolute PCE in the bottom c-Si solar cell by 1.4%. As a result, 4T perovskite/c-Si tandem solar cells with PCE up to 27.3% have been achieved. This PCE is one of the highest recorded PCEs in a 4T perovskite/c-Si tandem architecture to date. Furthermore, it is shown that replacing the highly absorbing rear ITO with a rear IZO layer in a s-PSC improves the transmission significantly in the near infrared wavelengths.

Finally, in order to maximize the PCE of the perovskite-based tandem PV and to determine the optimum bandgap of the top perovskite absorber, a detailed experimental investigation is carried out for perovskite/c-Si and perovskite/CIGS tandem solar cells in a 4T tandem configuration. The results reveal that the exact bandgap of the top perovskite absorber is not a critical requirement for obtaining high efficiencies. With bandgaps between 1.65-1.74 eV, comparable and yet high PCEs are achieved, which is in line with detailed-balance calculations. A deviation in the trend compared to the detailed-balance analysis is noted when much wider bandgaps (1.74-1.85 eV) of the perovskite absorber are used. This is due to the increased V_{OC} loss for these bandgaps. In this study, a surface passivation technique using a 2D/3D heterostucture has been employed to mitigate defects and non-radiative recombination process at the perovskite/hole transport layer interface. Although the V_{OC} loss for the bandgap range (1.74-1.85 eV) still remains, an overall improvement of ≈45 mV is achieved for bandgaps between 1.65 eV and 1.85 eV. The loss in V_{OC} for the bandgap range 1.74-1.85 eV occurs due to the presence of high amounts of bromide ions. These high amounts of bromide ions promote phase-segregation under illumination and lead to a poorer device performance.

7.1 Outlook

Although various strategies are presented in this thesis to reduce optical losses and improve the PCE of perovskite-based tandem solar cells, further improvements are still possible. In this section, an outlook is presented that discusses various ways in further enhancing the performances.

While this thesis employs np-TiO_2 as the ETL for n-i-p perovskite solar cells, dispersing these np-TiO_2 in other solvents such as chlorobenzene or toluene would mean they could

likely be used in the p-i-n architecture (inverted architecture) of perovskite solar cells as well. This implies that np-TiO_2 can be deposited on top of the perovskite absorber layer. The advantage of np-TiO_2 in the p-i-n architecture would be to circumvent the common combination of organic ETL (C_{60}) and with a buffer layer of atomic layer deposited SnO_2.[80] As a result, the layer stack would be simplified and can potentially improve the long-term stability of perovskite solar cells.

In terms of nanophotonic front electrodes, several aspects can be investigated in future studies. The significant potential improvement of by 2.1% highlights the importance of overcoming V_{OC} losses in NS ITO based tandem devices. In order to overcome this V_{OC} loss, different deposition methods for the charge transport layer or alternative materials can be explored to improve the NS ITO and the subsequent layer interface that is the root of the observed increase in non-radiative recombination. Future studies can investigate thermal[80] or electron beam evaporation,[108,206] or sputtering techniques[207] to deposit high-quality charge transport layers and improve said interface. As alternative materials, self-assembled monolayers may also be employed.[120] In a recent study, perovskite solar cells with nanostructured TCO exhibited very small V_{OC} losses when they employed such self-assembled monolayers.[43] Another important aspect, which is highly important to consider for the NS ITO is the formation of cracks between the nanostructures. These cracks are the probable cause of increased sheet resistance for nanostructures with smaller geometries. Although the effect of increased sheet resistance is not so severe in s-PSCs that are fabricated in this thesis (because the area is small at only 10.5 mm^2), any large-area PSCs will observe a significant detrimental effect on their PCE. In order to reduce sheet resistance, future studies can include investigations of different sputtering conditions or the use of metal grids for NS TCO.[15,58] Next to this, it is also important to employ different strategies to transfer the nanostructures directly to the glass substrate,[208,209] thus circumventing the usage of polystyrene that limits the processing temperature[210] of the PSC and long-term stability.

With respect to further improving the transmission, a rear IO:H TCO can be investigated. As IO:H absorbs below 5% of light in the near infrared wavelengths shown in this thesis, a further increase in the transmission would be possible if the rear IZO is replaced with a rear IO:H. One challenge to deposit this high-quality IO:H as a rear electrode is the requirement for a post annealing crystallization at ≈200 °C. This high temperature is not suitable for perovskite absorbers used here as they are prone to degradation from thermal stress. Therefore, future works can include an investigation into reducing the crystallization temperature of IO:H to deposit it as a rear TCO in s-PSCs for perovskite-based tandem PV.

In regard to the optimization of the bandgap for perovskite-based tandem devices, future studies can involve improving the s-PSC performance for wider bandgap materials. One possible way is to deposit perovskite absorbers with higher amounts of cesium ions. It has been reported that increasing the amount of the monovalent cation cesium in the crystal structure raises the bandgap of the perovskite absorber.[25] Therefore, future studies can

involve a closer look at various other monovalent cations and their impact in reducing phase-segregation.

Appendix

Appendix for Chapter 4

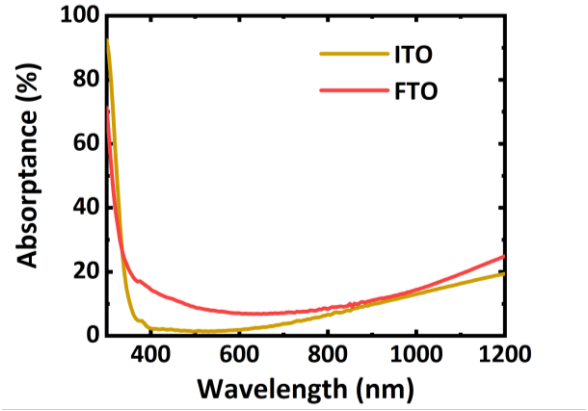

Fig. A. 4.1: Absorptance of ITO and FTO.

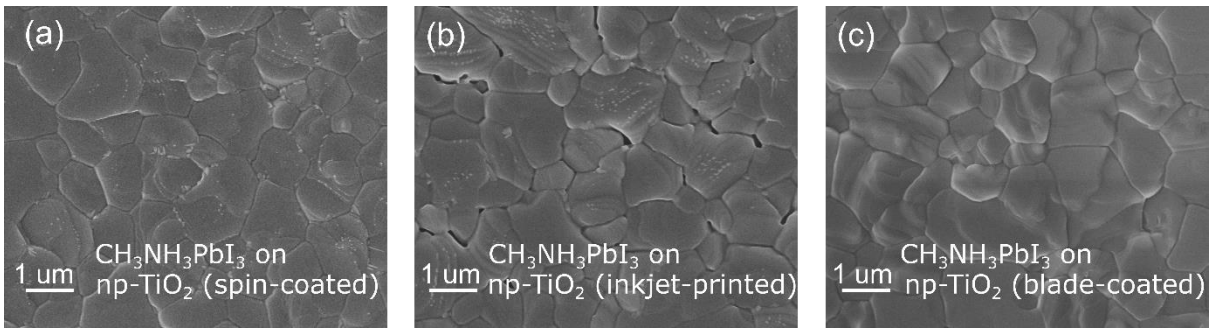

Fig. A. 4.2: Scanning electron microscopy image of perovskite ($CH_3NH_3PbI_3$) absorber on np-TiO_2 deposited by spin coating, inkjet printing and blade coating. Reproduced with permission from ACS Applier Energy Materials, [139] © American Chemical Society.

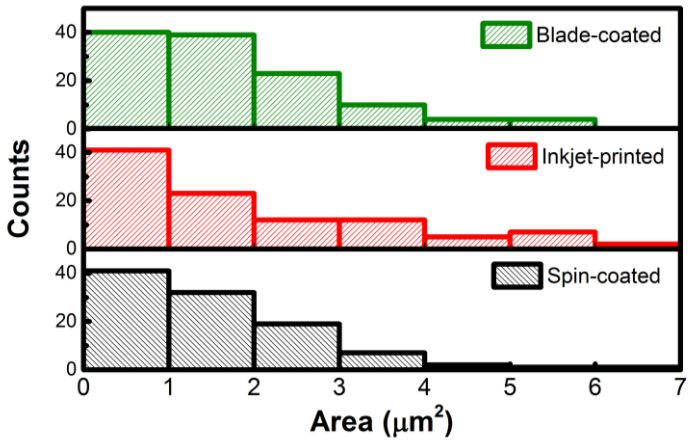

Fig. A. 4.3: Grain size distribution of the perovskite absorber on np-TiO_2 deposited by spin coating, inkjet printing and blade coating. Reproduced with permission from ACS Applier Energy Materials, [139] © American Chemical Society.

Appendix for Chapter 5

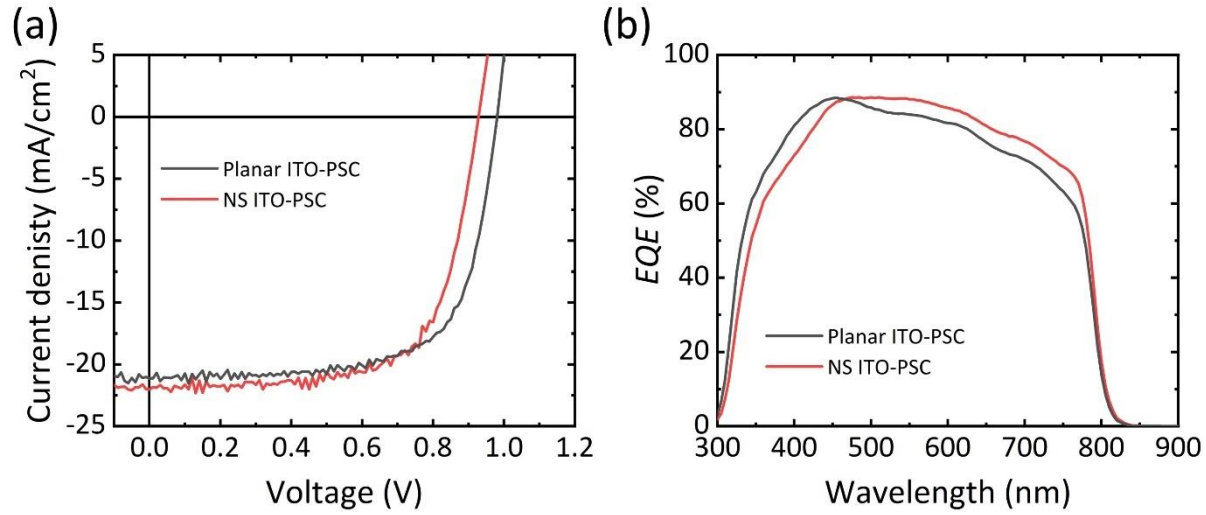

Fig. A. 5.1: (a) Current density-voltage (*J-V*) characteristic and (b) external quantum efficiency (EQE) of the perovskite solar cells (PSCs) with nanostructured ITO, and PSCs with planar ITO for Batch 2. Adapted with permission from reference [71], © 2020 Optical Society of America.

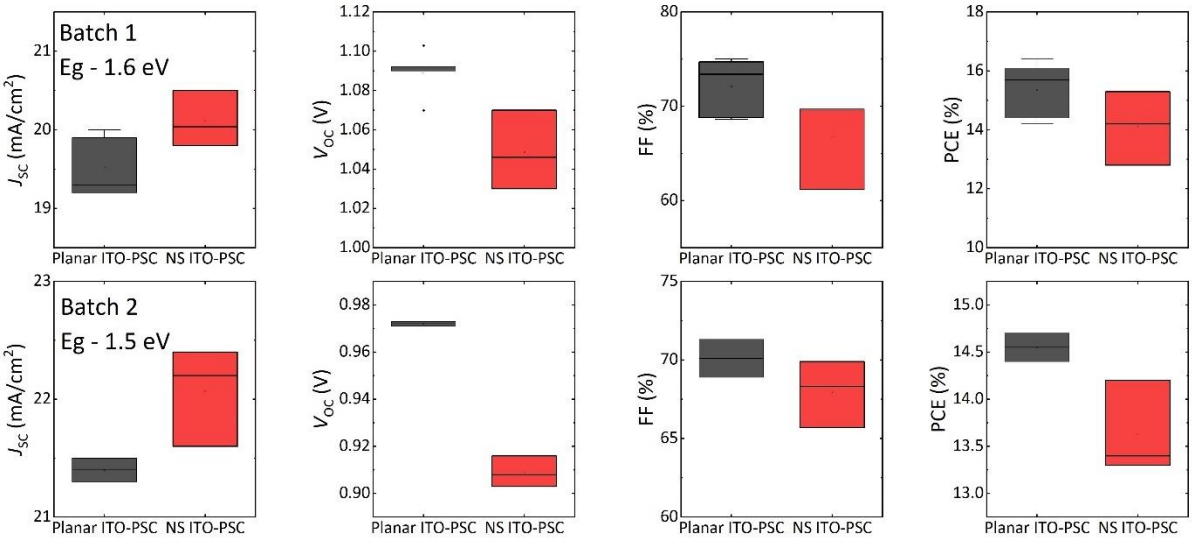

Fig. A. 5.2: Statistical distribution of short-circuit current density (J_{SC}), open-circuit voltage (V_{OC}), fill factor (FF) and the power conversion efficiency (PCE) for perovskite solar cells (PSCs) with planar and nanostructured ITO. Adapted with permission from reference [71], © 2020 Optical Society of America.

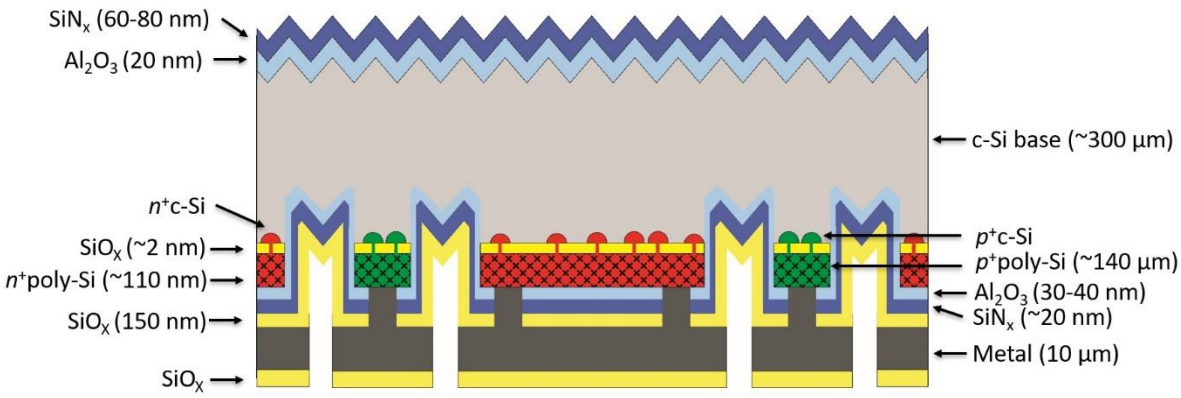

Fig. A. 5.3: Schematic of interdigitated back contact crystalline-silicon (c-Si) bottom solar cell. Adapted with permission from reference [71], © 2020 Optical Society of America.

Appendix for Chapter 6

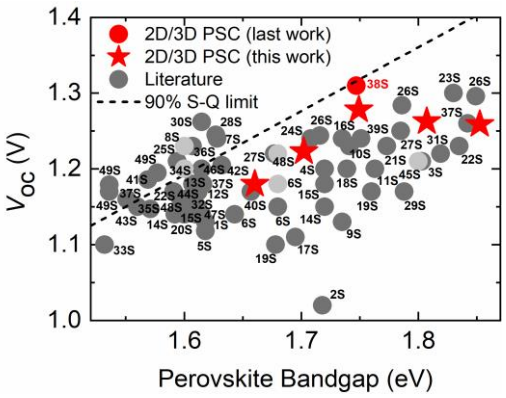

Figure A. 6.1. Champion open-circuit voltage (V_{OC}) as a function of perovskite bandgap (E_g) for the best mixed-halide perovskite solar cells with decent power conversion efficiency (>12%) reported in the literature (dark grey circles) in comparison to the best V_{OC} obtained in our last (red circle, 38S) and this work (red stars). The dashed line indicates a V_{OC} representing 90% of the maximum defined by the Shockley-Queisser (S-Q) limit. Note that in order to have a meaningful comparison between all results (due to the various methods used to estimate E_g), we derived E_g based on the differential of the reported EQE (extracted with WebPlotDigitizer) curves close to the absorption edge, i.e. the maximum of d(EQE)/d(E) (determined with a Gaussian fit to the extracted experimental data). More details are provided in **Table A. 6.1**. Adapted with permission from reference [99], © John Wiley & Sons.

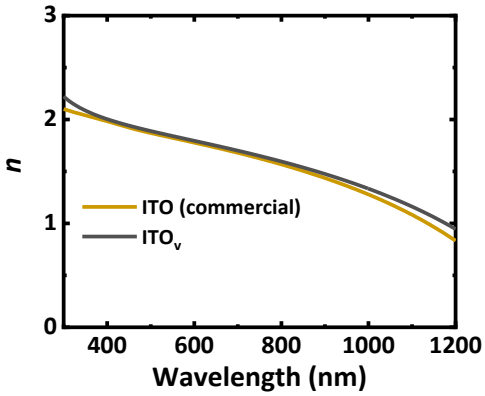

Figure A. 6.2. Refractive index (n) of the commercial ITO and in-house sputtered ITO_v used in section 6.1.

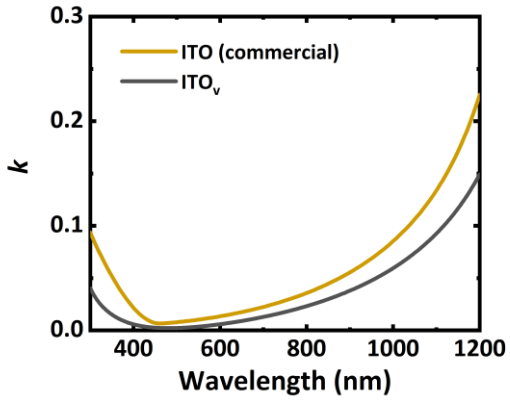

Figure A. 6.3. Extinction coefficient (*k*) of the commercial ITO and in-house sputtered ITO_v used in section 6.1.

Table A. 6.1: Detailed information for the references in **Figure A. 6.1**, sorted by publication date. Nominal perovskite composition and bandgap (E_g) as reported in the reference, E_g determined from the differential of the EQE (d(EQE)/dE) close to the absorption edge as described in the caption of Figure A. 6.1, champion open-circuit voltage (V_{OC}) as reported and V_{OC} deficit calculated by subtracting V_{OC} from E_g (from d(EQE)/dE). For the V_{OC} deficit in brackets E_g as reported in the reference was used, as no EQE data was provided, and these values should be considered with care. All references are provided at the end of the in Appendix. Adapted with permission from reference [99], © John Wiley & Sons.

Nominal perovskite composition as reported	E_g as reported	E_g (from d(EQE)/dE)	V_{OC} (V)	V_{OC} deficit	Reference
$CH_3NH_3PbI_{3-x}Cl_x$	1.55	1.618	1.13	0.488	1S
$CH_3NH_3PbI_{3-x}Br_x$	1.72	1.718	1.02	0.698	2S
$MAPbBr_xI_{3-x}$	1.75	1.803	1.21	0.593	3S
$FA_{0.83}Cs_{0.17}Pb(I_{0.6}Br_{0.4})_3$	1.74	1.72	1.2	0.52	4S
$(FAPbI_3)_{0.85}(MAPbBr_3)_{0.15}$	1.6	1.618	1.118	0.5	5S
$FA_{0.67}MA_{0.33}Pb(I_{0.83}Br_{0.17})_3$	1.64	1.643	1.14	0.503	6S
$FA_{0.83}MA_{0.17}Pb(I_{0.67}Br_{0.33})_3$	1.68	*no EQE*	1.18	*(0.5)*	6S
$FA_{0.67}MA_{0.33}Pb(I_{0.67}Br_{0.33})_3$	1.68	1.684	1.15	0.534	6S
$Rb_{0.05}(Cs_{0.05}(FA_{0.83}MA_{0.17})_{0.95})_{0.95}Pb(I_{0.83}Br_{0.17})_3$	1.63	1.628	1.24	0.388	7S
$Cs_{0.05}(FA_{0.83}MA_{0.17})_{0.95}Pb(I_{0.83}Br_{0.17})_3$	1.6	*no EQE*	1.23	*(0.37)*	8S
$Rb_{0.05}(FA_{0.75}MA_{0.15}Cs_{0.1})_{0.95}Pb(I_{0.67}Br_{0.33})_3$	1.73	1.735	1.13	0.605	9S
$FA_{0.8}Cs_{0.2}Pb(I_{0.7}Br_{0.3})_3$ w/ Pb(SCN)	1.75	1.741	1.23	0.511	10S
$Cs_{0.05}(FA_{0.83}MA_{0.17})_{0.95}Pb(I_{0.6}Br_{0.4})_3$	1.71	1.763	1.2	0.563	11S
$MAPbI_3$	1.59	1.612	1.17	0.442	12S
$Cs_{0.07}Rb_{0.03}FA_{0.765}MA_{0.135}Pb(I_{0.85}Br_{0.15})_3$	*non*	1.607	1.18	0.427	13S
$FA_{0.85}MA_{0.15}Pb(I_{0.85}Br_{0.15})_3$	1.592	1.592	1.14	0.452	14S

$FA_{0.83}MA_{0.17}Pb(I_{0.6}Br_{0.4})_3$	1.72	1.72	1.15	0.57	14S
$BA_{0.05}(FA_{0.83}Cs_{0.17})_{0.95}Pb(I_{0.8}Br_{0.2})_3$	1.61	1.61	1.14	0.47	15S
$BA_{0.09}(FA_{0.83}Cs_{0.17})_{0.91}Pb(I_{0.6}Br_{0.4})_3$	1.72	1.72	1.18	0.54	15S
$FA_{0.85}Cs_{0.15}Pb(I_{0.73}Br_{0.27})_3$	1.72	1.735	1.24	0.495	16S
$MAPb(I_{0.8}Br_{0.2})_3$	1.72	1.695	1.11	0.585	17S
$FA_{0.8}Cs_{0.2}Pb(Br_{0.3}I_{0.7})_3$	1.75	1.739	1.2	0.539	18S
$FA_{0.6}Cs_{0.4}Pb(I_{0.7}Br_{0.3})_3$	1.75	1.76	1.17	0.59	19S
$FA_{0.75}Cs_{0.25}Pb(I_{0.8}Br_{0.2})_3$	1.68	1.678	1.1	0.578	19S
$Cs_{0.1}FA_{0.74}MA_{0.13}PbI_{2.48}Br_{0.39}$	1.62	1.6	1.14	0.46	20S
$FA_{0.83}Cs_{0.17}Pb(I_{0.6}Br_{0.4})_3$	1.75	1.773	1.23	0.543	21S
$K_{0.1}(Cs_{0.06}FA0_{0.79}MA_{0.15})_{0.9}Pb(I_{0.85}Br_{0.15})_3$	1.56	1.591	1.17	0.421	22S
$K_{0.1}(Cs_{0.06}FA0_{0.79}MA_{0.15})_{0.9}Pb(I_{0.4}Br_{0.6})_3$	1.78	1.835	1.23	0.605	22S
$MAPb(I_{0.6}Br_{0.4})_3$	1.82	1.83	1.30	0.53	23S
$MAPb(I_{1-x}Br_x)_3$	1.71	1.708	1.24	0.468	24S
$(FA_{0.95}PbI_{2.95})_{0.85}(MAPbBr_3)_{0.15}$	1.62	1.594	1.21	0.384	25S
$FA_{0.83}Cs_{0.17}Pb(I_{0.73}Br_{0.27})_3$ w/ Pb(SCN)	1.72	1.716	1.244	0.472	26S
$FA_{0.83}Cs_{0.17}Pb(I_{0.6}Br_{0.4})_3$ w/ Pb(SCN)	1.79	1.786	1.284	0.502	26S
$FA_{0.83}Cs_{0.17}Pb(I_{0.5}Br_{0.5})_3$ w/ Pb(SCN)	1.86	1.849	1.296	0.553	26S
$FA_{0.83}Cs_{0.17}Pb(I_{0.4}Br_{0.6})_3$ w/ Pb(SCN)	1.93	1.91	1.312	0.598	26S
$Cs_{0.12}MA_{0.05}FA_{0.83}Pb(I_{0.6}Br_{0.4})_3$	1.74	1.785	1.25	0.535	27S
$Cs_{0.05}MA_{0.15}FA_{0.8}Pb(I_{0.75}Br_{0.25})_3$	1.65	1.677	1.22	0.457	27S
$Cs_{0.05}((FA_{0.85}MA_{0.15})Pb(I_{0.85}Br_{0.15})_3)_{0.95}$	1.61	1.627	1.245	0.382	28S
$MA_{0.6}FA_{0.4}Pb(I_{0.6}Br_{0.4})_3$	1.76	1.788	1.17	0.618	29S
$MAPbI_3$	1.6	1.615	1.262	0.353	30S
$FA_{0.85}Cs_{0.15}Pb(I_{0.71}Br_{0.29})_3$	1.72	1.819	1.22	0.599	31S
$Cs_{0.05}MA_{0.14}FA_{0.81}Pb(I_{0.85}Br_{0.15})_3$	*non*	1.611	1.15	0.461	32S
$FA_{0.8}Cs_{0.2}PbI_3$	1.56	1.532	1.1	0.432	33S
$GA_5(Cs_5(MA_{0.17}FA_{0.83})_{0.95})_{0.95}Pb(I_{0.83}Br_{0.17})_3$	1.6	*no EQE*	1.2	*(0.4)*	34S
$Cs_y(FA_{0.57}MA_{0.43})_{1-y}Pb(I_{1-x}Br_x)_3$	1.56	1.571	1.147	0.413	35S
$Cs_{0.05}MA_{0.14}FA_{0.81}Pb(I_{0.85}Br_{0.15})_3$	1.57	1.607	1.23	0.34	36S
$Cs_{0.05}FA_{0.70}MA_{0.25}PbI_3$	1.51	1.551	1.16	0.391	37S
$MAPbI_3$	1.55	1.616	1.18	0.436	37S

$FA_{0.8}Cs_{0.2}Pb(I_{0.6}Br_{0.4})_3$	1.82	1.842	1.26	0.582	37S
$FA_{0.83}Cs_{0.17}Pb(I_{0.6}Br_{0.4})_3$	1.72	1.747	1.31	0.434	38S
$GA_xFA_{0.8}Cs_{0.2}Pb(I_{0.7}Br_{0.3+x/3})_3$	1.75	1.751	1.24	0.511	39S
$(FA_{0.65}MA_{0.20}Cs_{0.15})Pb(I_{0.8}Br_{0.2})_3$	1.68	1.657	1.17	0.487	40S
$(FAPbI_3)_{0.92}(MAPbBr_3)_{0.08}$	1.53	1.569	1.186	0.383	41S
$(CsPbI_3)_{0.05}[(FAPbI_3)_{0.83}(MAPbBr_3)_{0.17}]_{0.95}$	1.6	1.632	1.205	0.427	42S
$Cs_{0.07}FA_{0.9}MA_{0.03}Pb(I_{0.92}Br_{0.08})_3$	*non*	1.56	1.15	0.41	43S
$Cs_{0.05}FA_{0.81}MA_{0.14}PbI_{2.55}Br_{0.45}$	1.6	1.6	1.16	0.44	44S
$FA_{0.6}Cs_{0.4}Pb(I_{0.65}Br_{0.35})_3$	1.8	*no EQE*	1.21	*(0.59)*	45S
$Cs_{0.07}Rb_{0.03}FA_{0.765}MA_{0.135}Pb(I_{0.85}Br_{0.15})_3$	1.6	1.615	1.2	0.415	46S
$Cs_{0.05}FA_{0.81}MA_{0.14}Pb(I_{0.86}Br_{0.14})_3$	1.61	1.615	1.14	0.46	47S
$MAPbI_3$	1.59	1.597	1.16	0.43	48S
$MAPb(I_{0.8}Br_{0.2})_3$	1.68	*no EQE*	1.22	*(0.46)*	48S
Not stated	--	1.577	1.195	0.382	49S
Not stated	--	1.536	1.17	0.366	49S
Not stated	--	1.536	1.179	0.357	49S
$FA_{0.83}Cs_{0.17}Pb(I_{0.76}Br_{0.24})_3$	1.65	1.667	1.18	0.487	This work
$FA_{0.83}Cs_{0.17}Pb(I_{0.68}Br_{0.32})_3$	1.69	1.702	1.223	0.479	This work
$FA_{0.83}Cs_{0.17}Pb(I_{0.6}Br_{0.4})_3$	1.74	1.748	1.278	0.47	This work
$FA_{0.83}Cs_{0.17}Pb(I_{0.52}Br_{0.48})_3$	1.79	1.809	1.263	0.546	This work
$FA_{0.83}Cs_{0.17}Pb(I_{0.44}Br_{0.56})_3$	1.85	1.855	1.259	0.596	This work

Additional references for Table A. 6.1

[1S] H. Zhou, Q. Chen, G. Li, S. Luo, T. -b. Song, H.-S. Duan, Z. Hong, J. You, Y. Liu, Y. Yang, Science **2014**, 345, 542.

[2S] C. Bi, Y. Yuan, Y. Fang, J. Huang, Adv. Energy Mater. **2015**, 5, 1401616.

[3S] M. Hu, C. Bi, Y. Yuan, Y. Bai, J. Huang, Adv. Sci. **2016**, 3, 1500301.

[4S] D. P. McMeekin, G. Sadoughi, W. Rehman, G. E. Eperon, M. Saliba, M. T. Horantner, A. Haghighirad, N. Sakai, L. Korte, B. Rech, M. B. Johnston, L. M. Herz, H. J. Snaith, Science **2016**, 351, 151.

[5S] F. Giordano, A. Abate, J. P. Correa Baena, M. Saliba, T. Matsui, S. H. Im, S. M. Zakeeruddin, M. K. Nazeeruddin, A. Hagfeldt, M. Graetzel, Nat. Commun. **2016**, 7, 10379.

[6S] T. Jesper Jacobsson, J.-P. Correa-Baena, M. Pazoki, M. Saliba, K. Schenk, M. Grätzel, A. Hagfeldt, Energy Environ. Sci. **2016**, 9, 1706.

[7S] M. Saliba, T. Matsui, K. Domanski, J.-Y. Seo, A. Ummadisingu, S. M. Zakeeruddin, J.-P. Correa-Baena, W. R. Tress, A. Abate, A. Hagfeldt, M. Gratzel, Science **2016**, 354, 206.

[8S] J. P. Correa-Baena, W. Tress, K. Domanski, E. H. Anaraki, S. H. Turren-Cruz, B. Roose, P. P. Boix, M. Grätzel, M. Saliba, A. Abate, A. Hagfeldt, Energy Environ. Sci. **2017**, 10, 1207.

[9S] T. Duong, Y. Wu, H. Shen, J. Peng, X. Fu, D. Jacobs, E.-C. Wang, T. C. Kho, K. C. Fong, M. Stocks, E. Franklin, A. Blakers, N. Zin, K. McIntosh, W. Li, Y.-B. Cheng, T. P. White, K. Weber, K. Catchpole, Adv. Energy Mater. **2017**, 7, 1700228.

[10S] Y. Yu, C. Wang, C. R. Grice, N. Shrestha, D. Zhao, W. Liao, L. Guan, R. A. Awni, W. Meng, A. J. Cimaroli, K. Zhu, R. J. Ellingson, Y. Yan, ACS Energy Lett. **2017**, 2, 1177.

[11S] Y. Lin, B. Chen, F. Zhao, X. Zheng, Y. Deng, Y. Shao, Y. Fang, Y. Bai, C. Wang, J. Huang, Adv. Mater. **2017**, 29, 1700607.

[12S] Y. Bai, S. Xiao, C. Hu, T. Zhang, X. Meng, H. Lin, Y. Yang, S. Yang, Adv. Energy Mater. 2017, 7, 1701038.

[13S] J. Peng, Y. Wu, W. Ye, D. A. Jacobs, H. Shen, X. Fu, Y. Wan, T. Duong, N. Wu, C. Barugkin, H. T. Nguyen, D. Zhong, J. Li, T. Lu, Y. Liu, M. N. Lockrey, K. J. Weber, K. R. Catchpole, T. P. White, Energy Environ. Sci. **2017**, 10, 1792.

[14S] X. Zheng, B. Chen, J. Dai, Y. Fang, Y. Bai, Y. Lin, H. Wei, X. C. Zeng, J. Huang, Nat. Energy **2017**, 2, 17102.

[15S] Z. Wang, Q. Lin, F. P. Chmiel, N. Sakai, L. M. Herz, H. J. Snaith, Nat. Energy **2017**, 2, 17135.

[16S] Y. Zhou, F. Wang, Y. Cao, J.-P. Wang, H.-H. Fang, M. A. Loi, N. Zhao, C.-P. Wong, Adv. Energy Mater. **2017**, 7, 1701048.

[17S] G. Longo, C. Momblona, M.-G. La-Placa, L. Gil-Escrig, M. Sessolo, H. J. Bolink, ACS Energy Lett. **2018**, 3, 214.

[18S] D. Zhao, C. Wang, Z. Song, Y. Yu, C. Chen, X. Zhao, K. Zhu, Y. Yan, ACS Energy Lett. **2018**, 3, 305.

[19S] K. A. Bush, K. Frohna, R. Prasanna, R. E. Beal, T. Leijtens, S. A. Swifter, M. D. McGehee, ACS Energy Lett. **2018**, 3, 428.

[20S] K. T. Cho, G. Grancini, Y. Lee, E. Oveisi, J. Ryu, O. Almora, M. Tschumi, P. A. Schouwink, G. Seo, S. Heo, J. Park, J. Jang, S. Paek, G. Garcia-Belmonte, M. K. Nazeeruddin, Energy Environ. Sci. **2018**, 11, 952.

[21S] J. Kim, M. I. Saidaminov, H. Tan, Y. Zhao, Y. Kim, J. Choi, J. W. Jo, J. Fan, R. Quintero-Bermudez, Z. Yang, L. N. Quan, M. Wei, O. Voznyy, E. H. Sargent, Adv. Mater. **2018**, 30, 1706275.

[22S] M. Abdi-Jalebi, Z. Andaji-Garmaroudi, S. Cacovich, C. Stavrakas, B. Philippe, J. M. Richter, M. Alsari, E. P. Booker, E. M. Hutter, A. J. Pearson, S. Lilliu, T. J. Savenije, H. Rensmo, G. Divitini, C. Ducati, R. H. Friend, S. D. Stranks, Nature **2018**, 555, 497.

[23S] A. Rajagopal, R. J. Stoddard, S. B. Jo, H. W. Hillhouse, A. K. Y. Jen, Nano Lett. **2018**, 18, 3985.

[24S] D. B. Khadka, Y. Shirai, M. Yanagida, T. Noda, K. Miyano, ACS Appl. Mater. Interfaces **2018**, 10, 22074.

[25S] D. Luo, W. Yang, Z. Wang, A. Sadhanala, Q. Hu, R. Su, R. Shivanna, G. F. Trindade, J. F. Watts, Z. Xu, T. Liu, K. Chen, F. Ye, P. Wu, L. Zhao, J. Wu, Y. Tu, Y. Zhang, X. Yang, W. Zhang, R. H. Friend, Q. Gong, H. J. Snaith, R. Zhu, Science **2018**, 360, 1442.

[26S] Y. Zhou, Y.-H. Jia, H.-H. Fang, M. A. Loi, F.-Y. Xie, L. Gong, M.-C. Qin, X.-H. Lu, C.-P. Wong, N. Zhao, Adv. Funct. Mater. **2018**, 28, 1803130.

[27S] H. Tan, F. Che, M. Wei, Y. Zhao, M. I. Saidaminov, P. Todorović, D. Broberg, G. Walters, F. Tan, T. Zhuang, B. Sun, Z. Liang, H. Yuan, E. Fron, J. Kim, Z. Yang, O. Voznyy, M. Asta, E. H. Sargent, Nat. Commun. 2018, 9, 3100.

[28S] M. M. Tavakoli, W. Tress, J. V. Milić, D. Kubicki, L. Emsley, M. Grätzel, Energy Environ. Sci. **2018**, 11, 3310.

[29S] S. Chen, Y. Hou, H. Chen, X. Tang, S. Langner, N. Li, T. Stubhan, I. Levchuk, E. Gu, A. Osvet, C. J. Brabec, Adv. Energy Mater. **2018**, 8, 1701543.

[30S] Z. Liu, L. Krückemeier, B. Krogmeier, B. Klingebiel, J. A. Márquez, S. Levcenko, S. Öz, S. Mathur, U. Rau, T. Unold, T. Kirchartz, ACS Energy Lett. **2019**, 4, 110.

[31S] M. Jaysankar, B. A. L. Raul, J. Bastos, C. Burgess, C. Weijtens, M. Creatore, T. Aernouts, Y. Kuang, R. Gehlhaar, A. Hadipour, J. Poortmans, ACS Energy Lett. **2019**, 4, 259.

[32S] P. Guo, Q. Ye, X. Yang, J. Zhang, F. Xu, D. Shchukin, B. Wei, H. Wang, J. Mater. Chem. A **2019**, 7, 2497.

[33S] D. Prochowicz, R. Runjhun, M. M. Tavakoli, P. Yadav, M. Saski, A. Q. Alanazi, D. J. Kubicki, Z. Kaszkur, S. M. Zakeeruddin, J. Lewiński, M. Grätzel, Chem. Mater. **2019**, 31, 1620.

[34S] D. Prochowicz, M. M. Tavakoli, A. Kalam, R. D. Chavan, S. Trivedi, M. Kumar, P. Yadav, J. Mater. Chem. A **2019**, 7, 8218.

[35S] Y. Chen, N. Li, L. Wang, L. Li, Z. Xu, H. Jiao, P. Liu, C. Zhu, H. Zai, M. Sun, W. Zou, S. Zhang, G. Xing, X. Liu, J. Wang, D. Li, B. Huang, Q. Chen, H. Zhou, Nat. Commun. **2019**, 10, 1112.

[36S] S. Yang, J. Dai, Z. Yu, Y. Shao, Y. Zhou, X. Xiao, X. C. Zeng, J. Huang, J. Am. Chem. Soc. **2019**, 141, 5781.

[37S] W.-Q. Wu, Z. Yang, P. N. Rudd, Y. Shao, X. Dai, H. Wei, J. Zhao, Y. Fang, Q. Wang, Y. Liu, Y. Deng, X. Xiao, Y. Feng, J. Huang, Sci. Adv. **2019**, 5, eaav8925.

[38S] S. Gharibzadeh, B. Abdollahi Nejand, M. Jakoby, T. Abzieher, D. Hauschild, S. Moghadamzadeh, J. A. Schwenzer, P. Brenner, R. Schmager, A. A. Haghighirad, L. Weinhardt, U. Lemmer, B. S. Richards, I. A. Howard, U. W. Paetzold, Adv. Energy Mater. **2019**, 9, 1803699.

[39S] C. Chen, Z. Song, C. Xiao, D. Zhao, N. Shrestha, C. Li, G. Yang, F. Yao, X. Zheng, R. J. Ellingson, C.-S. Jiang, M. Al-Jassim, K. Zhu, G. Fang, Y. Yan, Nano Energy **2019**, 61, 141.

[40S] D. H. Kim, C. P. Muzzillo, J. Tong, A. F. Palmstrom, B. W. Larson, C. Choi, S. P. Harvey, S. Glynn, J. B. Whitaker, F. Zhang, Z. Li, H. Lu, M. F. A. M. van Hest, J. J. Berry, L. M. Mansfield, Y. Huang, Y. Yan, K. Zhu, Joule **2019**, 3, 1734.

[41S] J. J. Yoo, S. Wieghold, M. C. Sponseller, M. R. Chua, S. N. Bertram, N. T. P. Hartono, J. S. Tresback, E. C. Hansen, J.-P. Correa-Baena, V. Bulović, T. Buonassisi, S. S. Shin, M. G. Bawendi, Energy Environ. Sci. **2019**, 12, 2192.

[42S] M. Stolterfoht, P. Caprioglio, C. M. Wolff, J. A. Márquez, J. Nordmann, S. Zhang, D. Rothhardt, U. Hörmann, Y. Amir, A. Redinger, L. Kegelmann, F. Zu, S. Albrecht, N. Koch, T. Kirchartz, M. Saliba, T. Unold, D. Neher, Energy Environ. Sci. **2019**, 12, 2778.

[43S] E. A. Alharbi, A. Y. Alyamani, D. J. Kubicki, A. R. Uhl, B. J. Walder, A. Q. Alanazi, J. Luo, A. Burgos-Caminal, A. Albadri, H. Albrithen, M. H. Alotaibi, J.-E. Moser, S. M. Zakeeruddin, F. Giordano, L. Emsley, M. Grätzel, Nat. Commun. **2019**, 10, 3008.

[44S] S. Yang, S. Chen, E. Mosconi, Y. Fang, X. Xiao, C. Wang, Y. Zhou, Z. Yu, J. Zhao, Y. Gao, F. De Angelis, J. Huang, Science **2019**, 365, 473.

[45S] Z. Yang, Z. Yu, H. Wei, X. Xiao, Z. Ni, B. Chen, Y. Deng, S. N. Habisreutinger, X. Chen, K. Wang, J. Zhao, P. N. Rudd, J. J. Berry, M. C. Beard, J. Huang, *Nat. Commun.* **2019**, *10*, 4498.

[46S] M. A. Mahmud, T. Duong, Y. Yin, H. T. Pham, D. Walter, J. Peng, Y. Wu, L. Li, H. Shen, N. Wu, N. Mozaffari, G. Andersson, K. R. Catchpole, K. J. Weber, T. P. White, Adv. Funct. Mater. **2019**, doi: 10.1002/adfm.201907962.

[47S] Y. Lv, X. Song, Y. Yin, Y. Feng, H. Ma, C. Hao, S. Jin, Y. Shi, ACS Appl. Mater. Interfaces **2020**, 12, 698.

[48S] C.-T. Lin, J. Lee, J. Kim, T. J. Macdonald, J. Ngiam, B. Xu, M. Daboczi, W. Xu, S. Pont, B. Park, H. Kang, J.-S. Kim, D. J. Payne, K. Lee, J. R. Durrant, M. A. McLachlan, Adv. Funct. Mater. 2019, 1906763, 1906763.

[49S] M. A. Green, A. W. Y. Ho-Baillie, ACS Energy Lett. **2019**, 4, 1639.

References

1. Masson-Delmotte, V. *et al. IPCC, 2018: Global Warming of 1.5°C.* https://www.ipcc.ch/site/assets/uploads/sites/2/2019/06/SR15_Full_Report_High_Res.pdf (2019) doi:10.1038/291285a0.

2. Nukunudompanich, M., Budiutama, G., Suzuki, K., Hasegawa, K. & Ihara, M. Dominant effect of the grain size of the MAPbI 3 perovskite controlled by the surface roughness of TiO 2 on the performance of perovskite solar cells . *CrystEngComm* (2020) doi:10.1039/d0ce00169d.

3. Heede, R. & Oreskes, N. Potential emissions of CO2 and methane from proved reserves of fossil fuels: An alternative analysis. *Glob. Environ. Chang.* **36**, 12–20 (2016).

4. Michael Oppenheimer. Global warming and the stability of the West Antarctic Ice Sheet. *Nature* **393**, 325–332 (1998).

5. Dobson, A., Jolly, A., Rubenstein, D. & Woodwell, G. The Greenhouse Effect and Biological Diversity. *Tree* **4**, 64–68 (1989).

6. UNFCCC. Conference of the Parties, Paris Agreement 2015. doi:FCCC/CP/2015/L.9/Rev.1.

7. IEA, World Energy Outlook 2019, Paris. https://www.iea.org/reports/world-energy-outlook-2019 (2019).

8. Kost, C. *et al. Fraunhofer ISE: Levelized Cost of Electricity - Renewable Energy Technologies, March 2018*. *Fraunhofer ISE: Levelized Cost of Electricity - Renewable Energy Technologies* (2018).

9. Howard, I. A. *et al.* Coated and Printed Perovskites for Photovoltaic Applications. *Adv. Mater.* **31**, 1806702 (2019).

10. NREL. National Renewable Energy Laboratory (NREL), Efficiency chart, 2020. https://www.nrel.gov/pv/cell-efficiency.html (2020).

11. Hwang, K. *et al.* Toward large scale roll-to-roll production of fully printed perovskite solar cells. *Adv. Mater.* **27**, 1241–1247 (2015).

12. Albrecht, S. & Rech, B. Perovskite solar cells: On top of commercial photovoltaics. *Nat. Energy* **2**, 16196 (2017).

13. Duong, T. *et al.* High Efficiency Perovskite-Silicon Tandem Solar Cells: Effect of Surface Coating versus Bulk Incorporation of 2D Perovskite. *Adv. Energy Mater.* **10**, 1–15 (2020).

14. Chen, B. *et al.* Enhanced optical path and electron diffusion length enable high-efficiency perovskite tandems. *Nat. Commun.* **11**, (2020).

15. Jacobs, D. A. *et al.* Light Management: A Key Concept in High-Efficiency Perovskite/Silicon Tandem Photovoltaics. *J. Phys. Chem. Lett.* **10**, 3159–3170 (2019).

16. Duong, T. *et al.* Semitransparent Perovskite Solar Cell With Sputtered Front and Rear Electrodes for a Four-Terminal Tandem. *IEEE J. Photovoltaics* **6**, 679–687 (2016).

17. Eperon, G. E., Hörantner, M. T. & Snaith, H. J. Metal halide perovskite tandem and multiple-junction photovoltaics. *Nat. Rev. Chem.* **1**, (2017).

18. Futscher, M. H. & Ehrler, B. Efficiency Limit of Perovskite/Si Tandem Solar Cells. *ACS Energy Lett.* **1**, 863–868 (2016).

19. Hoke, E. T. *et al.* Reversible photo-induced trap formation in mixed-halide hybrid perovskites for photovoltaics. *Chem. Sci.* **6**, 613–617 (2015).

20. Levine, I. *et al.* Deep Defect States in Wide-Band-Gap ABX 3 Halide Perovskites. *ACS Energy Lett.* **4**, 1150–1157 (2019).

21. Tan, H. *et al.* Dipolar cations confer defect tolerance in wide-bandgap metal halide perovskites. *Nat. Commun.* **9**, 3100 (2018).

22. Lin, Y. *et al.* Matching Charge Extraction Contact for Wide-Bandgap Perovskite Solar Cells. *Adv. Mater.* **29**, 1700607 (2017).

23. Belisle, R. A. *et al.* Impact of surfaces on photoinduced halide segregation in mixed-halide perovskites. *ACS Energy Lett.* **3**, 2694–2700 (2018).

24. Jaysankar, M. *et al.* Minimizing Voltage Loss in Wide-Bandgap Perovskites for Tandem Solar Cells. *ACS Energy Lett.* **4**, 259–264 (2019).

25. Bush, K. A. *et al.* Compositional Engineering for Efficient Wide Band Gap Perovskites with Improved Stability to Photoinduced Phase Segregation. *ACS Energy Lett.* **3**, 428–435 (2018).

26. Unger, E. L. *et al.* Roadmap and roadblocks for the band gap tunability of metal halide perovskites. *J. Mater. Chem. A* **5**, 11401–11409 (2017).

27. Yang, T. C. J., Fiala, P., Jeangros, Q. & Ballif, C. High-Bandgap Perovskite Materials for Multijunction Solar Cells. *Joule* **2**, 1421–1436 (2018).

28. Mahmood, K., Sarwar, S. & Mehran, M. T. Current status of electron transport layers in perovskite solar cells: materials and properties. *RSC Adv.* **7**, 17044–17062 (2017).

29. Wu, W.-Q., Chen, D., Caruso, R. A. & Cheng, Y.-B. Recent progress in hybrid perovskite solar cells based on n-type materials. *J. Mater. Chem. A* **5**, 10092–10109 (2017).

30. Yang, G., Tao, H., Qin, P., Ke, W. & Fang, G. Recent progress in electron transport layers for e ffi cient perovskite solar cells. *J. Mater. Chem. A Mater. energy Sustain.* **4**, 3970–3990 (2016).

31. Yang, W. S. *et al.* Iodide management in formamidinium-lead-halide–based perovskite layers for efficient solar cells. *Science* **356**, 1376–1379 (2017).

32. Saliba, M. *et al.* Cesium-containing triple cation perovskite solar cells: improved stability, reproducibility and high efficiency. *Energy Environ. Sci.* **9**, 1989–1997 (2016).

33. Saliba, M. *et al.* Incorporation of rubidium cations into perovskite solar cells improves photovoltaic performance. *Science* **354**, 206–209 (2016).

34. Duong, T. *et al.* Rubidium Multication Perovskite with Optimized Bandgap for Perovskite-Silicon Tandem with over 26% Efficiency. *Adv. Energy Mater.* **7**, 1700228 (2017).

35. Kim, H. S. & Park, N. G. Parameters affecting I-V hysteresis of CH3NH3PbI3 perovskite solar cells: Effects of perovskite crystal size and mesoporous TiO2 layer. *J. Phys. Chem. Lett.* **5**, 2927–2934 (2014).

36. Schultes, M. *et al.* Sputtered Transparent Electrodes (IO:H and IZO) with Low Parasitic Near-Infrared Absorption for Perovskite-Cu(In,Ga)Se2 Tandem Solar Cells. *ACS Appl. Energy Mater.* **2**, 7823–7831 (2019).

37. Schultes, M. Four – Terminal Perovskite – CIGS Tandem Solar Cells with Improved Near – Infrared Response. (2019).

38. Jaysankar, M. *et al.* Perovskite-silicon tandem solar modules with optimised light harvesting. *Energy Environ. Sci.* **11**, 1489–1498 (2018).

39. Brewer, S. H. & Franzen, S. Indium tin oxide plasma frequency dependence on sheet resistance and surface adlayers determined by reflectance FTIR spectroscopy. *J. Phys. Chem. B* **106**, 12986–12992 (2002).

40. Sathiaraj, T. S. Effect of annealing on the structural, optical and electrical properties of ITO films by RF sputtering under low vacuum level. *Microelectronics J.* **39**, 1444–1451 (2008).

41. Paetzold, U. W., Qiu, W., Finger, F., Poortmans, J. & Cheyns, D. Nanophotonic front electrodes for perovskite solar cells. *Appl. Phys. Lett.* **106**, (2015).

42. Chen, D. *et al.* Nanophotonic Light Management for Perovskite-Silicon Tandem Solar Cells. 1–14 (2018) doi:10.1117/1.JPE.8.022601.

43. Tockhorn, P. *et al.* Improved Quantum Efficiency by Advanced Light Management in Nanotextured Solution-Processed Perovskite Solar Cells. *ACS Photonics* **7**, 2589–2600 (2020).

44. Langenhorst, M. *et al.* Energy yield of all thin-film perovskite/CIGS tandem solar modules. *Prog. Photovoltaics Res. Appl.* 290–298 (2018) doi:10.1002/pip.3091.

45. Kim, D. H. *et al.* Bimolecular Additives Improve Wide-Band-Gap Perovskites for Efficient Tandem Solar Cells with CIGS. *Joule* **3**, 1734–1745 (2019).

46. Scharber, M. C. & Sariciftci, N. S. Efficiency of bulk-heterojunction organic solar cells. *Prog. Polym. Sci.* **38**, 1929–1940 (2013).

47. Carlson, D. E. & Wronski, C. R. Amorphous silicon solar cell. *Appl. Phys. Lett.* **28**, 671–673 (1976).

48. Kojima, A., Teshima, K., Shirai, Y. & Miyasaka, T. Organometal halide perovskites as visible-light sensitizers for photovoltaic cells. *J. Am. Chem. Soc.* **131**, 6050–6051 (2009).

49. Kasap, S. O. *Principles of Electronic Materials and Devices*. (Tata McGraw-Hill, 2006).

50. Stranks, S. D. *et al.* Electron-hole diffusion lengths exceeding 1 micrometer in an organometal trihalide perovskite absorber. *Science* **342**, 341–344 (2013).

51. Hellmann, T. *et al.* The difference in electronic structure of MAPI and MASI perovskites and its effect on the interface alignment to the HTMs spiro-MeOTAD and CuI. *J. Mater. Chem. C* **7**, 5324–5332 (2019).

52. Byeon, J. *et al.* Charge transport layer dependent electronic band bending in perovskite solar cells and its correlation to device degradation. *arXiv* (2019).

53. Wurfel, U., Cuevas, A. & Wurfel, P. Charge carrier separation in solar cells. *IEEE J. Photovoltaics* **5**, 461–469 (2015).

54. NREL. AM 1.5G spectrum. https://www.nrel.gov/grid/solar-resource/spectra-am1.5.html.

55. Rau, U., Paetzold, U. W. & Kirchartz, T. Thermodynamics of light management in photovoltaic devices. *Phys. Rev. B - Condens. Matter Mater. Phys.* **90**, 1–16 (2014).

56. Mäckel, H. & Cuevas, A. Determination of the surface recombination velocity of unpassivated silicon from spectral photoconductance measurements. *Proc. 3rd World Conf. Photovolt. Energy Convers.* **A**, 71–74 (2003).

57. Köhler, A. & Bässler, H. *Electronic Processes in Organic Semiconductors*. (Wiley-VCH, 2015).

58. Shen, H. *et al.* Mechanically-stacked perovskite/CIGS tandem solar cells with efficiency of 23.9% and reduced oxygen sensitivity. *Energy Environ. Sci.* **11**, 394–406 (2018).

59. Deinega, A., Valuev, I., Potapkin, B. & Lozovik, Y. Minimizing light reflection from

dielectric textured surfaces. *J. Opt. Soc. Am. A* **28**, 770 (2011).

60. Schneider, B. W., Lal, N. N., Baker-Finch, S. & White, T. P. Pyramidal surface textures for light trapping and antireflection in perovskite-on-silicon tandem solar cells. *Opt. Express* **22**, A1422 (2014).

61. Schmager, R. *et al.* Texture of the Viola Flower for Light Harvesting in Photovoltaics. *ACS Photonics* **4**, 2687–2692 (2017).

62. Dottermusch, S. *et al.* Micro-cone textures for improved light in-coupling and retroreflection-inspired light trapping at the front surface of solar modules. *Prog. Photovoltaics Res. Appl.* **27**, 593–602 (2019).

63. Jošt, M. *et al.* Textured interfaces in monolithic perovskite/silicon tandem solar cells: Advanced light management for improved efficiency and energy yield. *Energy Environ. Sci.* **11**, 3511–3523 (2018).

64. Wei, J. *et al.* Enhanced Light Harvesting in Perovskite Solar Cells by a Bioinspired Nanostructured Back Electrode. *Adv. Energy Mater.* **7**, 1–7 (2017).

65. Zhang, H., Kramarenko, M., Osmond, J., Toudert, J. & Martorell, J. Natural Random Nanotexturing of the Au Interface for Light Backscattering Enhanced Performance in Perovskite Solar Cells. *ACS Photonics* **5**, 2243–2250 (2018).

66. Yablonovitch, E. Statistical Ray Optics. *J. Opt. Soc. Am.* **72**, 899–907 (1982).

67. Yablonovitch, E. & Cody, G. D. Intensity enhancement in textured optical sheets for solar cells. *IEEE Trans. Electron Devices* **2**, 300 (1982).

68. Yu, Z., Raman, A. & Fan, S. Fundamental limit of nanophotonic light trapping in solar cells. *Proc. Natl. Acad. Sci. U. S. A.* **107**, 17491–17496 (2010).

69. Schmager, R., Gomard, G., Richards, B. S. & Paetzold, U. W. Nanophotonic perovskite layers for enhanced current generation and mitigation of lead in perovskite solar cells. *Sol. Energy Mater. Sol. Cells* **192**, 65–71 (2019).

70. Jiang, Q. *et al.* Enhanced electron extraction using SnO2 for high-efficiency planar-structure HC(NH2)2 PbI3-based perovskite solar cells. *Nat. Energy* **2**, (2017).

71. Hossain, I. M. *et al.* Nanostructured front electrodes for perovskite/c-Si tandem photovoltaics. *Opt. Express* **28**, 8878 (2020).

72. Khan, I., Bauch, M., Dimopoulos, T. & Dostalek, J. Nanostructured as-deposited indium tin oxide thin films for broadband antireflection and light trapping. *Nanotechnology* **28**, 325201 (2017).

73. Shockley, W. & Queisser, H. J. Detailed balance limit of efficiency of p-n junction solar cells. *J. Appl. Phys.* **32**, 510–519 (1961).

74. Bremner, S. P., Levy, M. Y. & Honsberg, C. B. Analysis of tandem solar cell

efficiencies under AM1.5G spectrum using a rapid flux calculation method. *Prog. Photovoltaics Res. Appl.* **16**, 225–233 (2008).

75. Vos, a De, De Vos, A. & Vos, a De. Detailed balance limit of the efficiency of tandem solar cells. *J. Phys. D. Appl. Phys.* **13**, 839–846 (1980).

76. Schmager, R. *et al.* Methodology of energy yield modelling of perovskite-based multi-junction photovoltaics. *Opt. Express* **27**, A507 (2019).

77. Lehr, J. *et al.* Energy yield modelling of perovskite/silicon two-terminal tandem PV modules with flat and textured interfaces. *Sustain. Energy Fuels* **2**, 2754–2761 (2018).

78. Lal, N. N. *et al.* Perovskite Tandem Solar Cells. *Adv. Energy Mater.* **1602761**, 1–18 (2017).

79. Sahli, F. *et al.* Fully textured monolithic perovskite/silicon tandem solar cells with 25.2% power conversion efficiency. *Nat. Mater.* **17**, 820–826 (2018).

80. Al-Ashouri, A. *et al.* Conformal monolayer contacts with lossless interfaces for perovskite single junction and monolithic tandem solar cells. *Energy Environ. Sci.* **12**, 3356–3369 (2019).

81. Eperon, G. E. *et al.* Perovskite-perovskite tandem photovoltaics with optimized band gaps. *Science (80-.).* **354**, 861–865 (2016).

82. Abdollahi Nejand, B. *et al.* Vacuum-Assisted Growth of Low-Bandgap Thin Films (FA0.8MA0.2Sn0.5Pb0.5I3) for All-Perovskite Tandem Solar Cells. *Adv. Energy Mater.* **10**, (2020).

83. Eperon, G. E. *et al.* Formamidinium lead trihalide: A broadly tunable perovskite for efficient planar heterojunction solar cells. *Energy Environ. Sci.* **7**, 982–988 (2014).

84. Brenner, P. *et al.* Triple cation mixed-halide perovskites for tunable lasers. *Opt. Mater. Express* **7**, 4082 (2017).

85. Bailie, C. D. *et al.* Semi-transparent perovskite solar cells for tandems with silicon and CIGS. *Energy Environ. Sci.* **8**, 956–963 (2015).

86. Whitfield, P. S. *et al.* Structures, Phase Transitions and Tricritical Behavior of the Hybrid Perovskite Methyl Ammonium Lead Iodide. *Sci. Rep.* **6**, 1–16 (2016).

87. Baikie, T. *et al.* Synthesis and crystal chemistry of the hybrid perovskite (CH 3NH3)PbI3 for solid-state sensitised solar cell applications. *J. Mater. Chem. A* **1**, 5628–5641 (2013).

88. Goldschmidt, V. M. *et al.* Krystallbau und chemische Zusammensetzun. (1927).

89. Farooq, A. *et al.* Spectral Dependence of Degradation under Ultraviolet Light in Perovskite Solar Cells. *ACS Appl. Mater. Interfaces* **10**, 21985–21990 (2018).

90. Chen, Y. *et al.* 2D Ruddlesden–Popper Perovskites for Optoelectronics. *Adv. Mater.* **30**, 1–15 (2018).

91. Gharibzadeh, S. *et al.* Record Open-Circuit Voltage Wide-Bandgap Perovskite Solar Cells Utilizing 2D/3D Perovskite Heterostructure. *Adv. Energy Mater.* **9**, 1–10 (2019).

92. Ahmad, S. *et al.* Dion-Jacobson Phase 2D Layered Perovskites for Solar Cells with Ultrahigh Stability. *Joule* **3**, 794–806 (2019).

93. Lee, J. W. *et al.* 2D perovskite stabilized phase-pure formamidinium perovskite solar cells. *Nat. Commun.* **9**, 1–10 (2018).

94. Koh, T. M. *et al.* Enhancing moisture tolerance in efficient hybrid 3D/2D perovskite photovoltaics. *J. Mater. Chem. A* **6**, 2122–2128 (2018).

95. Liu, G. *et al.* Introduction of Hydrophobic Ammonium Salts with Halogen Functional Groups for High-Efficiency and Stable 2D/3D Perovskite Solar Cells. *Adv. Funct. Mater.* **29**, 1–9 (2019).

96. De Wolf, S. *et al.* Organometallic halide perovskites: Sharp optical absorption edge and its relation to photovoltaic performance. *J. Phys. Chem. Lett.* **5**, 1035–1039 (2014).

97. Wehrenfennig, C., Eperon, G. E., Johnston, M. B., Snaith, H. J. & Herz, L. M. High charge carrier mobilities and lifetimes in organolead trihalide perovskites. *Adv. Mater.* **26**, 1584–1589 (2014).

98. McMeekin, D. P. *et al.* A mixed-cation lead mixed-halide perovskite absorber for tandem solar cells. *Science (80-.).* **351**, 151–155 (2016).

99. Gharibzadeh, S. *et al.* 2D/3D Heterostructure for Semitransparent Perovskite Solar Cells with Engineered Bandgap Enables Efficiencies Exceeding 25% in Four-Terminal Tandems with Silicon and CIGS. *Adv. Funct. Mater.* (2020) doi:10.1002/adfm.201909919.

100. Kumawat, N. K., Liu, X. K., Kabra, D. & Gao, F. Blue perovskite light-emitting diodes: Progress, challenges and future directions. *Nanoscale* **11**, 2109–2120 (2019).

101. Mali, S. S. & Hong, C. K. P-i-n/n-i-p type planar hybrid structure of highly efficient perovskite solar cells towards improved air stability: Synthetic strategies and the role of p-type hole transport layer (HTL) and n-type electron transport layer (ETL) metal oxides. *Nanoscale* **8**, 10528–10540 (2016).

102. Yang, G., Tao, H., Qin, P., Ke, W. & Fang, G. Recent progress in electron transport layers for efficient perovskite solar cells. *J. Mater. Chem. A* **4**, 3970–3990 (2016).

103. Chueh, C. C., Li, C. Z. & Jen, A. K. Y. Recent progress and perspective in solution-processed Interfacial materials for efficient and stable polymer and organometal

perovskite solar cells. *Energy Environ. Sci.* **8**, 1160–1189 (2015).

104. Xiong, L. *et al.* Review on the Application of SnO2 in Perovskite Solar Cells. *Adv. Funct. Mater.* **28**, 1–18 (2018).

105. Hu, Z. *et al.* Effects of heteroatom substitution in spiro-bifluorene hole transport materials. *Chem. Sci.* **7**, 5007–5012 (2016).

106. Saliba, M. *et al.* How to Make over 20% Efficient Perovskite Solar Cells in Regular (n-i-p) and Inverted (p-i-n) Architectures. *Chem. Mater.* **30**, 4193–4201 (2018).

107. Wu, C.-G. *et al.* High efficiency stable inverted perovskite solar cells without current hysteresis. *Energy Environ. Sci.* **8**, 2725–2733 (2015).

108. Abzieher, T. *et al.* Electron-Beam-Evaporated Nickel Oxide Hole Transport Layers for Perovskite-Based Photovoltaics. *Adv. Energy Mater.* **9**, 1802995 (2019).

109. Bastos, J. P. *et al.* Low-cost electrodes for stable perovskite solar cells. *Appl. Phys. Lett.* **110**, (2017).

110. Li, L. *et al.* The Additive Coordination Effect on Hybrids Perovskite Crystallization and High-Performance Solar Cell. *Adv. Mater.* **28**, 9862–9868 (2016).

111. Zheng, X. *et al.* Defect passivation in hybrid perovskite solar cells using quaternary ammonium halide anions and cations. *Nat. Energy* **2**, 1–9 (2017).

112. Yin, W. J., Shi, T. & Yan, Y. Unusual defect physics in CH3NH3PbI3 perovskite solar cell absorber. *Appl. Phys. Lett.* **104**, (2014).

113. Aranda, C., Guerrero, A. & Bisquert, J. Ionic Effect Enhances Light Emission and the Photovoltage of Methylammonium Lead Bromide Perovskite Solar Cells by Reduced Surface Recombination. *ACS Energy Lett.* **4**, 741–746 (2019).

114. Yang, D. *et al.* Stable Efficiency Exceeding 20.6% for Inverted Perovskite Solar Cells through Polymer-Optimized PCBM Electron-Transport Layers. *Nano Lett.* **19**, 3313–3320 (2019).

115. Abdi-Jalebi, M. *et al.* Charge extraction via graded doping of hole transport layers gives highly luminescent and stable metal halide perovskite devices. *Sci. Adv.* **5**, 1–10 (2019).

116. Halvani Anaraki, E. *et al.* Low-Temperature Nb-Doped SnO2 Electron-Selective Contact Yields over 20% Efficiency in Planar Perovskite Solar Cells. *ACS Energy Lett.* **3**, 773–778 (2018).

117. Arora, N. *et al.* Perovskite solar cells with CuSCN hole extraction layers yield stabilized efficiencies greater than 20 %. **5655**, 1–9 (2017).

118. Snaith, H. J. *et al.* Anomalous hysteresis in perovskite solar cells. *J. Phys. Chem. Lett.* **5**, 1511–1515 (2014).

119. Van Reenen, S., Kemerink, M. & Snaith, H. J. Modeling Anomalous Hysteresis in Perovskite Solar Cells. *J. Phys. Chem. Lett.* **6**, 3808–3814 (2015).

120. Hermes, I. M., Hou, Y., Bergmann, V. W., Brabec, C. J. & Weber, S. A. L. The Interplay of Contact Layers: How the Electron Transport Layer Influences Interfacial Recombination and Hole Extraction in Perovskite Solar Cells. *J. Phys. Chem. Lett.* **9**, 6249–6256 (2018).

121. Christians, J. A., Manser, J. S. & Kamat, P. V. Best practices in perovskite solar cell efficiency measurements. Avoiding the error of Making Bad Cells Look Good. *J. Phys. Chem. Lett.* **6**, 852–857 (2015).

122. Khenkin, M. V. *et al.* Consensus statement for stability assessment and reporting for perovskite photovoltaics based on ISOS procedures. *Nat. Energy* **5**, 35–49 (2020).

123. Wang, R. *et al.* A Review of Perovskites Solar Cell Stability. *Adv. Funct. Mater.* **29**, 1–25 (2019).

124. Leijtens, T. *et al.* Overcoming ultraviolet light instability of sensitized TiO2 with meso-superstructured organometal tri-halide perovskite solar cells. *Nat. Commun.* **4**, 2885 (2013).

125. Du, T. *et al.* Formation, location and beneficial role of PbI2 in lead halide perovskite solar cells. *Sustain. Energy Fuels* **1**, 119–126 (2017).

126. Ren, H. *et al.* Efficient and stable Ruddlesden–Popper perovskite solar cell with tailored interlayer molecular interaction. *Nat. Photonics* **14**, 154–163 (2020).

127. Kim, D. *et al.* Efficient, stable silicon tandem cells enabled by anion-engineered wide-bandgap perovskites. *Science (80-.).* **368**, 155–160 (2020).

128. Christians, J. A. *et al.* Tailored interfaces of unencapsulated perovskite solar cells for >1,000 hour operational stability. *Nat. Energy* **3**, 68–74 (2018).

129. Yang, D. *et al.* High efficiency planar-type perovskite solar cells with negligible hysteresis using EDTA-complexed SnO2. *Nat. Commun.* **9**, (2018).

130. Frank, G. & Köstlin, H. Electrical properties and defect model of tin-doped indium oxide layers. *Appl. Phys. A Solids Surfaces* **27**, 197–206 (1982).

131. Chen, J., Cranton, W. & Fihn, M. Handbook of visual display technology. *Handb. Vis. Disp. Technol.* 1–3564 (2016) doi:10.1007/978-3-319-14346-0.

132. Karabanov, A. Sputtered Indium Tin Oxide for Semi-transparent Perovskite Solar Cells Erklärung. (2018).

133. Lippens, P., Segers, A., Haemers, J. & De Gryse, R. Chemical instability of the target surface during DC-magnetron sputtering of ITO-coatings. *Thin Solid Films* **317**, 405–408 (1998).

134. Wahl, T., Hanisch, J., Meier, S., Schultes, M. & Ahlswede, E. Sputtered indium zinc oxide rear electrodes for inverted semitransparent perovskite solar cells without using a protective bu ff er layer. *Org. Electron.* **54**, 48–53 (2018).

135. Tvaroěk, V., Novotný, I., Harman, R. & Kováč, J. Rf reactive sputtering of indium-tin-oxide films. *Vacuum* **36**, 479–482 (1986).

136. Sytchkova, A. *et al.* Depth dependent properties of ITO thin films grown by pulsed DC sputtering. *Mater. Sci. Eng. B Solid-State Mater. Adv. Technol.* **178**, 586–592 (2013).

137. Schackmar, F. *et al.* Perovskite Solar Cells with All-Inkjet-Printed Absorber and Charge Transport Layers. *Adv. Mater. Technol.* (2020) doi:10.1002/admt.202000271.

138. Goth, K. Reducing reflection losses in perovskite silicon tandem solar cells by introducing nanophotonic front contacts.

139. Hossain, I. M. *et al.* Scalable processing of low-temperature TiO 2 nanoparticles for high-efficiency perovskite solar cells. *ACS Appl. Energy Mater.* **2**, 47–58 (2019).

140. Jaysankar, M. *et al.* Crystallisation dynamics in wide-bandgap perovskite films. *J. Mater. Chem. A* **4**, 10524–10531 (2016).

141. Baena, J. P. C. *et al.* Highly efficient planar perovskite solar cells through band alignment engineering. *Energy Environ. Sci.* **8**, 2928–2934 (2015).

142. Ke, W. *et al.* Low-temperature solution-processed tin oxide as an alternative electron transporting layer for efficient perovskite solar cells. *J. Am. Chem. Soc.* **137**, 6730–6733 (2015).

143. Rueda-Delgado, D. *et al.* Solution-processed and evaporated C60 interlayers for improved charge transport in perovskite photovoltaics. *Org. Electron.* **77**, 105526 (2020).

144. Ponseca, C. S. *et al.* Organometal halide perovskite solar cell materials rationalized: Ultrafast charge generation, high and microsecond-long balanced mobilities, and slow recombination. *J. Am. Chem. Soc.* **136**, 5189–5192 (2014).

145. Wu, Y. *et al.* Highly compact TiO2 layer for efficient hole-blocking in perovskite solar cells. *Appl. Phys. Express* **7**, 52301 (2014).

146. Matas Adams, A., Marin-Beloqui, J. M., Stoica, G. & Palomares, E. The influence of the mesoporous TiO2 scaffold on the performance of methyl ammonium lead iodide (MAPI) perovskite solar cells: charge injection, charge recombination and solar cell efficiency relationship. *J. Mater. Chem. A* **3**, 22154–22161 (2015).

147. Choi, K. H., Chung, K. B. & Kim, H. K. D-orbital ordering of oxygen-deficient amorphous and anatase TiO2-xchannels for high mobility thin film transistors.

Appl. Phys. Lett. **102**, 153511 (2013).

148. Snaith, H. J. & Ducati, C. SnO2-Based dye-sensitized hybrid solar cells exhibiting near unity absorbed photon-to-electron conversion efficiency. *Nano Lett.* **10**, 1259–1265 (2010).

149. Fedorov, F. *et al.* Toward new gas-analytical multisensor chips based on titanium oxide nanotube array. *Sci. Rep.* **7**, 9732 (2017).

150. Gardecka, A. J., Goh, G. K. L., Sankar, G. & Parkin, I. P. On the nature of niobium substitution in niobium doped titania thin films by AACVD and its impact on electrical and optical properties. *J. Mater. Chem. A* **3**, 17755–17762 (2015).

151. Fuchs, M. *et al.* Characterization of core/shell nanoparticle thin films for gas analytical applications. *Surf. Interface Anal.* **42**, 1131–1134 (2010).

152. Zydziak, N., Hübner, C., Bruns, M. & Barner-Kowollik, C. One-step functionalization of single-walled carbon nanotubes (SWCNTs) with cyclopentadienyl-capped macromolecules via diels-alder chemistry. *Macromolecules* **44**, 3374–3380 (2011).

153. Zhang, J., Zhou, P., Liu, J. & Yu, J. New understanding of the difference of photocatalytic activity among anatase, rutile and brookite TiO_2. *Phys. Chem. Chem. Phys.* **16**, 20382–20386 (2014).

154. Niederberger, M., Bartl, M. H. & Stucky, G. D. Benzyl Alcohol and Titanium Tetrachloride s A Versatile Reaction System for the Nonaqueous and Low-Temperature Preparation of Crystalline and Luminescent Titania Nanoparticles. *Chem. Mater.* **14**, 4364–4370 (2002).

155. Zhou, H. *et al.* Interface engineering of highly efficient perovskite solar cells. *Science* **345**, 542–546 (2014).

156. Wojciechowski, K., Saliba, M., Leijtens, T., Abate, A. & Snaith, H. J. Sub-150 °C processed meso-superstructured perovskite solar cells with enhanced efficiency. *Energy Environ. Sci.* **7**, 1142–1147 (2014).

157. Chen, B. *et al.* Origin of J-V Hysteresis in Perovskite Solar Cells. *J. Phys. Chem. Lett.* **7**, 905–917 (2016).

158. Unger, E. L. *et al.* Hysteresis and transient behavior in current–voltage measurements of hybrid-perovskite absorber solar cells. *Energy Environ. Sci.* **7**, 3690–3698 (2014).

159. Rao, H. S. *et al.* Improving the Extraction of Photogenerated Electrons with SnO2 Nanocolloids for Efficient Planar Perovskite Solar Cells. *Adv. Funct. Mater.* **25**, 7200–7207 (2015).

160. Roose, B. *et al.* Mesoporous SnO2 electron selective contact enables UV-stable perovskite solar cells. *Nano Energy* **30**, 517–522 (2016).

161. Song, J. *et al.* Lowerature SnO2-based electron selective contact for efficient and stable perovskite solar cells. *J. Mater. Chem. A* **3**, 10837–10844 (2015).

162. Dong, Q. *et al.* Insight into perovskite solar cells based on SnO2 compact electron-selective layer. *J. Phys. Chem. C* **119**, 10212–10217 (2015).

163. Liu, Q. *et al.* Enhanced Stability of Perovskite Solar Cells with Low-Temperature Hydrothermally Grown SnO2 Electron Transport Layers. *Adv. Funct. Mater.* **26**, 6069–6075 (2016).

164. Anaraki, E. H. *et al.* Highly efficient and stable planar perovskite solar cells by solution-processed tin oxide. *Energy Environ. Sci.* **9**, 3128–3134 (2016).

165. Wojciechowski, K. *et al.* Heterojunction modification for highly efficient organic-inorganic perovskite solar cells. *ACS Nano* **8**, 12701–12709 (2014).

166. Wang, F., Bai, S., Tress, W., Hagfeldt, A. & Gao, F. Defects engineering for high-performance perovskite solar cells. *npj Flex. Electron.* **2**, (2018).

167. Zhao, C. *et al.* Revealing Underlying Processes Involved in Light Soaking Effects and Hysteresis Phenomena in Perovskite Solar Cells. *Adv. Energy Mater.* **5**, 1–6 (2015).

168. Moghadamzadeh, S. *et al.* Spontaneous enhancement of the stable power conversion efficiency in perovskite solar cells. *J. Mater. Chem. A* **8**, 670–682 (2020).

169. Werner, J., Niesen, B. & Ballif, C. Perovskite/Silicon Tandem Solar Cells: Marriage of Convenience or True Love Story? - An Overview. *Adv. Mater. Interfaces* **5**, 1700731 (2018).

170. Ramírez Quiroz, C. O. *et al.* Balancing electrical and optical losses for efficient 4-terminal Si-perovskite solar cells with solution processed percolation electrodes. *J. Mater. Chem. A* **6**, 3583–3592 (2018).

171. Schmager, R. Advanced light management concepts for perovskite photovoltaics. (Karlsruhe Institute of Technology, 2020). doi:10.5445/IR/1000119647.

172. Luo, Y., Liu, S., Barange, N., Wang, L. & So, F. Perovskite Solar Cells on Corrugated Substrates with Enhanced Efficiency. *Small* **12**, 6346–6352 (2016).

173. Zheng, X. *et al.* Designing nanobowl arrays of mesoporous TiO2as an alternative electron transporting layer for carbon cathode-based perovskite solar cells. *Nanoscale* **8**, 6393–6402 (2016).

174. Jang, S. *et al.* Facile fabrication of three-dimensional TiO2 structures for highly efficient perovskite solar cells. *Nano Energy* **22**, 499–506 (2016).

175. Wang, Y. *et al.* Diffraction-Grated Perovskite Induced Highly Efficient Solar Cells through Nanophotonic Light Trapping. *Adv. Energy Mater.* **8**, 1–8 (2018).

176. Meng, K. *et al.* Two-Dimensional Organic-Inorganic Hybrid Perovskite Photonic

Films. *Nano Lett.* **16**, 4166–4173 (2016).

177. Tavakoli, M. M. *et al.* Efficient, flexible and mechanically robust perovskite solar cells on inverted nanocone plastic substrates. *Nanoscale* **8**, 4276–4283 (2016).

178. Oskooi, A. *et al.* Partially disordered photonic-crystal thin films for enhanced and robust photovoltaics. *Appl. Phys. Lett.* **100**, 1–5 (2012).

179. Python, M. *et al.* Influence of the substrate geometrical parameters on microcrystalline silicon growth for thin-film solar cells. *Sol. Energy Mater. Sol. Cells* **93**, 1714–1720 (2009).

180. Siddique, R. H. *et al.* Bioinspired phase-separated disordered nanostructures for thin photovoltaic absorbers. (2017).

181. Donie, Y. J. *et al. Phase-separated nanophotonic structures by inkjet printing (submitted)*.

182. Haase, F. *et al.* Laser contact openings for local poly-Si-metal contacts enabling 26.1%-efficient POLO-IBC solar cells. *Sol. Energy Mater. Sol. Cells* **186**, 184–193 (2018).

183. Jackson, P. *et al.* Properties of Cu(In,Ga)Se2 solar cells with new record efficiencies up to 21.7%. *Phys. Status Solidi - Rapid Res. Lett.* **9**, 28–31 (2015).

184. Shen, H. *et al.* Metal halide perovskite: a game-changer for photovoltaics and solar devices via a tandem design. *Sci. Technol. Adv. Mater.* **19**, 53–75 (2018).

185. Tockhorn, P. *et al.* Improved Quantum Efficiency by Advanced Light Management in Nanotextured Solution-Processed Perovskite Solar Cells.

186. Moghadamzadeh, S. *et al.* Triple-cation low-bandgap perovskite thin-films for high-efficiency four-terminal all-perovskite tandem solar cells. *J. Mater. Chem. A* 24608–24619 (2020) doi:10.1039/d0ta07005j.

187. Holman, Z. C. *et al.* 23.6%-Efficient Monolithic Perovskite/Silicon Tandem Solar Cells With Improved Stability. *Nat. Energy* **2**, 1–7 (2017).

188. Chen, B. *et al.* Grain Engineering for Perovskite/Silicon Monolithic Tandem Solar Cells with Efficiency of 25.4%. *Joule* **3**, 177–190 (2019).

189. Luo, Y. *et al.* The Relationship between Chemical Flexibility and Nanoscale Charge Collection in Hybrid Halide Perovskites. *Adv. Funct. Mater.* **28**, 1–22 (2018).

190. Bailie, C. D. *et al.* Semi-transparent perovskite solar cells for tandems with silicon and CIGS. *Energy Environ. Sci.* **8**, 956–963 (2015).

191. Fu, F. *et al.* Low-temperature-processed efficient semi-transparent planar perovskite solar cells for bifacial and tandem applications. *Nat. Commun.* **6**, 8932 (2015).

192. Chen, A., Zhu, K., Zhong, H., Shao, Q. & Ge, G. A new investigation of oxygen flow influence on ITO thin films by magnetron sputtering. *Sol. Energy Mater. Sol. Cells* **120**, 157–162 (2014).

193. Ruf, F. *et al.* Excitonic nature of optical transitions in electroabsorption spectra of perovskite solar cells. *Appl. Phys. Lett.* **112**, (2018).

194. Krückemeier, L., Rau, U., Stolterfoht, M. & Kirchartz, T. How to Report Record Open-Circuit Voltages in Lead-Halide Perovskite Solar Cells. *Adv. Energy Mater.* **10**, (2020).

195. Jesper Jacobsson, T. *et al.* Exploration of the compositional space for mixed lead halogen perovskites for high efficiency solar cells. *Energy Environ. Sci.* **9**, 1706–1724 (2016).

196. Stolterfoht, M. *et al.* The impact of energy alignment and interfacial recombination on the internal and external open-circuit voltage of perovskite solar cells. *Energy Environ. Sci.* **12**, 2778–2788 (2019).

197. Leijtens, T., Bush, K. A., Prasanna, R. & McGehee, M. D. Opportunities and challenges for tandem solar cells using metal halide perovskite semiconductors. *Nat. Energy* **3**, 828–838 (2018).

198. Hosseinian Ahangharnejhad, R. *et al.* Irradiance and temperature considerations in the design and deployment of high annual energy yield perovskite/CIGS tandems. *Sustain. Energy Fuels* **3**, 1841–1851 (2019).

199. Hörantner, M. T. & Snaith, H. J. Predicting and optimising the energy yield of perovskite-on-silicon tandem solar cells under real world conditions. *Energy Environ. Sci.* **10**, 1983–1993 (2017).

200. Meng, L. J., Gao, J., Silva, R. A. & Song, S. Effect of the oxygen flow on the properties of ITO thin films deposited by ion beam assisted deposition (IBAD). *Thin Solid Films* **516**, 5454–5459 (2008).

201. Fallah, H. R., Ghasemi, M., Hassanzadeh, A. & Steki, H. The effect of deposition rate on electrical, optical and structural properties of tin-doped indium oxide (ITO) films on glass at low substrate temperature. *Phys. B Condens. Matter* **373**, 274–279 (2006).

202. Thirumoorthi, M. & Thomas Joseph Prakash, J. Structure, optical and electrical properties of indium tin oxide ultra thin films prepared by jet nebulizer spray pyrolysis technique. *J. Asian Ceram. Soc.* **4**, 124–132 (2016).

203. Kim, Y. S., Park, Y. C., Ansari, S. G., Lee, B. S. & Shin, H. S. Effect of substrate temperature on the bonded states of indium tin oxide thin films deposited by plasma enhanced chemical vapor deposition. *Thin Solid Films* **426**, 124–131 (2003).

204. Gwamuri, J., Marikkannan, M., Mayandi, J., Bowen, P. K. & Pearce, J. M. Influence

of oxygen concentration on the performance of ultra-thin RF magnetron sputter deposited indium tin oxide films as a top electrode for photovoltaic devices. *Materials (Basel).* **9**, (2016).

205. Cojocaru, L. *et al.* Effect of TiO2 Surface Treatment on the Current–Voltage Hysteresis of Planar-Structure Perovskite Solar Cells Prepared on Rough and Flat Fluorine-Doped Tin Oxide Substrates. *Energy Technol.* **5**, 1762–1766 (2017).

206. Qiu, W. *et al.* Pinhole-free perovskite films for efficient solar modules. *Energy Environ. Sci.* **9**, 484–489 (2016).

207. Li, G. *et al.* Overcoming the Limitations of Sputtered Nickel Oxide for High-Efficiency and Large-Area Perovskite Solar Cells. *Adv. Sci.* **4**, 1–8 (2017).

208. Langenhorst, M. *et al.* Liquid Glass for Photovoltaics: Multifunctional Front Cover Glass for Solar Modules. *ACS Appl. Mater. Interfaces* **11**, 35015–35022 (2019).

209. Ji, S., Song, K., Nguyen, T. B., Kim, N. & Lim, H. Optimal moth eye nanostructure array on transparent glass towards broadband antireflection. *ACS Appl. Mater. Interfaces* **5**, 10731–10737 (2013).

210. Rieger, J. The glass transition temperature of polystyrene. *J. Therm. Anal.* **46**, 965–972 (1996).

211. Manzoor, S. *et al.* Optical modeling of wide-bandgap perovskite and perovskite/silicon tandem solar cells using complex refractive indices for arbitrary-bandgap perovskite absorbers. *Opt. Express* **26**, 27441 (2018).

212. Green, M. A. Self-consistent optical parameters of intrinsic silicon at 300 K including temperature coefficients. *Sol. Energy Mater. Sol. Cells* **92**, 1305–1310 (2008).

213. Kirchartz, T. Generalized detailed balance theory of solar cells. *Booksgooglecom* **38**, 203 (2009).

214. Lai, W. C., Lin, K. W., Guo, T. F., Chen, P. & Liao, Y. Y. Perovskite-based solar cells with inorganic inverted hybrid planar heterojunction structure. *AIP Adv.* **8**, (2018).

List of publications and contributions to conferences

Peer-review publication (first author)

I. M. Hossain, D. Hudry, F. Mathies, T. Abzieher, S. Moghadamzadeh, D. Rueda-Delgado, F. Schackmar, M. Bruns, R. Andriessen, T. Aernouts, F. Di Giacomo, U. Lemmer, B. S. Richards, U. W. Paetzold, and A. Hadipour, "Scalable processing of low-temperature TiO 2 nanoparticles for high-efficiency perovskite solar cells," ACS Appl. Energy Mater. 2(1), 47–58 (2019).

S. Gharibzadeh, **I. M. Hossain**, P. Fassl, B. A. Nejand, T. Abzieher, M. Schultes, E. Ahlswede, P. Jackson, M. Powalla, S. Schäfer, M. Rienäcker, T. Wietler, R. Peibst, U. Lemmer, B. S. Richards, and U. W. Paetzold, "2D/3D Heterostructure for Semitransparent Perovskite Solar Cells with Engineered Bandgap Enables Efficiencies Exceeding 25% in Four-Terminal Tandems with Silicon and CIGS," Adv. Funct. Mater. (2020).

I. M. Hossain, Y. J. Donie, R. Schmager, M. S. Abdelkhalik, M. Rienäcker, T. F. Wietler, R. Peibst, A. Karabanov, J. A. Schwenzer, S. Moghadamzadeh, U. Lemmer, B. S. Richards, G. Gomard, and U. W. Paetzold, "Nanostructured front electrodes for perovskite/c-Si tandem photovoltaics," Opt. Express 28(6), 8878 (2020).

Peer-reviewed publications (co-author)

A. Farooq, **I. M. Hossain**, S. Moghadamzadeh, J. A. Schwenzer, T. Abzieher, B. S. Richards, E. Klampaftis, and U. W. Paetzold, "Spectral Dependence of Degradation under Ultraviolet Light in Perovskite Solar Cells," ACS Appl. Mater. Interfaces 10(26), 21985–21990 (2018).

I. A. Howard, T. Abzieher, **I. M. Hossain**, H. Eggers, F. Schackmar, S. Ternes, B. S. Richards, U. Lemmer, and U. W. Paetzold, "Coated and Printed Perovskites for Photovoltaic Applications," Adv. Mater. 31(26), 1806702 (2019).

R. Schmager, **I. M. Hossain**, F. Schackmar, B. S. Richards, G. Gomard, and U. W. Paetzold, "Light coupling to quasi-guided modes in nanoimprinted perovskite solar cells," Sol. Energy Mater. Sol. Cells 201(May), 110080 (2019).

S. Ternes, T. Börnhorst, J. A. Schwenzer, **I. M. Hossain**, T. Abzieher, W. Mehlmann, U. Lemmer, P. Scharfer, W. Schabel, B. S. Richards, and U. W. Paetzold, "Drying Dynamics of Solution-Processed Perovskite Thin-Film Photovoltaics: In Situ Characterization, Modeling, and Process Control," Adv. Energy Mater. 9(39), 1901581 (2019).

M. Schultes, T. Helder, E. Ahlswede, M. F. Aygüler, P. Jackson, S. Paetel, J. A. Schwenzer, **I. M. Hossain**, U. W. Paetzold, and M. Powalla, "Sputtered Transparent Electrodes (IO:H and IZO) with Low Parasitic Near-Infrared Absorption for Perovskite-Cu(In,Ga)Se2 Tandem Solar Cells," ACS Appl. Energy Mater. 2(11), 7823–7831 (2019).

S. Moghadamzadeh, **I. M. Hossain**, M. Jakoby, B. Abdollahi Nejand, D. Rueda-Delgado, J. A. Schwenzer, S. Gharibzadeh, T. Abzieher, M. R. Khan, A. A. Haghighirad, I. A. Howard, B. S. Richards, U. Lemmer, and U. W. Paetzold, "Spontaneous enhancement of the stable power conversion efficiency in perovskite solar cells," J. Mater. Chem. A 8(2), 670–682 (2020).

D. Rueda-Delgado, **I. M. Hossain**, M. Jakoby, J. A. Schwenzer, T. Abzieher, I. A. Howard, B. S. Richards, U. Lemmer, and U. W. Paetzold, "Solution-processed and evaporated C60 interlayers for improved charge transport in perovskite photovoltaics," Org. Electron. 77, 105526 (2020).

B. Abdollahi Nejand, **I. M. Hossain**, M. Jakoby, S. Moghadamzadeh, T. Abzieher, S. Gharibzadeh, J. A. Schwenzer, P. Nazari, F. Schackmar, D. Hauschild, L. Weinhardt, U. Lemmer, B. S. Richards, I. A. Howard, and U. W. Paetzold, "Vacuum-Assisted Growth of Low-Bandgap Thin Films (FA0.8MA0.2Sn0.5Pb0.5I3) for All-Perovskite Tandem Solar Cells," Adv. Energy Mater. 10(5), (2020).

J. A. Schwenzer, L. Rakocevic, T. Abzieher, Di. Rueda-Delgado, S. Moghadamzadeh, S. Gharibzadeh, **I. M. Hossain**, R. Gehlhaar, B. S. Richards, U. Lemmer, and U. W. Paetzold, "Toward Stable Perovskite Solar Cell Architectures: Robustness Against Temperature Variations of Real-World Conditions," IEEE J. Photovoltaics 10(3), 777–784 (2020).

T. Duong, H. Pham, T. C. Kho, P. Phang, K. C. Fong, D. Yan, Y. Yin, J. Peng, M. A. Mahmud, S. Gharibzadeh, B. A. Nejand, **I. M. Hossain**, M. R. Khan, N. Mozaffari, Y. L. Wu, H. Shen, J. Zheng, H. Mai, W. Liang, C. Samundsett, M. Stocks, K. McIntosh, G. G. Andersson, U. Lemmer, B. S. Richards, U. W. Paetzold, A. Ho-Ballie, Y. Liu, D. Macdonald, A. Blakers, J. Wong-Leung, T. White, K. Weber, and K. Catchpole, "High Efficiency Perovskite-Silicon Tandem Solar Cells: Effect of Surface Coating versus Bulk Incorporation of 2D Perovskite," Adv. Energy Mater. 10(9), 1–15 (2020).

S. Moghadamzadeh, **I. M. Hossain**, T. Duong, S. Gharibzadeh, T. Abzieher, H. Pham, H. Hu, P. Fassl, U. Lemmer, B. A. Nejand, and U. W. Paetzold, " Triple-cation low-bandgap perovskite thin-films for high-efficiency four-terminal all-perovskite tandem solar cells," J. Mater. Chem. A 24608–24619 (2020) doi:10.1039/d0ta07005j.

M. M. Byranvand , F. Behboodi-Sadabad, A. A Eliwi, V. Trouillet, A. Welle, S. Ternes, **I. M. Hossain**, M. R. Khan, J. A. Schwenzer, A. Farooq, B. S. Richards, J. Lahann, and U. W. Paetzold, " Chemical vapor deposited polymer layer for efficient passivation of planar perovskite solar cells," J. Mater. Chem. A 8, 20122–20132 (2020).

Submitted articles (co-author)

Y. J. Donie, S. Schlisske, R. H. Siddique, A. Mertens, V. Narasimhan, F. Schackmar, M. Pietsch, **I. M. Hossain**, G. Hernandez-Sosa, U. Lemmer, G. Gomard, "Phase-separated nanophotonic structures by inkjet printing," (submitted).

Contributions to conferences

I. M. Hossain, F. Mathies, T. Abzieher, S. Moghadamzadeh, U. Lemmer, B. S. Richards, U. W. Paetzold, and A. Hadipour, "Printable Low-temperature TiO_2 Nanoparticles for High Efficiency Stable Perovskite Solar Cells," Oral talk, ABXPV-Peroopto18, Rennes, France (2018).

I. M. Hossain, F. Mathies, T. Abzieher, S. Moghadamzadeh, B. S. Richards, U. Lemmer, D. Hudry, U. W. Paetzold, and A. Hadipour, "Printable Low-Temperature TiO_2 Nanoparticles for High Efficiency Stable Perovskite Solar Cells," Oral talk, MRS Spring Meeting, Arizona, USA (2018).

I. M. Hossain, Y. J. Donie, R. Schmager, M. S. Abdelkhalik, A. Karabanov, S. Moghadamzadeh, J. A. Schwenzer, U. Lemmer, B. S. Richards, G. Gomard, and U. W. Paetzold, "Nanophotonic front electrodes for perovskite-based tandem photovoltaics," Oral talk, HOPV19, Rome, Italy (2019).

I. M. Hossain, K. Goth, Y. J. Donie, R. Schmager, S. Gharibzadeh, M. Rienäcker, T. Wietler, R. Peibst, S. Moghadamzadeh, J. A. Schwenzer, U. Lemmer, B. S. Richards, G. Gomard, and U. W. Paetzold, "Periodic and disordered nanophotonic front electrodes for perovskite-based tandem photovoltaics," Oral talk, SPIE Optics + Photonics 2020 Digital Forum (2020).

I. M. Hossain, S. Gharibzadeh, P. Fassl, A. Mertens, S. Schäfer, M. Rienäcker, T. Wietler, R. Peibst, U. Lemmer, B. S. Richards, G. Gomard, and U. W. Paetzold, " 2D surface passivation for semi-transparent perovskite solar cells with engineered bandgap for 4T tandem photovoltaics," Oral talk, EUPVSEC online, (2020).

Acknowledgements

First of all, I would like to thank the Almighty Allah (SW) for everything.

I also would like to take the opportunity to thank everyone who supported me on my journey in my PhD. A special thanks go to Dr. Ulrich W. Paetzold for giving me the opportunity to pursue my PhD as one of the first students in his research group “Advanced Optics for Photovoltaics”. I would like to express my sincere gratitude for his guidance, motivation, patience and enthusiasm in supervising me during this time. Moreover, I would like to offer my special thanks to Prof. Dr. Bryce S. Richards and Prof. Dr. Uli Lemmer for their continuous support during my time at the Institute of Microstructure Technology and the Light Technology Institute at KIT. Furthermore, I would like to thank Prof. Dr. Heinz Kalt for taking his time and agreeing to act as my second referee.

A special thanks goes to my best friends at the institute, Saba Gharibzadeh (Saaba Jaan) and Isabel Allegro (Lsa), who were always there to provide me with intellectual and emotional support whenever it was needed. Without them, the time during my PhD would not be as fun and exciting as it has been.

I would also like to take the opportunity to thank my first friend at LTI: Sara, with whom I spent some of my best times during my PhD. I would also like to thank Diana (Dianita), who has been there always as a constant supportive friend.

Also, I would like to thank my colleagues Donie, Raphael, Abzieher, Schwenzer and Malte, with whom I have had the pleasure to start my PhD. On our journey, we shared many successful joint projects, had endless scientific and non-scientific discussions and truly an exciting time.

Additionally, I am very grateful to all my colleagues during my thesis. Special thanks go to Fassl (der übersetzer), Thomas, Ahmed, Julie, Mahdi, Roja, David, Simon, Fabrizio, Felix, Bahram (Bahru Jaan), Schackmar, Helge, Christian, Jonathan, Dominik, Henning, Brenner, Qihao, Adrian, Damien, Desky, Natalia, Marius, and Moritz. And indeed, all other former and current group members as well. It was really an enjoyable time with many scientific discussions and lots of fun activities.

I am particularly grateful to Dr. Guillaume Gomard for numerous fruitful discussions during our project together.

Moreover, special thanks go to all the external collaboration partners, namely Dr. Afshin Hadipour (IMEC), Dr. Erik Ahlswede (ZSW), Michael Rienaecker (ISFH), Dr. Robby Peibst (ISFH), Dr. Tobias Wietler (ISFH) and Dr. The Duong (ANU).

I also want to thank the Karlsruhe School of Optics and Photonics (KSOP) for providing a graduate program and for the great organization of many social events.

A very special thanks is directed to all my students: Andrei, Mathias, Sheri, Pramit, Ashif and Lovro.

Moreover, my PhD journey would not be completed without my Karlsruhe family: Salek, Rimi, Adib bhai, Nabila, Dewan and Asif bhai. Also, I would like to show my deepest gratitude towards the Karlsruhe Bangladeshi Community.

And last but not the least, I would like to thank my family: my Mom, who had to endure this long distance for the last few years, my Dad, who can now change the name tag on the door, my brother Mishu, who had the most awesome time at home without me, and Khalamoni, Khalu, Nishi, Zayyan, Mim, Babu mama and Khasru mama.